COMPUTER-AIDED, MULTI-MODAL, AND COMPRESSION DIFFUSE OPTICAL STUDIES OF BREAST TISSUE

David Richard Busch Jr.

A Dissertation

in

Physics and Astronomy

Presented to the Faculties of the University of Pennsylvania in Partial

Fulfillment of the Requirements for the Degree of Doctor of Philosophy

2011

Supervisor of Dissertation

Arjun G. Yodh

James M. Skinner Professor of Science, Department of Physics and Astronomy

Graduate Group Chairperson

Alan T. Johnson

Professor, Department of Physics and Astronomy

Dissertation Committee

Mark Goulian, Associate Professor, Department of Physics and Astronomy

Edmund J. and Louise W. Kahn Endowed Term Associate Professor of Biology

Philip Nelson, Professor, Department of Physics and Astronomy

Burt A. Ovrut, Professor, Department of Physics and Astronomy

Ravinder Reddy, Professor, Department of Radiology

Acknowledgements

The simultaneous optical and MR breast imaging project discussed in Chapter 4-6 were the results of a long standing collaboration between Prof. Arjun Yodh and Prof. Britton Chance. The late Prof. Chance, in whose lab I was based for several years, consistently provided unique and simplified solutions to scientific problem, often tying in a wide range of historical precedents. Dr. Xavier Intes and Jiangsheng Yu constructed opto-electronics of the second generation (GenII, Chapter 4-5) University of Pennsylvania Optical/MR Imaging system used in much of my work; Dr. Intes also patiently taught me the concepts and realities of time-domain instrumentation and analysis. Dr. Thomas Connick designed and constructed the (GenII and GenIII Chapter 4-6) electronics for MR Imaging. I thank Jun Zhang and Zhongyao Zhao, who assisted in the GenII and GenIIm optical/MR clinical data collection, along with the research MR technical team, Tanya Kurtz, and Doris Cain. Norman Butler patiently taught me how to run the MR scanners and answered a huge number of naive questions on clinical procedures. Dr. Saurav Pathak spent a great deal of time and effort in adapting and improving reconstruction software for diffuse optical tomography with the GenIII optical-MR imaging system; the reconstructions in Chapter 6 are due to his work. Design, construction, modification, and repair of theses multi-modal instruments were heavily dependent on the skills of the instrumentation specialists in the Department of Physics and School of Medicine, especially Mike Carman, William Pennie, and Harold ('Buddy') Borders. Barry Chen, David L. Minkoff, and Daniel Friedman assisted in various opto-electronic instrumentation used in the work described in Chapter 4-6; Han Y. Ban's assistance in construction and debugging were especially helpful.

Moving novel instrumentation into clinical settings is fraught with difficulty; Dr. Mark A. Rosen and Dr. Mitchell D. Schnall were instrumental in providing the opportunity to apply our instrumentation during their clinical research MRI studies. They also greatly assisted in clinical data collection and introduced me to clinical breast imaging. The ABI clinical coordinator team of Kathleen Thomas, Tamara April, Deborah Arnold, and Stephanie Damia, was extremely helpful in recruiting subjects for our study.

Dr. Mary Putt and Dr. Wensheng Guo provided guidance among statistical pitfalls as I put together the work in Chapter 7; Dr. Regine Choe was unstinting generous in her assistance, interpretation, and data sets. Data used in this chapter was derived from work by Dr. Joseph P. Culver, Dr. Soren D. Konecky, Dr. Alper Corlu, Dr. Kijoon Lee, Dr. Turgut Durduran, Dr. Regine Choe, Han Y. Ban, and Dr. Saurav Pathak. Our clinical collaborators include Dr. Mark A. Rosen, Dr. Mitchell D. Schnall, Dr. Brian J. Czerniecki, Dr. Julia Tchou, Dr. Douglas L. Fraker, and Dr. Angela DeMichele.

The compression study in Chapter 8 grew out of a series of conversations I had with Dr. Mark A. Rosen; Dr. Turgut Durduran and Dr. Regine Choe helped guide it to practical application. Alpha Kamara, Lauren Chaby, Avinash Rajput, and David L. Minkoff assisted in construction of various portions of the

opto-electronics; Jiaming Liang and Dr. Turgut Durduran in writing software; and Wesley Baker and Dr. Turgut Durduran in data analysis. Dr. Daniel Chen significantly eased my interpretation of the response of breast tissue to external loading. Our clinical coordinators Dalton Hance, Tiffany Alverna, Monika Koptyra, and Ellen Foster made human testing possible.

I thank the other members of Dr. Yodh's lab during my time at University of Pennsylvania not directly involved in the projects above, especially Dr. Rickson C. Mesquita, Dr. Ulas Sunar, Dr. Soren D. Konecky, Dr. Jonathan Fisher, and Aninidita Basu. Dr. Erin M. Buckley is a generous and helpful colleague, in whose company I deciphered University of Pennsylvania's regulations on graduation. My classmates at University of Pennsylvania, especially Dr. Daniel Swetz, Dr. Charles Ratliff, Dr. Jesse Kinder, and Dr. Michelle Caler, were of indubitable help in my graduate school career. Dr. Gregory Faris and Dr. George Alexandrakis introduced me to diffuse optical theory and experiment.

Dr. Turgut Durduran and Dr. Regine Choe became my mentors during the second half of my PhD work; their patience, insightful comments, and support were essential to its completion.

My parents, aunts, uncles, and, especially, siblings and cousins have supported, encouraged, and prompted me throughout my education, as well as being a reservoir of esoteric facts and contacts; I particularly thank Andrew, Megan, and Shannon. My first introduction to working science came from my uncle and godfather, the late Prof. James J. O'Leary M.D., Ph.D., who introduced me to scientific inquiry, chess, and the use of lasers to answer biological questions.

The clarity, readability, and science of Prof. Yodh's papers drew me into University of Pennsylvania and his lab. Prof. Yodh's weekly lab meetings focused not only on extracting the important kernels amidst the chaff of complicated data sets, but also on how to efficiently communicate results. His high standards and patience defined my graduate career.

Lastly, I would like to thank the volunteers who participated in these studies.

ABSTRACT

Computer-Aided, Multi-Modal, and Compression Diffuse Optical Studies of Breast Tissue

David Richard Busch Jr.
Arjun G. Yodh

Diffuse Optical Tomography and Spectroscopy permit measurement of important physiological parameters non-invasively through $\sim$10 cm of tissue. I have applied these techniques in measurements of human breast and breast cancer. My thesis integrates three loosely connected themes in this context: multi-modal breast cancer imaging, automated data analysis of breast cancer images, and microvascular hemodynamics of breast under compression.

As per the first theme, I describe construction, testing, and the initial clinical usage of two generations of imaging systems for simultaneous diffuse optical and magnetic resonance imaging. The second project develops a statistical analysis of optical breast data from many spatial locations in a population of cancers to derive a novel optical signature of malignancy; I then apply this data-derived signature for localization of cancer in additional subjects. Finally, I construct and deploy diffuse optical instrumentation to measure blood content and blood flow during breast compression; besides optics, this research has implications for any method employing breast compression, e.g., mammography.

Contents

List of Tables

List of Figures

Chapter 1

Introduction and Organization

Diffuse Optical Spectroscopy (DOS) utilizes light in the low absorption near-infra red (NIR) window, between 650 and 950 nm, to measure chromophore concentrations and scattering in thick tissues, e.g., through $\sim$10 cm of human breast tissue. Information about tissue concentrations of water, lipid, oxy- (HbO_2), deoxy- (Hb), and total-hemoglobin (Hb_t), as well as blood oxygen saturation (StO_2), and tissue scattering (i.e., the reduced scattering coefficient, μ_s') are readily derived using diffuse optics. These non-invasive, low-risk diagnostics are emerging as useful clinical tools for detection, diagnosis, and monitoring of breast cancer[1] and other pathologies[2–4]. Indeed, various studies have successfully compared Diffuse Optical Tomography (DOT) and DOS against more established clinical modalities[5–11] and have correlated pathologic findings with optically measured chromophores[12–15].

Diffuse Optical Tomography (DOT) utilizes many DOS measurements at different locations on a tissue surface to reconstruct spatially heterogeneous concentrations of chromophores and scattering parameters within the tissue interior. Images are obtained by inverting the heterogeneous diffusion equation[16–25]. The resulting tomograms are 3D maps of optical properties and chromophore concentrations, which are correlated with physiological signatures of tumors. For example, optically measured total hemoglobin concentration (Hb_t) has been correlated with micro-vessel density measured by histopathology[15]; similarly, the reduced scattering coefficient (μ_s') has been correlated with cellular and organelle volume fraction and mean size[14]. The diffuse optics community is still in the process of discovering which optically measured parameters are the most important indicators of malignancy; recent work, for example, on H_2O[26] and collagen[27] has opened up new possibilities along these lines. Furthermore, researchers at University of Pennsylvania and elsewhere have expanded the optical portfolio to measure tissue physiology via Diffuse Correlation Spectroscopy (DCS), which permits direct measurement of microvasculature blood *flow* with NIR light.

In a different vein, the combination of diffuse optics with other modalities has a rich history at the University of Pennsylvania. Pioneering clinical research combining diffuse optical measurements with ultrasound[28] and magnetic resonance imaging (MRI)[5,6], as well as sequential optical imaging and co-registration with positron emission tomography (PET)[29] and MRI,[30,31] have provided road maps for the development of multi-modal clinical diffuse optical measurements.

The work described herein focuses on applications of diffuse optics to breast cancer under three loosely connected themes: multi-modal imaging, statistical image analysis, and hemodynamic changes under compressive perturbation.

Chapter 1 provides a brief introduction to the subject and organization of this thesis. The mathematical formalism underlying diffuse optical analysis and measurable data types is presented in Chapter 2, and is followed by a description of some applications of diffuse optics to clinical problems in Chapter 3.

Some of the research described in this thesis expands upon previous multi-modality work in our group. Specifically, I have constructed new instrumentation combining optical and MR imaging, and I have begun to test these systems in the clinic (Chapter 4-6). The basic construction and application of the University of Pennsylvania 2^{nd} Generation multi-modality MR-optical imaging system is described in Chapter 4 and Chapter 5, respectively. Then, in Chapter 6, I describe my development of a new, 3^{rd} Generation, modular bilateral diffuse optical system for simultaneous imaging of breast cancer with 3 Tesla MRI.

DOT provides 3D maps of multi-parameter data about breast cancer; a major contribution of my thesis research shows how to use all of these optical parameters simultaneously to derive a probability of malignancy. In Chapter 7, I describe development and application of a novel Computer Aided Detection (CAD) schema for breast cancer in tomographic optical images. The new approach enables improved identification and localization of tumors. I also describe results from a pilot studies applying this technique to distinguish benign from malignant lesions and for tracking changes in breast cancer during chemotherapy.

In Chapter 8, I describe my work under the third theme: a set of pilot studies measuring microvascular blood flow with DCS during 'simulated' mammography. These data provide the first direct measurements of changes in microvascular blood flow during external compression, and the experiments provide proof-of-principle data for tomographic optical imaging of blood flow in breast. Finally, conclusions and future directions are summarized in Chapter 9.

Chapter 2

Introduction to Diffuse Optics

2.1 Introduction to Diffuse Optics

In this chapter, we introduce diffuse optical spectroscopy and tomography in the context of breast cancer, with some focus on multi-modal and contrast enhanced imaging. Diffuse optics is introduced in Section 2.1 and the mathematics required to interpret data are developed in Section 2.2. Experimental data types, geometries, and applications are described in Section 2.3.

Optical imaging of breast cancer traces its roots back to Cutler's 1929 observations[32,33] in tissue using broadband transillumination and ocular detection. Jobsis[34] later noted that near-infrared light (∼650-950 nm) passed through tissue with very little absorption. Part of this phenomena can be observed when one holds a flashlight against one's hand in a dark room; in this case, one can observe red light passing through the tissue. Traditional imaging methods, however, do not reveal internal tissue morphology, because of the high degree of tissue scattering. Of course, multiple light scattering by suspended particles is frequently observed in everyday life (e.g., milk or fog). Diffuse optics applies to *highly* scattering media, where the directionality of input light is quickly lost and wherein the absorption is low enough so that photons travel long distances in the media. This effect is demonstrated in Figure 2.1.

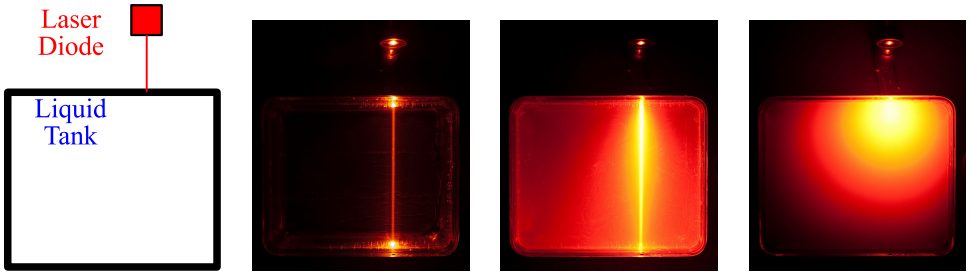

Figure 2.1: Images of laser light propagation through samples with increasing amounts of scattering agent (Intralipid, an emulsion of soy oil). Note how the input light loses direction very quickly in the rightmost figure; in this case, the input pencil beam is approximately converted into an isotropic point source just inside the scattering liquid interface. (Figure courtesy of R. Mesquita and H. Ban.)

2.2 Mathematical Basis of Diffuse Optical Specroscopy & Tomography

The diffusion equation for light fluence rate in an absorbing and highly scattering media can be rigorously derived via approximations to the radiative transport equation (RTE). See, for example, the P1 approximation in Case[35] applied to the problem of neutron transport. Durduran *et al.*[25] recently added to the many useful reviews on the topic available in the literature[22,24,36], providing a detailed derivation of the diffusion equation from the RTE. In tissue, these limits of high scattering and low absorption are often satisfied by light with wavelengths in the range of 650-950 nm, i.e., in the near-infrared (NIR) region of the spectrum. If the diffusion approximation is not valid, then the full RTE, or other approximations of the RTE, are required to properly model light transport. These alternate approaches are especially superior for modeling light transport within a few photon scattering lengths of the source position. Klose and Hielscher[37] have provided an overview of optical tomography in these latter contexts.

Photon transport of NIR light in tissue is microscopically described as a random walk characterized by two length scales, l_a and l_s, the photon absorption and scattering lengths, respectively. The photon absorption length is a strongly wavelength-dependent function of chromophore concentration; in most tissues, oxy- and deoxy-hemoglobin dominate light absorption in the NIR. The photon scattering length depends on the number and size of scattering particles. In soft tissue, organelles, collagen matrices, and other cellular and sub-cellular structures with sizes on the order of the wavelength contribute to scattering. In many tissues, the scatterer size distribution produces a 'Mie-like' wavelength dependence of the photon scattering length, and a typical scattering event tends to send photons mostly in the forward direction. The mean of the cosine of the scattering angle associated with a typical photon scattering event (i.e., the anisotropy, $g =< cos[\theta] >$, explained further in Equation 2.7), ranges[38,39] in tissue from $\sim 0.7-0.99$. Thus many forward-biased single

scattering events are typically required in tissue for a photon to loose memory of its initial direction. The net scattering effect of these 'composite events' is to isotropically scatter the "incident" photon; the distance traveled on average, by photons to become isotropic is called the photon random walk step-length or the 'reduced' photon scattering length $l_s' = l_s(1-g)^{-1}$. Typically, $l_s \sim 100$ μm and $l_s' \sim 1$ mm in tissues. This situation is depicted schematically in Figure 2.2.

The diffusion approach generally assumes that $l_a \ll l_s'$, that is, photons are scattered much more often than they are absorbed. Jacques and Pogue[22] showed that light transport in media with $l_s'/l_a > 20$ is very well approximated with the photon diffusion equation. These limits apply to measurements of many tissues with light in the NIR. For example, human breast tissue ($l_a \sim 20$ cm, $l_s' \sim 0.1$ cm) has $l_a/l_s' \sim 200$ at ~800 nm (other tissues are shown in Table 2.1).

The next few sub-sections will provide a mathematical underpinning for the analysis presented throughout this thesis. Section 2.2.1 introduces notation. Section 2.2.2 briefly describes the derivation of the photon diffusion equation from the radiative transport equation. Section 2.2.3 describes the diffusion equation for photon fluence; Section 2.2.4 describes the accompanying boundary conditions. Several analytic solutions to the diffusion equation for photon fluence in the Time (Section 2.2.5) and Frequency (Section 2.2.6) domains

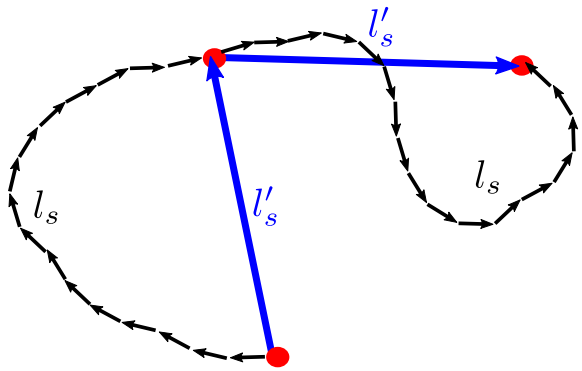

Figure 2.2: Schematic of light scattering in tissue. Most individual scattering events (black) are strongly forward biased with scattering path length $l_s \sim 10$ μm. However, many (~100) of these forward scattering events can be lumped together into a single, isotropic, event (red) with reduced scattering path length $l_s' \sim 1$ mm (blue). The absorption path length (not shown) in the diffusion regime is many times l_s'.

Tissue	l_a [cm]	l_s' [cm]	l_a/l_s'
Muscle	5	0.2	25
Brain	10	0.1	100
Breast	20	0.1	200
Liver	0.1	0.7	7

Table 2.1: Approximate Optical Properties in the NIR for various tissues near 800nm. Note that liver is *not* in the diffusion regime due to high hemoglobin content (and therefore high absorption).

are then described; these solutions are used in the analysis of Diffuse Optical Spectroscopy (DOS) measurements. We then introduce Diffuse Correlation Spectroscopy (DCS; Section 2.2.7) and Diffuse Optical Tomography (DOT; Section 2.2.8).

2.2.1 Diffuse Optical Notation

Diffusion models of photon transport are parameterized by l_a and l_s', the mean free paths for absorption and isotropic scattering. However, in the Biomedical Optics Community, these models of photon transport are typically written in terms of the inverses of the photon scattering lengths (i.e., the scattering coefficient, $\mu_s = 1/l_s$, the reduced scattering, $\mu_s' = 1/l_s'$ coefficient, and the absorption coefficient, $\mu_a = 1/l_a$).

If tissue had a single absorbing species, then $\mu_a = C \cdot \epsilon[\lambda]$. Here $\epsilon[\lambda]$ is the species wavelength dependent extinction coefficient, and C is the species concentration. Scattering and absorbing cross-sections vary with wavelength, and therefore both μ_s' and μ_a are wavelength dependent. This notation is summarized in Table 2.2.

D	Photon Diffusion Coefficient; $D = \frac{v}{3(\mu_s' + \mu_a)}$, see Equation 2.11 [cm^2 s^{-1}].
g	Anisotropy, mean cosine of scattering angle, see Equation 2.7.
l_a	Photon absorption length [cm].
l_s	Photon scattering length [cm].
l_s'	*Isotropic* photon scattering length $l_s = (1-g)l_s'$ [cm].
μ_a	Absorption coefficient, inverse of the absorption length, $\mu_a = 1/l_a$ [cm^{-1}].
$\mathbf{J}$ [$\boldsymbol{r}$,t]	Photon flux, vector sum of radiance emanating from an infinitesimal volume centered at $\boldsymbol{r}$, see Equation 2.4 [W cm^{-2}].
$L[\boldsymbol{r}, \hat{\Omega}, t]$	Light radiance at $\boldsymbol{r}$ and t in direction $\hat{\Omega}$, see Equation 2.1 and Equation 2.2 [W cm^{-2} Sr^{-1}].
μ_s	Scattering coefficient, inverse of the scattering length, $\mu_s = 1/l_s$ [cm^{-1}].
μ_s'	Reduced scattering coefficient, inverse of the isotropic scattering length, $\mu_s' = \mu_s(1-g)$ [cm^{-1}].
$\Psi[\boldsymbol{r}]$	Photon fluence rate; angular integral of the radiance at position $\boldsymbol{r}$ [W cm^{-2}].
R_{eff}	Effective Fourier reflection coefficient from a diffuse non-diffuse boundary (e.g. tissue-air).
$S[\boldsymbol{r}]$	Isotropic source term; photons emitted per volume per time at position $\boldsymbol{r}$ [W cm^{-3}].
v	Speed of light in the medium [cm s^{-1}].

Table 2.2: Important quantities and symbols in diffuse optics, to simplify discussion. Further context and definition is provided in Eqn. 2.13.

2.2.2 Approximation to the Radiative Transport Equation

Transport theory may be used to describe the propagation of light in tissues and other multiply scattering media. The Radiative Transport Equation (RTE) is a conservation equation for radiance, i.e., $L[\boldsymbol{r}, \hat{\Omega}, t]$, the power per area traveling in direction $\hat{\Omega}$, [W cm^{-2} Sr^{-1}] in an infinitesimal volume centered at $\boldsymbol{r}$. (This description follows that in Durduran *et al.*[25].) The RTE is given below.

$$\frac{1}{v}\frac{\partial L[\boldsymbol{r}, \hat{\Omega}, t]}{\partial t} + \hat{\Omega} \cdot \nabla L[\boldsymbol{r}, \hat{\Omega}, t] = -\mu_t L[\boldsymbol{r}, \hat{\Omega}, t] + Q[\boldsymbol{r}, \hat{\Omega}, t] + \mu_s \int_{4\pi} L[\boldsymbol{r}, \hat{\Omega}', t] f[\hat{\Omega}, \hat{\Omega}'] d\hat{\Omega}' \tag{2.1}$$

Here, $f[\hat{\Omega}, \hat{\Omega}']$ is the normalized differential scattering cross section associated with a tissue scattering (single-scattering) event (i.e., the probability of a photon traveling in $\hat{\Omega}$ to scatter into $\hat{\Omega}'$); $Q[\boldsymbol{r}, \hat{\Omega}, t]$ is the power per volume emitted by sources at position $\boldsymbol{r}$ in direction $\hat{\Omega}$ at time t, and v is the speed of light in the medium. The loss of radiance in an infinitesimal volume is dependent on the total attenuation coefficient $\mu_t = \mu_s + \mu_a$. The RTE describes photon transport under a wide range of conditions, but must be solved numerically for most cases of interest. However, if $L[\boldsymbol{r}, \hat{\Omega}, t]$ is nearly isotropic (e.g., in a scattering medium far from the source), an expansion of the RTE in spherical harmonics truncated after the first term turns out to be useful. This so-called P1 approximation (e.g., as in Case[35]) simplifies the radiance to

$$L[\boldsymbol{r}, \hat{\Omega}, t] = \frac{1}{4\pi}\Psi[\boldsymbol{r}, t] + \frac{3}{4\pi} J[\boldsymbol{r}, t] \cdot \hat{\Omega}. \tag{2.2}$$

Equation 2.2 introduces two terms describing photons emerging from an infinitesimal volume at $\boldsymbol{r}$ and time t:

$$\Psi[\boldsymbol{r}, t] \equiv \int_{4\pi} L[\boldsymbol{r}, \hat{\Omega}, t] d\Omega, \tag{2.3}$$

the photon fluence rate (W cm^{-2}, total power per area), and

$$\mathbf{J}[\boldsymbol{r}, t] \equiv \int_{4\pi} L[\boldsymbol{r}, \hat{\Omega}, t] \hat{\Omega} d\Omega, \tag{2.4}$$

the photon flux (W cm^{-2}, vector sum of emitted radiance). Note that $\mathbf{J}[\boldsymbol{r}, t] \cdot \hat{\Omega}$ gives a power per area traveling in direction $\hat{\Omega}$.

Integrating Equation 2.1 over all solid angle results in an equation relating Ψ and J:

$$\frac{1}{v}\frac{\partial \Psi}{\partial t} + \nabla \cdot \mathbf{J}[\boldsymbol{r}, t] + \mu_a \Psi[\boldsymbol{r}, t] = S[\boldsymbol{r}, t]. \tag{2.5}$$

Here we have introduced an 'isotropic' source term $S[\boldsymbol{r}, t] = \int Q[\boldsymbol{r}, \hat{\Omega}, t] d\Omega$ (the total power per volume emitted at position $\boldsymbol{r}$ and time t; W cm^{-3}). Multiplying Equation 2.1 by $\hat{\Omega}$ and substituting in Equation 2.2 we arrive at

$$\nabla \Psi[\boldsymbol{r}, t] = -\frac{3}{v}\frac{\partial \mathbf{J}[\boldsymbol{r}, t]}{\partial t} - 3\mu_t \mathbf{J}[\boldsymbol{r}, t] + 3\int Q[\boldsymbol{r}, \hat{\Omega}, t] \hat{\Omega} d\Omega + 3\mu_s \mathbf{J}[\boldsymbol{r}, t] \int_{4\pi} f[\hat{\Omega}, \hat{\Omega}'] \hat{\Omega} \cdot \hat{\Omega}' d\hat{\Omega}'. \tag{2.6}$$

The rightmost integral in Equation 2.6 is an ensemble average of the cosine of the scattering angle θ

$$g \equiv \langle \cos[\theta] \rangle = \int_{4\pi} f[\hat{\Omega}, \hat{\Omega}'] \hat{\Omega} \cdot \hat{\Omega}' d\hat{\Omega}' \tag{2.7}$$

and defines the anisotropy g. As scattering in tissue becomes more forward scattering, g becomes closer to 1; $g \sim 0.7 - 0.99$ for most soft tissues[38,39].

We next assume that we have isotropic sources, i.e.,

$$\int Q[\boldsymbol{r}, \hat{\Omega}, t] \hat{\Omega} d\Omega = 0, \tag{2.8}$$

and slow temporal changes in $\mathbf{J}$, i.e.,

$$\frac{1}{v} \frac{\partial \mathbf{J}}{\partial t} \ll (\mu_t - \mu_s g) \mathbf{J}. \tag{2.9}$$

In this case, Equation 2.6 reduces to Fick's law of diffusion:

$$\begin{aligned} \nabla \Psi[\boldsymbol{r}, t] &= -3 (\mu_a + \mu_s) \mathbf{J}[\boldsymbol{r}, t] + 3 g \mu_s \mathbf{J}[\boldsymbol{r}, t], \\ &= -3 (\mu_a + \mu_s (1 - g)) \mathbf{J}[\boldsymbol{r}, t], \\ &= -3 (\mu_a + \mu_s') \mathbf{J}[\boldsymbol{r}, t], \\ \nabla \Psi[\boldsymbol{r}, t] &= -\frac{v}{D} \mathbf{J}[\boldsymbol{r}, t], \end{aligned} \tag{2.10}$$

where we have utilized the reduced scattering coefficient $\mu_s' \equiv (1 - g)\mu_s$ and defined the photon diffusion coefficient

$$D \equiv \frac{v}{3(\mu_s + \mu_a)} \simeq \frac{v}{3\mu_s} = \frac{v l_s'}{3}, \tag{2.11}$$

since $\mu_a << \mu_s'$.

With Equation 2.10, Equation 2.5 becomes

$$\left(\frac{\partial}{\partial t} - \nabla \cdot (D[\boldsymbol{r}] \nabla) + v \mu_a[\boldsymbol{r}] \right) \Psi[\boldsymbol{r}, t] = v S[\boldsymbol{r}, t]. \tag{2.12}$$

Equation (2.12) is the time dependent photon diffusion equation for light in a medium with heterogeneous optical properties under the assumptions noted above.

2.2.3 Time and Frequency Domain Diffusion Equation for Photon Fluence

For time-domain experiments, it is useful to consider the time domain diffusion equation with losses. The diffusion equation for photon fluence rate (Equation 2.12, $\Psi[\boldsymbol{r}, t]$, [W cm^{-2}]) at a point $\boldsymbol{r}$ and time t due to an infinitely short, pulsed, isotropic point source at the origin ($S[\boldsymbol{r}, t] = S_0 \delta[t] \delta[\boldsymbol{r}]$) is:

$$\left(\frac{\partial}{\partial t} - \nabla \cdot \big(D[\boldsymbol{r}] \nabla\big) + v \mu_a[\boldsymbol{r}] \right) \Psi[\boldsymbol{r}, t] = v S_0 \delta[t] \delta[\boldsymbol{r}] \tag{2.13}$$

where $\delta[x]$ denotes the Kroneker Delta Function for x.

For frequency domain analysis, it is convenient to separate the point source term into oscillating (ac) and constant (dc) components: $S[\boldsymbol{r},t] = \left(S_{dc} + S_{ac}e^{-i\omega t}\right)\delta[\boldsymbol{r}]$. Solutions to the diffusion equation (Equation 2.13) which oscillate at the same frequency will have the form

$$\Psi[\boldsymbol{r},t] = U[\boldsymbol{r}]e^{-i\omega t}. \tag{2.14}$$

By substituting Equation 2.14 into Equation 2.13, we arrive at

$$\left(\nabla\cdot\left(D[\boldsymbol{r}]\nabla\right) - \left(v\mu_a[\boldsymbol{r}] - i\omega\right)\right)U[\boldsymbol{r}] = -vS_{ac}\delta[\boldsymbol{r}] \tag{2.15}$$

In a homogeneous medium, this reduces to

$$\left(\nabla^2 - k^2\right)U[\boldsymbol{r}] = -\frac{v}{D}S_{ac}\delta[\boldsymbol{r}] \tag{2.16}$$

with

$$k^2 = \frac{\left(v\mu_a - i\omega\right)}{D}. \tag{2.17}$$

Note that the frequency domain diffusion equation has a general solution in the form of an over-damped 'diffusive' wave.

Boundary conditions are discussed in Section 2.2.4; solutions in the time (Section 2.2.5) and frequency (Section 2.2.6) domains are then presented in several important experimental geometries.

2.2.4 Boundary Conditions

The spatial boundary condition for an infinite medium is simple: $\Psi \to 0$ as $\boldsymbol{r} \to \infty$. However, this geometry has limited practical utility; various geometries used in practical experiments are discussed in Section 2.3.2.

Here we will discuss the boundary conditions for 'semi-infinite' geometry (planar boundary between clear and turbid half spaces). In the case of biomedical optics, tissue in air will typically be reasonably well modeled as such a system; the resulting index of refraction mismatch will cause some photons to be reflected from the boundary. The semi-infinite boundary conditions lead naturally into those for the 'infinite slab' (two parallel planar boundaries) geometries; solutions using these conditions are utilized for the data analysis presented in subsequent chapters.

In setting out the planar boundary conditions for the semi-infinite and slab solutions to the diffusion equation, we will use a number of derived quantities to simplify notation; these quantities are summarized in Table 2.3.

Consider a turbid medium occupying an infinite half space. It is convenient to shift to cylindrical coordinates; $+\hat{z}$ is directed into the slab and ρ is the transverse distance, as shown schematically in Figure 2.3.

$$
\begin{aligned}
z_0 &= \frac{1}{\mu_s'} \\
z_b &= 2(l_s' + l_a)\frac{1 + R_{eff}}{3(1 - R_{eff})} \\
z_{+,m} &= 2m(d + 2z_b) + z_0 \\
z_{-,m} &= 2m(d + 2z_b) - 2z_b - z_0 \\
r_{+,m}^2 &= \rho^2 + (z - z_{+,m})^2 \\
r_{-,m}^2 &= \rho^2 + (z - z_{-,m})^2 \\
z_{1,m} &= d(1 - 2m) - 4mz_b - z_0 = d - z_{+,m} \\
z_{2,m} &= d(1 - 2m) - (4m - 2)z_b + z_0 = d - z_{-,m} \\
r_{1,m}^2 &= r_{+,m}^2[\rho, z = d] = \rho^2 + z_{1,m}^2 \\
r_{2,m}^2 &= r_{-,m}^2[\rho, z = d] = \rho^2 + z_{2,m}^2 \\
k_{dos}^2 &= \frac{v\mu_a}{D} \\
k^2 &= \frac{v\mu_a - i\omega}{D}
\end{aligned}
$$

Table 2.3: Notation used in describing semi-infinite and slab solutions to the diffusion equation in both time and frequency domain, where m is the index of an infinite sum of dipoles used in the method of images, d is the thickness of the slab, z_b is the extrapolated boundary condition (Equation 2.30), and z_0 is the effective source position. $r_{\{1,2\},m}$ and $z_{\{1,2\},m}$ simplify notation when one is discussing transverse measurements through a slab (i.e., $z = d$).

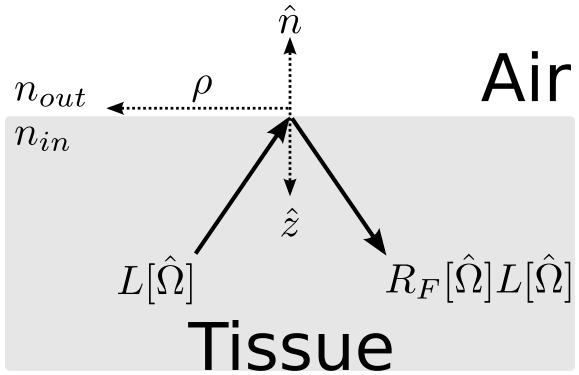

Figure 2.3: Schematic of reflection of radiance ($L[\hat{\Omega}]$) off tissue-air boundary. The fraction of light reflected is the Fresnel coefficient ($R_F[\hat{\Omega}]$); both quantities dependent on the input angle. $\hat{n}$ is the surface normal; n_{in} and n_{out} the indices of refraction in and outside the medium, respectively.

Assume input light impinges on the boundary in a narrow beam (e.g. from an optical fiber) at the origin. This input light is generally well modeled as a point source at position $z_0 = 1/\mu_s'$ into the medium.

Photons which exit the turbid medium are permanently lost. To determine the quantity of light which reflects off the boundary, we return to the discussion in Section 2.2.2 and note that the photon flux into the tissue at the boundary is equal the angular integral of the radiance in the positive $\hat{z}$ (as in Figure 2.3)

direction:

$$J_{in} = \int_{\hat{\Omega}\cdot\hat{n}<0} L[\hat{\Omega}]\hat{\Omega}\cdot(-\hat{n})d\Omega. \tag{2.18}$$

Thus, at the boundary, all of the inward diffuse radiance is due to outward radiance reflected from the index of refraction mismatch at the air-tissue boundary, i.e.,

$$J_{in} = \int_{\hat{\Omega}\cdot\hat{n}>0} R_F[\hat{\Omega}]L[\hat{\Omega}]\hat{\Omega}\cdot(\hat{n})d\Omega, \tag{2.19}$$

where $R_F[\hat{\Omega}]$ is the angularly dependent Fresnel reflection coefficient. By setting Equation 2.18 equal to Equation 2.19

$$\int_{\hat{\Omega}\cdot\hat{n}<0} L[\hat{\Omega}]\hat{\Omega}\cdot(-\hat{n})d\Omega = \int_{\hat{\Omega}\cdot\hat{n}>0} R_F[\hat{\Omega}]L[\hat{\Omega}]\hat{\Omega}\cdot(\hat{n})d\Omega.$$

Substituting in Equation 2.2 we arrive at:

$$\int_{\hat{\Omega}\cdot\hat{n}<0}\left(\frac{1}{4\pi}\Psi[\boldsymbol{r},t]+\frac{3}{4\pi}J[\boldsymbol{r},t]\cdot\hat{\Omega}\right)\hat{\Omega}\cdot(-\hat{n})d\Omega = \int_{\hat{\Omega}\cdot\hat{n}>0} R_F[\hat{\Omega}]\left(\frac{1}{4\pi}\Psi[\boldsymbol{r},t]+\frac{3}{4\pi}J[\boldsymbol{r},t]\cdot\hat{\Omega}\right)\hat{\Omega}\cdot(\hat{n})d\Omega. \tag{2.20}$$

The azimuthal angular dependence integrates out, leaving only the component in the $\hat{z}$ direction:

$$\begin{aligned}&\frac{1}{4\pi}\int_0^{\pi/2}\left(\Psi[\boldsymbol{r},t]+3J_z[\boldsymbol{r},t]cos[\theta]\right)\cos[\theta]\sin[\theta]d\theta,\\ &=\frac{1}{4\pi}\int_0^{\pi/2} R_F[\theta]\left(\Psi[\boldsymbol{r},t]+3J_z[\boldsymbol{r},t]cos[\theta]\right)\cos[\theta]\sin[\theta]d\theta.\end{aligned} \tag{2.21}$$

We define

$$R_\Psi = 2\int_0^{\pi/2} R_F[\theta]\cos[\theta]\sin[\theta]d\theta, \tag{2.22}$$

$$R_{\mathbf{J}} = 3\int_0^{\pi/2} R_F[\theta]\cos^2[\theta]\sin[\theta]d\theta, \tag{2.23}$$

and perform the angular integrals on the left side of Equation 2.21, which can then be rewritten as

$$\begin{aligned}\frac{\Psi[\boldsymbol{r},t]}{4}+\frac{\mathbf{J}_z[\boldsymbol{r},t]}{2} &= R_\Psi\frac{\Psi[\boldsymbol{r},t]}{4}+R_{\mathbf{J}}\frac{\mathbf{J}_z[\boldsymbol{r},t]}{2},\\ \Psi[\boldsymbol{r},t](R_\Psi-1) &= 2\mathbf{J}_z(1-R_{\mathbf{J}}).\end{aligned}$$

Thus, we can write the fluence rate as a constant times the flux at the boundary:

$$\Psi[\boldsymbol{r},t] = \frac{1-R_{\mathbf{J}}}{R_\Psi-1}2\mathbf{J}_Z. \tag{2.24}$$

From Equation 2.10,

$$\mathbf{J}_z = -\frac{D}{v}\frac{\partial\Psi}{\partial z}, \tag{2.25}$$

and therefore, at the boundary,

$$\Psi[\boldsymbol{r},t] = \frac{R_{\mathbf{J}}-1}{R_{\Psi}-1}\frac{2D}{v}\frac{\partial\Psi}{\partial z}. \tag{2.26}$$

We then define an effective reflection coefficient for Ψ

$$R_{eff} = \frac{R_{\Psi}+R_{\mathbf{J}}}{2-R_{\Psi}+R_{\mathbf{J}}}, \tag{2.27}$$

and arrive at

$$\Psi[\boldsymbol{r},t] = \frac{1+R_{eff}}{1-R_{eff}}\frac{2D}{v}\frac{\partial\Psi}{\partial z} \tag{2.28}$$

or more generally

$$\Psi[\boldsymbol{r},t] = \frac{1+R_{eff}}{1-R_{eff}}\frac{2D}{v}\hat{n}\cdot\nabla\Psi. \tag{2.29}$$

Where $\hat{n}$ is the surface normal as shown in Figure 2.3. We then define an extrapolated boundary position:

$$z_b = \frac{1+R_{eff}}{1-R_{eff}}\frac{2D}{v} \tag{2.30}$$

and arrive at the typical formulation of the so-called partial flux or Robin boundary condition (which includes boundary Fresnel reflection effects):

$$\Psi[\boldsymbol{r},t] = z_b\hat{n}\cdot\nabla\Psi[r,t]. \tag{2.31}$$

While exact, the partial flux boundary condition is relatively difficult use in obtaining analytical solutions to Equation 2.13. However, if we perform a Taylor expansion on Equation 2.31 and truncate after the first derivative term, we obtain a condition for which the fluence rate equals zero, i.e.,

$$\Psi[\rho, z=-z_b, t] = 0. \tag{2.32}$$

This is the so-called extrapolated zero boundary condition[40,41]; in this approximation, the fluence rate goes to zero in the plane parallel to the interface, but at a distance z_b into the 'air' side of the interface. A schematic of this extrapolated boundary is shown in Figure 2.4.

R_{eff}, and therefore z_b, is somewhat cumbersome to calculate, but can be well approximated by a polynomial in the ratio of the indices of refraction. Contini[42] writes z_b as

$$z_b = \frac{2D}{v}A \tag{2.33}$$

$$A = \frac{1+R_{eff}}{1-R_{eff}} \tag{2.34}$$

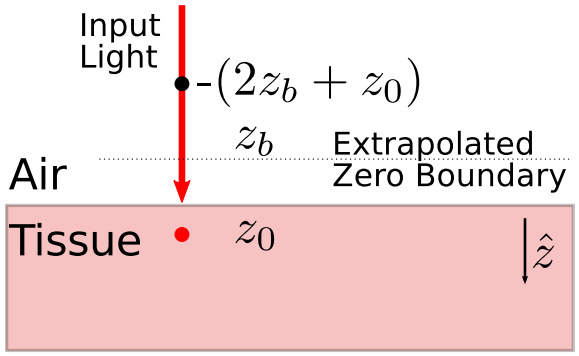

Figure 2.4: Schematic of geometry for extrapolated zero boundary condition between air and tissue. The z-axis points into the medium. A narrow beam of light (red) impinges on the surface of the tissue. This light is modeled as a point source $z_0 = 1/\mu_s'$ below the surface (red). An extrapolated boundary is placed at $-z_b$ and an image source at $-(2z_b + z_0)$ (black dot); superposition of solutions from these sources produces $\Psi[z_b] = 0$.

and approximates A as

$$\begin{aligned} A \simeq & 504.332889 - 2641.00214n + 5923.699064n^2 \\ & - 7376.355814n^3 + 5507.53041n^4 \\ & - 2463.357945n^5 + 610.956547n^6 \\ & - 64.8047n^7 + \ldots \end{aligned} \tag{2.35}$$

for $n = \frac{n_{in}}{n_{out}} > 1$ (n_{in} is inside the turbid medium and n_{out} outside) and

$$\begin{aligned} A \simeq & 3.084635 - 6.531194n + 8.357854n^2 \\ & - 5.082751n^3 + 1.171382n^4 + \ldots \end{aligned} \tag{2.36}$$

for $n = \frac{n_{in}}{n_{out}} < 1$.

With this effective zero fluence rate interface, analytic solutions to the diffusion equation (Equation 2.13 and Equation 2.15) for the semi-infinite and slab geometries can be obtained using the solutions in the infinite medium along with the method of images[43,44]; the negative image source required for modeling a semi-infinite boundary is shown in Figure 2.4. A similar analysis for two interfaces can be applied to an infinite slab. These solutions will be discussed in 2.2.5 and 2.2.6. For these simple geometries, the Green's functions and solutions are just superpositions of the infinite-media solutions (with different coefficients).

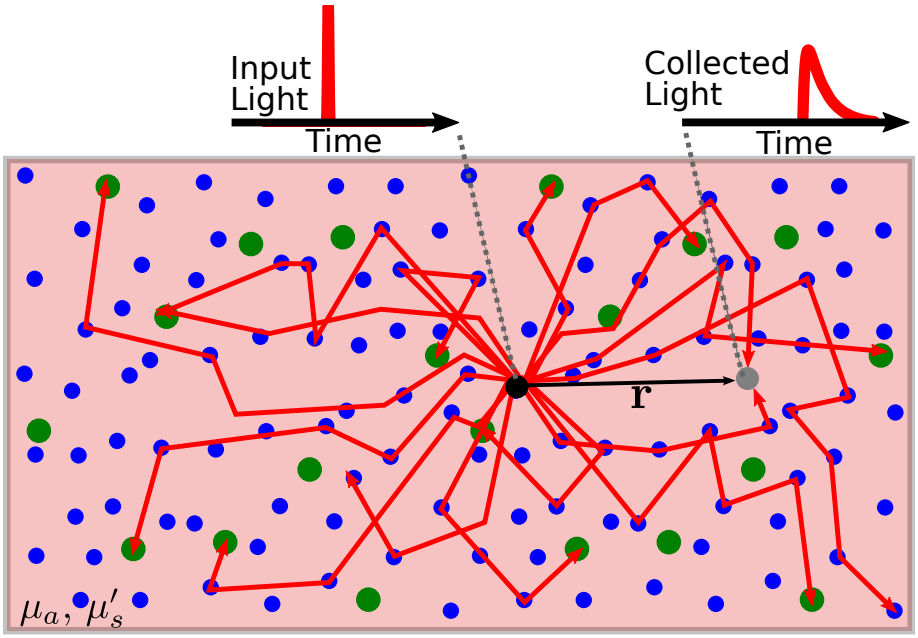

Figure 2.5: A schematic of a time domain measurement in an infinite homogeneous medium (i.e., μ_a and μ_s' are constants). A narrow input pulse is introduced into the medium (black dot, e.g. with an optical fiber). Photons scatter off the scattering centers (blue) and are absorbed by the absorbing centers (green). Most photons travel considerable distance from the input site; a few of these will arrive at a detector (gray dot, e.g., an collection optical fiber). As photons will travel many different paths to arrive at the detector, the input pulse is broadened by the time it reaches the detector.

2.2.5 Time Domain Solution to the Diffusion Equation

2.2.5.1 Solution to the Diffusion Equation in an Infinite Medium (Time-Domain)

The Green's function for Eqn. 2.13 in an infinite homogeneous turbid medium ($\mu_a[\boldsymbol{r}] = \mu_a$, $D[\boldsymbol{r}] = D$) is:

$$G_\infty[\boldsymbol{r}; \boldsymbol{r}_s, t] = \frac{v}{(4\pi Dt)^{3/2}} e^{-\frac{|\boldsymbol{r}-\boldsymbol{r}_s|^2}{4Dt} - \mu_a v t} \tag{2.37}$$

where $r = |\boldsymbol{r}|$, and the source is positioned at $\boldsymbol{r}_s$. Note $G_\infty \to 0$ as $\boldsymbol{r} \to \infty$ and $t \to \infty$. Figure 2.5 provides a schematic of this process for a source positioned at the origin. Real physical sources will have finite spatial size and temporal width, and the fluence rate in these cases will be derived from a convolution of the Green's function with some spatial and temporal form characteristic of the source. In typical experiments, the temporal form is measured; this measured signal is often called the 'Instrument Response Function' (IRF; discussed in detail in Section 2.3.3) and included in the analysis by convolution with the solution for an infinitely-short pulsed source.

Note that this analysis permits calculation of the average photon dwell time in tissue: $G[\boldsymbol{r}, t]$ describes a distribution function of photon arrival times due to a source at the origin and a detector at $\boldsymbol{r}$. The time integral of this function is the CW photon transmission probability; higher order moments can also be used

directly for calculation of optical properties[45]. Arridge[46,47] has calculated these mean transit times (first temporal moments) for several geometries; Eqn. 2.38, below, is the mean time for an infinite homogeneous medium, where $\boldsymbol{r}$ is the displacement between the source and detector.

$$\langle t \rangle = \frac{1}{2} \frac{|\boldsymbol{r}|^2}{D + |\boldsymbol{r}| \sqrt{\mu_a \cdot v \cdot D}} \tag{2.38}$$

This mean transit time is sometimes converted into a Differential Path Length Factor (DPF) or Differential Path length (DP) where $DPF = \frac{v \langle t \rangle}{|\boldsymbol{r}|}$ and $DP = v \langle t \rangle$ (see also Sassaroli[48]).

2.2.5.2 Solution to the Diffusion Equation in a Semi-Infinite Medium (Time Domain)

In the semi-infinite geometry (Figure 2.6), we apply the method of images to account for the boundary:

$$G_{semi-\infty}[\boldsymbol{r}; \boldsymbol{r}_s, t] = G_\infty[\boldsymbol{r}; \boldsymbol{r}_s, t] - G_\infty[\boldsymbol{r}; \boldsymbol{r}'_s, t] \tag{2.39}$$

where $\boldsymbol{r}'_s$ is the position of the so-called image source.

Light is generally introduced into tissue using an optical fiber or a thin 'pencil' beam; for simplicity of notation, we choose to place our input position at the origin (e.g., at $\rho = 0$, $z = 0$ or $\boldsymbol{r} = 0$). This situation is well modeled by a point source displaced one reduced scattering path length into the medium ($\rho = 0$, $z = z_0 = l'_s$ or $\boldsymbol{r}_s = [0, 0, z_0]$); i.e.,

$$S[\rho = 0, z, t] = S_0 \delta[t] \delta[\rho] \delta[z - z_b]. \tag{2.40}$$

This geometry is shown schematically in Figure 2.6.

Utilizing this model for the source and the extrapolated zero boundary condition described in Section 2.2.4, we obtain

$$G_{semi-\infty}[\boldsymbol{r}; \boldsymbol{r}_s, t] = G_\infty[\boldsymbol{r}; \boldsymbol{r}_s, t] - G_\infty[\boldsymbol{r}; \boldsymbol{r}'_s, t] \tag{2.41}$$

$$G_{semi-\infty}[\rho, z; \rho_s = 0, z_s = z_0, t] = \frac{v}{(4\pi D t)^{3/2}} e^{-\mu_a v t} \left(e^{-\frac{(z-z_0)^2+\rho^2}{4Dt}} - e^{-\frac{(z+z_0+2z_b)^2+\rho^2}{4Dt}} \right) \tag{2.42}$$

where $\boldsymbol{r}'_s = [0, 0, -(2z_b + z_0)]$ (see Figure 2.4).

Note, the analytical solution for the fluence rate Ψ from a source at $\boldsymbol{r}_s$ of the form $S = S_0 \delta[t] \delta[\boldsymbol{r}_s]$ is simply

$$\Psi[\boldsymbol{r}, t] = S_0 G[\boldsymbol{r}; \boldsymbol{r}_s, t]. \tag{2.43}$$

Combining the source term described in Equation 2.40 with the Green's function solution to the diffusion equation in Equation 2.42, we can express the photon fluence rate in a semi-infinite medium $\Psi_{semi-\infty}$ as

$$\Psi_{semi-\infty}[\rho, z, t] = S_0 \frac{v}{(4\pi D t)^{3/2}} e^{-\mu_a v t} \left(e^{-\frac{(z-z_0)^2+\rho^2}{4Dt}} - e^{-\frac{(z+z_0+2z_b)^2+\rho^2}{4Dt}} \right); \tag{2.44}$$

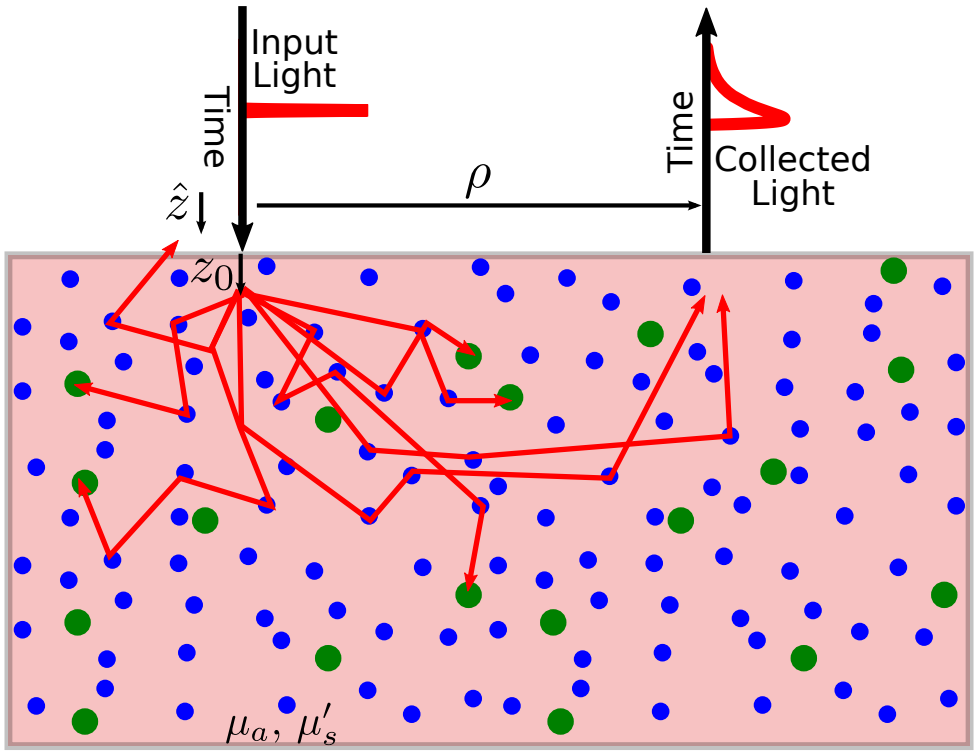

Figure 2.6: Schematic of semi-infinite (remission) geometry DOS, for a measurement on the input plane.

see Kienle [49] for additional details.

Evaluating this expression on the clear-turbid (air-tissue, $z = 0$) interface results in

$$\Psi_{semi-\infty}[\rho, z = 0, t] = S_0 \frac{v}{(4\pi Dt)^{3/2}} e^{-\mu_a v t} \left(e^{-\frac{z_0^2+\rho^2}{4Dt}} - e^{-\frac{(z_0+2z_b)^2+\rho^2}{4Dt}} \right) \tag{2.45}$$

and measurable signal (power crossing the boundary or the integration over all possible photon angles exiting the turbid medium a distance ρ from the source)[42] is

$$R[\rho, t] = \frac{D}{v} \frac{\partial}{\partial z} \Psi_{semi-\infty}[\rho, z = 0, t] \tag{2.46}$$

$$= \frac{S_0}{2(4\pi D)^{3/2} t^{5/2}} e^{-\mu_a v t} \left(z_0 e^{-\frac{z_0^2-\rho^2}{4Dt}} + (z_0 + 2z_b)\, e^{-\frac{(z_0+2z_b)^2-\rho^2}{4Dt}} \right) \tag{2.47}$$

2.2.5.3 Solution to the Diffusion Equation in an Infinite Slab (Time Domain)

Similarly, we can apply the extrapolated boundary conditions to a pair of parallel planar interfaces making up an infinite slab (Figure 2.7). Various derived quantities which permit simplification of the equations are shown in Table 2.3. The source is positioned at [$\rho = 0$, $z = z_0$] for notational convenience. This geometry is shown schematically in Figure 2.8.

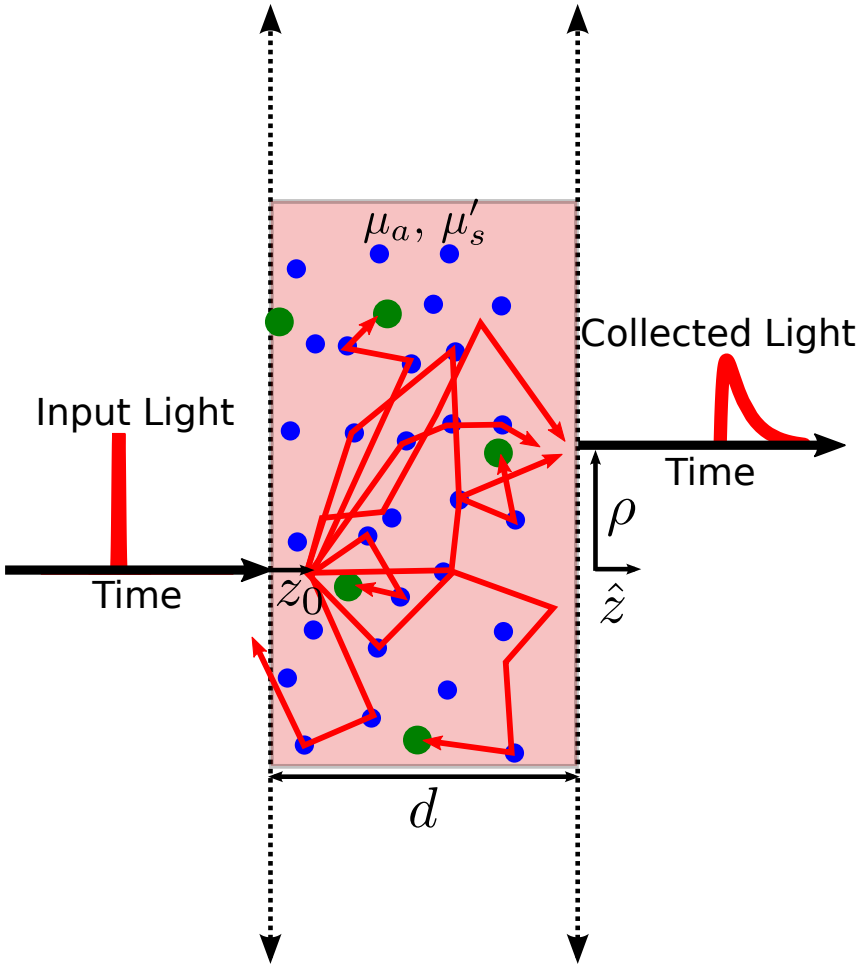

Figure 2.7: Schematic of infinite slab geometry DOS. A thin 'pencil' beam of light introduced to the tissue at $\rho = 0$, $z = 0$ is well modeled as a point source at $\rho = 0$, $z = z_0 \sim l_s'$.

The Green's function in such a slab with extrapolated boundary conditions, solved with the method of images is[42]:

$$G_{slab}[\rho, z; \rho_s = 0, \rho_z = 0, t] = \frac{v e^{-\mu_a v t} e^{-\frac{\rho^2}{4\pi D t}}}{2(4\pi D t)^{3/2}} \left(\sum_{m=-\infty}^{+\infty} \left[e^{-\frac{(z - z_{+,m})^2}{4Dt}} \right] - \sum_{m=-\infty}^{+\infty} \left[e^{-\frac{(z - z_{-,m})^2}{4Dt}} \right] \right). \tag{2.48}$$

However, this solution does not yet describe the detected light (i.e., the radiance integrated over the collection solid angle). Integrating over all possible photon angles existing the slab at a distance ρ from the source, the detectable light transmission can be shown to be

$$T[\rho, t] = -\frac{D}{v} \frac{\partial}{\partial z} \Psi[\rho, z = d, t]. \tag{2.49}$$

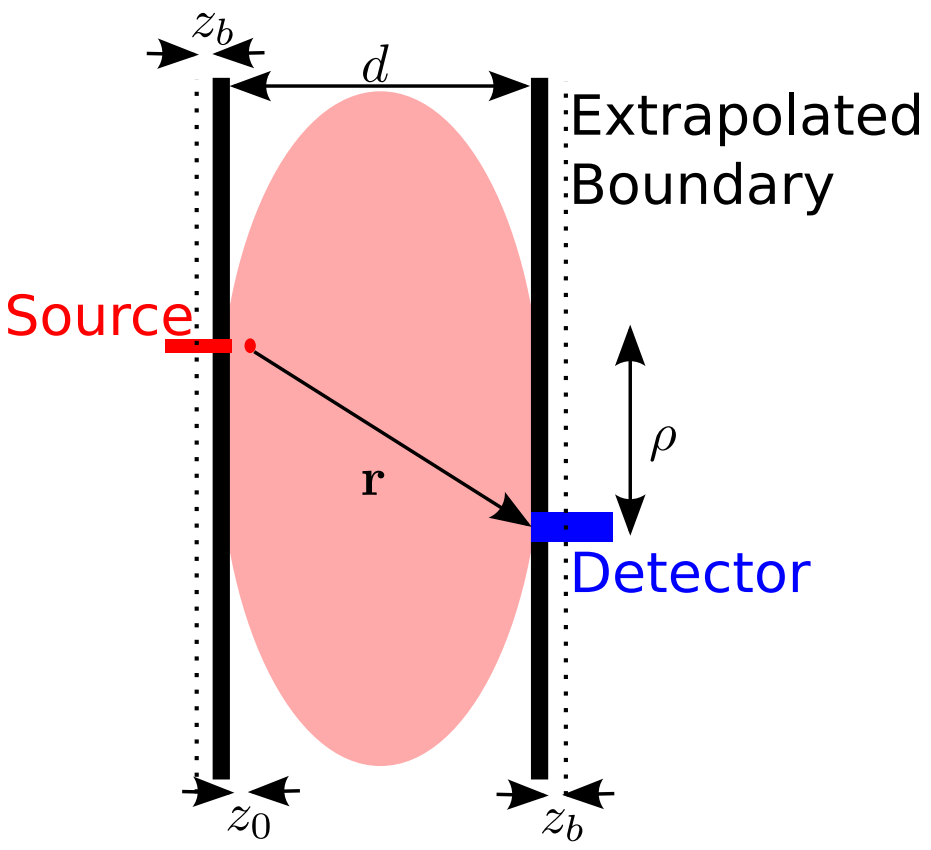

Figure 2.8: Compressed breast geometry ('slab'). $\boldsymbol{r}$ distance between source and detector, ρ lateral (in plane) separation between source and detector, d plate separation, $z_0 = (\mu_s')^{-1}$ extrapolated source position, and z_b is the location of the extrapolated boundary.

Combining Equation 2.43 and Equation 2.49, the transmitted light is described by

$$T[\rho,t] = \frac{S_0 e^{-\mu_a v t} e^{-\frac{\rho^2}{4\pi D t}}}{2(4\pi D)^{3/2} t^{5/2}} \sum_{m=-\infty}^{+\infty} \left[z_{1,m} e^{-\frac{z_{1,m}^2}{4Dt}} - z_{2,m} e^{-\frac{z_{2,m}^2}{4Dt}} \right]. \tag{2.50}$$

This expression usually is truncated after sufficient terms have been included to fit experimental data to the required accuracy. Note that we have not yet included the finite temporal width of a physical source in this expression; as mentioned above, this is accounted for by convoluting the solution for an infinitely short pulse with the measured Instrument Response Function for a particular instrument.

Equation 2.50 can be integrated over time to provide the CW transmission as a function the transverse distance ρ:

$$\begin{aligned} T[\rho] = \frac{S_0}{4\pi} \sum_{m=-\infty}^{\infty} & \frac{z_{1,m}}{r_{1,m}^3} \left(1 + k_{dos} r_{1,m}\right) e^{-k_{dos} r_{1,m}} \\ & - \frac{z_{2,m}}{r_{2,m}^3} \left(1 + k_{dos} r_{2,m}\right) e^{-k_{dos} r_{2,m}}. \end{aligned} \tag{2.51}$$

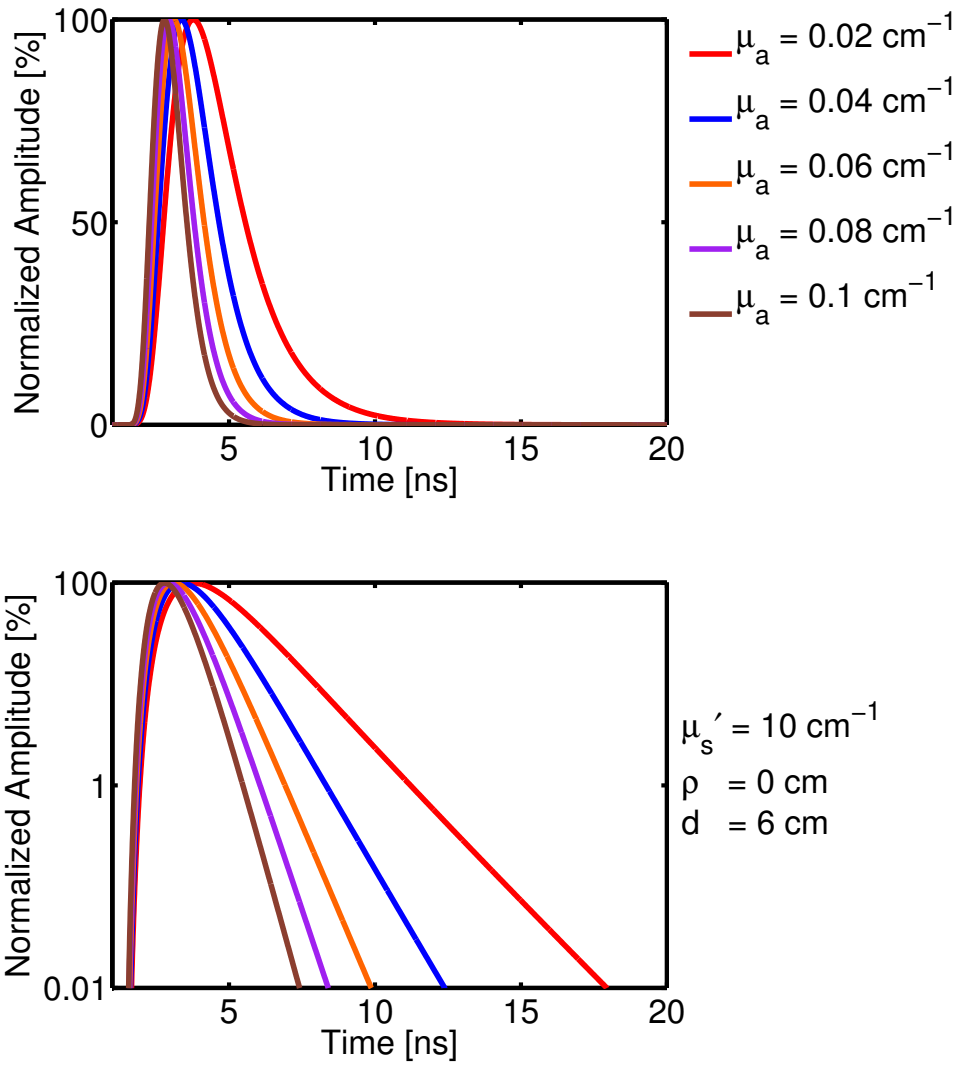

Figure 2.9: Graphs of Equation 2.50 for a slab with d=6 cm, $\rho = 0$ cm, $\mu_s' = 10$ cm^{-1}, and μ_a as noted in the legend. The amplitude for all the curves is normalized to show how longer photon paths (i.e., longer times) are suppressed as the absorption is increased.

This is the probability per unit area of a photon exiting the medium at ρ on the output plane. Examples of Equation 2.50 with various combinations of parameters are shown in Figures 2.9 through 2.11.

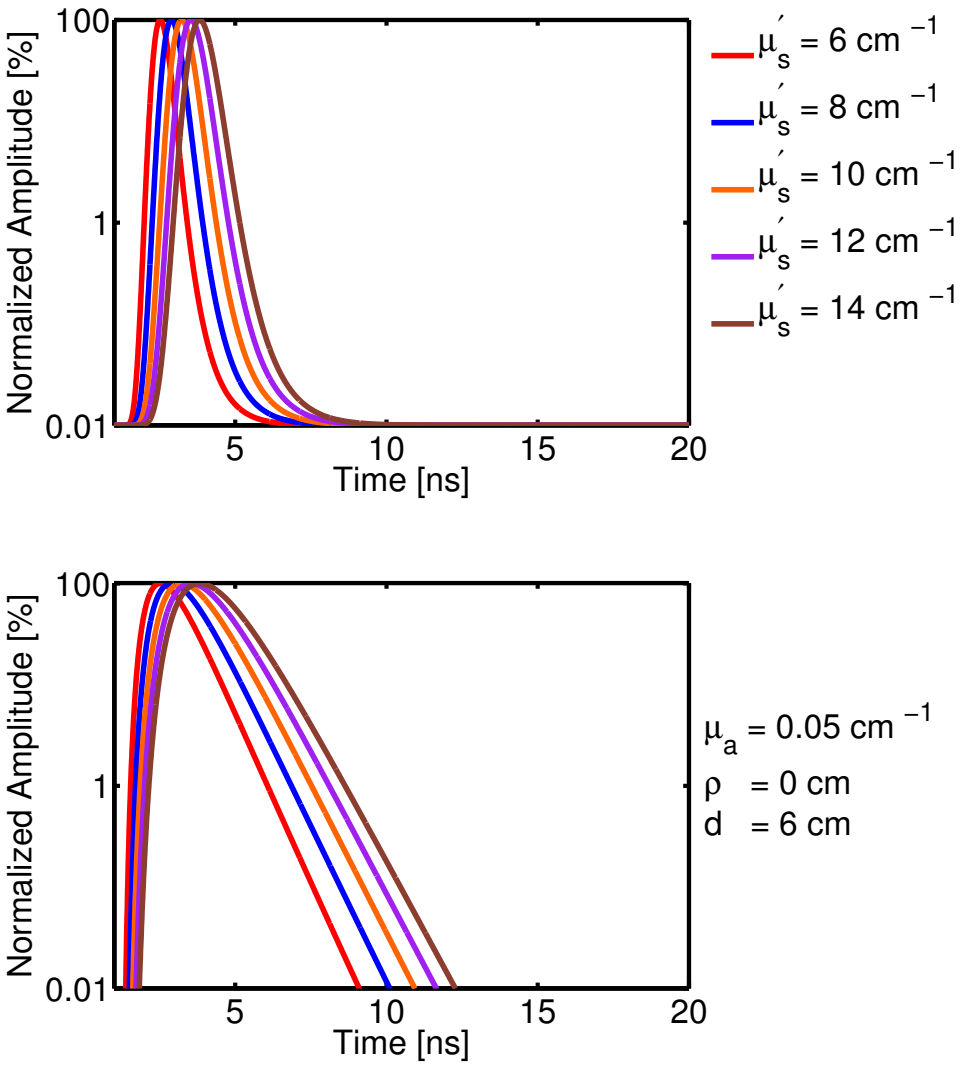

Figure 2.10: Graphs of Equation 2.50 for a slab with d=6 cm, $\rho = 0$ cm, $\mu_a = 0.05$ cm^{-1}, and μ_s' as noted in the legend. The amplitude is normalized for all curves. Note that the primary effect of increasing scattering is to delay the time-to-peak of the curve; the terminal slopes of all of the scattering values are approximately equal.

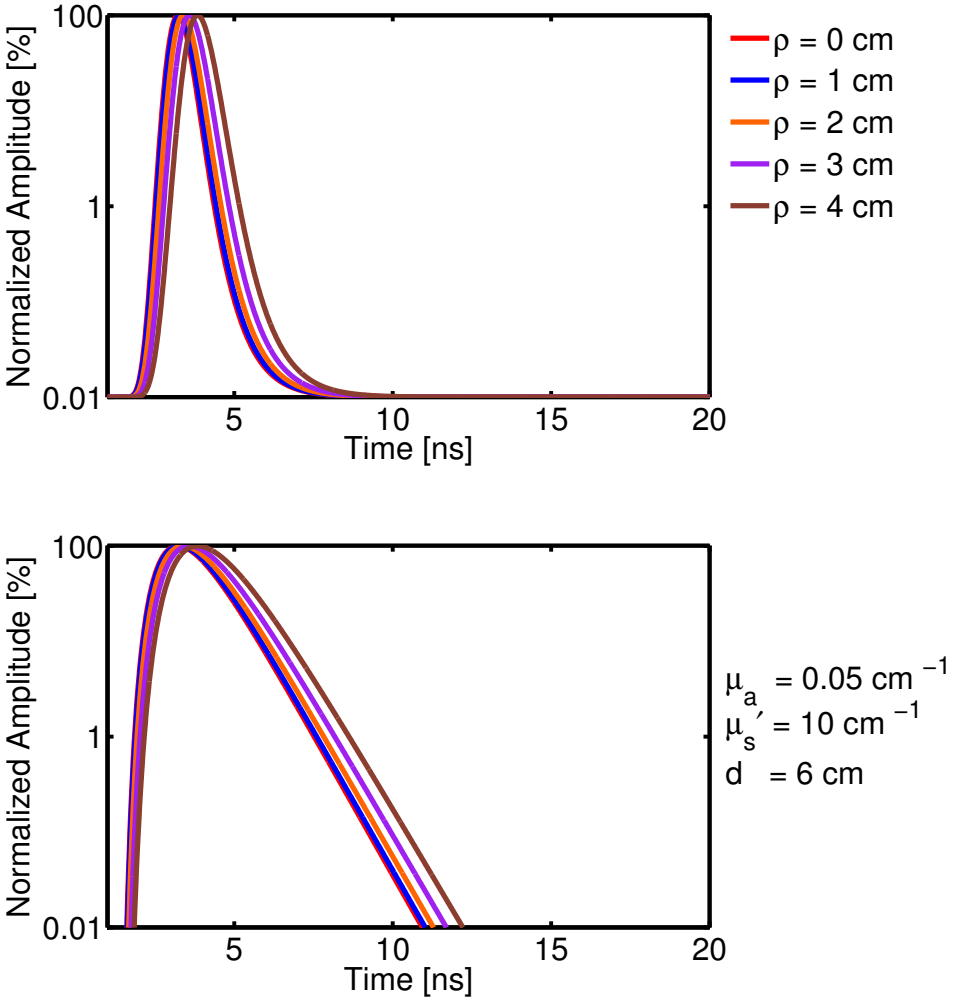

Figure 2.11: Graphs of Equation 2.50 for a slab with d=6 cm, μ_a =0.05 cm^{-1}, $\mu_s' = 10$ cm^{-1}, and ρ as noted in the legend. Note, as the transverse distance between the source and detector increases, the entire curve is shifted to later times.

2.2.6 Frequency Domain Solution to the Diffusion Equation

This section summarizes some important results solving the photon diffusion equation in the frequency domain (Equation 2.15). The geometries used are identical to those shown schematically in Section 2.2.5.

2.2.6.1 Solution to the Diffusion Equation in an Infinite Medium (Frequency Domain)

In an infinite homogeneous medium, Equation 2.16 has a well known Green's function:

$$G_{\infty}[\boldsymbol{r};\boldsymbol{r}_s,\omega] = \frac{1}{4\pi|\boldsymbol{r}-\boldsymbol{r}_s|}e^{-k|\boldsymbol{r}-\boldsymbol{r}_s|}. \tag{2.52}$$

Where $\boldsymbol{r}_s$ is the location of the source $k^2 = \frac{\mu_a v - i\omega}{D}$ (note that this reduces to the k_{dos} defined in Table 2.3 for $\omega = 0$).

2.2.6.2 Solution to the Diffusion Equation in a Semi-Infinite Medium (Frequency Domain)

Again applying the method of images and the boundary conditions described in Section 2.2.4, the Green's function solution for a semi-infinite medium can be written as

$$G_{semi-\infty}[\rho,z;\rho_s=0,z_s=z_0,\omega] = \frac{1}{4\pi}\left(\frac{e^{-k|\boldsymbol{r}_a|}}{\boldsymbol{r}_a} - \frac{e^{-k|\boldsymbol{r}_b|}}{\boldsymbol{r}_b}\right) \tag{2.53}$$

for a source positioned at $[\rho = 0, z = z_0]$, $\boldsymbol{r}_a^2 = (z-z_0)^2 + \rho^2$, and $\boldsymbol{r}_b^2 = (z+2z_b+z_0)^2 + \rho^2$.

2.2.6.3 Solution to the Diffusion Equation in an Infinite Slab (Frequency Domain)

$$G_{slab}[\rho,z;\rho_s=0,z_s=z_0,\omega] = \frac{1}{4\pi}\sum_{m=-\infty}^{\infty}\left(\frac{e^{-k|\boldsymbol{r}_{+,m}|}}{\boldsymbol{r}_{+,m}} - \frac{e^{-k|\boldsymbol{r}_{-,m}|}}{\boldsymbol{r}_{-,m}}\right) \tag{2.54}$$

for a source positioned at $[\rho = 0, z = z_0]$. For the $\omega = 0$ CW case, $k \to k_{dos} = \frac{v\mu_a}{D}$, and the Green's function is

$$G_{slab}[\rho,z;\rho_s=0,z_s=z_0,\omega=0] = \frac{1}{4\pi}\sum_{m=-\infty}^{\infty}\left(\frac{e^{-k_{dos}|\boldsymbol{r}_{+,m}|}}{\boldsymbol{r}_{+,m}} - \frac{e^{-k_{dos}|\boldsymbol{r}_{-,m}|}}{\boldsymbol{r}_{-,m}}\right) \tag{2.55}$$

evaluating this in transmission (i.e., $z = d$ as in Table 2.3), $\boldsymbol{r}_{\pm,m} \to \boldsymbol{r}_{\{1,2\},m}$

$$G_{slab}[\rho,z=d;\rho_s=0,z_s=z_0,\omega=0] = \frac{1}{4\pi}\sum_{m=-\infty}^{\infty}\left(\frac{e^{-k_{dos}|\boldsymbol{r}_{1,m}|}}{\boldsymbol{r}_{1,m}} - \frac{e^{-k_{dos}|\boldsymbol{r}_{2,m}|}}{\boldsymbol{r}_{2,m}}\right). \tag{2.56}$$

As with Equation 2.50, these Green's function solutions can be used to compute the photon current at the surface of the boundary[50]; examples are shown in Figure 2.12.

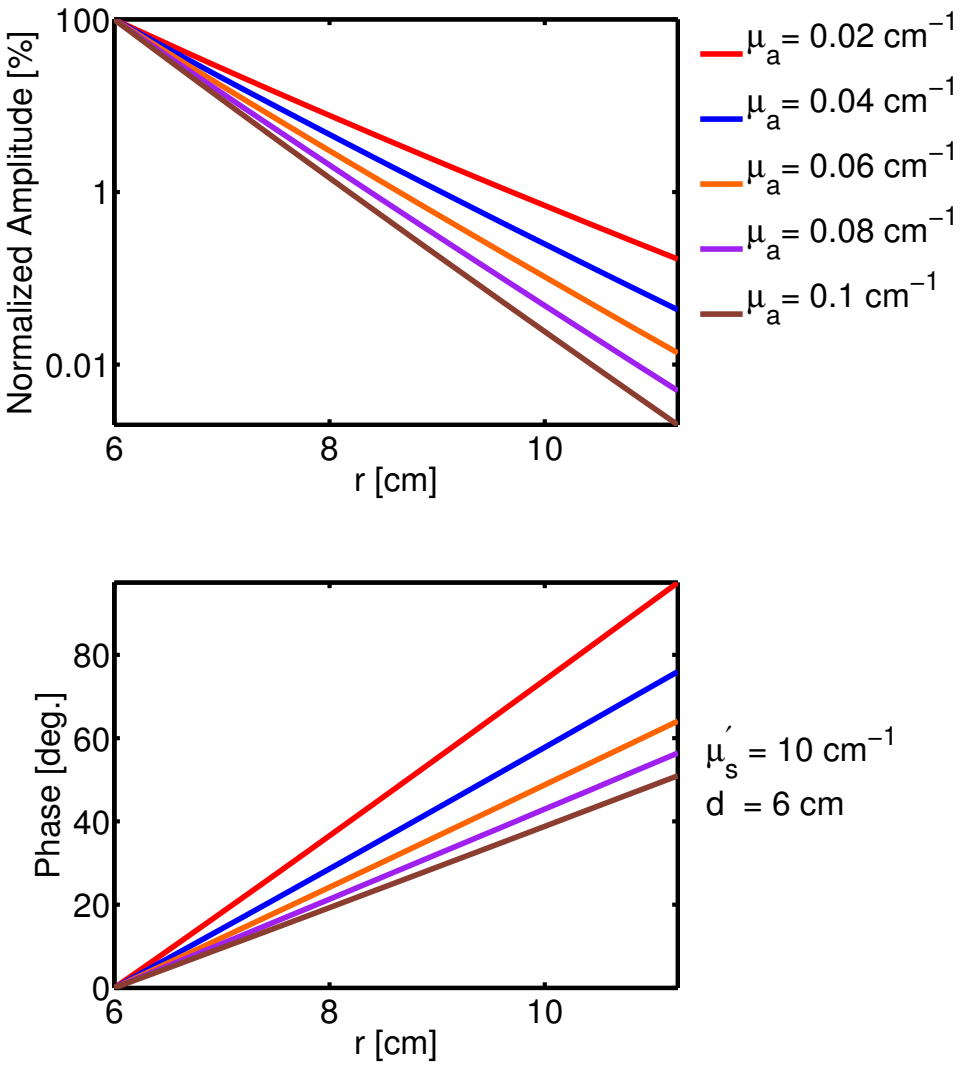

Figure 2.12: Graphs of Equation 2.56 for a slab with d=6 cm, μ_a =0.05 cm^{-1}, $\mu_s' = 1$ mm^{-1}, and ρ as noted in the legend. Note, these graphs are plotted vs. $|\boldsymbol{r}|$, not ρ, to linearize the change in phase and amplitude.

2.2.7 Diffuse Correlation Spectroscopy (DCS)

Diffusing light can also probe the *dynamics* of scatterers in tissue. It is well known that coherent light reflected off a surface or passed through a sample of dilute scatterers (single scattering limit) will form an interference ('speckle') pattern. Similarly, in the multiple scattering limit, an interference pattern is formed on tissue surfaces after illumination with a coherent source. At any one point, the speckle intensity is due to the summation of the electric fields over all arriving photons, each with a different path. If one monitors a speckle as a function of time, the temporal fluctuations of intensity or field can be used to derive information about the scatterer motions in the sample.

Diffuse Correlation Spectroscopy (DCS) is a technique wherein light from a long-coherence-length (narrow bandwidth) laser illuminates tissue. Diffuse (multiply scattered) light from the tissue is then detected one photon at a time and then the intensity temporal auto-correlation function of the diffuse light is calculated. As scatterers move, the superimposed contributions of the scattered light from different photon paths are detected as an intensity fluctuation. The temporal autocorrelation of this intensity as a function of delay time τ is dependent on the mean-squared displacement, $< \Delta r^2[\tau] >$, of the scattering particles (e.g. Figure 2.13). It turns out that the transport of the associated field auto-correlation function through the medium can also be modeled using a diffusion equation of a slightly different form than for fluence rate. (Note, DOS does not measure these dynamics; it measures only the average intensity.)

The key concept behind the use of DCS in tissues is that an increase in blood flow leads to an increased rate of fluctuations of the phase of the diffuse light field. A schematic of this technique is shown in Figure 2.13. Essentially, light from a long coherence length laser is introduced into tissue and a single mode fiber collects scattered light, and the light is thus routed into a photon-counting APD operating in Geiger mode. A multi-delay auto-correlator then computes the temporal intensity auto-correlation function and transmits it to a computer for storage. An example experimental apparatus is shown in Figure 2.13.

In the remainder of this section, we will sketch out key assumptions and results for DCS, including solutions for the correlation diffusion equation in several geometries. A recent review by Durduran[25] provides a more complete explanation and many detailed references.

Dynamic light scattering (sometimes called quasi-elastic light scattering) is a well known technique to measure the motion of dilute suspensions of scatterers (e.g. in the single scattering limit)[52–54]. Light from an illumination beam induces a dipole in each of the scatterers; these oscillating dipoles emit scattered light fields in all directions. A detector measures the superposition of the radiating dipole electric fields as a function of time. When the scattering particles move, the relative phases of the scattered light fields at the detector change; thus, the detected intensity fluctuates with time.

In the single scattering limit for independent particles with isotropic dynamics, the detected normalized electric field temporal auto-correlation function is

$$g_1[\tau] \equiv \frac{< \mathbf{E}^*[t] \cdot \mathbf{E}[t+\tau] >}{< |\mathbf{E}[t]|^2 >} = e^{i2\pi f \tau} e^{-\mathbf{q}^2 < \Delta r^2[\tau] > /6} \tag{2.57}$$

where f is the light frequency, $\mathbf{q} = \mathbf{k}_{out} - \mathbf{k}_{in}$ is the scattered wave vector, $< \Delta r^2[\tau] >$ is the mean-square displacement of the typical scatterer in time τ, $\mathbf{E}$ is the total electric field at the detector, and brackets $<>$ denote time or ensemble averages. In practice, it is much easier to measure intensity ($I[t] = |E[t]|^2$), than the field auto-correlation function:

$$g_2[\tau] \equiv \frac{< I[t] \cdot I[t+\tau] >}{< |I[t]|^2 >}. \tag{2.58}$$

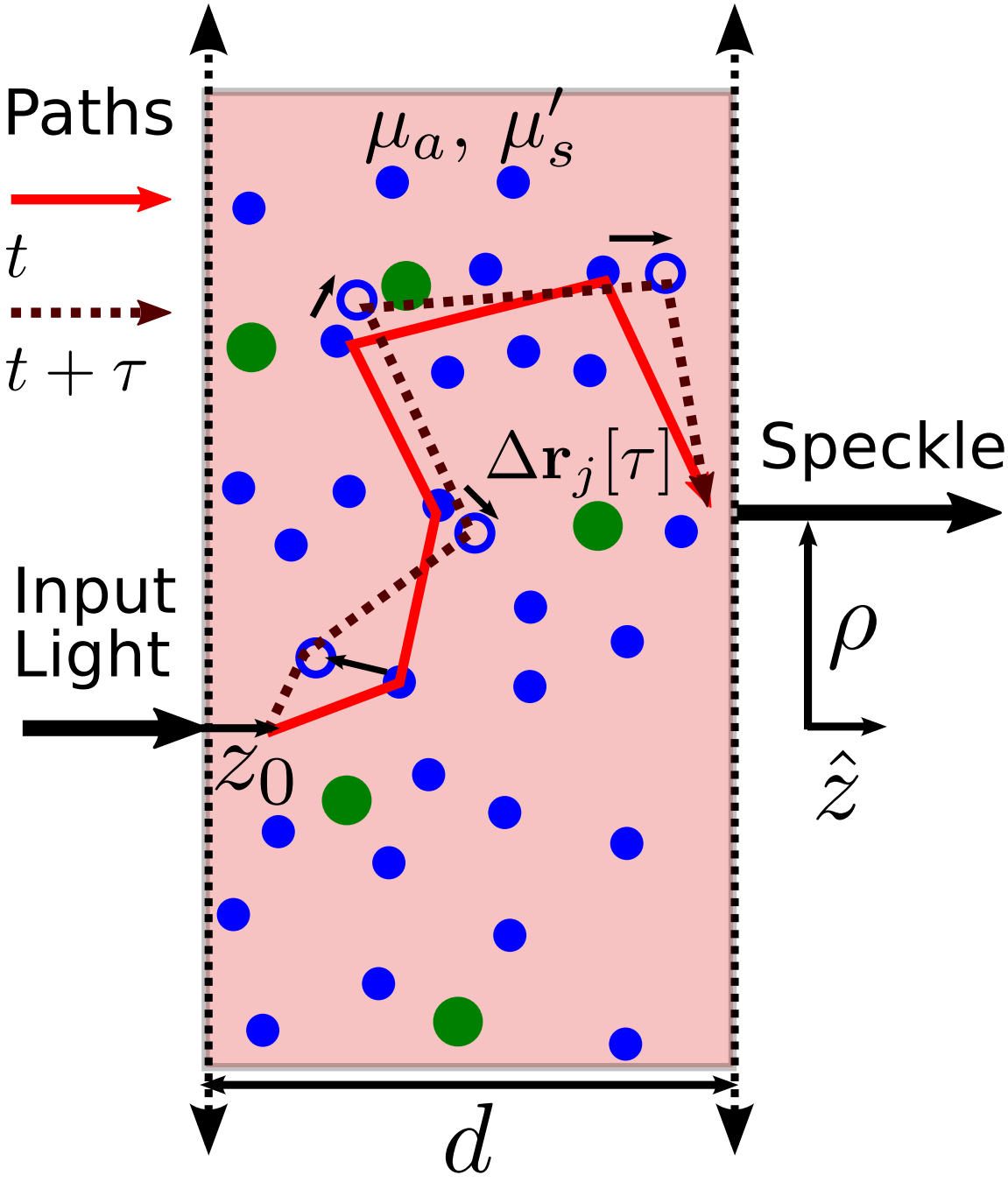

Figure 2.13: Conceptual Diffuse Correlation Spectroscopy (DCS) schematic. A long coherence length (∼50m) laser is coupled to tissue. If we consider a single optical path at time t, the total phase change between the input and output fiber will be the sum of the magnitude of the wave vectors between each scattering event ($\sum_j \|k_j\|$). At a later time, $t+\tau$, the scatters will have shifted slightly ($\Delta r_j[\tau]$), and thus change the phase of the detected light. The interference pattern due to all such paths produces a speckle pattern; we utilize a single mode fiber to couple light from a single speckle output light to a photon-counting APD. An autocorrelator produces an intensity autocorrelation curve. Increased blood flow changes the path length of light in tissue more rapidly, leading to faster fluctuations in intensity and therefore faster decay of the correlation curve[51].

The Siegert relation relates the electric field and intensity auto-correlation functions[55]:

$$g_2[\tau] = 1 + \beta|g_1[\tau]|^2 \tag{2.59}$$

where β is a constant dependent on the experimental optics. This relationship is valid when $\mathbf{E}[t]$ is a Gaussian variable with zero mean. The input light $\mathbf{E}[t]$ does not satisfy this condition, but this condition *is* satisfied after many statistically independent scattering events, provided the input light is sufficiently coherent and there is not a static contribution to $\mathbf{E}[t]$. An ideal apparatus collecting a single mode of polarized light would produce $\beta = 1$; for unpolarized light, $\beta = \frac{1}{2}$.

Boas[56] showed how to construct a diffusion equation that describes the transport of electric field temporal autocorrelation functions in turbid media, and thence access blood flow in microvasculature. A full description of this technique is beyond the scope of this work; various authors[57–61] have studied biomedical applications and validations of this technique against other modalities. Note that a different (original) integral formulation of this technique is also referred to as 'Diffusing Wave Spectroscopy'[62] (DWS) in the condensed matter community.

The unnormalized light electric field autocorrelation function is

$$G_1^T[\boldsymbol{r}, \hat{\Omega}, \tau] = < \mathbf{E}^*[\boldsymbol{r}, \hat{\Omega}, t] \cdot \mathbf{E}[\boldsymbol{r}, \hat{\Omega}, t + \tau] > . \tag{2.60}$$

Integrating over all angles, we define a 'correlation fluence rate'[57,63]:

$$\begin{aligned} G_1[\boldsymbol{r}, \tau] &= \int_{4\pi} G_1^T[\boldsymbol{r}, \hat{\Omega}, \tau] d\Omega \\ &= < E^*[\boldsymbol{r}, t] \cdot E[\boldsymbol{r}, t + \tau] > . \end{aligned} \tag{2.61}$$

where $E[\boldsymbol{r}, t]$ is the total electric field at $\boldsymbol{r}$ and t.

As shown for photon fluence rate in Section 2.2.2, the P_1 approximation to the correlation transport equation[64,65] produces a diffusion equation for G_1 in turbid media:

$$\left(\nabla \cdot (D[r]\nabla) - v\mu_a[r] - \frac{\alpha}{3} v\mu_s' \kappa_0^2 < \Delta r^2[\tau] > \right) G_1[\boldsymbol{r}, \tau] = -vS[\boldsymbol{r}]. \tag{2.62}$$

Here $S[\boldsymbol{r}]$ is an isotropic source term, $\kappa_0 = 2\pi/\lambda$ is the wave number for the light source, α is the fraction of scattering events from moving particles, and the remaining variables are as defined for DOS. This formulation has the same requirements as the photon diffusion equation (e.g., $\mu_a << \mu_s'$, measurement distant from source, etc.) and also requires isotropic scatterer dynamics and a CW source. Note that in a typical measurement of biological tissue, the moving scatterers are primarily red blood cells, which make up a small percentage of the total body mass (blood as a whole makes up $\sim$7%[66–68]); thus α will be quite small (e.g., $\sim$0.05-0.1).

The correlation diffusion equation (Equation 2.61) has the same form as the photon diffusion equation (2.13). Thus, an analogous set of boundary conditions arise for the correlation diffusion equation as those

described for the photon diffusion equation in Section 2.2.4. We can therefore utilize the solutions worked out for the photon diffusion equation (i.e. Equation 2.53) with the correlation rate taking the place of the photon fluence rate and k_{dcs} taking the place of k_{dos}. Again using the extrapolated zero condition ($G_1[z = -z_b, \tau] = 0$, in the semi-infinite geometry the solution to Equation 2.62 is

$$G_1[\rho, z, \tau] = \frac{v}{4\pi D}\left(\frac{e^{-k_{dcs}[\tau]\left((z-z_0)^2+\rho^2\right)}}{(z-z_0)^2+\rho^2} - \frac{e^{-k_{dcs}[\tau]\left((z+2z_b+z_0)^2+\rho^2\right)}}{(z+2z_b+z_0)^2+\rho^2}\right) \tag{2.63}$$

$$= \frac{v}{4\pi D}\left(\frac{e^{-k_{dcs}[\tau]r_a}}{r_a} - \frac{e^{-k_{dcs}[\tau]r_b}}{r_b}\right) \tag{2.64}$$

where

$$k_{dcs}[\tau]^2 = \frac{v}{D}\left(\mu_a + \frac{\alpha\mu_s'\kappa_0^2 < \Delta r^2[\tau] >}{3}\right) \tag{2.65}$$

for a source positioned at $[\rho = 0, z = z_0]$, and the remaining parameters are as defined in Equation 2.53. Note that $k_{dcs}[\tau]$ contains the dynamical information about the tissue sample.

As mentioned above, measuring intensities is much more practical than electric fields; we again rely upon the Siegert relation (Equation 2.59) to convert the intensity autocorrelation function, G_2, into that for the field, G_1:

$$G_2[\boldsymbol{r}, \tau] =< I[\boldsymbol{r}, t]I[\boldsymbol{r}, t+\tau] > \tag{2.66}$$

where $I[\boldsymbol{r}, t] = |E[\boldsymbol{r}, t]|^2|$.

The mean square particle displacement $< \Delta r^2[\tau] >$ is dependent on the type of particle motion (e.g. diffusion or random flow). Various researchers have found that $< \Delta r^2[\tau] >$ in biological tissue is best described with a Brownian model[51,61,69–73]:

$$< \Delta r^2[\tau] >= 6D_B\tau \tag{2.67}$$

where D_B is an *effective* diffusion coefficient that is several orders of magnitude larger than the thermal (Einstein) coefficient for particles the size of red blood cells; see Durduran *et. al*[25] for a discussion of D_B. In this case of 'effective' Brownian motion, the diffuse correlation wave number is

$$k_{dcs}^2[\tau] = \frac{v}{D}(\mu_a + 2k_D^2{\mu_s'}^2\alpha D_B\tau). \tag{2.68}$$

Note that for $\tau = 0$

$$k_{dcs}^2[\tau = 0] = \frac{v\mu_a}{D} = k_{dos}^2 \tag{2.69}$$

as defined in Table 2.3.

All of the data presented in the remainder of this thesis is collected in transmission geometry. Solutions to the photon diffusion equation for the infinite slab are well known (e.g. Contini[42]) and were presented in

Section 2.2.5. Chapter 8 presents data taken with Diffuse Correlation Spectroscopy (DCS); as with DOS, the analysis is performed using a solution to the DCS diffusion equation for an infinite slab.

Recall from Table 2.3:

$$r_{1,m}^2 = \rho^2 + z_{1,m}^2$$
$$r_{2,m}^2 = \rho^2 + z_{2,m}^2.$$

In analogy to Equation 2.56, we write the DCS solution for every decay time τ at transverse distance ρ as

$$G_{slab}^{dcs}[\rho, z = d] = \frac{1}{4\pi} \sum_{m=-\infty}^{\infty} \left(\frac{e^{-k_{dcs}|\boldsymbol{r}_{1,m}|}}{\boldsymbol{r}_{1,m}} - \frac{e^{-k_{dcs}|\boldsymbol{r}_{2,m}|}}{\boldsymbol{r}_{2,m}} \right) \tag{2.70}$$

with the diffuse correlation wave number k_{dcs} as defined in Equation 2.69.

To summarize, we collect an intensity auto-correlation function, we convert it to a field auto-correlation function using the Siegert relation, and then we fit this to a solution of the diffusion equation for correlation fluence rate. Experimental applications will be discussed in Section 2.3.5 and my applications of this technique to measurement of hemodynamics during simulated mammograms will be discussed in Chapter 8.

2.2.8 Diffuse Optical Tomographic (DOT) Reconstruction

The simplest diffuse optical spatial information comes from making a series of measurements on a surface and projecting the results onto a 2-D map[74,75]. This approach is sometimes used for functional brain studies and with hand-held probes[76]. More sophisticated volume imaging strategies rely on tomography wherein we seek to answer the question:

> What is the distribution of absorbers and scatterers inside a medium which would produce the measured outputs, given the known inputs?

Diffuse Optical Tomography (DOT) localizes and quantifies heterogeneities in a volume based on measurements of photon fluence rate on the surface of the volume. Calculation of a simulated set of measurements (the 'calculated measurement vector') from known inputs, i.e., from known $\mu_a[\lambda, \boldsymbol{r}]$ and $\mu_s'[\lambda, \boldsymbol{r}]$, is termed 'the forward problem'. The inverse problem aims to derive the distribution of optical properties within the tissue volume from the measurement vector; it is generally ill-posed and is much more computationally complex than the forward problem. In contrast to X-Ray CT, which uses a columnated thin beam of incident photons which will reach the far side of the medium at approximately the same beam size as it had on the input side, in diffuse optics, the volumes probed by photons arriving at adjacent detectors overlap significantly. The DOT reconstruction problem is therefore more complex than X-Ray CT. In the following sections, we will introduce the 'forward problem' and formulate it for a medium with heterogeneous optical properties. We will then explain the 'inverse problem', which enables us to extract the spatial absorption maps from optical measurements on the surface of a medium.

2.2.8.1 Formulation of the DOT Problem

For small variations in optical properties, the heterogeneous forward problem can be treated within perturbation theory: small heterogeneities will slightly perturb the measurement vector from the homogeneous tissue case, to which solutions are known or can be calculated (e.g. the Green's functions for homogeneous media in Section 2.2.5 and Section 2.2.6). The background or bulk optical properties ($\mu_a^{(0)}$, $D^{(0)}$) can be measured using DOS and we can write these perturbations as

$$\begin{aligned} \mu_a[\boldsymbol{r}] &= \mu_a^{(0)} + \delta\mu_a[\boldsymbol{r}] \\ D[\boldsymbol{r}] &= D^{(0)} + \delta D[\boldsymbol{r}]. \end{aligned} \tag{2.71}$$

The tomographic problem is now to find the spatially varying values of $\delta\mu_a[\boldsymbol{r}]$ and $\delta D[\boldsymbol{r}]$, given some distribution of fluence rates on the tissue surface and the bulk optical properties. Recall Equation 2.13, the time dependent diffusion equation for spatially varying optical properties:

$$\left(\frac{\partial}{\partial t} - \nabla\cdot\big(D[\boldsymbol{r}]\nabla\big) + v\mu_a[\boldsymbol{r}]\right)\Psi[\boldsymbol{r},t] = vS_0\delta[t]\delta[\boldsymbol{r}]$$

can be written in the frequency domain as Equation 2.15

$$\nabla\cdot(D[\boldsymbol{r}]\nabla U[\boldsymbol{r}]) - (v\mu_a[\boldsymbol{r}] - i\omega)U[\boldsymbol{r}] = -vS\delta[\boldsymbol{r}], \tag{2.72}$$

where we have dropped the subscript 'ac' off the source term for clarity. Equation 2.13 and Equation 2.72 are used for the 'forward problem' calculation, i.e., determining the fluence rate at a detector position due to light input at a source position for a given spatial distribution of optical properties.

If we assume that heterogeneities in the tissue are slowly varying in space, we may apply the Rytov approximation[77] to describe the scattered fluence. (See Kak[78] and Arridge[17] for overviews and perspectives of linear approximations.) Here, we write the total fluence rate (U_t) in terms of the 'unperturbed' input wave (U_0) and a spatially dependent exponential factor $e^{\phi_s[\boldsymbol{r}]}$, i.e.,

$$U_t[\boldsymbol{r}] = U_0[\boldsymbol{r}]e^{\phi_s[\boldsymbol{r}]}. \tag{2.73}$$

Then, plugging Equation 2.73 and Equation 2.71 into Equation 2.72, collecting leading order terms, and (for simplicity) assuming $\delta D = 0$, it is straightforward to show for a source positioned at $\boldsymbol{r}_s$ and a detector at $\boldsymbol{r}_d$ that

$$\ln\left[\frac{U_t[\boldsymbol{r}_s,\boldsymbol{r}_d]}{U_0[\boldsymbol{r}_s,\boldsymbol{r}_d]}\right] = \phi_s[\boldsymbol{r}_s,\boldsymbol{r}_d] = \frac{1}{U_0[\boldsymbol{r}_s,\boldsymbol{r}_d]}\int_V U_0[\boldsymbol{r}_s,\boldsymbol{r}]\frac{v\delta\mu_a[\boldsymbol{r}]}{D^{(0)}}G[\boldsymbol{r},\boldsymbol{r}_d]d^3\boldsymbol{r}. \tag{2.74}$$

Here, $G[\boldsymbol{r}_s,\boldsymbol{r}_d]$ is the Green's function solution for the heterogeneous diffusion equation and $\boldsymbol{r}$ is integrated over the entire tissue volume.

The fluence rate in a homogeneous medium, U_0, due to a point source is the homogeneous Green's function multiplied by a source term, i.e. $U_0 = S \cdot G_0$. The Green's functions for homogeneous media in simple geometries are well known (e.g., as in Section 2.2.4). Furthermore, since we are working in the small perturbation regime, the heterogeneous Green's function is approximately equal to the homogeneous Green's function (i.e., $G \simeq G_0$), allowing us to rewrite Equation 2.74 as:

$$\ln\left[\frac{U_t[\boldsymbol{r}_s,\boldsymbol{r}_d]}{U_0[\boldsymbol{r}_s,\boldsymbol{r}_d]}\right] = \phi_s[\boldsymbol{r}_s,\boldsymbol{r}_d] = \frac{1}{G_0[\boldsymbol{r}_s,\boldsymbol{r}_d]}\int_V G_0[\boldsymbol{r}_s,\boldsymbol{r}]\frac{v\delta\mu_a[\boldsymbol{r}]}{D^{(0)}}G_0[\boldsymbol{r},\boldsymbol{r}_d]d^3\boldsymbol{r}. \tag{2.75}$$

In diffuse optical tomography, we consider measurements made by N_d detectors during serial illumination by N_s sources, all located on the surface of the tissue. We then reconstruct N_v volume elements (voxels) in the interior of the tissue. One can formulate this problem in matrix or operator form based on Equation 2.75. Specifically, we discretize Equation 2.75 as

$$\phi_s[\boldsymbol{r}_s,\boldsymbol{r}_d] = \frac{v}{D^{(0)}}\frac{1}{G_0[\boldsymbol{r}_s,\boldsymbol{r}_d]}\sum_{j=1}^{N_v} G_0[\boldsymbol{r}_s,\boldsymbol{r}_j]\delta\mu_a[\boldsymbol{r}_j]G_0[\boldsymbol{r}_j,\boldsymbol{r}_d]h^3 \tag{2.76}$$

where h^3 is the voxel volume, s and d index the sources and detectors, and j indexes the voxels. Equation 2.76 describes a series of coupled linear equations, shown in matrix form below.

$$\begin{bmatrix} W_{1,1} & W_{1,2} & \dots & W_{1,N_v} \\ W_{2,1} & W_{2,2} & \dots & W_{2,N_v} \\ \vdots & \vdots & \dots & \vdots \\ W_{N_s\times N_d,1} & W_{N_s\times N_d,2} & \dots & W_{N_s\times N_d,N_v} \end{bmatrix} \begin{bmatrix} \delta\mu_a[\boldsymbol{r}_1] \\ \delta\mu_a[\boldsymbol{r}_2] \\ \approx \\ \vdots \\ \delta\mu_a[\boldsymbol{r}_{N_v}] \end{bmatrix} = \begin{bmatrix} \phi_s[\boldsymbol{r}_s^{(1)},\boldsymbol{r}_d^{(1)}] \\ \phi_s[\boldsymbol{r}_s^{(2)},\boldsymbol{r}_d^{(2)}] \\ \approx \\ \vdots \\ \phi_s[\boldsymbol{r}_s^{(N_s\times N_d)},\boldsymbol{r}_d^{(N_s\times N_d)}] \end{bmatrix} \tag{2.77}$$

where

$$W_{i,j} = \frac{v}{D^{(0)}}\frac{G_0[\boldsymbol{r}_s^{(i)},\boldsymbol{r}_j]G_0[\boldsymbol{r}_j,\boldsymbol{r}_d^{(i)}]}{G_0[\boldsymbol{r}_s^{(i)},\boldsymbol{r}_d^{(i)}]}. \tag{2.78}$$

and the index i runs over all source-detector pairs. $W_{i,j}$ are the 'weights'[18] or 'hitting density'[79] which give the importance of the absorption in any particular voxel in a measurement from a given source-detector pair. Note that the elements of the weight matrix are proportional to the three-point Green's function between $\boldsymbol{r}_s$, $\boldsymbol{r}_j$, and $\boldsymbol{r}_d$, that gives the probability that a photon entering the turbid medium at $\boldsymbol{r}_s$ will pass through the voxel at $\boldsymbol{r}_j$ and then be detected at $\boldsymbol{r}_d$.

The desired output of a DOT measurement is a spatial map of absorption and scattering over all the volume elements in the medium (i.e., $\delta\mu_a[\boldsymbol{r}]$ in Equation 2.77). However, we measure light at points on the surface of the tissue (i.e., the left hand size of Equation 2.77). $\mathbf{W}$ is therefore a forward operator, converting a distribution of absorption within the sample into a detected light output for a given light input. In DOT, we

seek to find an inverse operator, which will use surface measurements to find the distribution of absorption within the sample. This is known as the 'inverse problem'. This problem is sometimes complicated by the fact that in many experiments $N_v > N_s \times N_d$. In this case, the problem is under-determined (i.e., more unknowns then measurements/equations).

2.2.8.2 Example Solution to the Inverse Problem in Diffuse Optical Tomography: Singular Value Decomposition

The most intuitive approach to obtaining the inverse solution to Equation 2.77 is to simply invert the weight matrix $\mathbf{W}$ to obtain $\delta\mu_a[\boldsymbol{r}]$. For example,

If $\mathbf{W}\delta\mu_a[\boldsymbol{r}] = \phi_s$,

then $\delta\mu_a[\boldsymbol{r}] = \mathbf{W}^{-1}\phi_s$.

However, an analytic inverse of $\mathbf{W}$ does not generally exist as $\mathbf{W} = \mathbf{W}_{\mathbf{N_s}\times\mathbf{N_d},\mathbf{N_v}}$. The number of measurements, $N_s \times N_d$, will often be less than the number of voxels, N_v, i.e., $\mathbf{W}$ is not square. The Moore-Penrose pseudo-inverse[80] is defined for rectangular matrices, but is not unique. We therefore approach this problem by first pre-multiplying by the transpose of $\mathbf{W}$, i.e., $\mathbf{W}^T$ to form a symmetric square matrix:

$$\mathbf{W}^T\mathbf{W}\delta\mu_a[\boldsymbol{r}] = \mathbf{W}^T\phi_s. \tag{2.79}$$

The matrix $\mathbf{M} = \mathbf{W}^T\mathbf{W}$ is now square and symmetric, but can be poorly conditioned (i.e., the range of eigenvalues is large).

We calculate the Moore-Penrose pseudo-inverse ($\mathbf{M}^+$) by decomposing $\mathbf{M}$:

$$\mathbf{M} = \mathbf{U}\mathbf{\Lambda}\mathbf{U}^T \tag{2.80}$$

$$\mathbf{M}^+ = \left(\mathbf{U}\mathbf{\Lambda}\mathbf{U}^T\right)^+ \tag{2.81}$$

$$= \left(\mathbf{U}^T\right)^+ \mathbf{\Lambda}^+ \left(\mathbf{U}\right)^+ \tag{2.82}$$

$$= \mathbf{U}\mathbf{\Lambda}^+\mathbf{U}^T \tag{2.83}$$

where $\mathbf{\Lambda}$ is a diagonal matrix of the ordered eigenvalues of $\mathbf{M}$ and the columns of $\mathbf{U}$ are the corresponding orthonormal eigenvectors of $\mathbf{M}$. Note that $(\mathbf{U}^T)^+ = \mathbf{U}$, and $\mathbf{U}^+ = \mathbf{U}^T$, because $\mathbf{U}$ is orthogonal. The smaller eigenvalues of $\mathbf{M}^+$ correspond to high spatial frequency modulations in the image. We therefore choose to use 'Truncated Singular Value Decomposition' (tSVD), in which we set all eigenvalues smaller than a regularization parameter (γ_r) to zero thus reducing the effect of high frequency noise[81]. The components of $\mathbf{\Lambda}^+$ are

$$\lambda_i^+ = \begin{cases} \lambda_i^{-1} & \text{if } \lambda_i > \gamma_r, \\ 0 & \text{if } \lambda_i \leq 0. \end{cases} \tag{2.84}$$

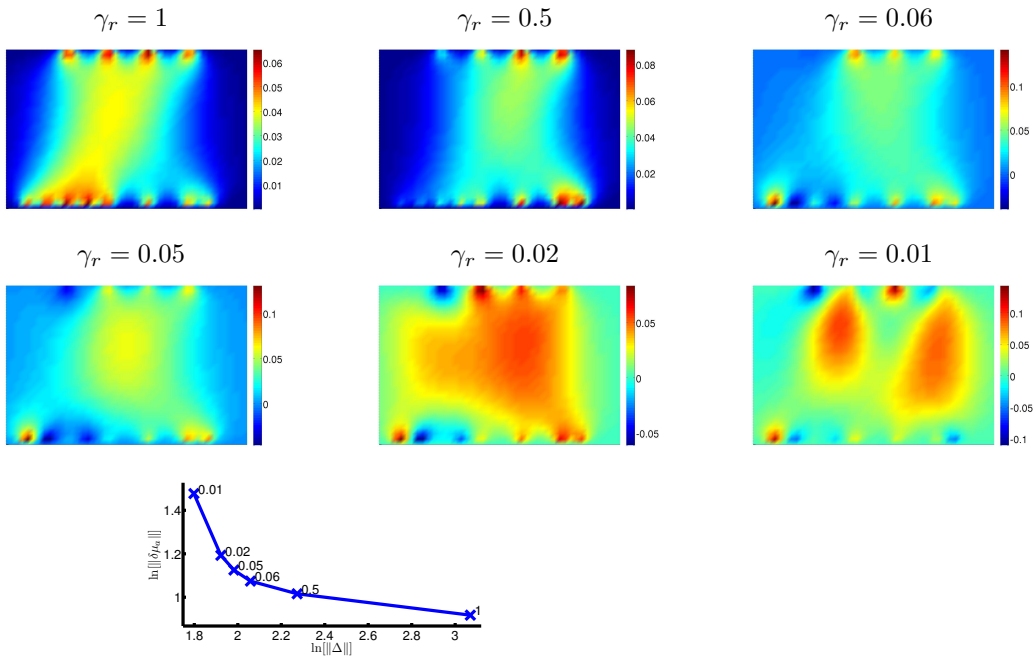

Figure 2.14: Example of regularization parameter (γ_r) selection using an 'L-Curve', in which the image norm ($\|\delta\mu_a[\boldsymbol{r}][\boldsymbol{r}]\|$) is plotted against the residual ($\Delta \equiv \|\mathbf{W}\delta\mu_a[\boldsymbol{r}] - \phi_s\|$). The optimal regularization parameter is at the corner of the 'L', here, 0.05.

As there is no abrupt change in the magnitude of the singular values, we choose the value of γ_r using the so-called 'L-curve', which plots the norm of the solution ($\|\delta\mu_a[\boldsymbol{r}][\boldsymbol{r}]\|$) against the residual($\Delta \equiv \|\mathbf{W}\delta\mu_a[\boldsymbol{r}] - \phi_s\|$)[82,83] for various values of γ_r. We choose to use value of γ_r for the point of maximal curvature (closest to the 'corner' of the L) is then used for the remaining analysis. An example of this process is shown in Figure 2.14.

Therefore we have the solution for the spatial distribution of absorption,

$$\delta\mu_a[\boldsymbol{r}] \simeq \mathbf{U}\Lambda^{+}\mathbf{U}^T\mathbf{W}^T\phi_s. \tag{2.85}$$

This truncated SVD approach usually works at some level, and it was employed often in the early days of DOT. This and other linear 'subspace' techniques are superior to linear algebraic reconstruction techniques[84], but non-linear iterative techniques (e.g. TOAST, as in Section 2.2.8.3) are currently the standard in the field. However, the single computationally expensive step in the tSVD reconstruction allows images at many time points to be reconstructed quickly, in near real time.

2.2.8.3 DOT with Nonlinear Iterative Techniques and Spatial Regularization

As will be described in Chapter 6, our GenIII system enables acquisition of many more spatial data points than the GenII or GenIIm systems (Chapter 4). We therefore adopted a more sophisticated image reconstruction scheme to take advantage of this additional data. Building upon a long term collaboration with Dr. Simon Arridge and Dr. Martin Schweiger at University College London, we have applied the TOAST (Time-resolved Optical Absorption and Scattering Tomography)[85,86] software package to the reconstruction problem.

TOAST utilizes an iterative approach to the DOT inverse problem, adjusting a proposed map of chromophores until a computed measurement vector matches the experimental measurement vector, within an error. A sketch of the general iterative process is given below, which applies to many numerically-based iterative inverse problem schemes.

1) Define an objective function (χ^2), which characterizes the difference between predicted and experimental measurements.

2) Make an 'initial guess' chromophore map for the reconstructed volume ($\mu^0[\boldsymbol{r}]$, here $D[\boldsymbol{r}] = D^{(0)}$ for simplicity).

3) Compute measurement vectors (forward problem) based on the chromophore map ($\mu[\boldsymbol{r}]$).

4) Compare 'calculated' values to actual measurements; compute the objective function (χ_i^2) for this iteration.

5) Check objective function value against stopping criterion (e.g. $\chi_i^2 < \epsilon$).

6) If stopping criteria is realized, terminate procedure, otherwise, adjust the chromophore map and repeat.

Specifics of how this approach is applied to our experimental data are included in Section 2.3.6.

2.2.8.4 Other DOT Techniques

A number of mathematical techniques can be used to solve the integro-differential equations arising from inverting the diffusion equation in heterogeneous media; such algorithms are an area of current research. A complete discussion of the merits in accuracy and computational cost of these techniques is beyond the scope of this thesis; Arridge and Schotland have recently reviewed new developments in optical tomography[24].

Several academic groups have assembled diffuse optical tomography software packages: Arridge's TOAST[85,86] (University College London)[i], Dehghani's NIRFAST[ii] (University of Exeter), Ripoll's ART/SIRT

[i] http://web4.cs.ucl.ac.uk/research/vis/toast/
[ii] http://newton.ex.ac.uk/research/biomedical/hd/NIRFAST.html

codes[iii] (FORTH), the Oregon Medical Laser Center's Radiative Transport Software[iv], and Boas's HomER and PMI Toolbox[v] (MGH). Several of these packages are freely available to the academic community.

Recently, the trend in image reconstruction has been towards large numbers of source detector pairs ($> 10^6$)[31] frequently using CCD detectors. Deliolanis[87] and colleagues have applied this to small animal fluorescence imaging. Culver[88] and Choe[31] *et al.*applied CCD detection to 3D tomography of absorption properties in the breast; Corlu *et al.*[89] extended this work to perform 3D reconstruction of ICG fluorescence in breast cancer. The resulting data sets, especially when scaled up to the human brain or breast, require significant computational resources to reconstruct tomographically with Finite Element Modeling or Finite Difference methods. Konecky *et al.*[90] applied much more efficient inversion algorithms developed by Schotland, Markel, and Mital[91–93] to ultra large (10^7 source-detector pairs) data sets from phantoms and, in unpublished data, to healthy human breasts.

2.3 Experimental Realizations of Diffuse Optics

Several different types of diffuse optical instrumentation have been developed for use in both laboratory and clinical settings. The various data types are described in Section 2.3.1 and experimental geometries in Section 2.3.2. Section 2.3.3 describes Time Domain Diffuse Optical Spectroscopy (TD-DOS) and Section 2.2.7 describes blood flow measurements with Diffuse Correlation Spectroscopy (DCS). The research presented in this thesis was accomplished using several instrument and data types: the GenII Optical/MRI system described in Chapter 4 utilizes DOT and DOS; the GenIII Optical/MRI system described in Chapter 6 utilizes DOT, and DOS (future plans include DCS); and the compression study described in Chapter 8 utilizes DOS and DCS.

2.3.1 Experimental Data Types

Diffuse optical data is collected from pulsed (time domain, TD), modulated (frequency domain, FD), or steady state (continuous wave, CW), light sources. The relative information content per source-detector pair of these DOS systems is TD>FD>CW. Detectors include photo-multiplier tubes (PMT's), avalanche photo-diodes (APD's), photo-diodes (PD's), streak cameras, and CCDs. Some of the attributes of these data types are summarized in Table 2.4.

Time Domain (TD) or Time Resolved Spectroscopic (TRS) techniques introduce a brief pulse of light into a medium and measure the broadening of this pulse due to the different trajectories taken by photons transversing the medium. Together with the tissue index of refraction, the mean of this transit time gives

[iii] http://esperia.iesl.forth.gr/~jripoll/
[iv] Mostly forward problem, but includes adding-doubling inverse code http://omlc.ogi.edu/software/
[v] http://www.nmr.mgh.harvard.edu/PMI/resources.htm

Time Domain	TD or TRS	Absolute optical properties with a single source and detector.	Expensive components.
Frequency Domain	FD	Absolute optical properties require many frequencies or source-detector combinations	Relatively inexpensive components
Continuous Wave	CW	Only relative optical properties	Very inexpensive (∼$20) components.

Table 2.4: Diffuse optical data types; note that spatially modulated data can be collected using any of the temporally modulated techniques.

the average photon path length, which is related to the absorption and scattering of the tissue[44,46,94] (see also Section 3.1.1). Most modern techniques use a streak camera[95,96] or Time-Correlated Single Photon Counting (TCSPC)[5,97] devices to measure transmitted pulse profiles. The TCSPC technique relies on detectors (APDs or PMTs) operating in Geiger mode and a low photon flux: on average, each channel receives less than one photon per laser pulse (∼2-70 MHz). The time of each photon arrival is recorded and a histogram of arrival times is built up over an integration period; the results are fit to solutions of Eqn. 2.13 appropriate for the geometry and boundary conditions to obtain absolute values for μ_a [λ] and μ_s' [λ]. In practice, TD measurements are limited by the TCSPC electronics maximum count rate (∼1-10 MHz) to fairly low detected signal intensities, and thus longer integration times are required per source-detector position compared to similar FD measurements.

TD systems permit rejection of unwanted photons (e.g., those due to reflections in the system) through time-gating. For example, the length of optical fibers can be adjusted such that a reflection off the face of the fibers is separated in time from the data pulse; in an FD system, such a reflection could be a source of phase noise. Torricelli and colleagues[98] extended this concept by placing their source and detector directly adjacent to one another and enabling their short rise-time detector only *after* photons experiencing specular reflection from the surface or only a few scattering events had arrived.

TD systems permit use of time-resolved data directly by fitting to time-dependent solutions to the diffusion equation. Information can also be codified by decomposition into temporal moments or by application of the methods of FD analysis (discussed below) to Fourier transformed TD data. These data types are addressed in detail by E. M. C. Hillman in her thesis[99] and by Liebert *et al.*[45].

The phase of an amplitude modulated measurement (first suggested by Gratton[100]) encodes information similar to the mean tissue transit time; current instrumentation typically utilizes frequencies from 30-200 MHz[76,88,101–107] with a few groups using up to ∼800 MHz[108]. These frequency domain (FD) measurements are the Fourier analogues of the time domain measurements, but for practical reasons, most researchers measure one or a few frequencies instead of sweeping the frequency through a range (e.g. 300 kHz to

800 MHz as in Madsen *et al.*[108]). This frequency restriction reduces the information content of the FD measurements: those researchers (e.g. Bevilacqua *et al.*[109]) who use swept frequency devices have much more information per measurement than single frequency FD instrumentation. Swept frequency domain systems are currently limited to less than ∼1 GHz by the practical speed of modulation of source laser diodes and detector response time, while the frequency component of the TD signal extends to several GHz. However, single frequency lock-in electronics are relatively inexpensive and these single frequency instruments can be more economical than the TD or swept FD instruments, especially for systems with many detectors (e.g. Sevick-Muraca *et al.*[110]). FD systems also have the advantage of a significantly higher duty cycle than TD: the 'signal' is detected continuously, instead of a single photon per laser pulse, permitting very short (e.g. 10-100 ms) integration times for each source-detector pair.

Calculation of absolute optical properties is possible for homogeneous media with single frequency FD devices, but the measurement is markedly improved through use of multiple source-detector separations. Simple measurements of attenuation with continuous wave (CW) light cannot discriminate absolute absorption and scattering except under special circumstances[99,111–113].

Intes and Chance[114] addressed analysis of multi-frequency data, noting that 7-12 frequencies spanning 0-500 MHz provided optimal results. FD systems with more then one non-zero frequency have been implemented for DOS[109] and Tromberg's group at the Beckmann Laser Institute has applied this system in many clinical studies[74,115,116]. However, the Beckmann system relies upon a sophisticated network analyzer. Multiple frequency data for DOT are generally derived from TD measurements (e.g., by Fourier transformation) as discussed in Section 2.2.5 and Section 2.3.3.

In the $\omega = 0$ (steady state or continuous wave) case, it is difficult to separate changes in absorption and scattering, except in a few special cases[117]. However, especially in situations where scattering remains roughly constant, CW techniques have proven particularly useful to measure changes in the absorption both in space (e.g. hematomas[118]) and time (e.g. exercising muscle[119]); these techniques can be very inexpensive (e.g. ∼$20 in opto-electronic parts for a 1 wavelength, 1 source-detector system).

To summarize, CW data simply records intensity, typically referenced to a baseline value I_0 as $\frac{I}{I_0}$. FD data at a single frequency $\omega = \omega_1$ provides amplitude and phase; many FD systems can collect data at both a finite frequency (ω_1) and $\omega = 0$. The pulse broadening in the time domain of a brief pulse of light passing through a scattering medium is perhaps more intuitively obvious than the phase shift one observes in the more commonly used frequency domain measurements; the time domain is the natural formulation convenient for Monte Carlo simulations of photon transport. Most importantly, TD measurements permit absolute quantification of scattering and absorption coefficients in a homogeneous medium with a single measurement. Technically, FD measurements of phase, amplitude (AC), and average intensity (DC) are sufficient to calculate absolute optical properties, but this approach is more susceptible to systematic errors.

Thus most researchers using FD techniques rely upon either multiple source-detector separations or multiple frequencies. CW measurements lack sufficient information to separate attenuation due to scattering and absorption, unless spectral models are employed.

2.3.2 Experimental Geometries

In addition to the type of source modulation, a variety of data collection geometries are used. Hand-held probes with one or a few source-detector pairs offer simplicity and easy placement wherever measurements are desired. Probes for the muscle and brain are generally taped or otherwise fastened to the body, i.e., these probes are not hand-held, but the probes are similar in concept, since both function in the remission geometry (sometimes termed the reflection geometry). Hand-held probes have been used for cancer detection[75,109], and therapy monitoring[11,72]. The most basic of these hand-held measurements measure differential changes in absorption using an estimate of the diffuse path length (DPF, see Eqn. 2.38); a slightly more sophisticated analysis uses homogeneous, semi-infinite analytic solutions to the diffusion equation. The most sophisticated hand-held instruments permit limited imaging (e.g., distinct layers); multi-modal instruments can also use structural information from one modality (e.g., ultrasound) to image tissue (see Sec. 3.2.2). Li[120] has recently implemented a layered model and applied the technique to phantom studies. Layered techniques improve the quantification of optical properties deeper into a medium, which is important to those researchers using naturally layered (e.g., scalp/skull/brain) organs.

Spatial information for hand-held devices is mostly derived by moving the probe. Thus, hand-held devices produce a map of local optical properties, with practical resolution determined by the number of different positions used; given a sufficiently large number of positions, this scheme could be used for limited tomography or a surface map[74,75]. Note the average penetration depths for most surface remission measurements are dependent on the source-detector separation; this is part of the reason authors cite widely varying depth sensitivity[75,121]. Similarly, the most probable photon penetration depth for a remission geometry device in the frequency domain depends (weakly) on the modulation frequency of the source. In a phantom study of quantification possible with CW remission DOT, Kepshire *et al.*[122] found quantification of concentration to fall off significantly with a depth of only 5 mm. In the time domain, Liebert *et al.*[45] have used the difference in depth sensitivity of the 0^{th}, 1^{st}, and 2^{nd} temporal moments to separate signals originating in the scalp and brain of adult humans. Full tomographic measurements (i.e. 3D reconstructions) are generally made with many fixed or a few scanning sources and detectors, although Ge and colleagues have recently developed a two part hand-held breast FD tomographic probe[123].

In the breast, cylindrical or cone geometries have been used by several research[124–126] groups and commercially with the Phillips 'Optical Mammoscope'[127,128] and the breast version of the NIRx DYNOT

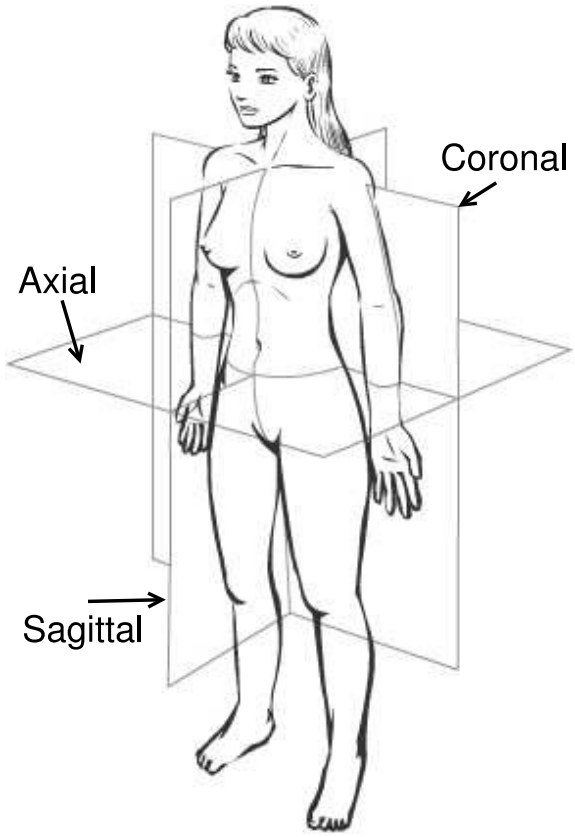

Figure 2.15: A schematic of clinical coordinate system terminology. Figure adapted from Choe[138]; courtesy of R. Choe and Y. K. Choe.

system[129]. Slab geometry (mild compression of the breast between two flat plates) is currently used by several groups for breast imaging, primarily with axial compression (see Figure 2.15). Scanning slab geometry, in which a few sources and detectors are raster scanned in tandem across the compression plates, has been used by academic groups[130–132] and in the ART 'SoftScan'®[96]. However, these measurements are all on or about an axis through the slab (paraxial, i.e., the source and detector are almost directly across from one another), with very few oblique measurements. Therefore, it is difficult to ascertain the depth into the slab of any lesion detected (the transverse resolution is much greater than the through-slab resolution). These measurements are sometimes known as 'transillumination', but are distinct from the planar transillumination pioneered by Culter[32,33] in 1929 as he illuminated with a planar source. Fixed position slab geometry, in which an array of optical fibers delivers light to the breast has been used primarily by Culver, Choe, and colleagues[31,88] and commercially in the DOBI 'ComfortScan'®[133,134]. Detection can be either by an array of optical fibers leading to detectors, detectors placed directly against the tissue surface, or lens-coupled CCD cameras. Leff[1] has recently reviewed DOS/DOT breast cancer contrast, adding to previous reviews by Nioka[135], Hebden[136], and Ntziachristos[137] and their colleagues.

2.3.3 Time Domain Diffuse Optical Spectroscopy (TD-DOS)

Time Domain Diffuse Optical Spectroscopy (TD-DOS) or Time resolved spectroscopic (TRS) techniques rely on introducing a brief pulse of light into a turbid medium and measuring the transit times of a distribution of many photons. Together with the index of refraction of tissue, the mean of this transit time gives the average photon path length, which is related to the absorption and scattering of the tissue[46]. This average path length can be utilized directly to derive chromophore concentrations (see Equation 3.3). Alternately, one can fit a diffusion model (e.g. Equation 2.50) to the data.

A TD-DOS measurement consists of the following steps:

1) Introduce a very short (∼300) pulse of light into tissue.

2) Collect diffuse output light using a high-speed photon counting PMT or APD.

3) Collect output pulses from detector to create a very high (∼10 ps) temporal resolution histogram.

4) Measure the Instrument Response Function (IRF) and convolute with a theoretical model (e.g. Eqn. 2.37).

5) Fit the data to the above convolution to extract μ_a [λ] and μ_s' [λ]; iterate parameters of theoretical model.

Alternatively, one could deconvolute the IRF from the measured data and fit the result to the theoretical curve, but this is computationally more expensive; the IRF will be discussed in detail below. Roughly speaking, scattering determines the peak of the photon arrival time histogram and absorption determines the terminal log-slope. The latter is obvious by rewriting Eqn. 2.37 as

$$\Psi[r,t] = \frac{vS_0}{(4\pi Dt)^{3/2}} e^{-\frac{r^2}{4Dt}} e^{-\mu_a vt}. \tag{2.86}$$

The last term dominates at long times (i.e. as $t \to \infty$, $\Psi \to e^{-\mu_a vt}$). An example histogram is shown in Figure 2.16; Figure 2.17 shows the effect of titrating an absorbing dye into a liquid phantom on the TD histograms.

Measurements using short source-detector separations (e.g. $< 10l^*$) generally require a more careful treatment of light propagation in scattering media, including realistic modeling of sources and detectors. In the context of DOS and DOT of the breast, sources and detectors are generally well separated (> 2.5 cm for hand-held systems, > 6 cm for parallel plate tomographic systems) and point approximations of the source and detector are reasonably accurate.

The output of a TD measurement is a histogram of photon arrival times, as shown in Figure 2.16. If the light source and detector have an infinitely fast response, this histogram can be directly fit to a solution

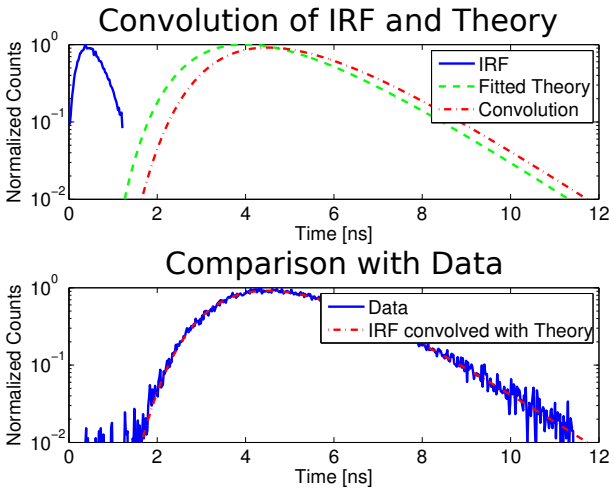

Figure 2.16: Example of IRF, fitted theoretical curve, and data for subject 61003 (8.3 cm compression, BMI 41.5, bra size 44 DDD) at 798 nm. Fitted parameters: $\mu_a = 0.034$ cm^{-1}, $\mu_s' = 13.3$ cm^{-1}, $t_0 = 0.029$ ns, and amplitude = 0.73. These correspond to a very fatty breast with fairly low signal (max 746) because of the thickness. Note, the IRF is clipped at 10% on the up slope and 5% on the down slope and t_0 is measured relative to a reference channel.

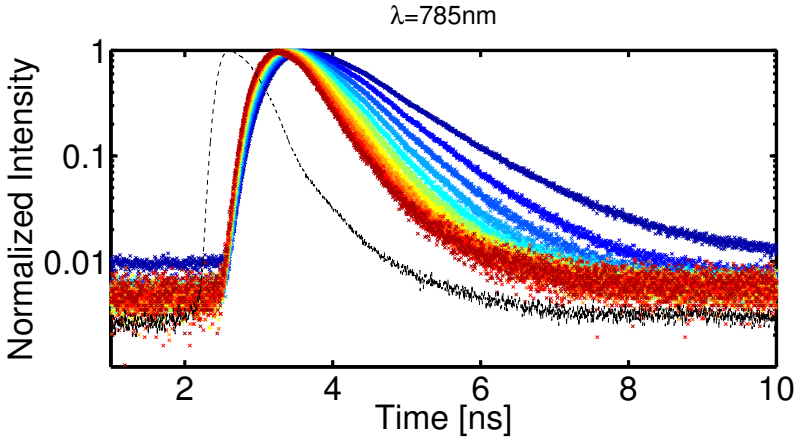

Figure 2.17: An example of the effect of increasing absorption on TD data histograms. Black is the IRF; as the colors change from blue to red, the absorption goes up from 0.02 cm^{-1}to 0.2 cm^{-1} in steps of 0.024 cm^{-1}.

of the time domain diffusion equation in the appropriate geometry (e.g. Eqn. 2.37). As with FD and CW measurements, a TD source is generally modeled as a point source located $z_0 = \frac{1}{\mu_s'}$ into the medium, where μ_s' is the average reduced scattering[44,46]. This extrapolated source position z_0 is shown schematically in Figure 2.8 and a schematic of a basic TD system is shown in Figure 2.18.

Dealing with the assumption of an infinitely narrow input pulse of light is somewhat more complicated. As a practical matter, one must consider the convolution of the laser output pulse, the pulse broadening

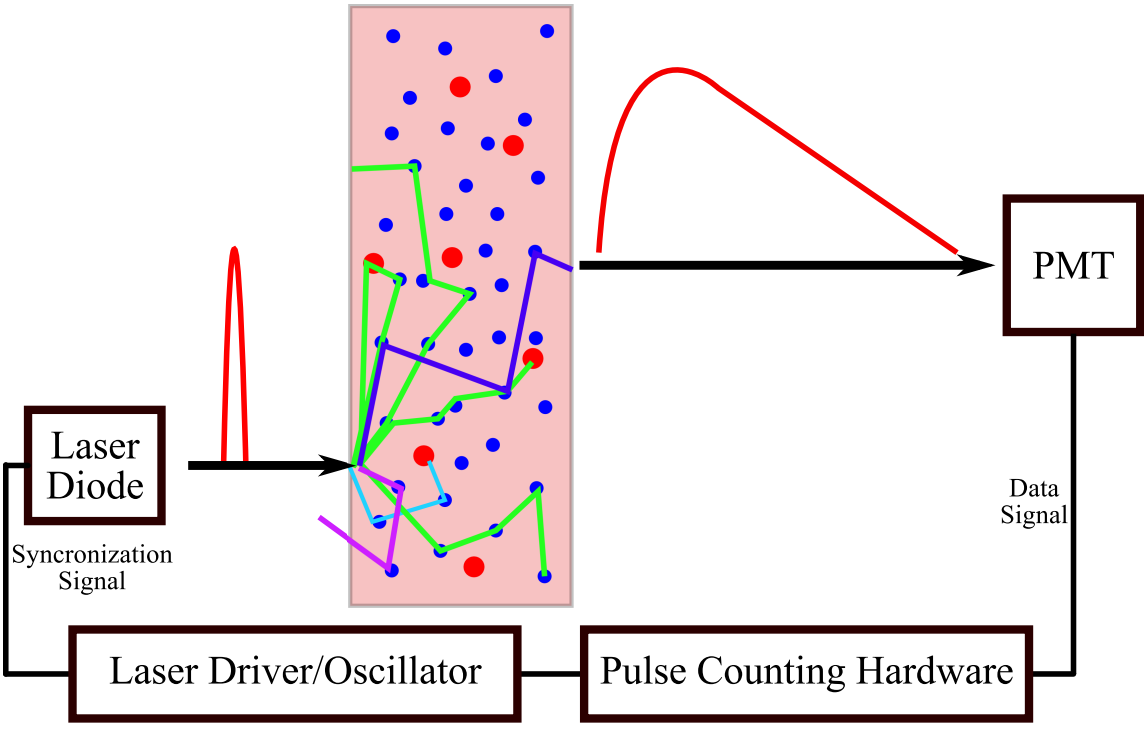

Figure 2.18: Conceptual schematic of TD-DOS measurements. A narrow pulse of light is introduced to the tissue from a laser diode, driven by an oscillator. Several possible photon paths through the scattering and absorbing centers of the media are shown. Light is detected using a PMT in Geiger mode; counting electronics determine the transit time of the detected photon compared to the input pulse.

(dispersion) in any optical elements (fibers, etc.), the transit time spread (TTS) of the detector, and any delays in recording electronics. The convolution of these elements is referred to as the 'Instrument Response Function' (IRF). For DOT in the breast, an IRF with full-width-at-half-max (FWHM) of ∼400 is sufficient for recovery of optical properties[139]. An example of the convolution and fit is shown in Figure 2.16.

Note: in order to properly replicate the detector fiber collecting light from a diffuse media, the IRF must be collected in such a manner that all of the fiber modes are excited. In practice, this consists of separating the source and detector fiber by ∼1 cm and inserting a plano-convex lens to quasi-collimate the beam from the source fiber. Additionally, one can insert a thin diffuser (e.g. a layer of tissue paper) after the plano-convex lens to further homogenize the input beam.

An offset t_0 accounts for time delays not originating in the diffuse media and would be included in Equation 2.86 as an offset (i.e., $t \rightarrow (t - t_0)$). This offset t_0 can change with time, for example, as a result of temperature changes in the opto-electronics[139].

2.3.4 TD-DOS Data Fitting

'Fitting' in this context is the process of minimizing an error function between measured data and a theoretical model characterized by some parameter set; different values of these parameters are used to produce a model which is then compared to data, until some stopping criterion (number of iterations, value of difference between fit and data, etc.) is reached. We define a background level (B) as the average photon count away from the data pulse ($D[t]$) (e.g. between 1 and 2 ns in Figure 2.17). We calculate an error as $\sigma[t]^2 = D[t] + StdDev[B]$; in other words, assuming Poisson noise at every point in the data plus a constant defined by the standard deviation of the background. We then calculate a theoretical temporal response using Eqn. 2.50 for a set of optical parameters and convolve it with the measured IRF to produce a fit function $F[t]$. We then compared the fit function to the measured data with an error function defined by

$$\chi^2 = \sum_{t,\lambda} \left[\frac{D[t] - F[t]}{\sigma[t]} \right]. \tag{2.87}$$

The χ_r^2 function is minimized using *fminsearchbnd*, a bounded version of the Matlab© (Mathworks, Inc.) function *fminsearch*[vi]. Parameters were scaled such that the numerical values passed to the fit were between ~0.1 and ~20 and the data and fit were normalized to a smoothed peak value: the resulting fits are therefore less sensitive to skin-optode coupling (i.e. pulse amplitude is ignored). Note that this overall amplitude is not important for calculation of μ_s' or μ_a. Parameter bounds were placed outside of physically expected values (typical bound values values: $10^{-4} < \mu_a < 1$, $1 < \mu_s' < 50$, normalized peak amplitude 1 ± 0.2; t_0 varies with the particular optical components). See Figure 2.16 for an example of a convolution and fitted curve.

After obtaining μ_a of each the measured wavelengths (λ), one can find chromophore concentrations by solving the system of equations

$$\mu_a[\lambda_i] = \sum_{i=1}^{N_c} \epsilon_i[\lambda] \cdot C_c \tag{2.88}$$

for each wavelength i and major tissue chromophore C. Note, all major chromophores must be included if one is fitting absolute absorption. Alternately, one can fit data directly for all λ simultaneously, as introduced by Corlu[117].

$$\mu_a[\lambda_i] = \sum_{i=1}^{N_c} \epsilon_i \cdot C_c \tag{2.89}$$

$$\mu_s'[\lambda_i] = A\lambda^{-b} \tag{2.90}$$

Here, $\mu_s'[\lambda]$ is modeled by simplified Mie approximation[140].

[vi] By John D'Errico; available at *http://www.mathworks.com/matlabcentral/fileexchange/loadFile.do?objectId=8277*; downloaded November 2006.

2.3.5 Applications of Diffuse Correlation Specroscopy

DCS measurements are typically conducted in the photon counting regime. A single mode fiber is used to collect light from tissue. Indeed, the correlator in common use at Penn (Digital Correlator, Flex05-8ch, Correlator.com, Bridgewater, NJ) requires the detected photon rate to be below ∼1 MHz (roughly the inverse of the smallest bin size); in typical experiments, the rate is ∼100-200 kHz in remission from tissue with a source-detector separation of 2.5 cm, ∼5 kHz at ∼6 cm separation in transmission. Most tissue work has been carried out in the remission geometry with source-detector separations of ∼2.5 cm in breast[73], brain[141], and muscle[142] tissue. Signal derived from adjacent DCS single mode fiber detectors can be summed to improve SNR.

In Chapter 8, I utilize DCS to measure blood flow in the human breast during mammogram-like compression. To our knowledge, this study provided the first reports of DCS blood flow measurements from light transmitted all the way through the human breast[143–145]. Our pilot results provided proof-of-principle information for *transmission* Diffuse Correlation *Tomography* (DCT) in breast. In Chapter 6, I describe instrumentation which may permit us to utilize *a priori* structural information from MRI to produce the first *in vivo* transmission DCT.

2.3.6 Applications of Diffuse Optical Tomography

Section 2.2.8, introduces the mathematics behind DOT in terms of the fluence rate. However, the *measured* signal is an intensity proportional to the fluence rate. This proportionality constant involves the integral over the numerical aperture of the detection optics, optical coupling constants, and is, in general, difficult to calculate. If one can normalize the measured signal to that from a phantom, the proportionality constant cancels out, e.g.:

$$\frac{U_m[\lambda_w, \boldsymbol{r}_s, \boldsymbol{r}_d]}{U_m^R[\lambda_w, \boldsymbol{r}_s, \boldsymbol{r}_d]} = \frac{I[\lambda_w, \boldsymbol{r}_s, \boldsymbol{r}_d]}{I^R[\lambda_w, \boldsymbol{r}_s, \boldsymbol{r}_d]} \tag{2.91}$$

for data (U_m, I) and reference (U_m^R, I^R) measured fluence rates and intensities. This cancellation relies on consistency in the proportionality constant between measurements. Such a normalization of DOT data generally requires detailed information on the reference phantom optical properties, but greatly simplifies the reconstruction task. In the data presented in this thesis, I normalize data using measurements from homogeneous liquid or gelatin phantoms (Chapter 6 and Chapter 7) and by pre-contrast agent injection data (Chapter 4). The latter depends utilizes an optically heterogeneous reference measurement (i.e., due to endogenous chromophores) to reconstruct the larger changes in optical properties due to an injected contrast agent (e.g., ICG), as shown by Ntziachristos[146].

The DOT reconstructions for the GenIII system (Chapter 6) were performed in TOAST[85,86] with an iterative conjugate gradient technique[147]. We also included the spatially dependent regularization scheme

I	Measured Intensity
L_i	Size of the reconstructed volume in the i^{th} direction
μ	Solution vector (i.e. μ_a and D)
$\mu^0[\boldsymbol{r}_k]$	Initial guess of solution vector
N_λ	Number of wavelengths
N_s	Number of sources
N_d	Number of detectors
N_t	Total number of voxels
$\boldsymbol{r}_s$	Source position
$\boldsymbol{r}_d$	Detector position
Q	Image Norm
$\gamma[\boldsymbol{r}_k]$	Spatial regularization term
χ^2	Objective function

Table 2.5: Notation for DOT reconstruction.

described by Choe *et al.*[31] in our algorithm; DOT is especially vulnerable to such artifacts at the source and detector positions, and so we vary the regularization parameter to be larger near the boundaries of the image. This spatially-dependent regularization reduces image artifacts. The specific reconstruction work-flow our work is based on were developed by Drs. Regine Choe, Kijoon Lee, Soren Konecky, and Alper Corlu[31]; DOT reconstructions using this work-flow was used to develop our statistical tumor localization technique (Chapter 7).

Iterative techniques require some measure of the reconstruction quality to determine if additional iterations should be performed. We define a common objective function χ^2. This quantity is a metric of the difference between the measured and calculated values of the fluence rate for each wavelength, source, and detector ($U_m[\lambda_w, \boldsymbol{r}_s, \boldsymbol{r}_d]$ and $U_m[\lambda_w, \boldsymbol{r}_s, \boldsymbol{r}_d]$, respectively), summed over all measurements. In practice, we normalize these values by the measured and calculated values of a homogeneous phantom (i.e. a reference measurement; $U_m^R[\lambda_w, \boldsymbol{r}_s, \boldsymbol{r}_d]$ and $U_c^R[\lambda_w, \boldsymbol{r}_s, \boldsymbol{r}_d]$). This normalization reduces the impact of differences between light detected at each fiber, since each will have a different skin coupling coefficient and a slightly different transmission. Table 2.5 summarizes the notation used to write out these functions. We define an objective function

$$\begin{aligned}
\chi^2 =& \frac{1}{2} \sum_{w=1}^{N_\lambda} \sum_{s=1}^{N_s} \sum_{d=1}^{N_d} \left(\ln \left[\frac{U_m[\lambda_w, \boldsymbol{r}_s, \boldsymbol{r}_d]}{U_m^R[\lambda_w, \boldsymbol{r}_s, \boldsymbol{r}_d]} \right] - \ln \left[\frac{U_c[\lambda_w, \boldsymbol{r}_s, \boldsymbol{r}_d]}{U_c^R[\lambda_w, \boldsymbol{r}_s, \boldsymbol{r}_d]} \right] \right)^2 + Q \\
\chi^2 =& \frac{1}{2} \sum_{w=1}^{N_\lambda} \sum_{s=1}^{N_s} \sum_{d=1}^{N_d} \left(\ln \left[\frac{U_m[\lambda_w, \boldsymbol{r}_s, \boldsymbol{r}_d]}{U_m^R[\lambda_w, \boldsymbol{r}_s, \boldsymbol{r}_d]} \frac{U_c^R[\lambda_w, \boldsymbol{r}_s, \boldsymbol{r}_d]}{U_c[\lambda_w, \boldsymbol{r}_s, \boldsymbol{r}_d]} \right] \right)^2 + Q. \qquad (2.92)
\end{aligned}$$

The image norm, Q,

$$Q = \sum_{k=1}^{N_t} \gamma[\boldsymbol{r}_k] \left| \mu[\boldsymbol{r}_k] - \mu^0[\boldsymbol{r}_k] \right|^2 \qquad (2.93)$$

computes the difference between the chromophore maps for the initial guess and the current iteration. Note

that Q includes a spatially dependent regularization factor

$$\gamma[\boldsymbol{r}_k] = \alpha \left(e^{-\left(\frac{x-x_{min}}{L_x/2}\right)^2} + e^{-\left(\frac{x-x_{max}}{L_x/2}\right)^2} + e^{-\left(\frac{y-y_{min}}{L_y}\right)^2} + e^{-\left(\frac{y-y_{max}}{L_y}\right)^2} + e^{-\left(\frac{z-z_{min}}{L_z}\right)^2} + e^{-\left(\frac{z-z_{max}}{L_z}\right)^2} \right) \tag{2.94}$$

which weights the relative importance of differences in μ as a function of spatial position. Work is ongoing to determine the optimal reconstruction parameters for the GenIII DOT-MR Imaging system (Chapter 6).

Chapter 3

Clinical Applications of Diffuse Optics in Biological Tissue

Diffuse optics can be used to measure concentrations of intrinsic and extrinsic chromophores in living tissue using the mathematical techniques discussed in Chapter 2. A wide range of interesting biomedical problems can be addressed with this information. For example, blood oxygenation levels provide information on aerobic exercise in muscle[119], total hemoglobin content appears to distinguish breast cancer from normal tissue[1], and an injected molecular tracers can show different blood transit times when an artery is blocked[148]. Measurements of endogenous contrasts permit frequent non-invasive measurements; exogenous contrasts, through more invasive, can potentially provide higher signal-to-background and more dynamic (e.g. pharmacokinetic) information compared to their endogenous cousins.

DOT and DOS utilize Near Infra-Red (NIR) wavelengths (∼650-950 nm). These wavelengths are safe for frequent and long-term measurements. NIR photons are non-ionizing, unlike X-Rays. Tissue damage mechanisms by radiation at these wavelengths are considered to be exclusively thermal by both ANSI[149] (American National Standards Institute) and the FDA[150] (United States Food and Drug Administration). Skin and eye maximum permissible exposures (MPE) both vary by wavelength, but are generally above the power levels required to obtain a useful diffuse optical signal at several centimeter source-detector separations; many of our instruments, for example, operate at about the same power as a common laser pointer. These low power requirements permit design of inexpensive, portable, instruments for continuous and rapid optical monitoring of tissue without physiological damage. MRI devices, on the other hand, are quite expensive, exclude patients with metal implants, have low throughput, and are never available at the bedside. Ultrasound gives some of the advantages of diffuse optical measurements, but generally provides structural or morphological tissue information, while diffuse optics provides functional information.

This chapter discusses contrasts in tissue due to activation and disease state, focusing especially on breast cancer (Section 3.1). Then it moves on to applications of DOT and DOS in breast cancer, placing the work described in this thesis into context (Section 3.2).

3.1 Tissue Optical Contrasts

3.1.1 Endogenous Optical Contrasts

Devices and techniques which obtain clinically useful information without use of contrast agents are attractive, in part, because they avoid potential allergic reactions and permit frequent repetition of measurements. Not surprisingly, most diffuse optical research has focused on the measurement of local concentrations of hemoglobin (Hb), oxyhemoglobin (HbO_2), lipid, and water to identify and diagnose disease states. Figure 3.1 shows the major chromophores in breast tissue and the approximate visible and NIR wavelength ranges.

Changes in total hemoglobin concentration (Hb_t=HbO_2+Hb) can identify angiogenesis and local blood volume responses. Changes in oxygen saturation (StO_2 =HbO_2/Hb_t) provide information on oxygen usage and metabolism. The lipid/H_2O ratio provides information on tissue composition. Diffuse optics is sensitive to micromolar concentrations of these chromophores in deep tissues; both absolute and relative measurements of chromophore concentrations are used. In addition to absolute measurements, data may be taken 'relative' to healthy tissue, relative to an artificial tissue reference 'phantom', or relative to some temporal baseline. Scattering (μ_s') changes provide information about cell and organelle density and structure. Relative measurements of both absorption and scattering can be made with less expensive instrumentation and simpler analysis techniques, but this approach requires a careful choice of normalization.

Absorption Diffuse Optical Spectroscopy (DOS) can be viewed as an extension of the familiar Beer-Lambert Law that relates incident (I_0) to detected (I) intensities after a beam of light passes through a sample of length d containing a solution with a concentration (C) of an absorbing species. A schematic is shown in Figure 3.2. (Originally, Bouguer[151] and Beer[152], but also described in many modern texts, for example, Born and Wolf[153].) The relationship between I and I_0 in optically thin sample is:

$$I = I_0 10^{-C\epsilon_{10}d}. \tag{3.1}$$

The diffuse optics community generally uses base e and $\mu_a = C \times \epsilon_e$, for a chromophore at concentration C with molar absorption coefficient of $\epsilon[\lambda]$. This convention matches that typically used in discussions of the radiative transport equation and random walks. Note that many authors tabulate the extinction coefficients in base 10 (ϵ_{10}), not the base e ($\epsilon_e = \log[e]\epsilon_{10}$) used here. With this substitution, Equation 3.1 becomes:

$$I = I_0 e^{-\mu_a d} \tag{3.2}$$

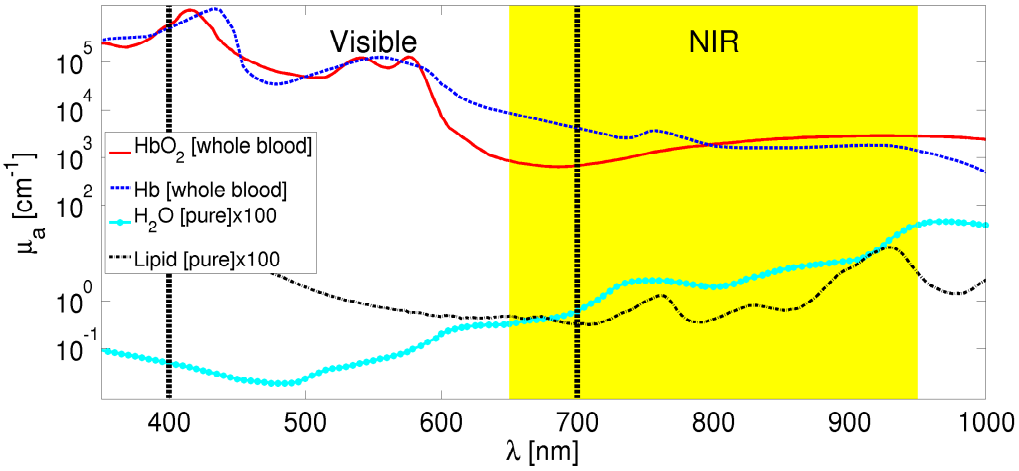

Figure 3.1: Spectra of major breast tissue chromophores on a semi-logarithmic scale, showing visible and NIR windows. Note that the H_2O and Lipid spectra have been scaled by a factor of 100 and that the Hb and HbO_2 spectra are for whole blood.

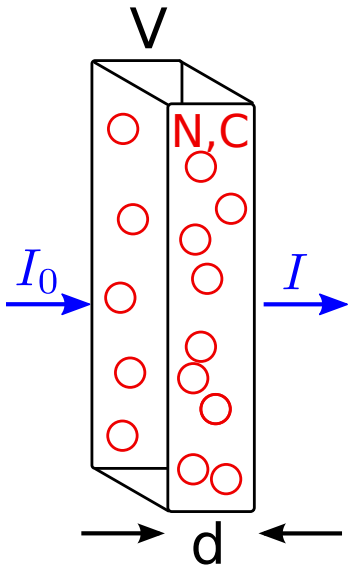

Figure 3.2: A schematic of a simple application of the Beer-Lambert Law. Light with intensity I_0 impinges on a vessel with thickness d and volume V from the left; photons are absorbed by the N chromophores, and a reduced intensity I exits the vessel from the right. The concentration of the absorbing species is $C = N/V$.

In the presence of tissue scattering, the path length (d) is not simply the width of the cuvette (as in standard bench-top spectroscopy of clear liquid samples, e.g. Figure 3.2), but rather is a 'typical' distance traveled by a diffusing photon from input to output. This distance can be measured or calculated from known tissue properties. The simplest correction to the Beer-Lambert Law is to include the so-called 'Differential

Path Length Factor' (DPF)[154,155] which, when multiplied by the distance between the source and detector on the tissue surface, approximates the mean distance traveled by a photon. This distance is also sometimes referred to as the 'Differential Path Length' (DP) and can be measured from the average tissue transit time between source and detector of a brief (sub-nanosecond) light pulse[94]; Patterson *et al.*[44] quantified this path length *in vivo* in 1989. Note, these path lengths are dependent on the tissue optical properties (μ_a, μ_s').

Recall from Section 2.2.5 that for the infinite medium, the average tissue transit time in terms of the optical properties of the tissue and spatial position for a source and detector separated by a displacement $\boldsymbol{r}$ is:

$$\langle t \rangle = \frac{1}{2} \frac{|\boldsymbol{r}|^2}{D + |\boldsymbol{r}| \sqrt{\mu_a v D}}$$

where v is the speed of light in the medium, $D = \frac{v}{3(\mu_s' + \mu_a)}$ is the photon diffusion coefficient, μ_s' is the scattering coefficient, and μ_a is the absorption coefficient. The average photon path length in the medium is thus $v < t >$. Arridge published a summary of these formulae for mean transit times for various geometries[46]. As an example, consider transport through an infinite medium with optical properties of human breast, assuming μ_s' =10 cm^{-1}, μ_a =0.05 cm^{-1}, index of refraction of 1.4, and $|\boldsymbol{r}|$=5 cm, we obtain $< t > \sim$ 2.5 ns and $d = c < t > \sim$ 53 cm. In a slab geometry with the same optical properties, $< t > \sim$ 2.1 ns and $d = c < t > \sim$ 45 cm.

Calculation of $< t >$ for a particular geometry permits simple interpretation of data from a homogeneous turbid medium: Beer's law (Figure 3.2) becomes

$$I = I_0 e^{-\mu_a v < t >}. \tag{3.3}$$

Next we consider multiple chromophores. The absorption coefficient, μ_a [λ], can be decomposed into the sum of the products of the concentrations (C_i) and extinction coefficients ($\epsilon_i[\lambda]$) of the chromophores in the tissue of interest. In most tissues, the primary absorbers are oxyhemoglobin (HbO_2), hemoglobin (Hb), lipid, and water[121,156] (Figure 3.1); myoglobin can also be an important absorber in muscle tissue. Equation 3.4 breaks the total wavelength-dependent, absorption down into the concentrations (C_x) of these chromophores and their extinction coefficients ($\epsilon_x[\lambda]$).

$$\begin{aligned} \mu_a[\lambda] &= \sum_{i=1}^{N_c} C_i \, \epsilon_i[\lambda] \\ &\simeq C_{HbO_2} \, \epsilon_{HbO_2}[\lambda] + C_{Hb} \, \epsilon_{Hb}[\lambda] \\ &\quad + C_{H20} \, \epsilon_{H_2O}[\lambda] + C_{Lipid} \, \epsilon_{Lipid}[\lambda] \end{aligned} \tag{3.4}$$

Where we have assumed there are no other chromophores absorbing at the wavelengths of interest. See Figure 3.3 for an example of this decomposition in breast tissue.

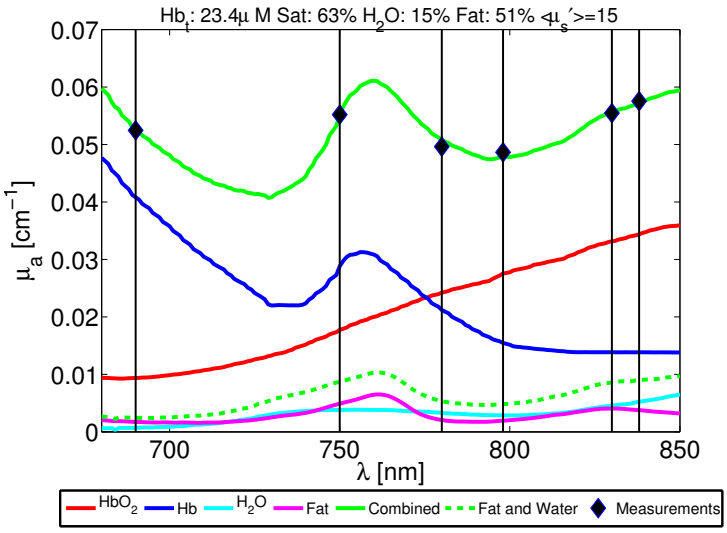

Figure 3.3: Time Domain measurements of absorption (black diamonds) at 6 wavelengths and fits to concentrations of major chromophores using known spectra (HbO_2, Hb, Fat, H_2O) in breast tissue for a 27 year old pre-menopausal female, transmission geometry (5.2 cm thickness), homogeneous slab solution. Unpublished data from the GenII Opt/MRI system.

Dr. Scott Prahl has tabulated the extinction coefficients of hemoglobin[157–159], water[160], porcine fat[161], and several other useful chromophores[i] from several sources.

As per scattering, Mourant and colleagues[140] suggested approximating the wavelength-dependent tissue scattering with a power law, after the dependence of the scattering efficiency factor on λ from a simplified version of Mie scattering theory, i.e.,

$$\mu_s'[\lambda] = A\lambda^{-b}. \tag{3.5}$$

Here, A is the 'scattering prefactor' and b the 'scattering power'. The scattering power depends on both the relative indices of refraction between scatterers and the bulk medium, as well as the size and number density of these particles. Nilsson *et al.*[162] successfully applied this approximation and it has been widely used since[31,109]. The scattering power (b) is often assumed to be constant in order to reduce the number of fitting parameters.

3.1.2 Intrinsic Optical Contrast in Breast Cancer

Leff and his colleagues at University College London[1] have recently published an exhaustive review of diffuse optics applied to breast cancer (studies published prior to 1 August 2006), summarizing the experimental conditions and results of some 34 studies, each having at least 5 subjects; the results of this tabulation

[i] Available at http://omlc.ogi.edu/spectra/hemoglobin/summary.html, downloaded Dec. 2006.

are summarized in Table 3.1.

Leff concentrates on Hb and HbO_2 contrasts in his review, as these chromophores dominate tissue spectra (e.g. Figure 3.3). Some researchers have therefore neglected other chromophores, permitting simplification of their instrumentation. Note the significant contrast between the means of the properties of malignant lesions and healthy tissue, and also the significant width of the distributions, especially in the malignant lesions. Some of the variance in each chromophore is probably due to grouping all malignant cancers into one group, as cancers are known to be heterogeneous both microscopically and between subjects. Similarly, each of the other intrinsic parameters measured by diffuse optics has a distribution function; this complicates developing diagnostic metrics. (See Section 7.1 for a discussion of how several research groups have attempted to resolve this difficulty.) In a recent study (not included in Leff) Choe *et al.*[31] found a 1.25-2x contrast between healthy tissue and 41 biopsy-confirmed malignant lesions in 3D tomographic reconstructions. Images from two of the subjects in this study are shown in Figure 3.4 and Figure 3.5; this data is utilized in Chapter 7, where I introduce our new intra- and inter-subject statistical normalization approach which accounts for these heterogeneities, and where I demonstrate a novel statistical technique to localize cancers based on DOT.

Several researchers have sought to correlate the tissue microstructure to DOT findings. Pogue *et al.* initiated a small study to compare DOT-reconstructed Hb_t and blood-vessel density in tumors[12]; Zhu and colleagues[15] have followed up on this research. Scattering in tissues is dominated by structures approximately the same size as the light wavelength ($\sim 1\mu$m). The cell proliferation of some cancer types has led some researchers to consider using μ_s' as a diagnostic parameter: Li broke this down into scatterer size and volume fraction in search of an indicator of malignancy[14] and Choe *et al.*[31] found it offered good discrimination between benign and malignant lesions. Several groups[31,74,164] have combined the various endogenous measurements into composite indices which enhance cancer contrast.

The vasculature of healthy tissue is organized and provides a hierarchical network for blood flow throughout the tissue volume. In contrast, angiogenesis in cancerous tissue produces blood vessels with chaotic organization, tortuous pathways, and higher concentration, shown schematically in Figure 3.6. Blood volume and perhaps saturation may change in cancerous tissue, as noted in Table 3.1, but the change in blood vessel organization suggests that blood flow may provide an additional contrast, as shown by Durduran[51] and Zhou[73]. A simple one source-detector hand-held probe, manually scanned across a cancer, showed significant change in localized tumor blood flow (Figure 3.7).

In addition to the static breast cancer contrasts discussed above, researchers have also examined the possibility of using external modulations of intrinsic contrast. The Valsalva maneuver (exhaling against a closed glottis) raises pressure in the chest cavity and possibly restricts venous return from the breasts of a woman lying in the prone position, thus increasing contrast in tumors[129]. External compression of the

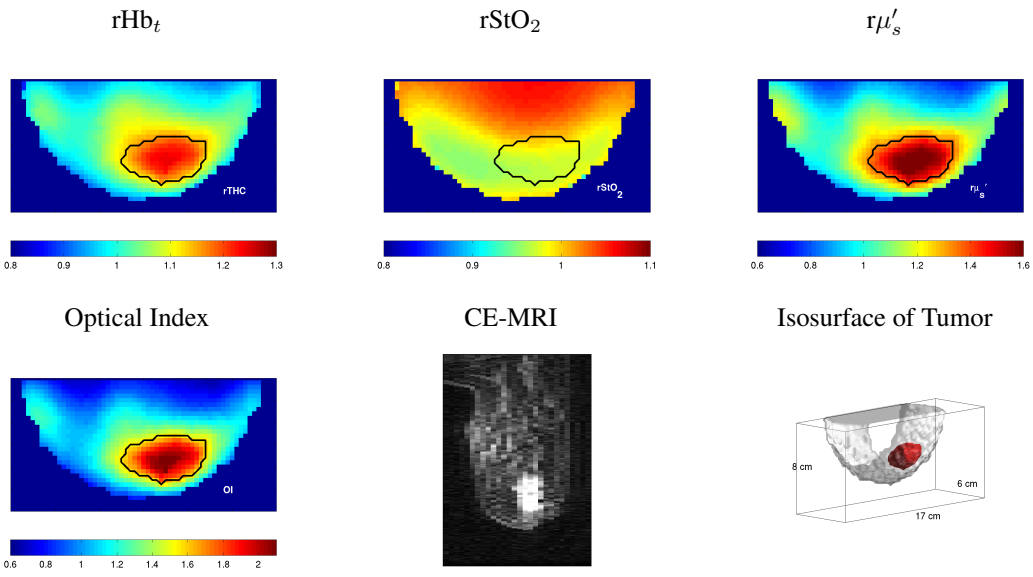

Figure 3.4: DOT reconstructions of a 2.2 cm invasive ductal carcinoma. In descending rows: (top row) Relative total hemoglobin ($rHb_t = Hb_t / \langle Hb_t \rangle_{Healthy}$), relative oxygen saturation (rStO$_2$), relative μ_s' at 780 nm (rμ_s'). (bottom row) A composite optical index ($OI = \frac{rHb_t r\mu_s'}{rStO_2}$), a 3D rendering of the tumor volume, and non-simultaneous Gd-DTPA contrast enhanced MRI. Note that the DOT imaging utilized axial compression and the MRI was performed with a sagittal compression. Image courtesy of R. Choe, data described in Choe *et al.*[31].

malleable breast can force out blood, reducing Hb$_t$, or even restrict blood flow; several groups[145,165–167] are currently working on compression-related projects. Restricted flow impairs the delivery of contrast agents, making this work of interest to researchers in other modalities. Additionally, several commercial companies including DOBI Medical and ViOptix[167] have or are attempting to commercialize devices using pressure modulation. Vascular dynamics can be modified through changes to inhaled gases. A carbogen (CO$_2$ and O$_2$ mixture) inhaled contrast agent has been applied to animal models by Kotz and colleagues[168] and breast cancer by Dixit[169].

We have applied DOS and DCS to mammogram-like compression[145], permitting direct measurement of blood flow changes during the perturbation (Chapter 8).

3.1.3 Exogenous Optical Contrast Agent: ICG

Contrast agents are used in medical imaging to enhance the difference in signal between tissue of interest and the surrounding background. In diffuse optics, contrast can be absorptive or fluorescent, and fluorescent agents are potentially detectable at much lower concentrations[170,171] as the background signal can be much lower. Unfortunately, only a single diffuse optical contrast agent is currently approved for clinical use in the United States. This situation should change as additional agents are developed and shepherded through

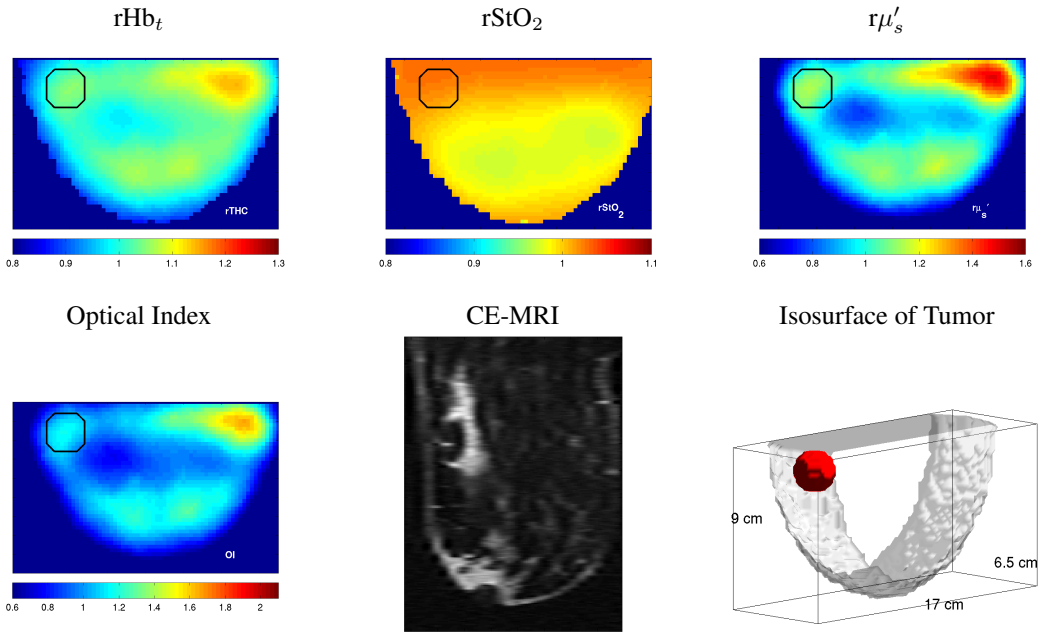

Figure 3.5: DOT reconstructions of a 0.5 cm fibroadenoma. In descending rows: (top row) Relative total hemoglobin ($rHb_t = Hb_t / \langle Hb_t \rangle_{Healthy}$), relative oxygen saturation (rStO$_2$), relative μ_s' at 780 nm (rμ_s'). (bottom row) A composite optical index ($OI = \frac{rHb_t r\mu_s'}{rStO_2}$), a 3D rendering of the tumor volume, and non-simultaneous Gd-DTPA contrast enhanced MRI. Note that the DOT imaging utilized axial compression and the MRI was performed with a sagittal compression. Image courtesy of R. Choe, data described in Choe *et al.*[31].

the regulatory process, but current clinical work focuses almost exclusively on Indocyanine Green (ICG), as this FDA approved agent absorbs and fluoresces in the NIR. It was first applied to diffuse optical imaging of breast cancer by Nioka[126,172]. Many animal studies have been conducted with diffuse optical contrast agents; one of the most useful studies from the standpoint of human measurements was Cuccia and colleagues combination of optical contrasts (ICG and Methylene Blue) with MR contrast (Gd-DTPA) in rat imaging[173]. A potentially useful attribute of optical contrast agents is the ability to image these agents across multiple scales during the course of identification and removal of a lesion. For example, a cancer could be imaged with ~0.5 cm resolution in DOT, ~0.5 mm resolution during surgical resection, and at ~1 μm resolution during pathological examination of the excised tumor. Bhushan and colleagues, for example, have investigated an agent specific to hydroxyapatite, a calcium salt deposited in breast cancer micro-calcifications, in the context of image guided surgery[174].

Fluorescent agents offer the potential for information beyond the agent concentration[175] and even beyond the potentially higher SNR[171]. For example, the fluorescent lifetime of some agents is sensitive to the local chemical micro-environment and can be imaged with fluorescence DOT[176]. At University of Pennsylvania, Corlu *et al.*[89] extended the work of O'Leary[177], Culver[88] and Choe *et al.*[31] to perform 3D reconstruction of

	Cancer to Tissue Contrasts			
	Hb_t[μmol/L]	Contrast	StO_2 [%]	Contrast
Healthy, pre meno	34±9	1.9	75±2	0.88
Healthy, post meno	14±0	4.6	80±4	0.83
Healthy, not spec.	21±6	3.1	68±5	0.97
Malignant lesion	65±34	1	66±24	1

Table 3.1: Optically detectable physiological contrasts in breast cancer: Summary of currently published (pre 2006) data by Leff[1], given as mean ± standard deviation. Contrasts are calculated as Y_{lesion}/Y_x. Pre- (Post-) menopausal data is calculated from 3 studies with 16 (13)[116], 15 (13)[121], and 4 (19)[163] subjects. Data with menopausal status not specified was averaged over 17 studies with several hundred subjects in total. Note that malignant lesions appear to be much more heterogeneous than healthy tissue; see text for discussion.

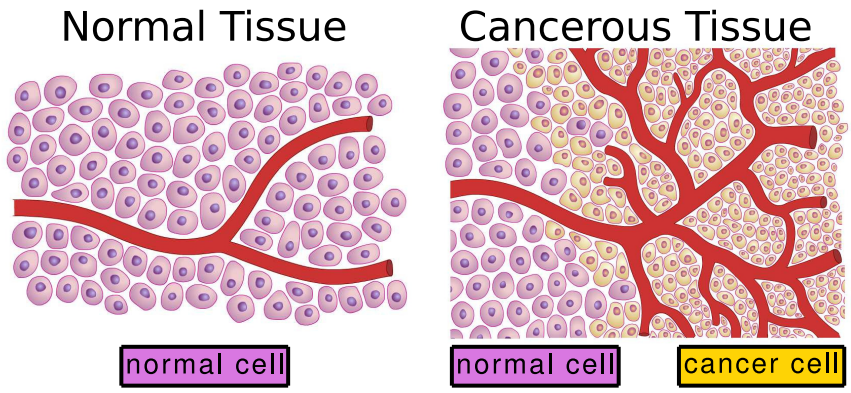

Figure 3.6: Cartoon of tissue level organization of healthy and cancerous tissues. Note the hierarchical organization of blood vessels in healthy tissue versus the chaotic vasculature in cancerous tissue- rapid angiogenesis caused by cancer does not produce efficient blood vessels. Figure courtesy of R. Choe and Y. K. Choe.

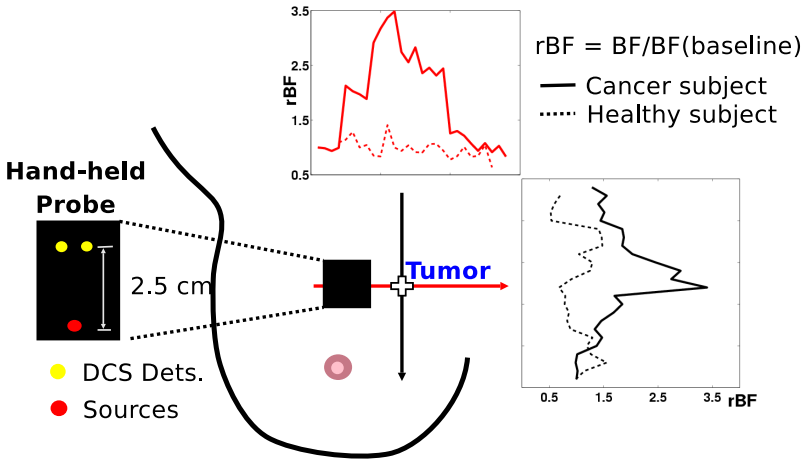

Figure 3.7: Example blood flow contrast in cancerous and healthy breast tissue, measured with a hand-held scanning probe. The probe was moved across the known position of each cancer in 1 cm increments along orthogonal lines. Figure adapted from T. Durduran *et al.*[51].

ICG fluorescence in breast cancer. For reviews of fluorescence imaging, see Frangioni[178].

Sevick-Muraca and Rasmussen have recently published[179] primer on molecular imaging, comparing optics to nuclear imaging and genetic techniques. Various other commercial agents have been developed for animal use, some with conjugating moieties, which can be attached to various ligands known to target specific disease states. Work in animals with these targeted agents, for example that by Reynolds and colleagues[180] has demonstrated *in vivo* detection of $\sim$1 cm lesions with micromolar concentrations of the agents in canine mammary tumors. Ke *et al.*[181] showed specific targeting of epidermal growth factor positive cells with a Cy5.5 fluorescent probe. Soubrane and colleagues [182] have demonstrated the importance of localizing and quantifying tissue absorption heterogeneities for quantitative fluorescence spectroscopy. Klohs[183] has provided a recent addition to a substantial body of reviews on the topic.

Various NIR absorbing and fluorescent agents have been developed for animal use[184]. Pre-clinical ICG derivatives are reviewed by Tung[185] and optical agents are more broadly reviewed by Licha, Schirner, and Henry[186]. Sevick-Muraca has also discussed ICG and recent developments in targeted contrast agents[170].

Indocyanine Green (ICG) is used extensively with all three generations of the University of Pennsylvania Opt/MR imaging system (see Section 4.2). A brief introduction is included below to facilitate discussion of these instruments and results from clinical studies. ICG is also known as Cardio-Green, available in the United States from Akorn Specialty Pharmaceutical Company, (*www.akorn.com/*).

ICG isn't an ideal NIR contrast agent in terms of fluorescent yield or absorption cross section, but FDA approval, its long history of safe use in humans[187], and the lack of alternate fluorophores or chromophores in the NIR approved for human use have rendered ICG the primary contrast agent for DOT and DOS in humans. Diffuse optics with ICG contrast has been applied to human breast cancer[5,6,89,97,126,146,172,188–192], human brain monitoring[148,193–195], and the flow of lymph in human limbs[179].

Fluorescence imaging with DOT has a lengthy history at University of Pennsylvania, including early experimental work with ICG imaging[126,172,196,197] and theoretical developments[171,175,176]. Sevick-Muraca and colleagues[170] explored the limits of ICG imaging and also compared CW and FD (100 MHz) fluorescent imaging on a phantom with a 100 μL target of 100 fM ICG at depths from 1 to 7 cm. This sensitivity is a key advantage of optical contrast agents. Previous work in our lab by Ntziachristos combined simultaneous diffuse optical measurements of ICG and Gd-DTPA enhanced MRI in human breast using a TD[5,198] instrument. The relative sensitivities of the techniques was not apparent from the experimental protocol: Ntziachristos describes injections of 0.1 millimoles of Gd-DTPA and 0.25 milligrams of ICG per kilogram bodyweight. ICG has a molecular weight of 775 g, so this corresponds to an injection of 323 nanomoles per kilogram bodyweight for ICG; a factor of 300 difference in concentrations.

ICG is quickly cleared from the blood stream by the liver, i.e., its half-life in the breast $\sim$3-5 minutes[197]. It is primarily a blood pooling agent (i.e. normally confined to the intravascular space), binding to albumin

when injected intravascularly. Several researchers[89,198] have found ICG concentrations in tumors are higher than in the surrounding tissue. Tumors are known to produce additional microvasculature (angiogenesis); this additional vasculature is one of the sources of intrinsic DOT contrast. The 'quickly grown' vessels are known to be more permeable, consistent with the hypothesized origin of ICG concentration contrast in tumors. This heightened permeability permits ICG or even ICG-bound albumin to exit the vasculature into tumors and produces a transient build up of ICG. The extra-vascular ICG apparently exchanges with vascular ICG and is eliminated fairly quickly ($\sim$10-20 minutes [197]) and all ICG is eventually removed by the liver. However, recent results by Hagen[190], who imaged following continuous infusion over the course of 15-25 minutes of 39-75 mg ICG, suggest that some ICG may persist in the extravascular tumor space for hours. Imaging at later times provided a lower signal, but higher contrast to background ratio.

The dosage of ICG required for diffuse optical measurements is well below the maximal dosages set by the FDA. During the research described here, ICG was administered as a bolus, followed by 5 ml of saline, and DOT data collected for $\sim$10 minutes. Dosage was 0.25 mg per kg of body weight, up to a maximum of 25 mg. The typical dosage (manufacturer's literature[199]) for an adult in an indicator-dilution study is 5 mg per injection, up to 2 mg/kg total. For hepatic function determination, the usual dosage is a bolus of 0.5 mg/kg and detection of ICG in the blood stream for tens of minutes. Ophthalmic angiography studies use a bolus of up to 40 mg in a single injection to detect vascular damage in the eye.

Anaphylactic or urticarial reactions to ICG have been reported in patients with history of allergy to iodides. These patients, along with pregnant women, were excluded from our study. Hope-Ross*et al.*[187] reported adverse reactions in 1923 ICG videoangiography exams (1226 patients). The dosage in this study varied between 1-5 mg/kg body weight and 12.5-50 mg total dosage. Hope-Ross found 0.15% mild, 0.2% moderate, and 0.05% severe adverse events, with no deaths. Research reported in this thesis utilized at most 0.25 mg/kg- a factor of ten less then the dosage used by Hope-Ross*et al.*. There have been two deaths associated with ICG injection during cardiac catheterization, per the manufacturer's literature[199].

3.1.4 Applications of ICG to Breast Cancer

Researchers at University of Pennsylvania have utilized ICG human breast cancer imaging for many years. The pioneering work of Nioka[126,172] was followed by important contributions from Ntziachristos[5,6,146], Intes[197], and Corlu[89].

Several researchers have attempted to determine if ICG uptake and clearance kinetics can be diagnostic for malignancy. Intes[197] used a CW stand alone instrument described by Nioka[126,172] for monitoring ICG kinetics in breast cancer and observed substantially different kinetic profiles between three subjects with a different types of cancer, see Figure 3.8. In a somewhat larger study, Rinneberg *et al.*[97], using a TD scanning system, did not observe a difference in ICG kinetics between types of lesions. Note that both of these studies

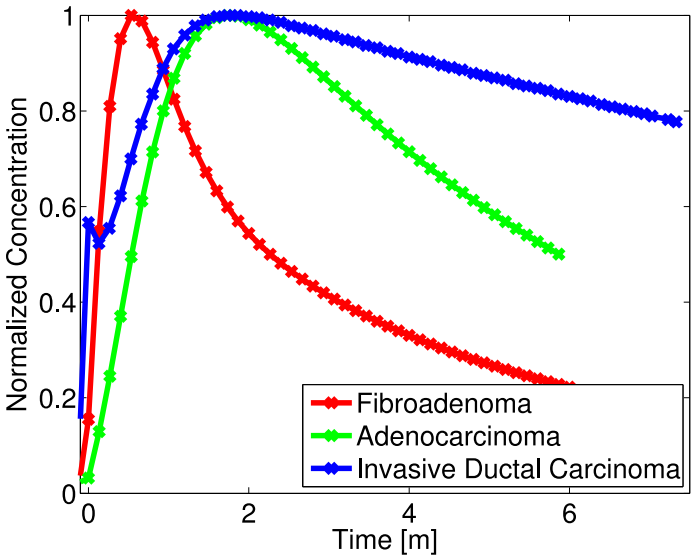

Figure 3.8: Results from optical-only kinetics imaging system. This device was not co-registered with another imaging modality and could only measure $\Delta\mu_a$, but had good time resolution. Data has been adapted from Intes *et al.*[197].

were quite small and focused on short time ($\sim$10 min.) kinetics. However, in later work from Rinneberg's group[190,192] tumor ICG kinetics at long times ($\sim$25 min.) post injection did distinguish cancerous from normal tissue.

Corlu and colleagues applied their 45 source, CCD detection (thousands of source detector pairs) instrument to imaging ICG deposition in cancers and published the first tomographic breast reconstructions using ICG fluorescence[89]. Examples of their images are shown in Fig. 3.9. These data were collected well down on the tail of the kinetics curve (i.e., $\sim$6 minutes post-ICG-injection). Among other things, this long delay reduces the effect of rapidly changing drug concentration on the reconstructions. This choice of imaging timing of course reduces the total ICG signal, albeit tumor-to-normal tissue contrast is likely better at the long delay.

Sevick-Muraca has examined the use of ICG to map Sentinel Lymph Nodes (SNL) in breast cancer patients and found that subcutaneous injections of 10 to 100 μg ICG permitted imaging of lymph drainage paths and the SNLs[200], comparing the technique to lymphoscintigraphy. Her work suggests ICG may help identify those SNLs to remove for pathological examination and those lymph nodes that can be safely left intact.

One potential point of concern for multi-modality contrast enhanced imaging is increased patient risk or signal degradation due to interference between the optical and MR contrast agents. Several researchers have reported joint ICG and Gd-chelate measurements without significant adverse events[201–205]. During $\sim$50 sequential Gd/ICG injections for breast imaging at Penn, we also observed no serious adverse events.

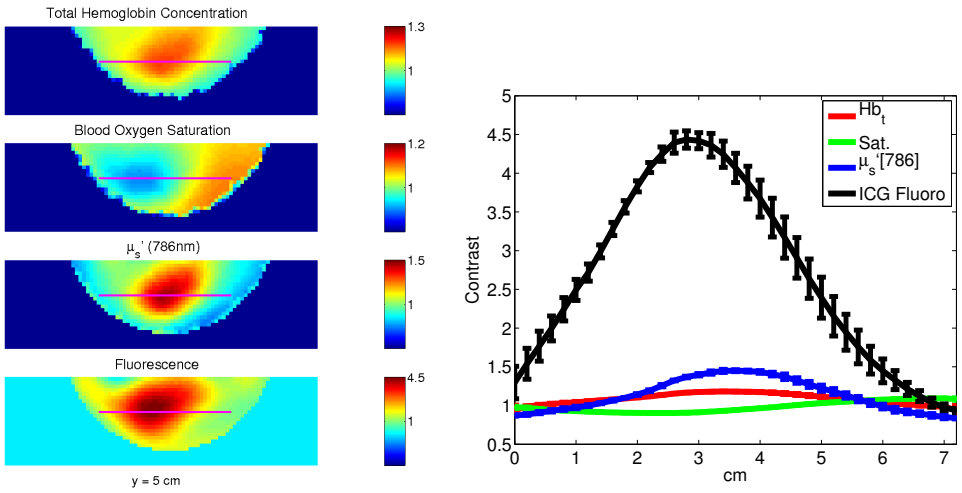

Figure 3.9: ICG fluorescence contrast in 3D tomographic imaging of the human breast; a single cranio-caudal slice is shown for a 52 year old post-menopausal female. ∼1.5 cm diameter retro-areolar invasive carcinoma was identified by a multi-modality (Gd-DTPA MRI, ultrasound, PET, mammogram) study. Left: Images of Hb_t, StO_2, μ_s', and ICG fluorescence. Right: Line plots, corresponding to the magenta line in images on the left, showing the lesion contrast for each chromophore. Adapted from Corlu[89].

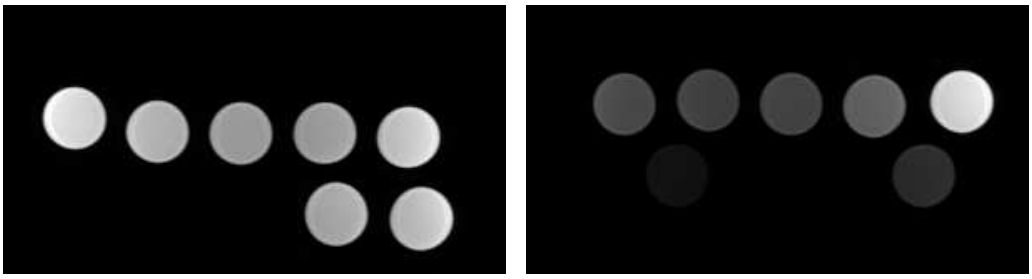

Figure 3.10: Test of influence of ICG on MRI signal from MultiHance (Gd chelate). (left) $0.25mM$ MultiHance and [12.9, 6.5, 3.2, 1.6, 0.8, 0.4, 0]μM ICG. The slight fall off in signal at the center of the image is due to inhomogeneity in the MR coil sensitivity; this was confirmed by moving and rotating the sample (data not shown). (right) 3.2μM ICG and [5, 0.5, 0.3, 0.25, 0.2,0.1,0] mM MultiHance.

We performed a simple test to confirm that ICG did not effect signal from gadolinium chelates using various physiological concentrations of 'MultiHance' (Gadobenate dimeglumine) and ICG in normal saline. If we assume blood is roughly 7% of female body weight[66–68], a 0.25 mg/kg body weight dose of ICG corresponds to

$$0.25\frac{mg\ ICG}{kg\ body}\frac{kg\ body}{0.07kg\ blood} = 3.571\frac{mg\ ICG}{kg\ blood} = 3.571\frac{mg\ ICG}{L\ blood}\frac{1mol\ ICG}{775g} \simeq 4.6\mu M$$

for peak arterial concentration (assuming the density of blood is equal to the density of water). Figure 3.10 shows the results of this experiment.

3.2 Clinical Diffuse Optics

3.2.1 Potential of Diffuse Optics to Improve Clinical Breast Cancer Care

Clinical advances in detection, diagnosis, and therapy monitoring for breast cancer offer potential benefit to both sufferers and, because of the high incidence of breast cancer[206] and the associated costs, to society. Current screening techniques rely heavily on the X-Ray mammogram, a technique which detects only ∼35% of cancers in women under age 50[207]; contrast enhanced MRI screening is much more sensitive (85%)[208], but also considerably less common, more time consuming, lower throughput, and more expensive. Breast cancer has attracted much attention from the diffuse optics community because, in addition to the clinical need, the human breast is somewhat easier to probe with diffuse light than other tissues. The deformability and low optical absorption of the breast permit researchers to use a variety of geometries (e.g. cylindrical, parallel plate) and to make measurements through more tissue (up to ∼12 cm) than is possible with many other organs, such as brain. This clinical need and reduced experimental difficulty may permit breast cancer to be one of the first clinical applications of molecular imaging agents in diffuse optics. Leff *et al.*[1], in a recent review of clinical applications of diffuse optics to breast cancer, suggested that ∼85% of cancers reported in these works are detectable using intrinsic optical contrast; Chance's study of over 100 women[75] suggests potential sensitivity and specificity above 90%, again with intrinsic contrasts. Choe *et al.*[31] provided 3D reconstructions of the entire breast and showed differentiation between benign and malignant lesions.

DOS/DOT also has a strong potential to be complimentary to existing clinical modalities: The tomographic reconstructions from DOT will not match the resolution of 3D images of tissue structure from MRI, X-ray imaging, or even ultrasound; however, DOT can provide functional information on tissue metabolism, does not use ionizing radiation, requires relatively inexpensive instrumentation, is suitable for long-term continuous monitoring, and has the potential to be very sensitive to contrast agents.

Diffuse Optics may prove to have several uses in a clinical breast cancer diagnosis and treatment; an example, developed in conjunction with our collaborators at the Hospital of the University of Pennsylvania, is shown in Figure 3.11.

Diffuse optics has potential applications in screening women at high or intermediate risk of developing cancer (i.e., as determined with the Gail model[209,210]; (1) in Figure 3.11). This population will be screened many times over their lives, starting as early as their twenties, and the radiation dose of annual mammograms can be of considerable concern. Thus, applications of DOT and DOS as a non-ionizing, relatively inexpensive, screening modality imaging would be advantageous for this population. As DOT systems would almost certainly be less expensive than an MRI, their use could be justified for lower-risk women, thereby increasing the screening pool. Furthermore, pre-menopausal women tend to have breasts with higher mammographic density, reducing the sensitivity and specificity of X-Ray mammography. Measurements from DOT or DOS

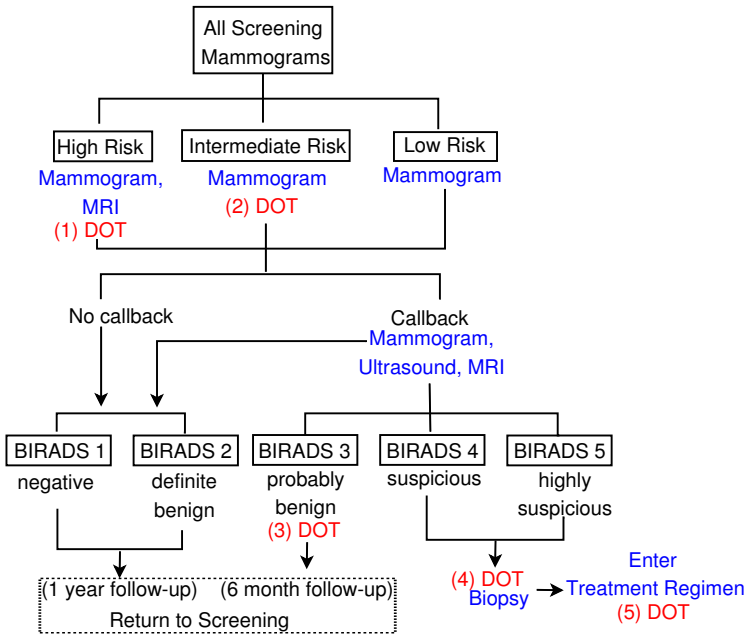

Figure 3.11: Example clinical work flow for breast cancer screening, derived from discussions with our clinical collaborators. Possible clinical uses of diffuse optical techniques are marked and expanded upon in the text. BIRADS: Breast Imaging Reporting and Data System (American College of Radiology).

'adjunct' systems could potentially be used to increase clinical imaging modality specificity. This potential increase in multi-modal imaging specificity can also be applied to women who have a 'probably benign' lesion or 'suspicious' ((3) and (4) in Figure 3.11). 'Probably benign' lesions can be followed up more rapidly and frequently with non-ionizing DOT or DOS that X-Ray.

Perhaps the most immediately useful application of DOT is for therapy monitoring ((5) in Figure 3.11). DOT and DOS are sensitive to tissue function and therefore may be able to identify tumors response to therapy more rapidly than an imaging technique like X-Ray mammography which depends on tissue structure.

However, prior to the clinical implementation of any of the above potential uses, diffuse optical techniques must be proven. Much of the work presented in the following chapters begins to pursue this goal via comparisons with data simultaneously acquired via magnetic resonance imaging.

3.2.2 Previous Work in Multi-Modal Imaging

Multi-modal imaging with diffuse optics can focus on *validation* of the diffuse optical measurement, *comparison* of diffuse optics with a measurement using another technique, or *synthesis* of different types of information into a composite index. A validation study, for example, might compare DOT to MRI imaging for detection of breast cancer. A comparison study might superpose functional MRI (fMRI) Blood Oxygenation Level Dependent (BOLD) imaging and functional DOS/DOT, as both signals depend on neurovascular

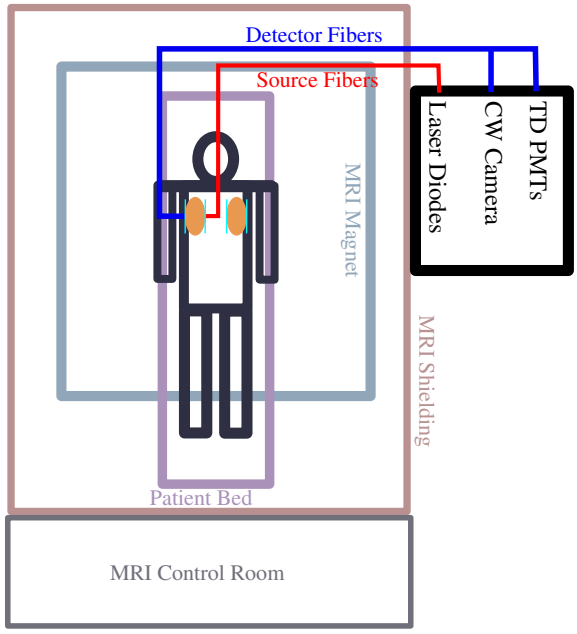

Figure 3.12: Cartoon of instrument and subject placement for simultaneous DOT and MRI measurement. This is the basic configuration of the GenIIm system, as described in detail in Chapter 4.

coupling[211]. A synthesis study could use the tissue structural information from X-ray mammography or ultrasound to constrain an optical tomographic reconstruction showing Hb_t and StO_2 distributions[212].

Diffuse optics can be combined relatively easily with several standard clinical techniques, such as MRI[7,198], ultrasound[9,28], magnetoencephalography[213,214] and X-ray mammography[10,215]. Fiber optics are often easily integrated into clinical devices with little disturbance to other instrumentation. For example, fiber optics can carry light more than 10 meters to and from the tissue of interest, permitting the opto-electronic portions of diffuse optical instruments to be placed outside of the shielding of an MRI device, as we have done with both our GenII and GenIII systems (Figure 3.12).

This ease of integration is inspiring researchers to conduct multi-modality studies. In this thesis, I focus on applications of optical-MR multi-modality imaging for breast cancer.

Various groups have focused on combining the functional information (i.e. oxygen metabolism, angiogenesis) from optical imaging with high resolution structural information provided by other modalities. Zhu[9] demonstrated that ultrasound is a natural co-modality for hand-held DOS. Both technologies are inexpensive, easily integrated into a hand-held probe, and non-ionizing[28,216,217]. This last point permits ultrasound and DOS to be used for frequently repeated measurements (for example, to monitor patients during the course of treatment[73]). Ultrasound provides structural information, permitting reconstruction of the tissue volume to improve quantification. DOS can alert operators to changes in blood oxygen saturation, total hemoglobin, etc.. The MGH group has combined X-ray tomosynthesis with a two wavelength FD system[215,218] and later

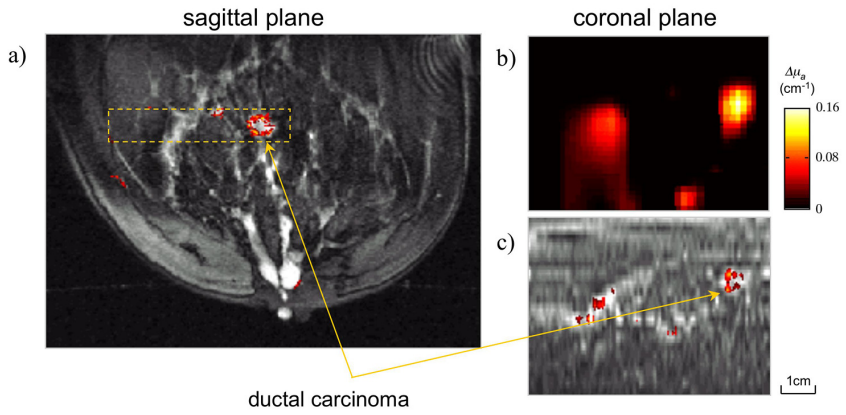

Figure 3.13: Simultaneous Optical and MRI measurements of ductal carcinoma by Ntziachristos[5], showing ICG and Gd-DTPA spatial correlation. (a) Sagittal Gd-enhanced MRI with optical field of view marked in yellow. (b) Coronal DOT image of ICG uptake. Note that this plane is perpendicular to that shown in (a). (c) Coronal Gd-enhanced MRI with the same field of view as (b).

incorporated an eight wavelength FD system[166] by ISS Inc. in their studies of the effects of compression on breast physiology; see Section 3.1.

Few researchers worldwide have concurrently utilized structural information from non-optical modalities and injected optical contrast agents for improved diffuse optics based diagnosis and detection. Ntziachristos, Yodh, Schnall, and Chance[198] pioneered simultaneous contrast-enhanced DOT and MRI (the University of Pennsylvania 'GenI' system). Figure 3.13 shows an example of co-localization of the two agents. This work employed a TD diffuse optical instrument to obtain simultaneous optical measurements of breast with ICG contrast and with Gd-DTPA enhanced MRI. The DOT system employed 24 sources, 8 detectors, and one optical wavelength (830 nm) across a 5x10 cm grid. Ntziachristos produced co-registered optical and Gd-subtraction images, permitting comparison of the spatial distribution of agent uptake and measurements of ICG kinetics. This system was later expanded to three optical wavelengths[5,6]

The Dartmouth optical breast cancer group conducted a study of 11 healthy subjects, with Brooksby[7,219] performing FD-DOT constrained with spatial tissue type distribution from Gd-enhanced MRI. Carpenter[8] extended this study into a cancerous subject with the addition of gadolinium contrast agent (Gd-DTPA), applying a regularization scheme permitting gradual changes inside a tissue type and abrupt changes on the boundaries between types. This instrument has 16 sources and 15 detectors, operated at 100 MHz, and uses a circular geometry. Combined DOT/MR imaging systems are summarized in Table 3.2.

Practical limitations on recruitment and restrictions on modification of clinical instruments have led many researchers to compare DOT images with sequentially acquired clinical data. Azar[30] has developed sophisticated deformation software to compare optical measurements with 3D images from other imaging

	Year	Sources	Detectors	λ	Type	Notes
Penn, GenI	1998	24	8	3	TRS	Parallel-Plate
Penn, GenII	2004	32	8	6	TRS	Parallel-Plate
Penn, GenIIm	2006	32	8 (16)	6 (1)	TRS/CW	Parallel-Plate
Penn, GenIII	2009	32	5 (54)	6 (5)	TRS/CW	Parallel-Plate (Current)
Penn, GenIII	2009	64	16 (256)	6 (6)	TRS/CW	Parallel-Plate (Planned)
PTB	2005	35	8	4	TRS	Parallel-Plate[220]
Dartmouth	2003	16	15	5	FD	Ring[221], later Parallel-Plate[222]

Table 3.2: Summary of Clinical Optical-MRI systems for breast cancer. Dates shown are year of first publication; previous generation systems shown only for Penn. Thayer at UCI has presented a progress report[223] on the development of a new FD system.

modalities taken non-concurrently; particularly, Gd-DTPA enhanced MRI. These fused data sets offer information from or comparison of both modalities, when simultaneous data acquisition is impractical. Positron emission tomography (PET) using fluoro-deoxyglucose (FDG) is a clinical imaging modality which shows cellular glucose uptake and therefore offers a measurement of glycolytic cellular metabolism; combining PET and DOT offers the opportunity to compare this to blood oxygenation saturation. At University of Pennsylvania, Konecky and collaborators have applied Azar's data set fusion techniques to show correlation between optical parameters, especially total hemoglobin and scattering with FDG uptake measured with whole body PET[29]. Saturation measured by optical methods had little correlation with FDG uptake, but the study was fairly small (N=9). These researchers also extended their study with an experimental breast-only PET scanner to show co-localization of tumors in three subjects. Work applying this deformation technique to hand-held optical measurements and MRI is ongoing in collaboration with University of California Irvine, who have previously correlated sequential hand-held DOS measurements with MRI[11].

3.2.3 Practical Diffuse Optics Clinical Instrumentation

Diffuse Optical instruments differ in the quantity of *spatial*, *spectral*, and *temporal* information provided (Figure 3.14). Spatially, an instrument with few source-detector pairs collects regional (a few cm^3 of tissue) information, while data from an instrument with hundreds or thousands of source-detector pairs can yield a 3D tomographic reconstruction. Spectrally, an instrument with only a single wavelength can monitor changes in absorption at that wavelength and therefore track the kinetics of a contrast agent, but it cannot separate two simultaneously changing chromophores, both of which absorb at the wavelength used. A multi-wavelength or even broadband instrument can distinguish between several chromophores. Instruments with temporal information (TD or FD) can separate absorption and scattering, permitting absolute quantification of the chromophore concentrations (Eqn. 3.4).

The information content of diffuse optical measurements therefore has dimensions of frequency (TD data has many frequencies), source-detector pairs, and wavelength. The most basic instrument consists of a single

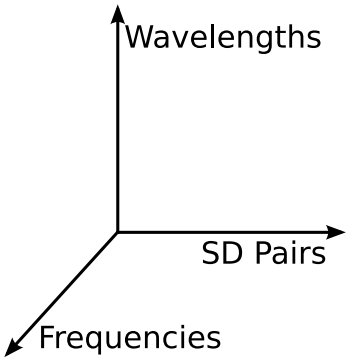

Figure 3.14: Information content of diffuse optical techniques. More wavelengths, source-detector pairs, and frequencies increase the completeness of the data set. Time domain measurements can be Fourier transformed into many frequencies; wavelength data can be transformed into chromophore concentrations. Cost, instrument complexity, and measurement time scale with each dimension.

source-detector combination and one wavelength, with a continuous (ω =0) light source; very similar to the 2 wavelength system described by Chance[224] and later commercialized as the 'RUNMAN' by NIM Inc. (Philadelphia, Pa., USA). The instrument with the most complete data set is TD (or swept frequency FD), with many source and detector positions and wavelengths. In the 'wavelength' and 'frequency' dimensions, the most complete data set so far reported is the 32 wavelength, TD instrumentation developed by the group at Politecnico di Milano for scanning mammography[225] and brain[226] measurements. However, the laser sources and detectors for such systems are complicated and expensive. The source-detector dimension is maximized by Choe *et al.*[31] (4×10^4 source-detector pairs) for human studies and 10^7 pairs by Konecky[90] in phantom studies. However, DOT images with these systems can take 10 minutes or longer to acquire. The cost, complexity, and measurement time are roughly correlated with each dimension and therefore the richness or completeness of the data set. For example, a pulsed super-continuum light source for multi-wavelength time domain measurements currently costs $\sim$\$70k while a single wavelength constant output LED might be available for \$1.

The work presented in this thesis describes simultaneous contrast-enhanced DOT and MR imaging (Chapter 4 and Chapter 5) and the development of a new modular platform for improved simultaneous imaging. Additionally, we develop a statistical analysis technique for DOT images and apply it to data from a stand-alone DOT imaging system (Chapter 7). Finally, we present a pilot study using unique optical data to measure hemodynamic changes during mammographic compression.

Chapter 4

Instrumentation for Simultaneous Diffuse Optical and Magnetic Resonance Imaging

Diffuse optical measurements add unique data to MR imaging. Over the years, collaborative research between the Departments of Physics (Yodh), Biochemistry and Biophysics (Chance), and Radiology (Schnall and Rosen) at the University of Pennsylvania has led to the development of combined MR and DOT imaging with applications to the breast cancer problem. This research effort began with the work of Ntziachristos[5,6,198,227,228] (Generation I, or GenI for short). Since then, DOT/DOS-MRI has been explored with and without exogenous contrast agents through three generations of optical instruments, summarized in Table 4.1. Intes and Yu[229] constructed the second generation multi-channel (GenII) system. My work has focused on an instrumentation upgrade of the GenII system (GenIIm; Chapter 4) and clinical measurements with the GenII and GenIIm systems (Chapter 5). This work led to my development of the third generation (GenIII) system, as described in Chapter 6.

Construction of the GenII system[229] was motivated by a need for additional wavelengths (3→6) and source positions (24→32) compared to the GenI system[227]. Additional wavelengths permit improved chromophore quantification, while additional source positions enable collection of more spatial information and thus improved tomographic reconstructions. The MR platform was transitioned from GE MRI systems to those of Siemens (due to a conversion at the Hospital of the University of Pennsylvania), and it was upgraded at the same time from 4 to 8 receive channels, improving spatial sensitivity uniformity. Initial work by Nioka[172] and Intes[197] monitoring the pharmacokinetics of ICG using a stand-alone CW DOT system

inspired the addition of a fast CW imaging mode in the GenII system. The resulting system (GenIIm) provided more spatial information and a significantly decreased DOT 'frame time' (i.e., time to collect data from all sources) from $\sim$4-7 minutes to $\sim$14 s. The latter improvement permitted much better tracking of the washout of ICG. Both the GenII and GenIIm systems were used in ongoing clinical research in conjunction with the Advanced Breast Imaging study (Section 5.1) in the Department of Radiology at the Hospital of the University of Pennsylvania.

System	Section	Sources	Detectors	λ	Data Type	SPF [s]	Notes
GenI	NA	24	8	1	TD	∼60	First report of simultaneous DOT and MR Imaging, 1.5T GE Signa MRI[198,228].
GenIm	NA	24	8	3	TD	∼60	Improved spectral information; additional subject recruitment[5,6,227].
GenII	Section 4.2	32	7	6	TD	∼60	Improved spectral and spatial resolution, conversion to Siemens 1.5T MRI[229].
GenIIm	Section 4.3	32	7	6	TD	∼240-560	Added hybrid TD-CW system for ICG kinetics tracking[230–233].
		32	14	1	CW	∼14	
GenIII	Chapter 6	32	5	6	TD	∼300	Hybrid modular system for larger data sets and greatly increased flexibility in optode positioning, conversion to 3T MRI[234].
		32	54	5	CW	∼30	'Current' GenIII system with one source and one detector module in use.
GenIII	In Progress	64	32	6	TD	∼600	'Complete' GenIII system with all modules in use.
		64	256	6	CW	∼30-60	

Table 4.1: Summary of Optical-MR imaging systems at the University of Pennsylvania. GenI and GenIm are not described in this thesis; the remaining systems (boldface) were either used or built as part of work on this thesis. Seconds Per Frame (SPF) are given for all sources at a single wavelength. The GenII and GenIIm system had a total of 32 source positions available, but a maximum of 21 were used in clinical measurements due to space constraints. Data collected with the GenII system is presented in Section 4.2, the upgrade to the GenIIm system in Section 4.3, and results from both systems in Chapter 5.

4.1 Advantages of Simultaneous Multi-Modal Imaging

Combining Diffuse Optical with MR Imaging has advantages from both technology development and clinical translation perspectives. Optical fibers can be introduced into the MR suite (e.g. Figure 4.1) without unduly disturbing clinical work. In terms of technology development, relatively low resolution DOT can utilize high spatial resolution MR images of tissue as spatial *a priori* information to constrain optical reconstructions. The Dartmouth group has perhaps developed this idea most extensively[219]; Guven applied Bayesian analysis[235] to this problem, and Intes[188] introduced simultaneous spatial and physiological constraints for the simultaneous MRI-DOT reconstruction problem.

The simultaneous measurements described herein also permit DOT to be validated against a well established clinical imaging modality. Furthermore, DOT/DOS measurements access different contrasts than that provided by the primarily structural images in MRI (Table 4.2) or by other standard clinical imaging modalities (X-Ray and Ultrasound). Thus, a joint measurement can potentially increase cancer sensitivity and specificity compared to either individual modality. Finally, DOT/DOS measurements are non-ionizing and utilize relatively inexpensive equipment, and, therefore, DOT provides additional information to the clinician at little additional risk or patient cost.

Current work on the development of targeted contrast agents for optical imaging will further increase the utility of optical measurements. To provide a concrete example, an untargeted (but FDA approved) optical contrast agent ICG can readily be detected at the micromolar range or lower[237]; Gd chelates that are typically imaged (by MRI), on the other hand, require hundreds of micromolar or higher concentrations. Higher sensitivity to the contrast agent can translate directly into lower drug doses, an ability to target more scarce receptors, and detection of smaller metastases. Additionally, the same optical agent utilized to detect a tumor could be visualized by a surgeon during resection to improve margin accuracy of tumor tissue removal. This idea has been shown to work in limited studies; for example, Sevick-Muraca[200] utilized ICG to identify sentinel lymph nodes (SNL) for resection.

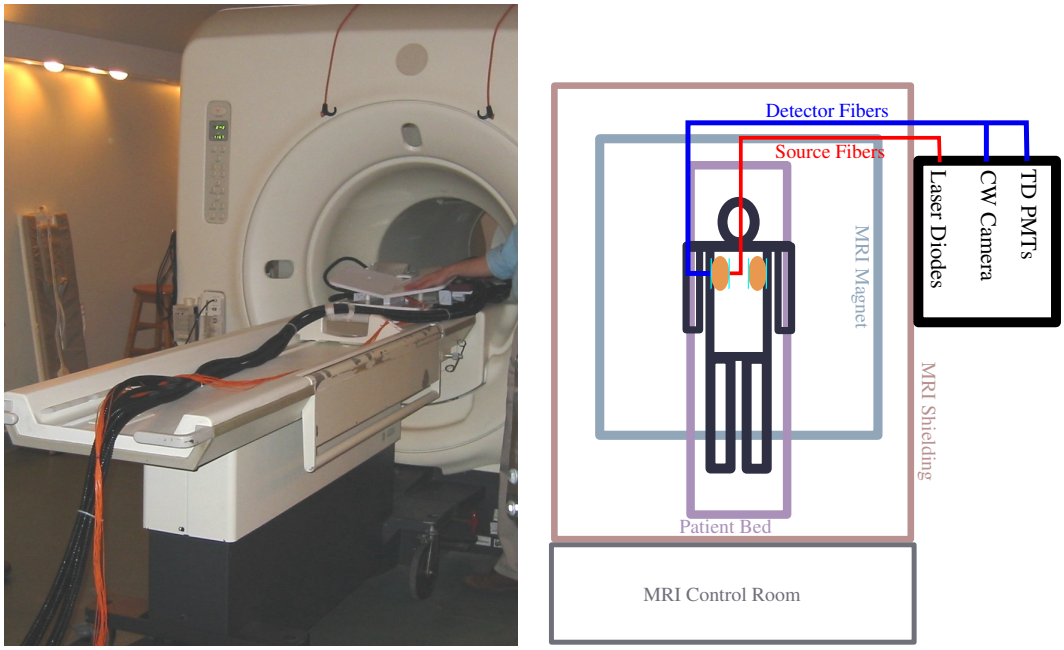

Figure 4.1: (left) Image of the GenII platform undergoing testing. Detector fibers (black) and source fibers (orange) are visible in this image. Note, although the GenII MR platform was adapted for the Siemens MRI this image was taken prior to the conversion from the GE system. (right) Cartoon of instrument and subject placement for simultaneous DOT and MRI measurement. Opto-electronics are located outside of the magnet shielding to both reduce the effects of magnetic fields on the components and to fulfill clinical safety requirements. This cartoon is replicated in Figure 3.12.

	Optical	MRI
Endogenous	Total Hemoglobin	
	Blood Oxygen Saturation	T_1
	Tissue Scattering	T_2
	Water Concentration	Tissue Structure (< 1 mm)
	Fat Concentration	ASL Blood Flow
	Micro-Vascular Blood Flow	
Exogenous	ICG Uptake/Washout	Gd Chelate Uptake/Washout

Table 4.2: Information content of Optical and MRI measurements of breast cancer. Note: breast ASL has only been demonstrated in a feasibility study[236] and optical DCS blood flow measurements have been primarily in remission[51], but some transmission data is presented in Chapter 8.

4.2 GenII Combined Time-Domain DOT and MR Imaging System

The GenII Optical-MR Imaging system at the University of Pennsylvania permitted simultaneous imaging with MRI (1.5 Tesla Sonata, Siemens) and TD DOT (summarized in Table 4.3) of both endogenous and exogenous tissue contrast. The optical/MR imaging platform and opto-electronics associated with this instrument are described in the following sections.

4.2.1 GenII Opto-Electronic System

The GenII opto-electronic system is composed of pulsed diode lasers coupled to a subject in an MR suite using $\sim$10 m source and detector fibers and an array of photon-counting PMTs. This optical instrumentation permits measurement of absolute tissue optical properties with each source-detector pair (with standard assumptions).

The GenII opto-electronics components are based around pulsed diode laser heads controlled by a common 'Sepia' driver-oscillator unit (Picoquant Gmbh., Berlin, Germany), an array of 16 single-photon-counting PMTs (Hamamatsu USA, Bridgewater NJ, H7422-50mod) modified to increase angle of acceptance, and a set of Time-Correlated Single Photon (TCSPC) counting PCI-cards and routers (Becker and Hickl, Gmbh.). Individual source fibers ($\sim$10 m long, 62.5/125 μm diameter, NA=0.17, step index) and detector bundles (5 mm active area, NA=0.33, step index, CeramOptic) couple light into and out of the tissue. A schematic of the optical components is shown in Figure 4.2.

The input pulse to the tissue for each wavelength has a temporal Full-Width-Half-Max (FWHM) of $\sim$400 ps. This pulse width is substantially larger than expected from the convolution of the PMT response time and the original laser pulse width ($\sim$200 ps). The pulse broadening is due primarily to the fairly high NA=0.33 of the $\sim$10 m detector fiber bundles, which allows propagation of multiple fiber modes all with slightly different path lengths. However, this high NA also increases the efficiency of light collection from tissue. In a practical sense, this pulse width constrains the instrument in this configuration to larger ($>$3 cm) source-detector separations and lower ($\mu_a < 0.1/cm$) absorptions. Outside these limits the difference between collected data and the IRF becomes small, and fitting to a theoretical model unreliable. Neither of these constraints are limiting factors for transmission measurements through breast tissue, however.

An example of TD data collected with the GenII system through the breast of a healthy volunteer is shown in Figure 4.3. Here, data is cropped at wavelength; in addition, the zero of time is adjusted using the peak of the reference channel. These time profiles are fit to an infinite slab solution of the diffusion equation, as described in Section 2.3.3, to derive tissue optical and physiological properties.

Multi-channel Pulsed Diode Laser Driver (Sepia)	PDL 808	PicoQuant GmbH
Laser Diode Heads (690, 750, 780, 808, 830, and 838 nm)	LDH series	PicoQuant GmbH
6x2 Fiber Optic Combiner	Dual Window Tree Coupler	Fiber Optic Communications Inc.
Fiber Optic Digital Attenuator	GP700	DiCon Fiber Optics
1x32 Fiber Optic Switch	GP700	DiCon Fiber Optics
32 (21 used clinically), ∼10 m, NA=0.17	62.5/125 μm, step index	Corning
16 (7 used clinically for TD), ∼10 m, NA=0.33	5 mm active area, step index	CeramOptic
Photon Counting PMTs	H7422-50mod	Hamamatsu
1x8 Routers	HRT-81	Becker and Hickl, GmbH
TCSPC Module	SPC-134	Becker and Hickl, GmbH
CW Laser Module	TCLDM9	Thor Labs
CW Laser Driver	LCD 500	Thor Labs
CW Laser Cooler	TEC 2000	Thor Labs
Back-Illuminated Frame Transfer CCD	iXon-887	Andor Technology

Table 4.3: GenII/GenIIm Instrument Components; see text for discussion and details. Schematics are shown in Figure 4.2 and Figure 4.6.

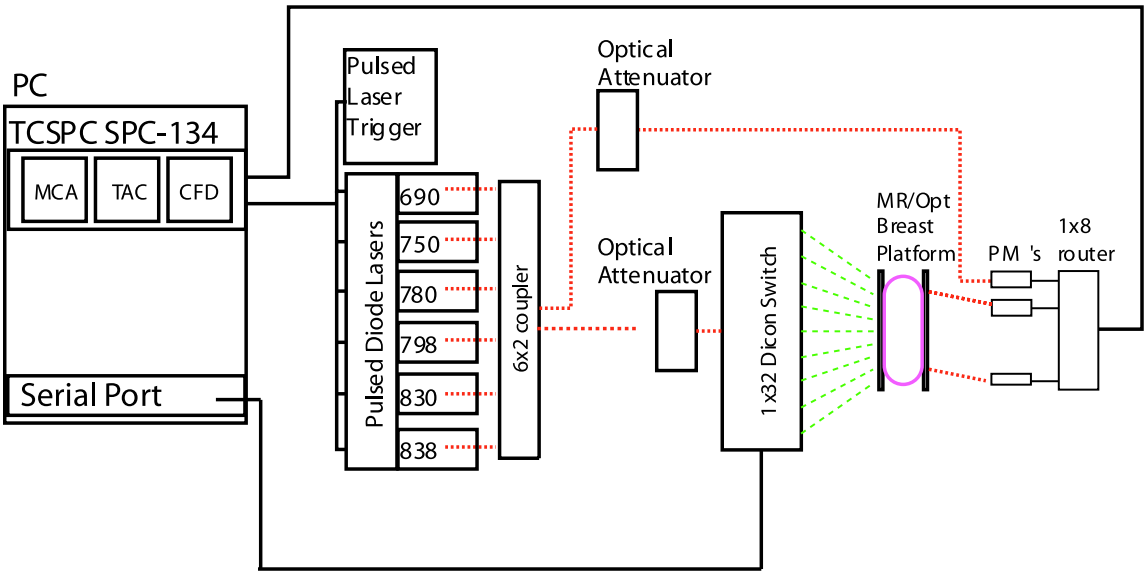

Figure 4.2: Opto-electronic schematic for GenII system. Note that this system uses a 'pulse-chain' (see Figure 4.3 for an example) and therefore only requires a single optical switch.

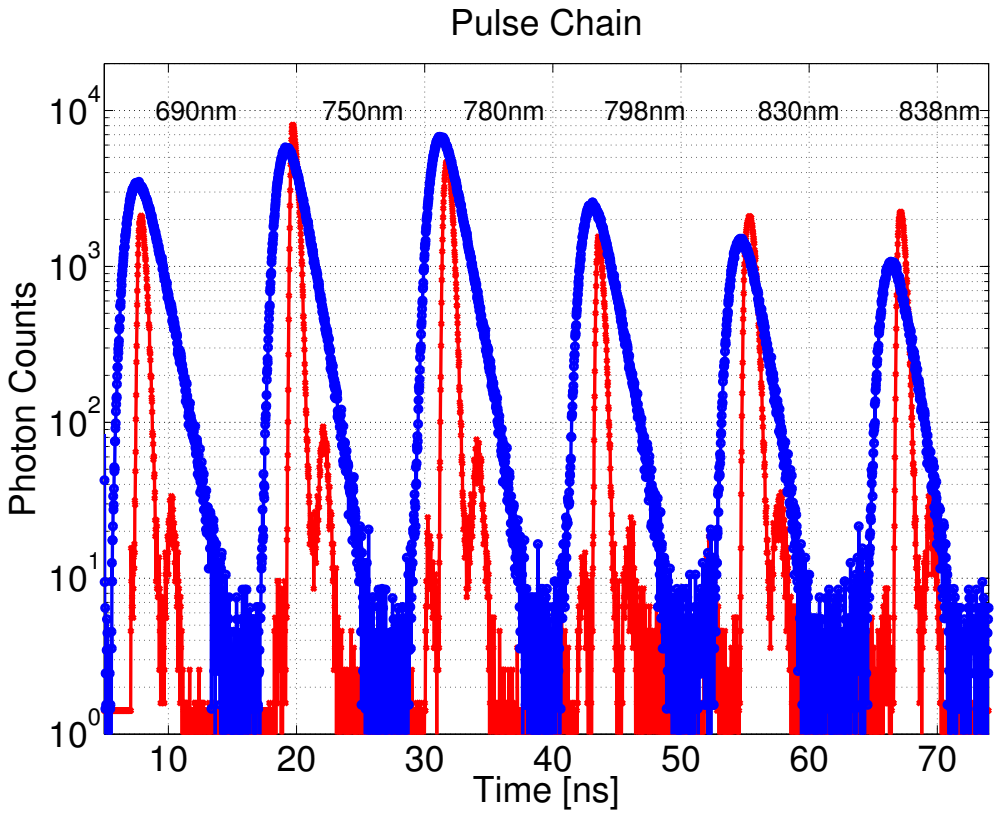

Figure 4.3: Example TD-DOS data, collected with the GenII system. Measurement (blue) and Reference Channel (red) pulse trains, measured in the breast of a 27 year old healthy volunteer. Data is shown for 6 λ in a 80 ns pulse train, repeated at 4 MHz. The Instrument Response Function (IRF) FWHM is $\sim$400 and roughly equal to the reference channel width.

4.2.2 GenII MR/Optical Imaging Platform

The GenII MR/Optical imaging platform contains bilateral optical fiber mounts and an 8 channel MR RF receive-only array, developed by Dr. Thomas Connick (an upgrade from the 4 channel receive array[238] used in the GenI system) for the Siemens Sonata 1.5T MRI. Sources are placed in the medial plate and detectors mounted laterally: this configuration is necessary as the source fibers are both much smaller and much more flexible than the detector fiber bundles. As can be seen in Figure 4.4, the platform is symmetric in both the axial and lateral dimensions and provides support for the subject's shoulders and abdomen during the exam. This platform was used routinely for bilateral MR imaging; however, due to lateral space constraints in the MRI bore ($\sim$59 cm diameter) and the large minimum bend radius ($\sim$15 cm) of the detector fibers, we typically only measured one breast optically in any given exam. In general, modification of the fiber mounting scheme necessitated alterations of the MR RF electronics (see Figure 4.4).

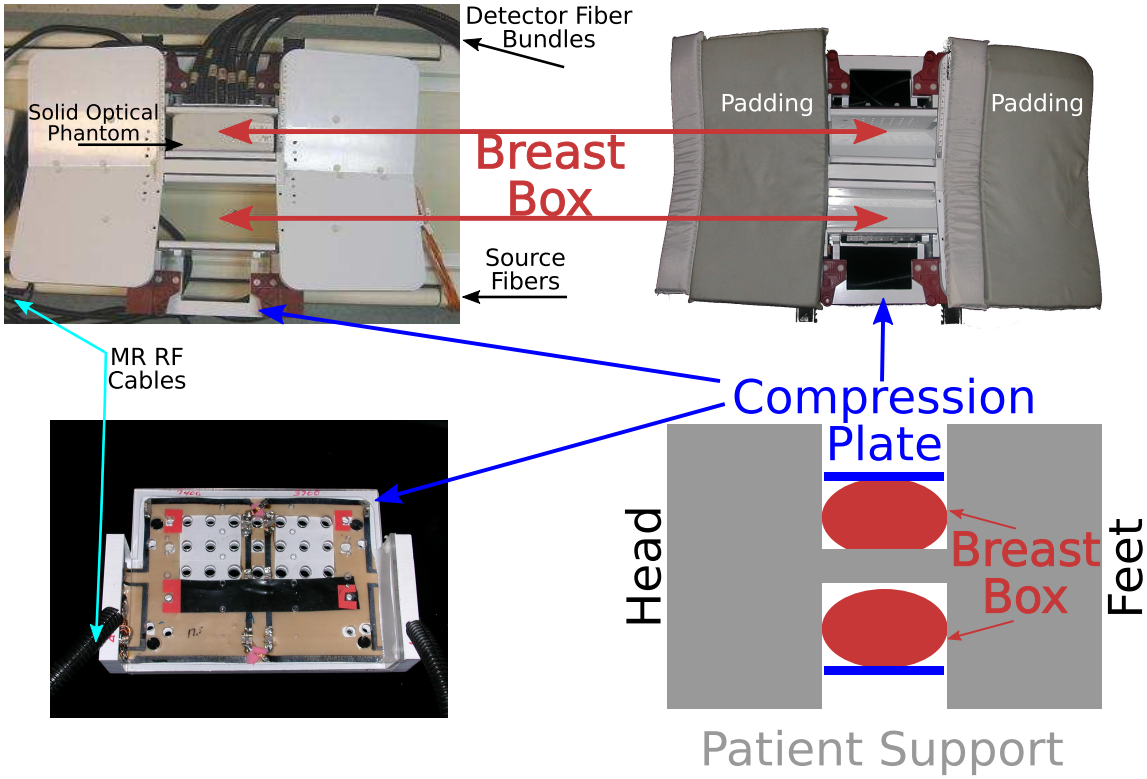

Figure 4.4: Images of the GenII and GenIIm optical-MRI breast platform.(left, upper) Overhead view of GenII and GenIIm optical-MRI breast platform with padding and light drapes removed. Note the significant bend in the black optical fibers at the top of the image. A solid phantom is positioned in place of the right breast; orange source fibers are visible in the lower right; black cables in the left of the image connect the RF receive coils with a pre-amplifier module (not shown). (right, upper) Overhead view of platform, with some padding in place. The platform is oriented with the head on the left of the image. (left, lower) Back view of MRI-Optical platform lateral compression plate containing RF coils. The detector fiber mounts have been removed to reveal the underlying electronics. (right, lower) Cartoon of platform.

Figure 4.5 shows several additional views of the platform, along with a schematic showing fiber placement. Although the GenII platform was designed to accept multiple rows of source and detector fibers on both breasts, in practice, space and tissue contact limitations precluded use of all but the top (i.e., closest to the chest wall) two rows of sources and typically the top-most row of detectors. Lateral constraints of the magnet bore generally precluded bilateral optical imaging. The tissue-fiber coupling shown in Figure 4.5 is fairly typical: we frequently did not get good fiber coupling on the second row of sources or detectors.

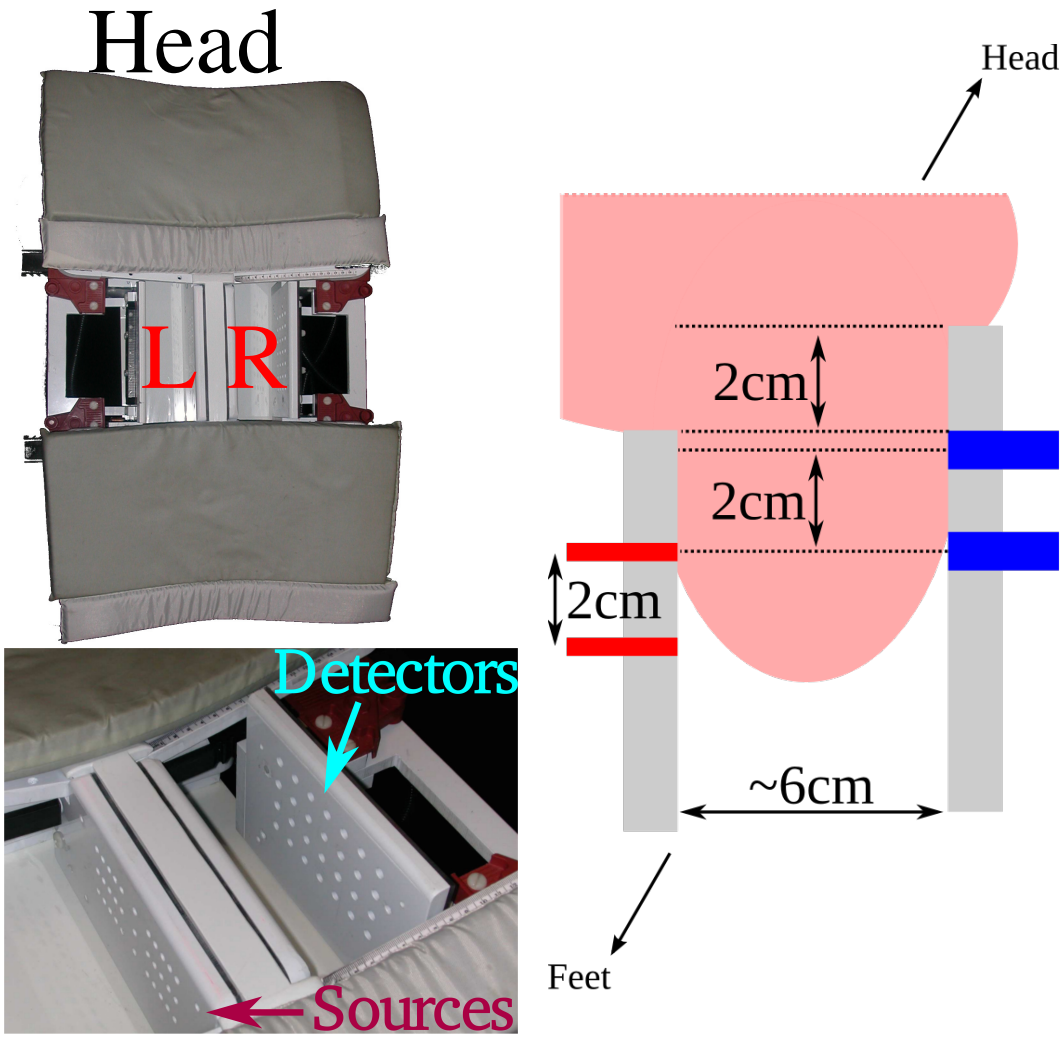

Figure 4.5: Optical/MRI Breast Imaging Platform schematic and images. (left,top) Top view- the left and right MR receive coils and optical fiber mounts are mirror images. (left, bottom) Oblique view of platform, showing fiber optic mounting holes. Note that only the top row of detectors and top two rows of sources were reliably in contact with the subject's skin. The lowest two rows of detector positions were unusable in the magnet, due to space constraints caused by the curvature of the bore. (right, top) Sketch of fiber optic positions relative to breast tissue. Sources (red) are located in a medial plate underneath the subject's sternum. Detectors (blue) are located on a slightly raised plate which makes better contact with the upward curving chest.

4.3 GenIIm HybridTime Domain-Continuous Wave DOT for Simultaneous Optical and MR Imaging

4.3.1 Rapid Continuous Wave Diffuse Optical Tomography

Exogenous contrast agents permit clinical imaging modalities to probe structures and tissue functionality which lack significant endogenous contrast. The only NIR contrast agent currently approved by the FDA, however, is Indocyanine Green (ICG, also called Cardio-Green). Research by Nioka[172] and Intes[197] at University of Pennsylvania suggested the potential for highly specific cancer diagnoses, based on local ICG kinetics. Gadolinium kinetics are well established in the MR breast imaging community; indeed, breast imaging guidelines *require* a gadolinium agent for diagnostic utility[239,240]. Imaging ICG simultaneously with Gd contrast agents offered us an obvious opportunity to test the diagnostic utility of contrast-enhanced DOT (CE-DOT) in direct comparison to contrast-enhanced MRI (CE-MRI). However, the DOT frame rate of the GenII system was too slow ($\sim$60s) to reliably *image* ICG washout (half-life $\sim$3-5 min., following the analysis by Intes[197] shown in Figure 3.8). The time resolution was sufficient, however, to obtain spectroscopic point measurements (e.g., as shown with the GenI system by Ntziachristos[227]). We therefore undertook the task to construct a higher frame rate optical instrument utilizing a hybrid of TD and CW technology. This combination provides both absolute optical properties and low resolution imaging. The new instrument could therefore measure changes in absorption due to ICG with higher temporal and spatial resolution than any previous in-magnet device.

4.3.2 GenIIm: DOT and MR Imaging at 1.5T

Figure 4.6 shows the addition of a 785 nm CW laser diode and lens-coupled CCD for detection to the existing GenII TD system. We were able to include an additional 9 CW detector fibers in the upgraded instrument; by manually transferring the TD detector fibers to the CW detection system, we were also able to increase our total available CW detectors to 16. Note, although 32 source fibers were available, space limitations usually restricted us to use of only 24 source fibers in clinical practice.

A critical specification for a kinetics monitoring system is stability; the CW portion of this system showed $\sim$2% (5% maximum) fractional standard deviation from the mean of intensity during a 30 minute kinetics imaging sequence on a static phantom. See Table 4.3 for specifications of system components.

Additionally, a number of minor improvements were made in optode mounting, padding for patient comfort, and improved integration into the MR Exam sequence.

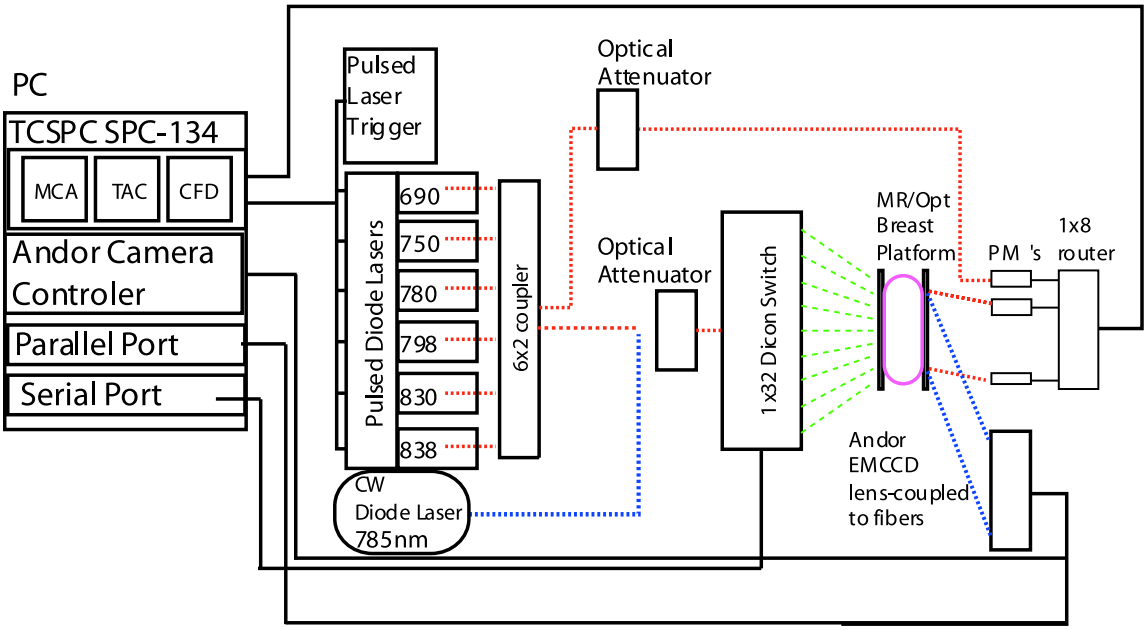

Figure 4.6: Schematic of the GenIIm system. 32 Shared Sources (24 clinically), CW: 16 detectors, 1λ, TRS: 7 detectors, 6λ. Table 4.3 contains details of the components.

4.3.3 GenIIm Pharmacokinetics Phantom Measurements

The GenIIm system focused on kinetics imaging; an example of a kinetics phantom measurement and reconstruction is shown in Figure 4.7. This phantom consisted of a liquid bath, an ellipsoidal latex shell, and two pipes for entrance and departure of a target solution. We utilized an adjustable speed syringe pump to produce a phantom with changes over the same time span as roughly expected from ICG *in vivo*. The target was formed by filling a latex balloon with a target solution with ~3x1 absorption contrast with respect to the background (μ_a =0.05 cm^{-1}). Data was reconstructed using a Singular Value Decomposition (SVD) reconstruction, Tikhonov regularization, and an infinite slab Green's function, as introduced in Section 2.2.8.

Figure 4.7 shows the temporal change in reconstructed μ_a of the phantom images as well as a schematic of the phantom. This SVD reconstruction contains significant artifacts, especially near the sources and detectors. Nevertheless, relative changes in the target absorption are clearly visible.

Applications of this instrumentation to clinical studies will be described in Chapter 5.

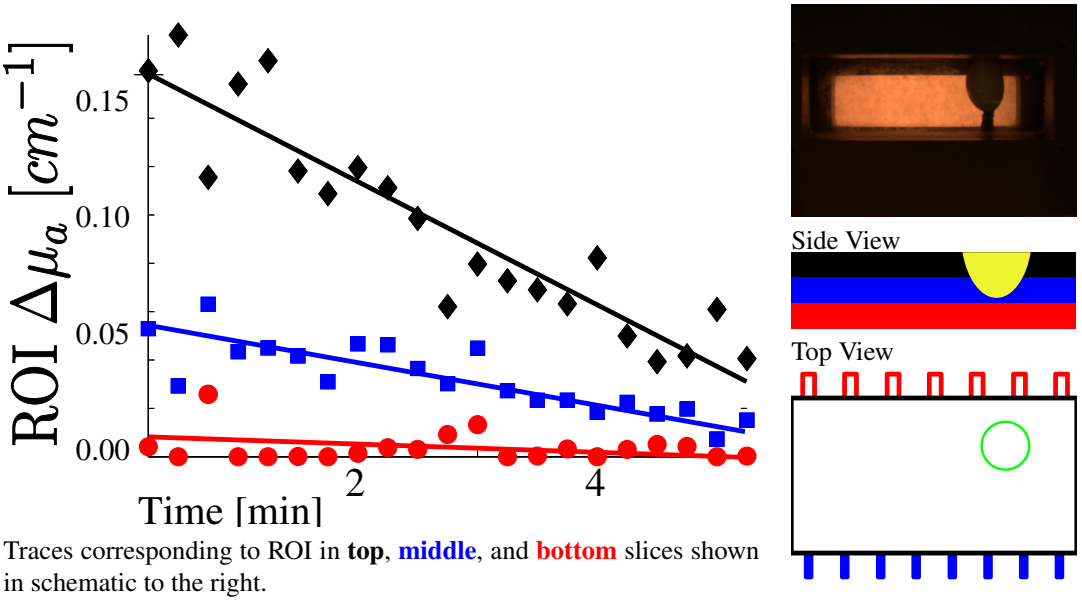

Traces corresponding to ROI in **top**, **middle**, and **bottom** slices shown in schematic to the right.

Figure 4.7: Kinetics phantom imaging with the GenIIm system. (left) Change in μ_a for each slice (colors match right center diagram). We found quantitative agreement with expected values. The Region Of Interest (ROI) was taken in the same lateral location for each plane. (right, top) Photo of inflated balloon phantom. (right, center) Diagram of reconstructed slices. (right, bottom) schematic of source and detector fiber placement and target location.

Chapter 5

In-Magnet Time-Domain Diffuse Optical Spectroscopy and Tomography of Human Breast Cancer

The GenII and GenIIm instruments described in Chapter 4 were employed in a series of clinical studies. In this work, we collected bulk optical property and ICG regional kinetics patient data. A summary of results from measurements on 19 subjects with data from intrinsic and extrinsic DOT/MR imaging are given in Section 5.1. Simultaneous contrast enhanced DOT and MR Imaging with GenIIm is described in Section 5.2. Section 5.3 describes the lessons learned from these systems that we have applied to construction of the GenIII system (Chapter 6).

Our subjects enrolled in the 'Advanced Breast Imaging Study' (ABI, NIH P01-CA-85424). The ABI focused on comparative studies of film and digital X-Ray mammography, ultrasonography, PET, and MRI[241]. Subjects were opportunistically recruited into the DOT investigations as an adjunct to the MR Exam. Our study was approved by the University of Pennsylvania Institutional Review Board under Protocol #803468. The ABI study recruited three groups of women: those at high-risk, those with a suspicious lesion, and those with a recent biopsy of a malignant lesion and for whom additional imaging was required for staging. Our study recruited primarily from the second ABI group in order to maximize the number of cancers and minimize contamination of data due to biopsy-induced bleeding. Recruitment also focused on women with C-cup or larger breasts, as the engineering of the GenII platform was sub-optimal for tissue contact with smaller breasted women.

Typical exam time-lines for the GenII and GenIIm systems are shown in Figure 5.1. ICG is not a

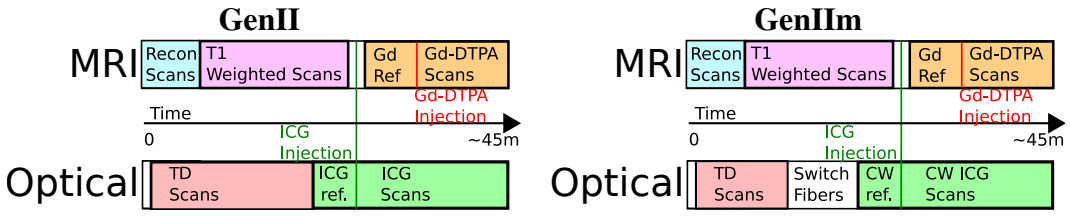

Figure 5.1: Experimental time-line for (left) GenII and (right) GenIIm simultaneous clinical optical/MRI measurements. The entire exam, complete with a pause to inject ICG, takes ∼45 minutes Descriptions of each scan are in text.

	Total Studied	Tumor in FOV	ICG Agreed	ICG Kinetics	ICG Imaging
GenII	27	4	21	12	0
GenIIm	18	3	15	11	5

Table 5.1: Summery of subjects studied with the GenII and GenIIm simultaneous DOT and MR imaging systems. 'Total Studied' includes all subjects who agreed to participate in the study. Subjects noted under 'Tumor in FOV' had their tumor positioned near (∼1 cm) the DOS/DOT Field of View. 'ICG Agreed' includes those subjects who *agreed* to ICG injection; due to logistical constraints, only a subset of these subjects actually received ICG. 'ICG Kinetics' enumerates subjects who had useful ICG data, but too few source-detector pairs for 'ICG Imaging'.

standard contrast agent in MR studies. Therefore, ICG injections were performed by an attending physician and timing was sometimes adjusted based on the physician's availability. ICG injection both preceded and followed Gd-DTPA injection; we did not utilize an auto-injector for ICG.

MR imaging was broken down as follows. In the first ∼5 minutes, reconnaissance scans were carried out to localize the breasts in the MR coordinate system and to optimize imaging volume selection. Then T_1 weighted scans were carried out; these scans involved repeated MR imaging at varying relaxation times to permit computation of a T_1 map. Then a baseline MR image was obtained prior to Gd-DTPA injection, and finally a series of kinetic imaging scans was taken to measure Gd-DTPA uptake and washout.

Optical exams began with measurements of absolute optical properties using the TD-DOS system; these measurements were relatively slow (∼5 minutes per frame). Then optical fibers were manually moved from the TD-PMTs to the CCD camera for CW imaging. We then collected baseline images prior to ICG injection. Finally, we collected CW ICG scans to image ICG uptake and washout (∼30 s per frame).

The broad objective of the ABI study was to compare the current state of the art in breast imaging techniques. Thus, over the course of the study, several modifications were made to the protocol, and the MR data available for our analysis varied somewhat as a result. Furthermore, during the period of the study, we converted from the GenII to the GenIIm system. Together, these factors limited the number of subjects with directly comparable data sets. In effect, we undertook a series of pilot studies rather than a single trial.

Multi-modal imaging offers rich data sets (e.g., here, T_1, Gd-DTPA, Hb_t, StO_2, and ICG uptake), but it

is frequently challenging to obtain a complete data set for an individual subject. For example, the subject shown in Section 5.2.1.1 was not included in the bulk property analysis (Section 5.1), because artifacts, probably due to subject movement during the T_1-weighted image series prevented calculation of a T_1 map.

5.1 Clinical Diffuse Optical Spectroscopy Results: GenII and GenIIm Systems

5.1.1 Endogenous Bulk Optical Properties

Bulk optical properties are important both in their own right and as inputs to DOT algorithms. For all subjects we measured bulk optical properties prior to contrast agent injection (i.e. $\mu_a^{(0)}[\lambda\ ]$ and $\mu_s'^{(0)}[\lambda\ ]$ at six wavelengths 690, 750, 785, 800, 830, and 838 nm; see time-line in Figure 5.1) with TD-DOS. The wavelength-dependent results were used to compute endogenous chromophore concentrations; an example multi-wavelength fit is shown in Figure 5.2. This data comes almost entirely from healthy tissue. A few subjects with tumors were included in this sample, but their tumors occupied a small fraction of the total volume probed optically.

Data sets collected during the course of studies with the GenII and GenIIm systems varied somewhat between subjects due to equipment upgrades (e.g., GenII $\rightarrow$GenIIm), modifications to experimental protocol (e.g., ICG not injected due to physician availability), subject-specific difficulties and compliance (e.g., optode-skin coupling, fidgeting), and available exam time. We have extracted a group of 19 subjects for whom consistent TD-DOS, T_1, and Gd-enhanced MR data was collected; data averaged across both subjects and population are presented in Table 5.2.

The average measured blood oxygen saturation in our data is within the range reported by others (62% vs. 68%, e.g. as summerized by Leff[1]). During menopause, breast glandular tissue atrophies. Thus, post-menopausal women tend to have both less glandular tissue volume and reduced metabolic activity in the remaining tissue, leading to a reduction in Hb_t seen in other work. Our values for total hemoglobin are in agreement with those presented by others for post-menopausal women; the values of total hemoglobin concentration for pre-menopausal women were roughly half of that seen in previous studies (summarized by Leff[1]). In fact, the distributions of Hb_t and StO_2 from the pre- and post-menopausal women in our population were essentially identical and therefore these groups were combined for much of the subsequent analysis; Figure 5.3 shows the distribution over all subjects and all source-detector pairs.

We note also that our recruitment was skewed towards women with larger breasts to improve mechanical skin-optode coupling. Furthermore, the fat content in the breast of the included subjects was unusually high: the average BMI of the studied group was 30.4 ± 6.7 (the CDC obesity standard is BMI$\geq$30) and the adipose

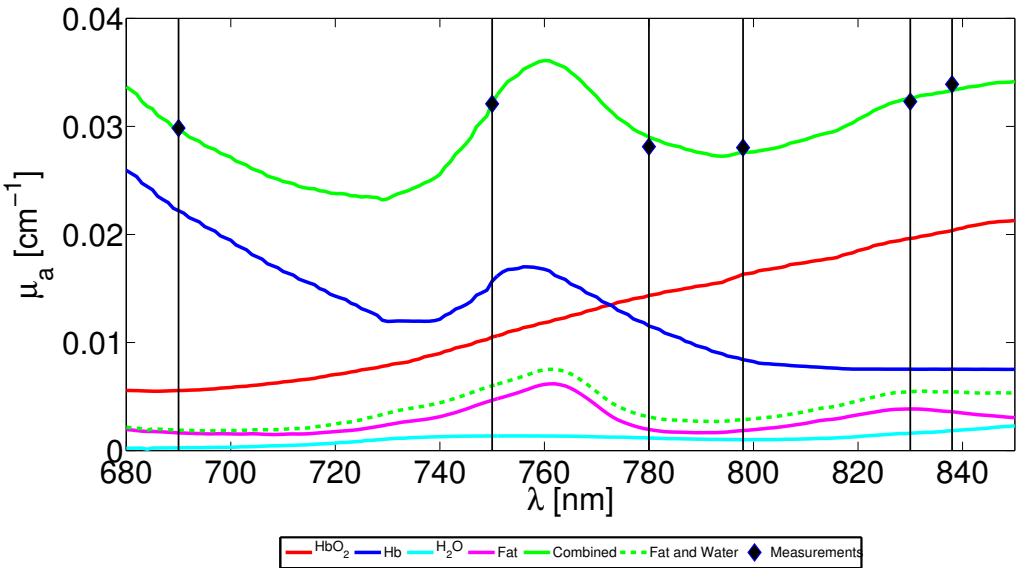

Figure 5.2: Example TD-DOS measurement of bulk optical properties of breast tissue with the GenII system. Hb_t (13.5 μM), StO_2 (65%), Lipid (5%), H_2O (48%) fit to six wavelength absorption data. Note that this instrument had limited sensitivity at longer wavelengths ($\lambda_{max} = 838$ nm) and therefore limited sensitivity to lipid and water concentrations. Imaging data from this subject is shown in Section 5.2.1.3.

tissue fraction in the breast was ~85% (from T_1 MRI). High adipose tissue content is inversely correlated with glandular tissue fraction and therefore Hb_t concentration. Together, these factors may explain the similarity observed between pre- and post-menopausal tissue properties in our data. Lipid and water content fit quality varied between subjects; as this instrument had limited data at longer wavelengths ($\lambda_{max} = 838$ nm), the analysis was less sensitive to errors in lipid and water quantification than Hb_t and StO_2. Despite this limitation in spectral sensitivity, the bulk optical Lipid fraction had a correlation of -0.62 ($p<0.01$) with average T_1, consistent with the known reduced T_1 in adipose tissue. Table 5.3 lists correlations between optical properties and T_1.

Hb_t	14.6 $\pm$ 3.4	μM
StO_2	62.2 $\pm$ 7.9	%
Lipid	18 $\pm$ 11	%
H_2O	28 $\pm$ 14.5	%
μ_s' [785nm]	10.8 $\pm$ 4	cm^{-1}
T_1 Fat Fraction	85 $\pm$ 2	%
BMI	30.4 $\pm$ 6.7	kg m^{-2}
Age	47.4 $\pm$ 14.8	yr.

Table 5.2: Bulk TD-DOS optical properties collected on 19 joint optical/MRI subjects with more than 5 useful source-detector pairs. Data is reported as mean $\pm$ standard deviation, except for the T_1 fat fraction, in which the mean and the changes due to varying the cutoff between adipose and glandular tissue by $\pm$ 10% are included.

		Optical	MR	r	p
Intrinsic	DOS	Hb_t	Fat Fraction	0.09	0.034
		StO_2	Fat Fraction	0.16	< 0.01
		Lipid	Fat Fraction	0.24	< 0.01
		Lipid	T_1 (bulk)	**-0.62**	< 0.01

Table 5.3: Correlations between regional DOS and MR parameters from DOS measurements in 19 subjects using the GenII and GenIIm systems. Although these correlations are significant at the 5% confidence level, the overall weak correlations may be a function of inter-subject variation in this small population. (Note, p-values are not corrected for the number of correlations examined.)

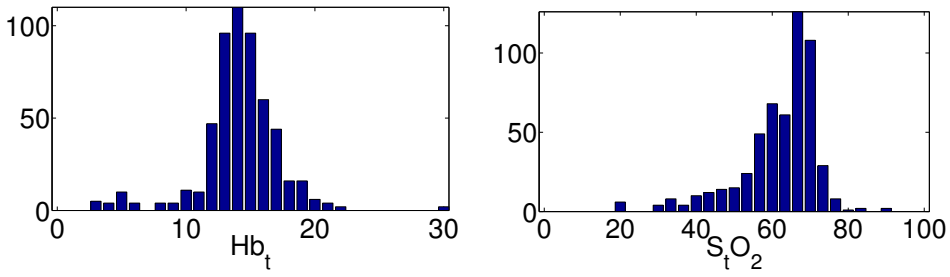

Figure 5.3: Histograms of Hb_t and StO_2 measured with TD-DOS for all source-detector pairs in 19 subjects. Numbers are assigned to each source-detector pair. Note, the distributions of results from pre- and post-menopausal women were almost identical and we therefore grouped these data.

5.1.2 Bulk ICG uptake kinetics

Data from the majority of our subjects lacked sufficient spatial information for DOT reconstruction; however, we were still able to use these data for spectroscopic or bulk analysis, similar to the endogenous property measurements described above. The bulk ICG uptake data set includes a few subjects with cancer in the optical field of view, but these cancers occupy only a small fraction of the optically probed volume. We fit ICG kinetic measurements to double exponential and two compartment models (e.g. Figure 5.4), and then we compared the ICG kinetics to the kinetics of Gd-DTPA. Note that the kinetics can vary considerably within a single subject (e.g. Figure 5.5), depending on the source-detector combination used.

Figures 5.4 and 5.5 demonstrate that the ICG concentrations change rapidly near the time of peak concentration and much more slowly after ∼300 s, although the total concentration (and therefore signal) is considerably lower at longer times. ICG imaging with low DOT frame rate instruments (e.g., ∼10 min. per frame in work by Corlu and colleagues[89]) collect data during the later period. As discussed in Section 5.2.1, the GenIIm instrument had a frame rate of ∼14 s per frame and could produce ICG uptake images during the entire ICG wash-in/wash-out period.

We make the simplifying assumption that the local fractional change in MR signal intensity can serve as a proxy for Gd-DTPA concentration in the following discussion, although this relationship is known to be non-linear. As will be discussed in Section 5.2.1, the Gd kinetics data was taken at fairly slow frame rates (∼94 s) and short total times (∼10 min.), which effectively limits the complexity of our models; we therefore limited our models to linear fits of the initial and terminal data points (Figure 5.6). We then extracted the initial slope, terminal slope, and terminal intercept for comparison with ICG kinetics parameters.

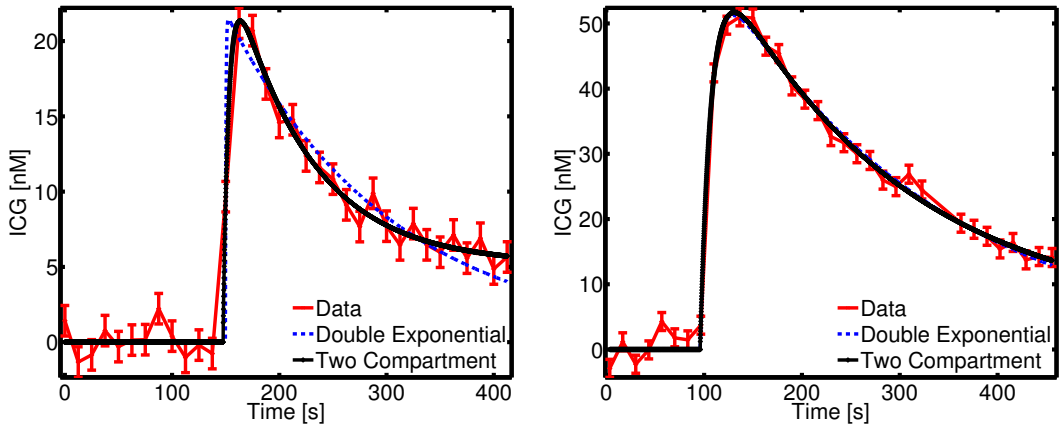

Figure 5.4: (left) ICG uptake measured at a single source-detector combination with TD information from GenII system. (right) ICG uptake from a single source-detector combination from the GenIIm, extracted from a CW imaging data set shown in Section 5.2.1.3. Data with double exponential (see Equation 5.2) and two compartment (see Equation 5.1) fits are shown.

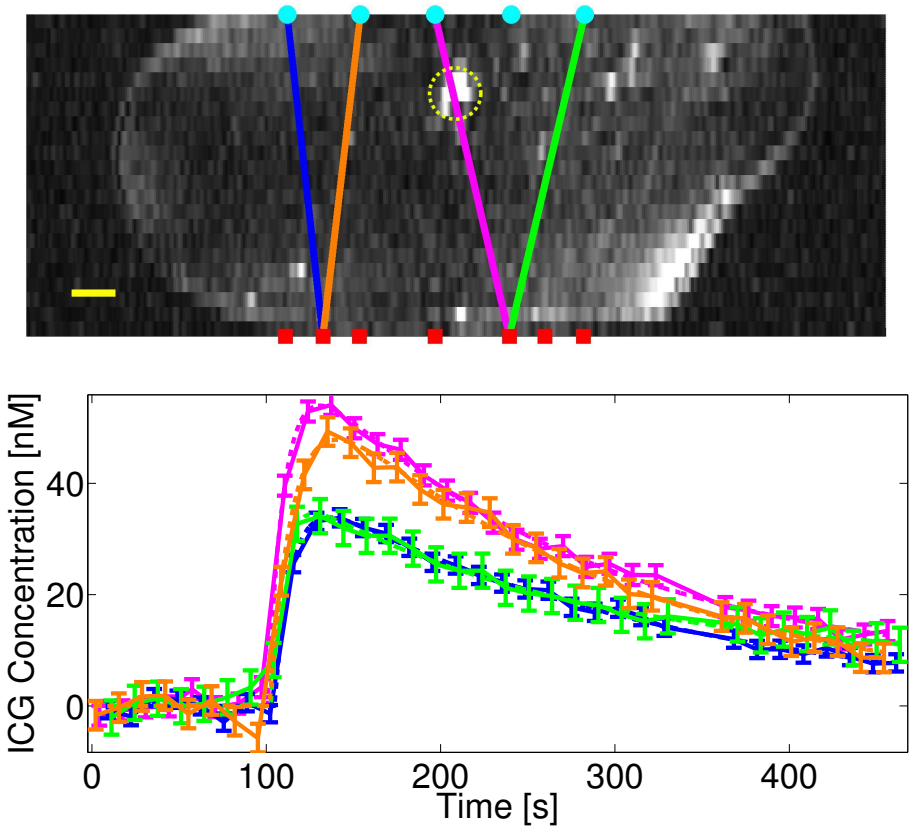

Figure 5.5: (top) Gd-DTPA enhanced MRI showing tumor (upper center, yellow dashed circle, intersected by magenta line, ~0.5 cm^3) in a coronal image slice. Color-coded lines connect the source-detector pairs plotted in the bottom curve. (bottom) Example ICG uptake curves on a single subject with an invasive carcinoma in the optical field of view (imaging data for this subject are shown in Section 5.2.1.3). ICG uptake and washout kinetics varied significantly between source-detector pairs on individual subjects. (Note, negative calculated ICG concentrations just prior to the upslope are due to the increased room illumination required to inject the contrast agent.) The similarity between the orange and magenta curves suggests that bulk ICG kinetics are less useful than those extracted from reconstructed images (e.g., as in Intes *et al.*[197]). Fits shown are from the two compartment model described in the text. Yellow scale bar is 1 cm.

We utilized a pair of ICG kinetics models: a two-compartment model from Cuccia[173]

$$\begin{aligned} C_{ICG}^{2cmpt}[t] =& A_1\left(Hb_t\zeta + \frac{\kappa}{k_{out}}\right) + A_2\left(Hb_t\zeta + \frac{\kappa}{k_{out}-\alpha_2}\right)e^{-\alpha_2 t} \\ &- \left[A_1\left(\frac{\kappa}{k_{out}}\right) + A_2\left(\frac{\kappa}{k_{out}-\alpha_2}\right)\right]e^{-k_{out}t} \end{aligned} \tag{5.1}$$

and an empirical double exponential model

$$C_{ICG}^{Exp}[t] = A\left(-e^{-k_1 t} + e^{-k_2 t}\right). \tag{5.2}$$

The quantities in these models are defined in Table 5.4 and 5.5; the models are explained in more detail in Appendix A.

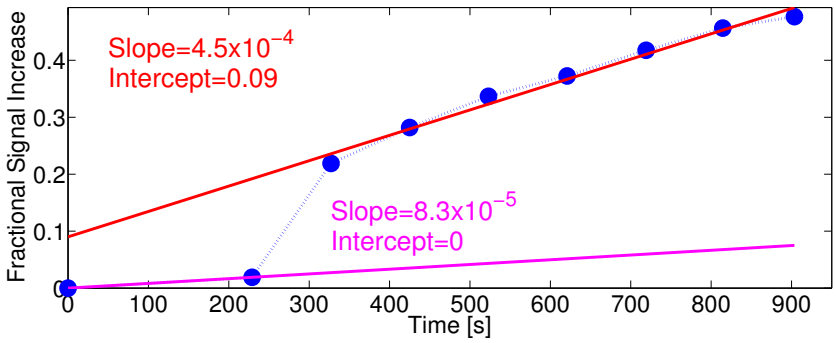

Figure 5.6: Example kinetics model fit to fractional changes in local MR image intensity due to Gd-DTPA uptake. The low temporal resolution of this data limits the complexity of kinetics models which may be applied. Note, the MR signal intensity is non-linearly related to the Gd-DTPA concentration. Data are solid blue circles.

A_1	Pre-factor in two compartment model
A_2	Pre-factor in two compartment model
α_1	Liver elimination constant 1
α_2	Liver elimination constant 2
C_e	ICG concentration in EES
C_p	ICG concentration in Plasma
C	Total ICG concentration
Hb_t	Total Hemoglobin Concentration from DOS
κ	$V_e k_{in}$
k_{in}	Rate constant from Plasma to EES
k_{out}	Rate constant from EES to Plasma
V_e	Volume of EES
V_p	Volume of Plasma
ζ	Conversion factor between Hb$_t$ and V_e

Table 5.4: Parameters in Equation 5.1.

A	Pre-factor in double exponential model
C	Total ICG concentration
k_1	Rate constant
k_2	Rate constant

Table 5.5: Parameters in Equation 5.2.

After various approximations and simplifications, A_1, the pre-factor on the leading order term is seen to be related to the magnitude of ICG uptake. Data for each source-detector pair was fit separately to obtain ICG absorption as a function of time; this information was then converted into ICG concentration and fit to the models. Only source-detector pairs with both ICG and Gd data were retained. We then calculated correlation coefficients between all ICG and Gd parameters.

Several ICG and Gd-DTPA parameters were mildly correlated locally as shown in Table 5.6. However,

there were no significant correlations between *bulk* ICG and Gd-DTPA uptake (i.e., ICG parameters averaged over all source-detector pairs and Gd-DTPA parameters averaged over the optical field of view) in each subject.

		Optical	MR	r	p
ICG	DoubleExponential	k_2	Initial Slope	0.29	< 0.01
		k_2	Terminal Intercept	0.45	< 0.01
		k_2	Fat Fraction	-0.3	< 0.01
	Two Compartment	A_2	Initial Slope	0.21	< 0.01
		A_2	Terminal Intercept	0.26	< 0.01
		A_2	Fat Fraction	-0.21	< 0.01
		k_{out}	Initial Slope	0.2	< 0.01

Table 5.6: Correlations with $|r| > 0.2$ between regional DOS and MR parameters from 8 subjects using the GenII and GenIIm systems. Note, p-values are not corrected for the number of correlations examined.

None of the correlations between localized MR and DOS results presented in Table 5.6 are strong: the highest correlation (between k_2 and the Gd fit terminal intercept) is 0.45. However, ICG (775 Da) is known to bind to blood albumin (66 kDa) while Gd-DTPA (590 Da) behaves as a small-molecule agent. Thus, while the molecular weight of both agents is similar, the *effective* molecular weight of the agents in the blood differs by $\sim$2 orders of magnitude, and therefore differences in the pharmacokinetics are to be expected (due to, for example, size-dependent differences in vascular permeability). Furthermore, each DOS measurement includes a weighted average across multiple tissue types. The spatial information in DOT reconstructions reduces this partial volume effect and enables more direct comparison of the effects of measured contrast agent uptake to tissue physiology on contrast agent dynamics. As will be discussed in Section 5.2.1, our DOT reconstructions of ICG uptake did correlate with the spatial distribution of Gd-DTPA, consistent with the results of Ntziachristos[5,6].

The models of ICG kinetics presented above differ in assumptions from that recently used by Hagen *et al.*[190]; most importantly, as Hagen collected data over tens of minutes to hours, he did not approximate the liver long term elimination constant as zero and included lymph circulation.

5.2 Clinical Imaging of Indocyanine Green with the GenIIm System

A major goal of the GenIIm system was to image ICG kinetics. Examples of 'Optical Only' reconstructions are given below in Section 5.2.1. Section 5.2.2 describes use of spatial information from MR images to constrain the reconstructions. However, due to limitations in our subject interface, high quality data for DOT reconstructions were difficult to obtain with GenII or GenIIm; the data sets useful for reconstruction were limited. Section 5.3 describes various problems found in the GenII and GenIIm systems, and some of the resulting solutions we applied in the GenIII system described in Chapter 6.

5.2.1 'Optical Only' DOT ICG Kinetics Imaging

The DOT reconstructions presented in this section utilize only optical data: no information sharing is employed for image construction. Images from the two modalities were co-registered *ex post facto* using fiducial markers built into the GenII platform. These markers were visible in the MR images and rigidly attached to the optical fiber mounts.

As noted in the introduction to Section 5.1, bulk optical properties are measured with TD-DOS for each subject. These properties are then used to calculate a weight matrix ($\mathbf{W}$) for an infinite homogeneous slab (see Section 2.2.8, especially Equation 2.78) which can be used in the all-optical image reconstruction via SVD matrix inversion (Section 2.2.8.2). This single step linear reconstruction technique has the advantage of requiring only a single computationally expensive inversion step. Additionally, as we are interested in changes between the images due to the contrast agent, use of a single inversion matrix across all time points reduces some systematic errors associated with multiple iterations (i.e., iterative DOT) for each frame.

The GenIIm system was designed to take advantage of the higher DOT frame rates available from CW-DOT. This choice permits tracking of ICG pharmacokinetics with much greater time resolution (e.g. $\sim$15 seconds vs. $\sim$5 minutes with TD-DOT in GenII). In this analysis, we utilize the Rytov formalism (Section 2.2.8.1), wherein input reconstruction data is normalized by a background or homogeneous data set. For imaging ICG kinetics, we used the average of a set of pre-injection data frames as our background data set. The remaining data frames are normalized to this pre-injection time period. In other words, for each time point, intensity data from each source-detector pair ($I_{s,d}[t]$) is divided by the average intensity of the same source-detector pair during the pre-injection period ($I^0_{s,d}$). Recall from Equation 2.73 that under the Rytov formulation, we write the total measured fluence rate due to an input fluence rate U_0 as

$$U_t[\boldsymbol{r}] = U_0[\boldsymbol{r}]e^{\phi_s[\boldsymbol{r}]}.$$

In our approximation (Section 2.2.8.1), the detected signal is proportional to the fluence rate, so we can

calculate ϕ_s (Equation 2.75) as:

$$I^0_{s,d} = \langle I_{s,d}[t] \rangle_{0 \leq t < t_{inj}}$$
$$\phi_s[\boldsymbol{r}_s, \boldsymbol{r}_d, t] = \ln \left[\frac{I_{s,d}[t]}{I^0_{s,d}} \right] \tag{5.3}$$

for an injection time of t_{inj}. Using $\mathbf{W}$ as defined in Equation 2.78, we transform this measurement vector into a 3D change in absorption map ($\delta\mu_a[\boldsymbol{r}, t]$) during the injection and washout of ICG.

The remainder of this section presents three example cases of simultaneous contrast enhanced MR and DOT imaging. In the first, we show data collected following a mock ICG injection (Section 5.2.1.1); in the second, we show data from a subject without a cancer in the optical field of view (Section 5.2.1.2); the third section includes data from a subject with an invasive carcinoma in the optical field of view (Section 5.2.1.3); finally, we summarize our results (Section 5.2.1.4).

5.2.1.1 Simultaneous Contrast Enhanced MRI and DOT: Mock Injection for System Validation ('Zero Image')

The ICG imaging protocol presented above measures the change in absorption with respect to a pre-injection image. This differential measurement requires the skin-optode coupling to remain consistent throughout the exam. In this study, we show a time series of data collected *without* ICG injection, but otherwise with the same protocol (see Figure 5.1). The results shown in Figures 5.7 through 5.9 show that the GenIIm system was stable under these conditions (note that the color scale in Figure 5.8 is the same as that in Figure 5.14).

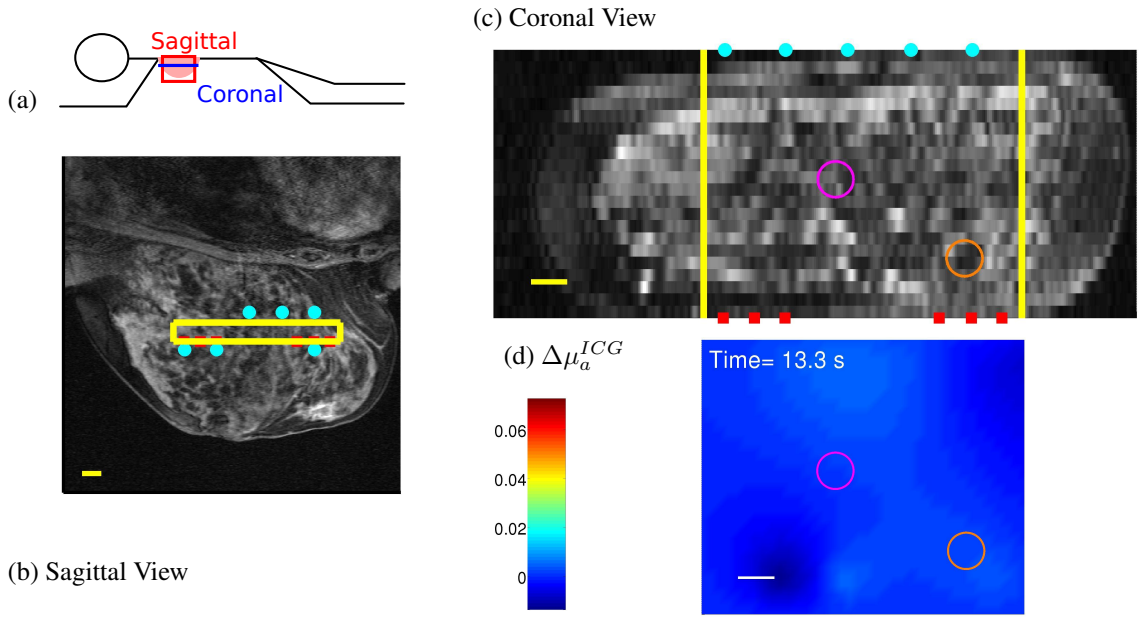

Figure 5.7: (a) Cartoon of image geometry. Gd-enhanced MRI sagittal (b) and coronal (c) of a subject with a previous positive core biopsy, but without any clinical findings in the optical field of view (d). (d) DOT image of $\Delta\mu_a$ *without* ICG injection. This particular subject did not receive an ICG injection; however, we utilized the same optical measurement protocol. The yellow boxes in the MR images mark the optical Field of View reconstructed in Figure 5.8; contrast agent uptake in the marked circles is shown in Figure 5.8 and 5.9; cyan dots are optical detector fibers and red squares source fibers. All scale bars are 1 cm.

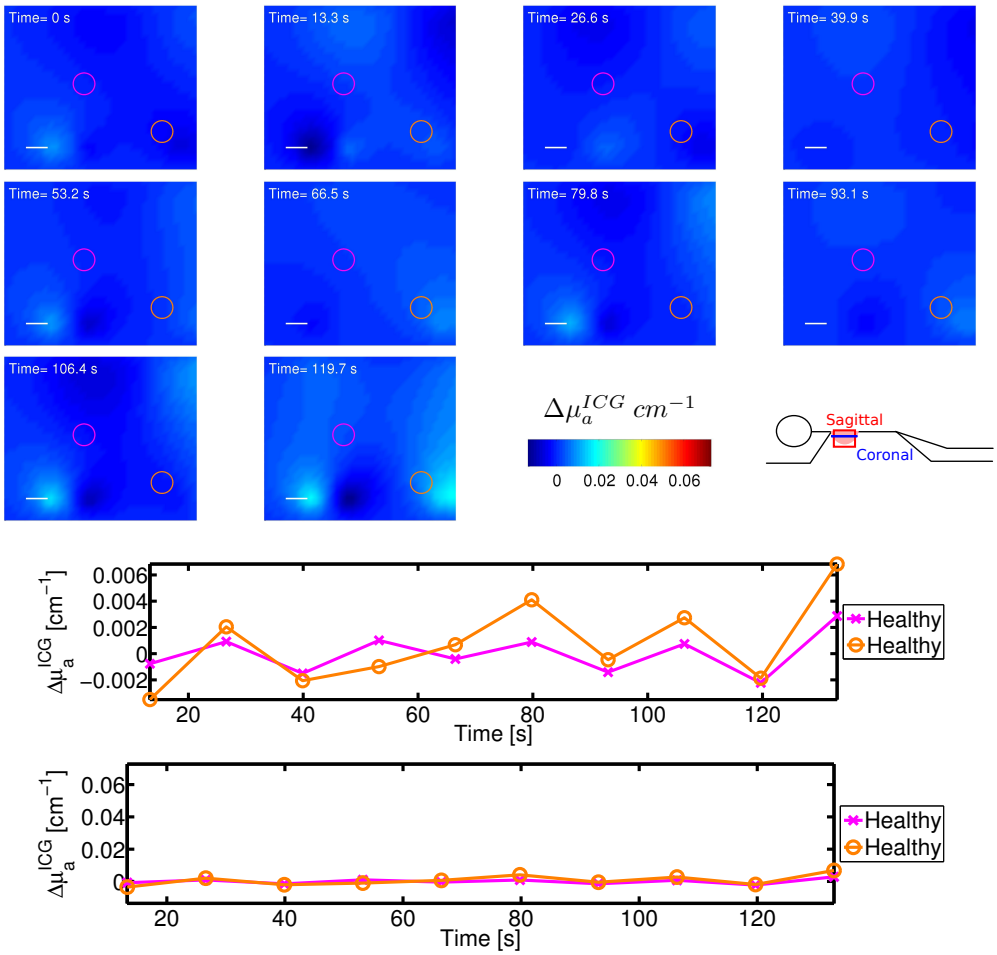

Figure 5.8: Mock ICG imaging (i.e. no injection) of a subject during an MRI. (top) Note that the scale on these images is the same as that in Figure 5.14. Data from two healthy tissue regions (magenta and orange circles) are presented in the time traces below. (bottom) Time trace of $\Delta\mu_a$ in two healthy regions (magenta and orange circles) on 2 absorption scales: one scale limited to the dynamic range of this data set, showing small fluctuations about zero, and the other scale chosen to match data shown in Figure 5.14. No significant changes in absorption were observed (as expected). The white scale bar is 1 cm.

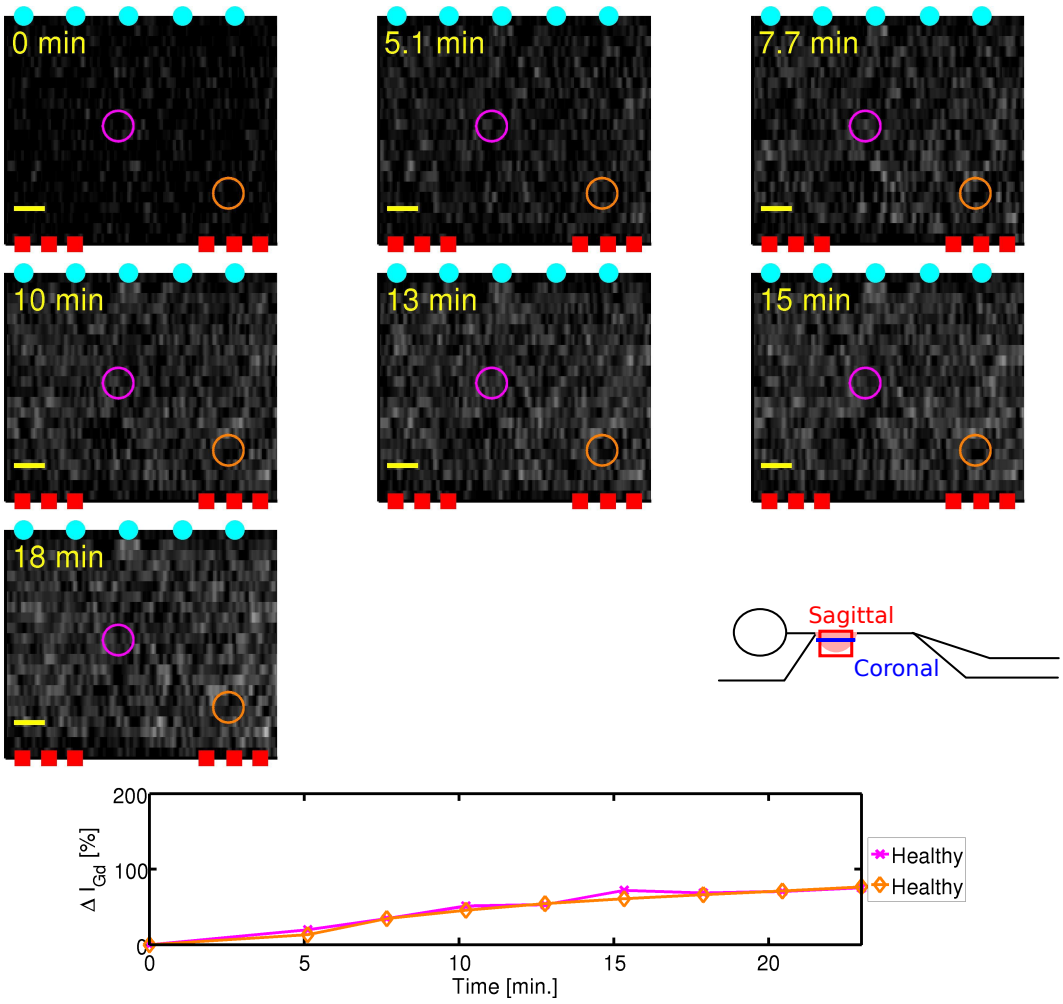

Figure 5.9: Example of Gd kinetics imaging. (top) Single coronal slices of Gd subtraction imaging reconstructions at eight time points. Images show differential enhancement to a baseline, pre-injection, image. MR image is cropped to match the Field of View for optical reconstruction as shown in Figure 5.7. Optical source (red squares) and detector (cyan dots) positions are marked. (bottom) Time trace of Gd uptake in 2 example healthy regions marked with magenta and orange circles. Note, the washout time for Gd-DTPA is much longer than the duration of the study. The yellow scale bar is 1 cm.

5.2.1.2 Simultaneous Contrast Enhanced MRI and DOT with no cancer in optical field of view

This subject had a biopsy-confirmed invasive carcinoma positioned well outside of the optical field of view (see Figure 5.10 for the measurement geometry). As expected, we observed a small diffuse increase in absorption during ICG injection (Figure 5.11), but no focal enhancements except some artifacts near the sources and detectors. The limited source-detector pairs available for this reconstruction resulted in little sensitivity to absorption changes near the edges of the reconstructed image and therefore the lower reconstructed absorption change near the superior-inferior boundaries (left-right in Figures 5.10 through 5.12). Gd-DTPA uptake for the same region is shown in Figure 5.12; again, there is no focal enhancement. Note that the color scale in Figure 5.11 is the same as that in Figure 5.14.

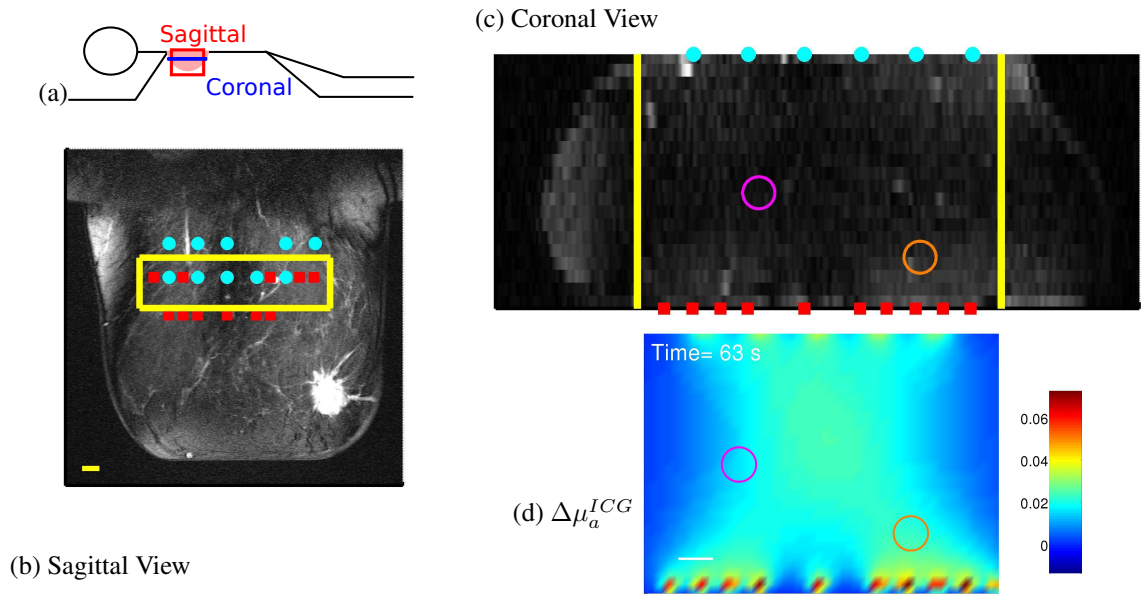

Figure 5.10: ICG and Gd Contrast Enhanced Imaging; invasive carcinoma outside of optical field of view. (a) Cartoon of image orientation. (b) Sagittal Gd-enhanced MRI view of an invasive carcinoma, ~10 minutes post injection, showing the optical Field of View in yellow; cyan dots are optical detector fibers and red squares source fibers. The tumor is clearly visible in the lower right of the image, but it is well out of the optical Field of View. (c) Same MR data as in (a), coronal view. (d) DOT image of peak $\Delta\mu_a{}^{ICG}$ in the optical Field of View marked in yellow on the MR images. The DOT color scale is chosen to match that in Figure 5.14. Note that only those sources and detectors used in the reconstruction are shown in these plots. Two regions, marked by magenta and orange circles in (c) and (d), will be used for kinetics analysis below. All scale bars are 1 cm. Data is co-registered across modalities using fiducial markers on the source and detector plates.

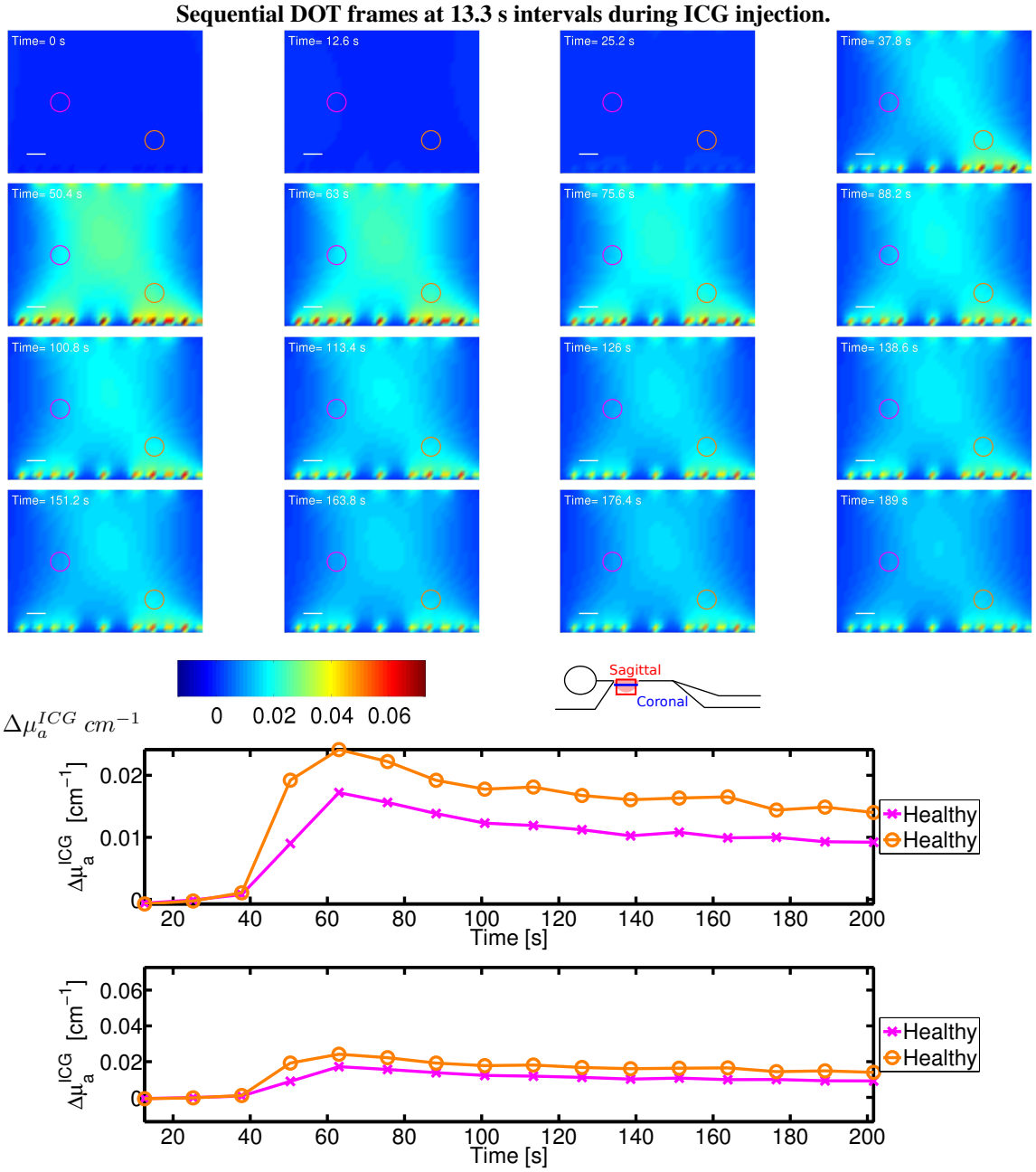

Figure 5.11: Example of ICG kinetics imaging: single coronal slices of SVD reconstructions at 16 time points of $\Delta\mu_a$ due to ICG uptake in a healthy tissue region of a subject with an invasive carcinoma. Field of View for optical reconstruction is shown in Figure 5.10. The color scale for $\Delta\mu_a$ is chosen to match Figure 5.14. (bottom) Kinetics traces of the regions marked with magenta and orange circles in two scales: one selected for this data set and one matching that in Figure 5.14. Data is co-registered across modalities using fiducial markers on the source and detector plates. Time stamps and 1 cm scale bars are marked in white in each frame.

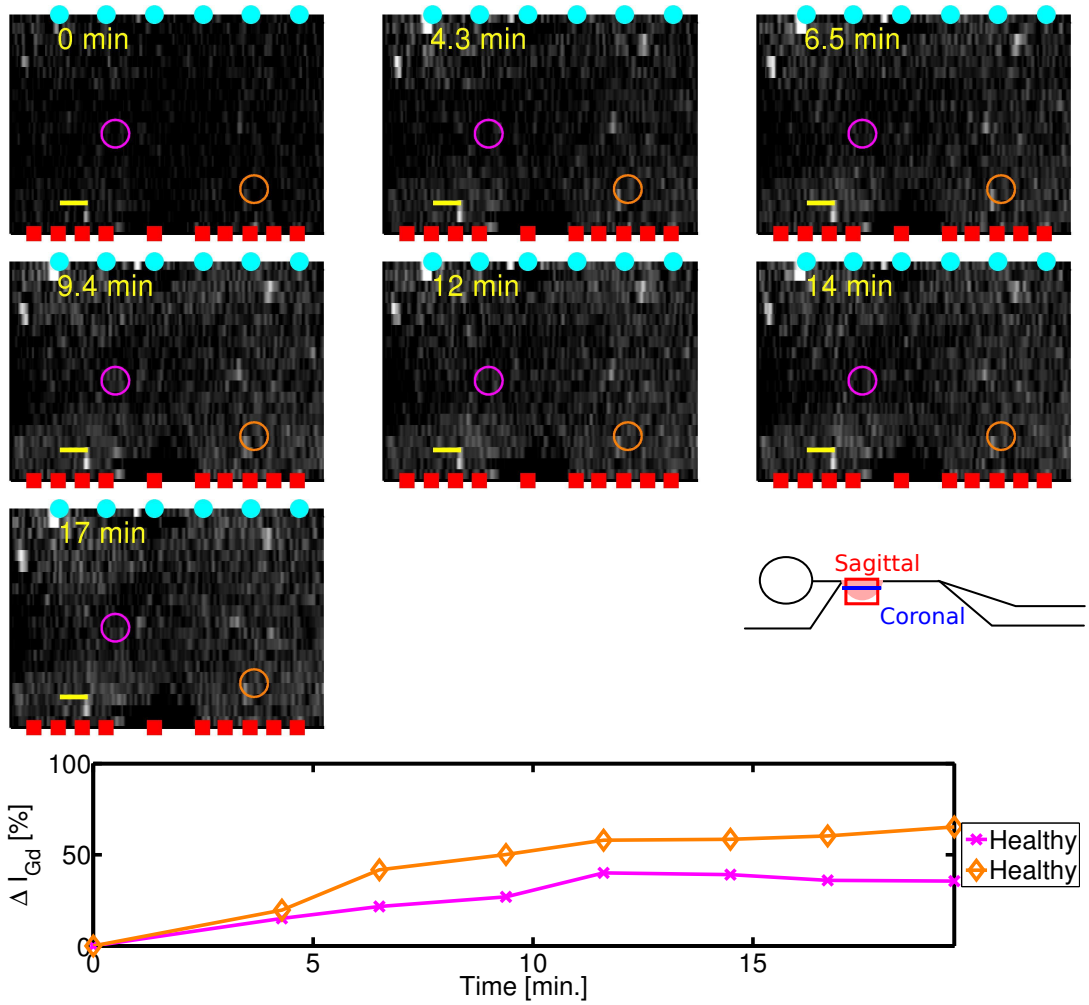

Figure 5.12: Example of Gd kinetics imaging: single coronal slices of Gd subtraction imaging reconstructions at 7 time points subject with an invasive carcinoma out of the optical Field of View; MR image is cropped to match the Field of View for optical reconstruction as shown in Figure 5.10. Data is co-registered across modalities using fiducial markers on the source and detector plates. Optical detectors (cyan) and sources (red) are marked. The average Gd enhancement for the regions marked in magenta and orange circles is shown at the bottom. The yellow scale bar is 1 cm.

5.2.1.3 Simultaneous Contrast Enhanced MRI and DOT of an Invasive Carcinoma

This subject had a biopsy-confirmed invasive ductal carcinoma, positioned between the two rows of detector fibers in the GenIIm system (see Figure 5.13 for the measurement geometry). ICG influx and washout is clearly visible in Figure 5.14, despite some artifacts near the source and the irregular tissue boundary (lower right of the image; clearly visible in Figure 5.13(c)). Gd-DTPA uptake for the same region is shown in Figure 5.15. This subject showed focal uptake of ICG (Figure 5.14). The limited number of useful source-detector combinations in this data set severely limited medio-lateral resolution (top-bottom in Figures 5.13 through 5.15), resulting in a 'blurring' of reconstructed absorption in this direction and displacement of the peak ICG uptake imaged in DOT ∼1 cm from the focal Gd-DTPA enhancement (Figure 5.15).

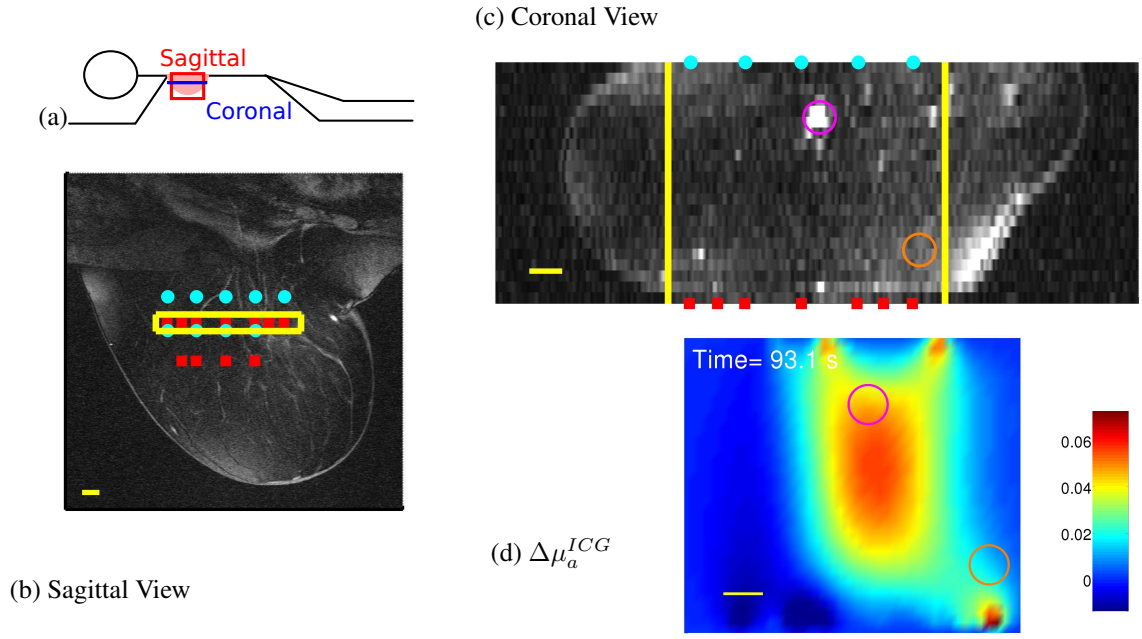

Figure 5.13: ICG and Gd Contrast Enhanced Imaging; invasive carcinoma in optical field of view. (a) Cartoon of image orientation. (b) Sagittal Gd-enhanced MRI view of an invasive ductal carcinoma, ∼10 minutes post injection, showing the optical Field of View in yellow; cyan circles are optical detector fibers and red squares source fibers. The tumor is clearly visible near the center of the image. (c) Same MR data as in (a), coronal view. Scale bar (yellow) is 1 cm. (d) DOT image of peak $\Delta\mu_a{}^{ICG}$ in the optical Field of View marked in yellow on the MR images. Source artifacts are visible in the lower right of the image, close to the irregular air boundary visible in the coronal MR. Regions of peak uptake of Gd-DTPA (magenta), along with a healthy region of the same size (orange), are marked with circles. Uptake kinetics from these regions is shown below. Note that only those sources and detectors used in the reconstruction are shown in these plots. All scale bars are 1 cm. Data is co-registered across modalities using fiducial markers on the source and detector plates.

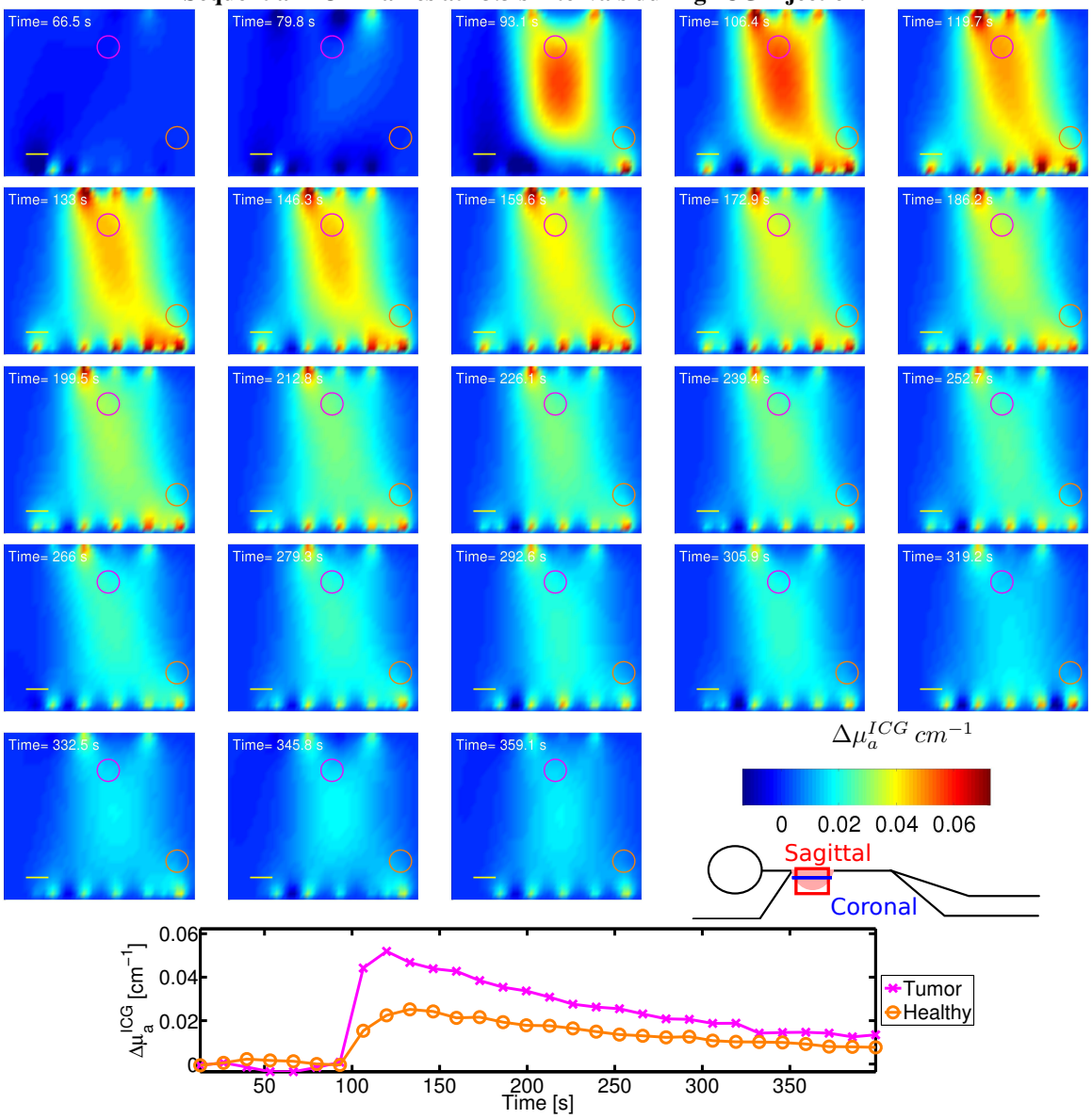

Figure 5.14: Example of ICG kinetics imaging: single coronal slices of SVD reconstructions at 28 time points of $\Delta\mu_a$ due to ICG uptake in a 51 year old post-menopausal woman (BMI 34.4) with an invasive ductal carcinoma. Field of View for optical reconstruction is shown in Figure 5.13. Images reconstructed using a hard spatial constraint are shown in Figure 5.17. Kinetics traces of the tumor (magenta) and example healthy (orange) regions marked with circles are shown at the bottom. Data is co-registered across modalities using fiducial markers on the source and detector plates. Time stamps and 1 cm scale bars are marked in white in each frame.

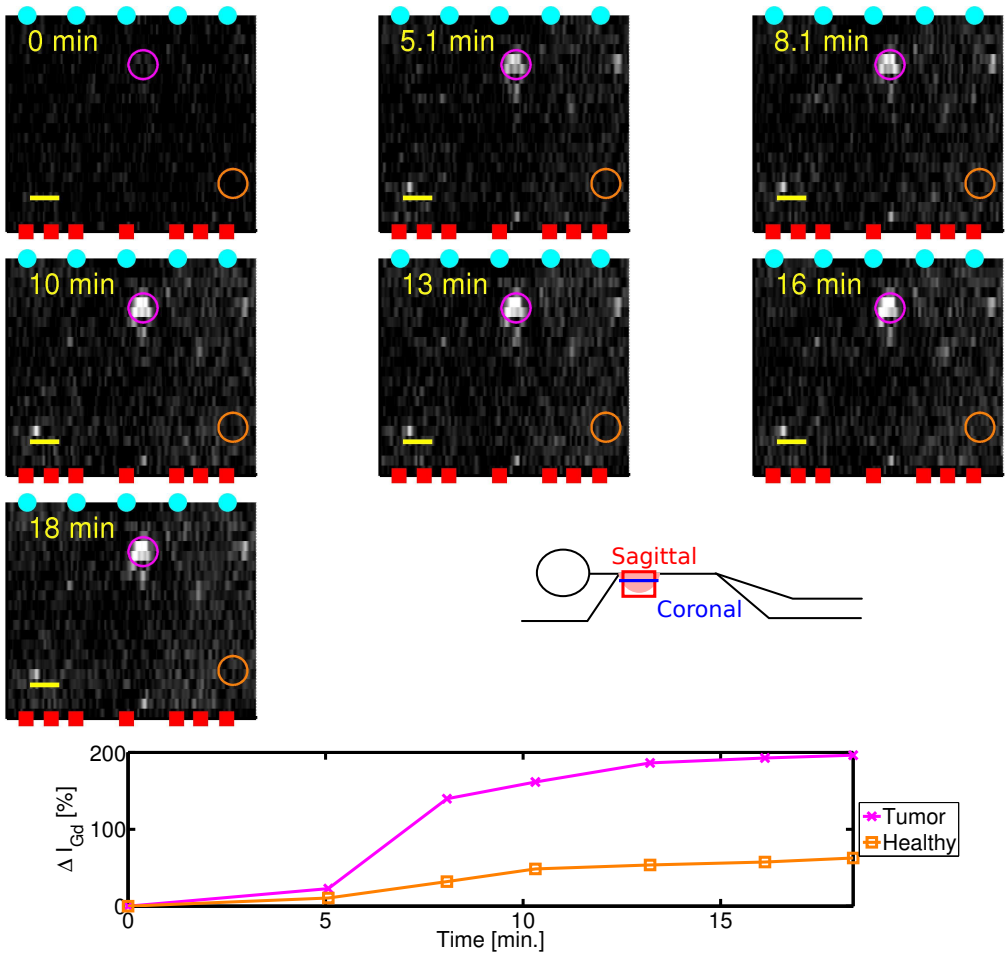

Figure 5.15: Example of Gd kinetics imaging: (top) single coronal slices of Gd subtraction imaging reconstructions at seven time points in a 51 year old post-menopausal woman (BMI 34.4) with an invasive ductal carcinoma. MR image is cropped to match the Field of View for optical reconstruction as shown in Figure 5.13. Data is co-registered across modalities using fiducial markers on the source and detector plates. The tumor (magenta) and an example healthy region (orange) are marked with circles. Optical detectors (cyan) and sources (red) are marked. The yellow scale bar is 1 cm. (bottom) Gd-DTPA uptake kinetics in the regions marked with circles.

5.2.1.4 Discussion and Conclusions: Human ICG Kinetics Imaging

Data presented in Section 5.2.1 demonstrates the capacity of the GenIIm system to successfully image ICG in human subjects during clinical MR imaging. Sequential imaging allows extraction of ICG pharmacokinetics and therefore spatially registered comparison of contrast agent uptake in each modality. In Section 5.2.1.3, we demonstrated simultaneous contrast enhanced imaging of a malignant cancer. Note that the data presented here were reconstructed using a fairly basic linear reconstruction technique (SVD matrix inversion). This choice of reconstruction technique, along with the inherent low resolution of DOT limits the utility of these DOT reconstructions. In Section 5.2.2, we utilize the MRI spatial information to model the tumor as a sphere in otherwise homogeneous tissue and reconstruct ICG uptake in each region

5.2.2 DOT with *a priori* Segmentation from MRI

5.2.2.1 MR Tissue Segmentation

A significant advantage of multi-modality imaging is the ability to utilize the strengths of one modality to improve the image quality of the other. Perhaps the best known example of this technique in clinical imaging is PET-CT: by constraining the PET reconstruction with the high resolution tissue imaging provided by CT, greatly improved maps of glucose metabolism can be reconstructed ($\sim$1 mm), a far cry from the $\sim$6-10 mm resolution in stand-alone PET imaging. Similarly, MRI provides high resolution ($\sim$0.3 mm in plane, $\sim$3 mm through plane) structural images of soft tissue, while diffuse optics provides hemodynamic functional information, but is limited to $\sim$0.5 cm spatial resolution in a typical breast imaging geometry[90].

The MRI data sets collected during this study contained a series of T_1-weighted images at various delay times, enabling calculation of T_1 maps. A simple T_1-threshold was used to separate glandular and fatty tissue with a reasonable degree of accuracy, producing images such as can be seen in Figure 5.16.

Similar masks are used in Section 5.2.2.2 to form 'hard priors' for DOT reconstruction, i.e., reconstructions in which all tissue of a particular type (glandular, adipose, tumor) is assumed to have identical optical

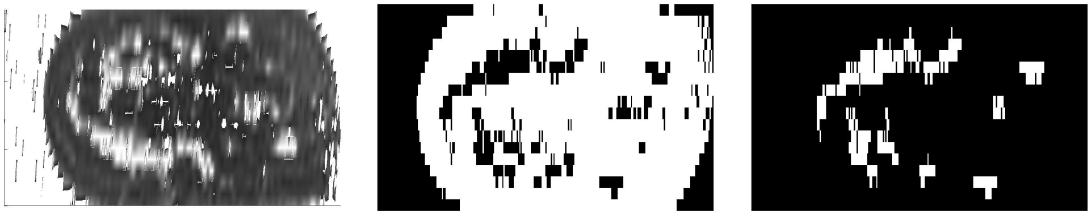

T_1 Map | Adipose Segmentation | Glandular Segmentation

Figure 5.16: Example segmentation of breast tissue into fat and glandular regions in a cancer-free breast. Data was collected at 1.5T; glandular tissue was defined as any regions with T_1>450ms. The region shown is $\sim$6 cm medio-lateral (vertical in images) and $\sim$10 cm superior-inferior (horizontal in images).

properties.

5.2.2.2 DOT Reconstruction with Geometry Extracted from MR Tissue Segmentation

If we assume that each tissue type defined by MRI has uniform ICG pharmacokinetics, then we can reduce the DOT inverse problem to calculation of ICG uptake in each tissue type. This transformation reduces unknowns in the reconstruction from the properties of hundreds or thousands of voxels to changes in the properties of 2-5 tissue types. Thus, the constrained approach yields a significantly simpler inverse problem (at the cost of some simplifying assumptions). Figure 5.17 shows an example of such an analysis. Generally speaking, a T_1 image can be used to calculate a glandular/adipose mask. The particular subject shown in Figure 5.17 however, had effectively no glandular tissue in the optical field of view. Since this subject was both post-menopausal and obese (BMI=34.4), this lack of glandular tissue is not surprising. (A similarly fatty breast from a different subject is shown in Figure 5.21.) Gd-DTPA uptake was used to segment out the tumor (note, in this subject, the tumor was also visible in T_1).

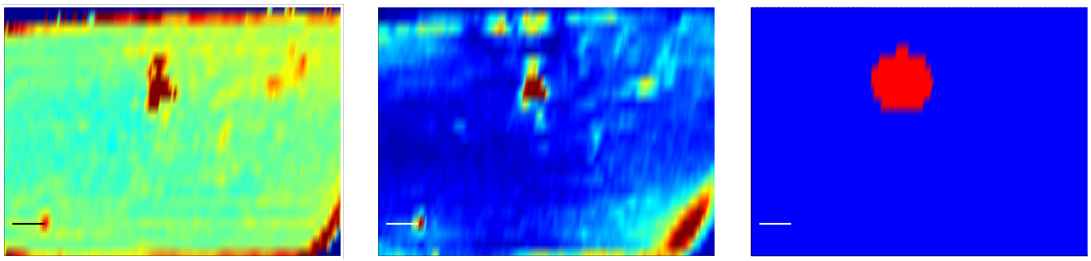

T_1 Gd-DTPA Mask

Figure 5.17: Segmentation of Adipose and Tumor tissue (no glandular tissue present) using MRI data (T_1 and Gd-DTPA uptake). This segmentation was utilized in the reconstruction shown in Figure 5.18. Images reconstructed without spatial constraint are shown in Figure 5.14. The region of high Gd-difference signal in the lower left is due to a skin artifact and possibly subject movement between the imaging and baseline scan. Note the field of view has been shifted slightly compared to the unconstrained images shown in Figure 5.13. Scale bars are 1 cm.

Figure 5.18 shows a comparison of the ICG and Gd-DTPA uptake in the regions demarcated in Figure 5.17. Both ICG and Gd-DTPA uptake in the tumor are substantially higher than the surrounding tissue, corroborating the earlier results of Ntziachristos[5]. One of the advantages of the DOT technique compared to current clinical contrast-enhanced MRI protocols is the much higher frame rate: a DOT image in Figure 5.17 was collected every 13.3 s, while the MR images were collected every 94 s. This relatively slow frame rate can cause difficulties in fitting pharamacokinetic models to the Gd uptake. Recent work on high speed image acquisition (including that by several of our Hospital of the University of Pennsylvania collaborators on rotating frame methods[242]) may eventually improve this MR frame rate. However, this frame rate is ultimately a function of contrast agent sensitivity. This and other DOT studies utilize an $\sim$300-fold lower

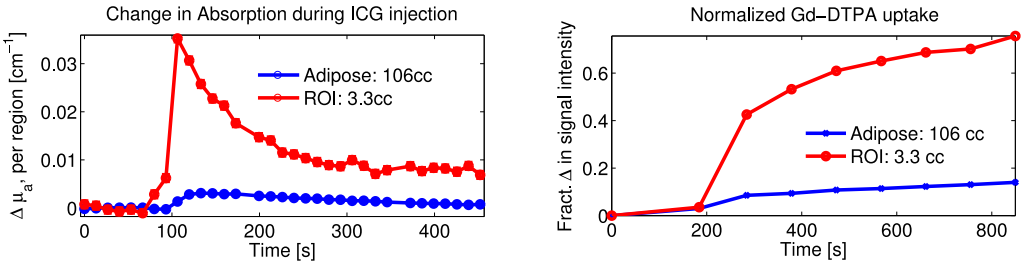

Figure 5.18: Comparison of ICG and Gd-DTPA kinetics, using tissue segmentation (Figure 5.17) as a hard spatial prior. DOT data is presented as $\Delta\mu_a = \mu_a[t] - \mu_a^{(0)}$. MRI data is presented as the fractional change in signal intensity ($(I - I_0)/I_0$). Note that the frame time for the DOT images was 13.3 s, while the MRI data took 94 s to acquire per frame. MR signal intensity is non-linearly related to local Gd-DTPA concentration.

blood concentration of ICG compared to the Gd-DTPA dose used clinically (see Section 3.1.1).

The T_1 and Gd-enhanced adipose-glandular-tumor segmentation discussed here is a simple initial application of rigid spatial priors in DOT reconstruction; previous theoretical work (e.g. Brooksby[7]) including from the University of Pennsylvania[188] suggest paths for future integration of spatial information from MR images with optical data from the GenIII Opt/MR Imaging system described in Chapter 6.

5.3 Lessons from the GenII and GenIIm systems

5.3.1 Tissue Contact

Diffuse optical measurements rely upon a stable physical connection between fiber optics and the tissue being measured. A key failing of the GenII/GenIIm platform is the difficulty in obtaining good optode-skin coupling for most subjects. A schematic axial view of the tissue compression plates used in the GenII and GenIIm systems is shown in Figure 4.5. A similar view, with a to-scale MR image in place of the cartoon of the breast, is shown in Figure 5.19. This particular subject had a fairly large breast (self reported: C/D cup), but even in the center of her breast, the second row of sources in the medial plate failed to make skin contact.

The poor source-detector skin coupling of the GenII Opt/MR platform (e.g. Figure 5.19) prevented DOT imaging in most of the subjects examined, as there were too few source-detector pairs to reconstruct an image. Our GenIII platform seeks to correct this difficulty both by placing many more source-detector pairs against the breast and by allowing optodes to be positioned individually for each subject.

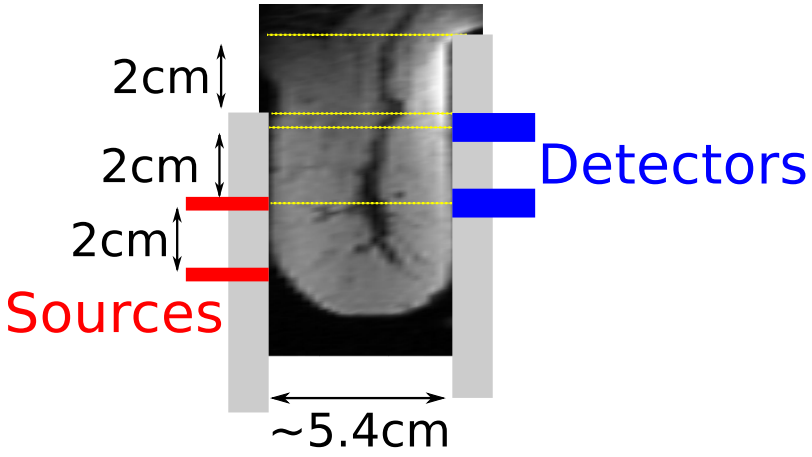

Figure 5.19: Schematic and axial T_1 image showing fiber optic coupling of the GenIIm Opt-MR platform. The T_1 slice is through the center of the breast (nipple is out of the image plane). The second row of sources is not in contact with the skin even in the center of this fairly large breast (C/D cup as reported by subject). Note that this is the 'best contact' axial plane: both rows of sources and detectors are not in contact ~3 cm superiorly and inferiorly of this slice. Sources are denoted by red boxes, detectors by blue boxes, and yellow lines dashed lines are included to show alignment.

5.3.2 Tissue Shaping

In an attempt to improve optode-skin coupling, we began a pilot study to determine if we could mold breast tissue against the compression plates (containing the optodes) without degrading the clinical imaging. Figure 5.20 shows an example of this work, in which a foam block was placed under the nipple, pushing tissue up and out against the compression plate. In the few subjects we had the opportunity to study, this scheme improved optode coupling without significant degradation in diagnostic information.

5.3.3 Fiber Placement

A second major failing of the GenII/GenIIm platform is limited flexibility in optode placement: sources and detectors were each confined to a pair of lines running parallel to the axis of the body (Figure 5.19). Figure 5.21 shows an egregious example of this problem wherein we had perfect skin-optode coupling, but the cancer was far away from optode locations.

The GenIII system permits adjustment of the vertical position of fiber optic modules. This flexibility, for example, would have facilitated imaging of the cancer shown in Figure 5.21.

5.3.4 Lessons applied to the GenIII system

In clinical experiments, we had little flexibility in the spatial placement of optical fibers, especially the roughly 2.5 cm diameter armored detector fiber bundles (0.5 cm diameter active area). Figure 4.4 (lower

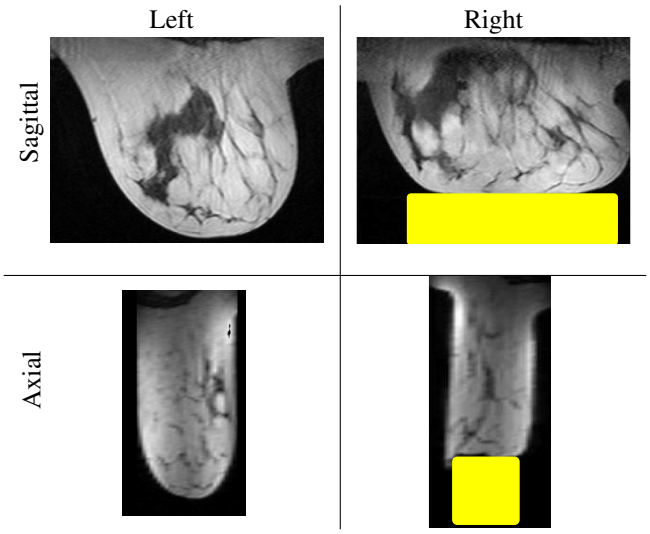

Figure 5.20: Example of application of tissue shaping inserts in a single subject, tested with the GenIIm platform. The left breast had no inserts, while the right breast had a ∼4 cm thick foam block positioned under the nipple. The foam does not show up in the MR image; it has been schematically shown in yellow. Note how the right breast has better contact with the compression plates then the left breast. See also Figure 5.19.

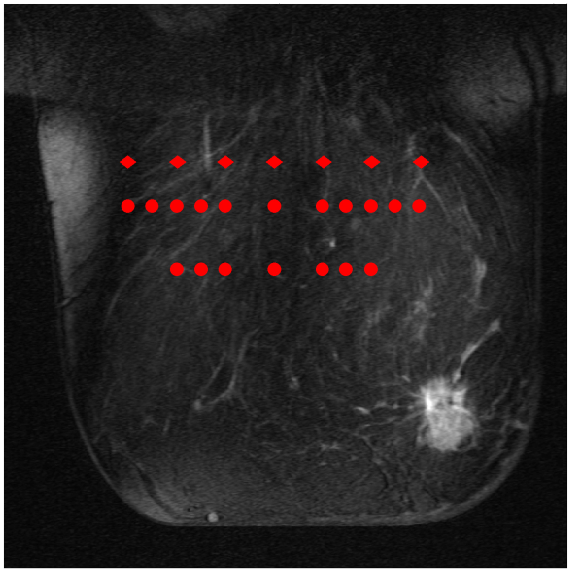

Figure 5.21: Example of difficulties with fiber optic placement in the GenII and GenIIm systems. Many cancers were missed due to the fixed location of the optodes using the GenII/GenIIm platform. The fixed position of the sources (red dots) and detectors (red circles) precluded imaging this cancer. With the very largest breasts, the optical fibers have sufficient clearance from the curving magnet bore only in the top row.

left) shows the available locations for mounting the detector fibers in the lateral compression plate. Note that the physical supports which hold the detector fibers in position have been removed for this photo. In addition to limited mounting points, these fiber bundles had a minimum bend radius of $\sim$15 cm. This constraint, together with the spatial limitations of the walls of the MRI bore (see Figure 4.1), forced us to place the detector fibers in the top two rows of holes seen in Figure 4.4. The size of the fibers and the placement of the RF electronics also limited how close to the chest wall the detector fibers could be placed. Together, these restrictions resulted in many cancers falling outside the optical field of view (Figure 5.21 shows an MRI image of a particularly dramatic case).

Furthermore, the size of these detector fibers was such that they could not be bundled together and still fit through the waveguides in the MRI room shielding. The GenII and GenIIm systems were constrained by the need to protect the photon-counting PMTs, which require shielding even when powered down. Together, these constraints necessitated complete removal of the detector fibers from both the PMTs and Opt/MRI platform during the setup/take-down of each experiment. Operators found this GenII instrument to be quite difficult to prepare and dismantle within the time allotted to us by the clinical team.

Additionally, the individual mounting of the fiber bundles directly on the compression plates made modification of the fiber layout very difficult, as it effected the RF electronics (shown in Figure 4.4). The GenII/GenIIm platform was constructed primarily of white PVC, which exacerbated light shielding difficulties.

5.4 GenII and GenIIm Results Summary

The GenII and GenIIm systems demonstrated the ability to make multiple DOS measurements of breast tissue simultaneously with MRI. Additionally, we were able to perform DOT imaging with the GenIIm system in a few subjects, demonstrating simultaneous contrast enhanced DOT and MR imaging. The limitations of the GenIIm system motivated the construction of the GenIII system, described in Chapter 6.

Chapter 6

Development of a Modular Hybrid Diffuse Optical and Magnetic Resonance Imaging Platform (GenIII)

Simultaneous breast cancer imaging with Magnetic Resonance Imaging (MRI) and Diffuse Optical Tomography (DOT) combines non-invasive and non-ionizing modalities which provide complimentary information (Section 3.2.2). Briefly, MRI provides high resolution (<0.5 mm) images, but only limited functional information through Gadolinium contrast agents. DOT provides 3D maps of hemodynamics and optical contrast agent uptake, but at limited spatial resolution ($\sim$6 mm in a 6 cm thick phantom[90]). Thus, combining DOT and MRI provides several scientifically interesting, and potentially clinically useful, opportunities.

This chapter describes further development of the University of Pennsylvania GenIII Diffuse Optical-Magnetic Resonance Imaging Platform, building off of the GenII and GenIIm instrumentation and the results described in Chapter 4 and 5. Future studies will validate the clinical utility of DOT through direct comparison of spatially co-registered DOT with MRI, especially in the context of neoadjuvant chemotherapy monitoring. In the course of these studies, we expect to utilize combined imaging, employing MR imaging to spatially constrain DOT reconstructions and thus improve DOT resolution and quantification. We have taken the first step towards these goals by developing a modular diffuse optical imaging system for simultaneous DOT and 3T MRI; the instrument permits optimized optode positioning for each subject and develops opto-electronics compatibility with future 7T MRI platforms. This system provides the largest in-magnet DOT spatial data sets yet reported.

The GenIII system is specifically designed to improve the collection of clinical imaging data by addressing difficulties with the GenII and GenIIm systems discussed in Section 5.4. In designing the GenIII system, we sought to eliminate or reduce these limitations through the inclusion of adjustable fiber modules, improved support for the subject's body, and acquisition of much more spatial optical data. Additionally, we included an option to utilize the GenIII platform for MRI-guided biopsy, permitting better integration into the clinical research work flow and thus increased recruitment.

6.1 GenIII Instrumentation

Our experience with the GenII and GenIIm system guided the modular design for fiber mounts in the GenIII system. We separated the optical mounts from the RF electronics, permitting the fibers to be repositioned or replaced independently of the electrical components. This design has the additional advantage of permitting the same optical components to be potentially used in several MRI platforms (e.g. 1.5, 3, and 7T available at Hospital of the University of Pennsylvania), despite the different MR electronics.

We also increased the number of source and detector positions, thereby increasing the spatial information content of our data. In order to accomplish this goal, we reduced the TD detector fiber bundles from 5 mm to 3 mm diameter active area and did not individually armor the fibers (as was done with the GenII and GenIIm systems). This permitted us to introduce many 1 mm diameter CW detector fibers. The initial pair of modules constructed to test our designs contain 32 source and 54 detector fiber positions compared with 24 source and 14 detector positions for DOS/DOT in the GenIIm system, in roughly the same spatial area. Eventually, when the full compliment of fiber optic modules are added to the GenIII system, we will have 64 sources and 256 CW detectors in modules we can position individually for each subject based on known or imaged tumor locations. Additionally, the GenIII modules will contain optics for DCS measurements (10 sources and 10 detectors in the initial pair of modules). The joint imaging platform is shown with the fiber optics mounted in Figure 6.1.

6.1.1 GenIII MRI Platform Design and Implementation

The MR components of the GenIII Optical-MR Imaging platform were developed by Dr. Thomas J. Connick, building off his earlier work on the MR platform in the GenII system[238] (Section 4.2.2), while adapting the design for 3T.

This platform contains an 8-coil SENSE (sensitivity encoding) surface coil array (2 lateral and 2 medial coils on each breast). The medial coils have local preamplifiers; the lateral coils currently use an external preamplifier box. Preamplifiers will be added to the lateral coils in the near future; we prioritized using our limited available supply of these specialized and long lead time components on the medial coils as the

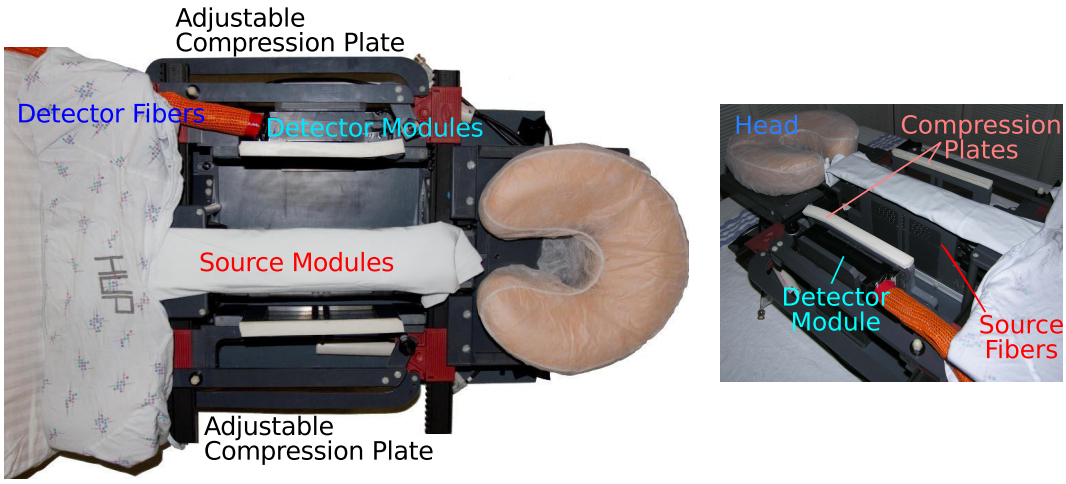

Figure 6.1: Photos of GenIII Optical-MR Imaging platform. A detector fiber module is mounted on the left breast lateral compression plate; a source fiber module is mounted on the medial plate (source fiber tips are visible as white dots on the medial plate in the left image).

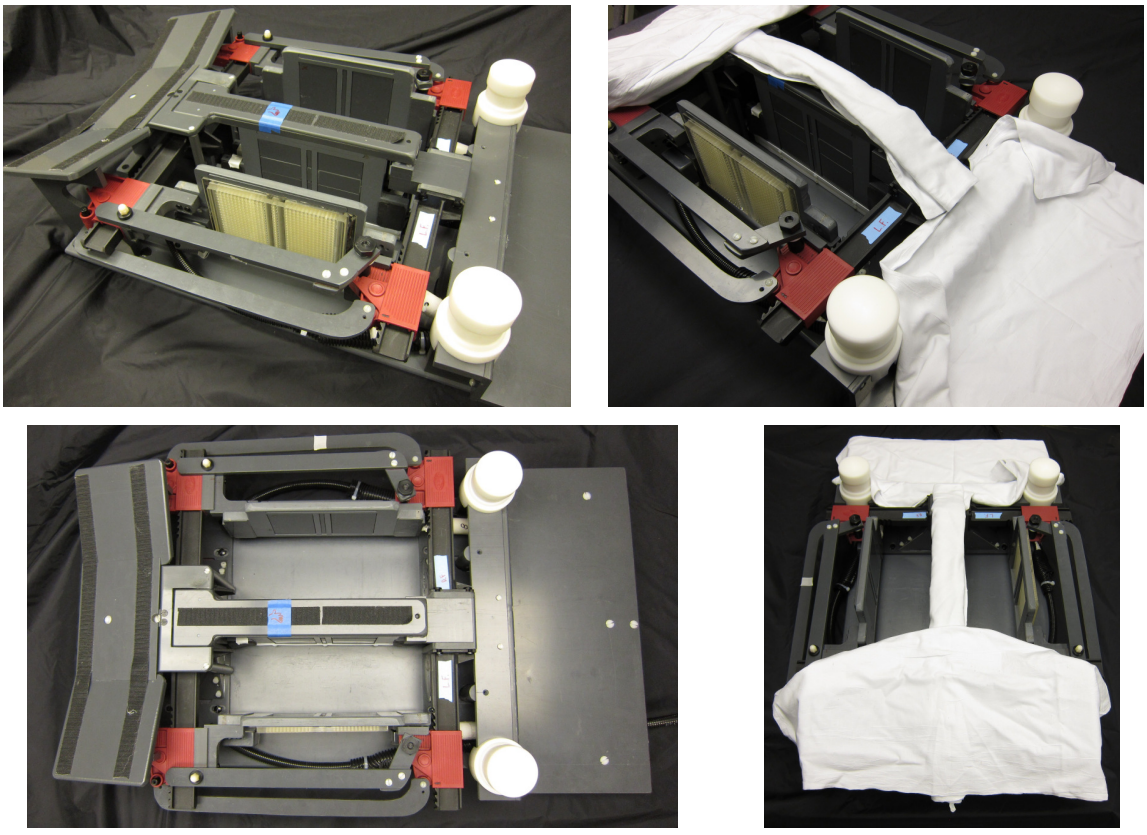

Figure 6.2: Several views of the GenIII Optical-MR Imaging platform. (right) Platform without padding or linens. (left) Platform with minimal padding and linens in place; with the linens in place the weight bearing elements of the platform are colored white to minimize the possibility of damage to the platform through excessive load on the mobile compression plates.

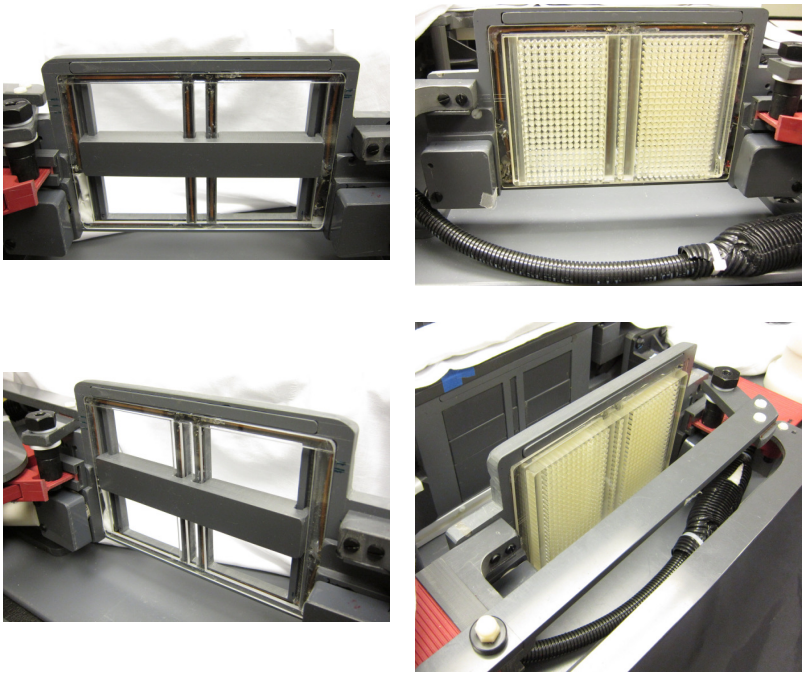

Figure 6.3: Images of the lateral compression plates in the GenIII system. (left) Left lateral plate with a fiber optic module blank (i.e. before machining for fiber optic mounting) in the center position. (right) Right lateral plate with a biopsy plate mounted. The cable visible in the bottom of the images connects the right lateral posterior coil to the external preamplifier box out of the frame to the right. The copper lateral coils are visible through the clear Plexiglas cover surrounding the biopsy plate.

coupling between these coils is problematic.

Portions of the RF electronics are visible through the clear Plexiglas covers of the lateral plates in Figure 6.3. A schematic of the space allotted to electronic and optical components is shown in Figure 6.4 and the entire platform in the MRI suite in Figure 6.5. The limited space for electronics created a number of practical difficulties and considerable effort was expended to maintain the large area of access for the optical modules.

MR phantom imaging (Figure 6.6) demonstrated that the system has sufficient resolution for clinical research use by our collaborators Drs. Angela DiMichele and Mark A. Rosen in the ISPY-2 trial[i].

As mentioned above, the GenIII platform utilizes fiber optic modules, permitting fast and simple repositioning of fibers. These modules also greatly reduce system set-up time in the clinic, a critical concern with tightly scheduled clinical instruments; designes are shown in Figure 6.7 and Figure 6.8. We have currently constructed one pair of source and detector modules to fully validate the design; we will construct the others after we have recruited several human subjects for simultaneous DOT and MRI. These initial modules (photos shown in Figure 6.9 and Figure 6.10) contain 5 TD and 54 CW detector fiber positions and 32 source

[i] *www.ispy2.org*

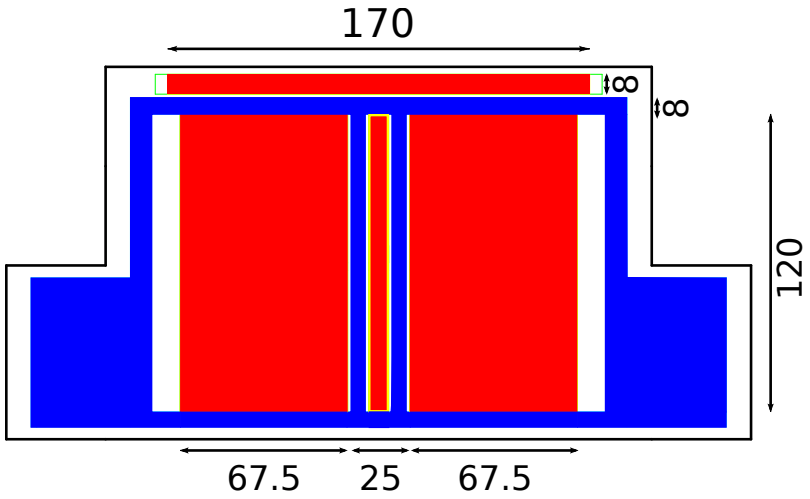

Figure 6.4: A schematic of the compression plates for the GenIII system. Blue areas are available for the RF electronics; red areas are cutouts for the placement of optical fiber modules; white areas were reserved for mechanical support and mounting. Note the upper optical access region, which permits optodes to be placed a few mm from the chest wall. Dimensions are in mm.

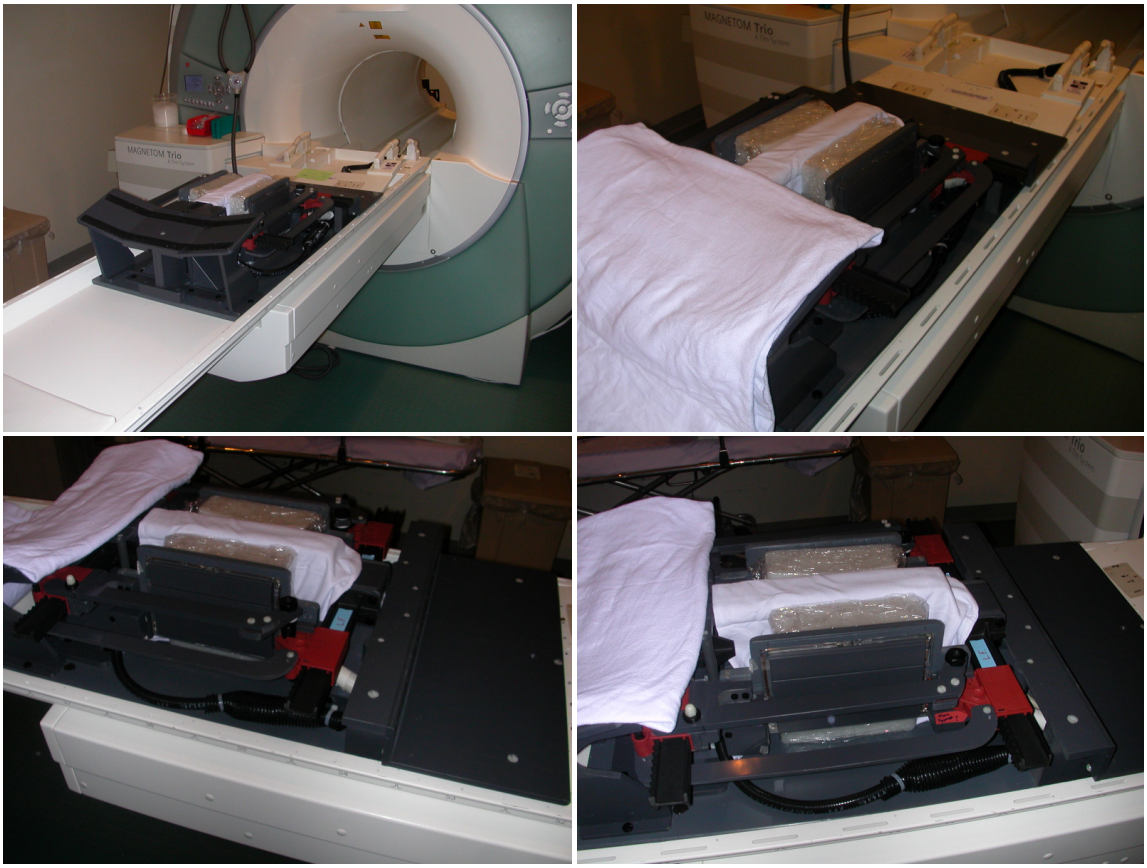

Figure 6.5: Photos of the GenIII Opt/MR platform during a phantom imaging study. The fiber optic modules were not mounted when these photos were taken.

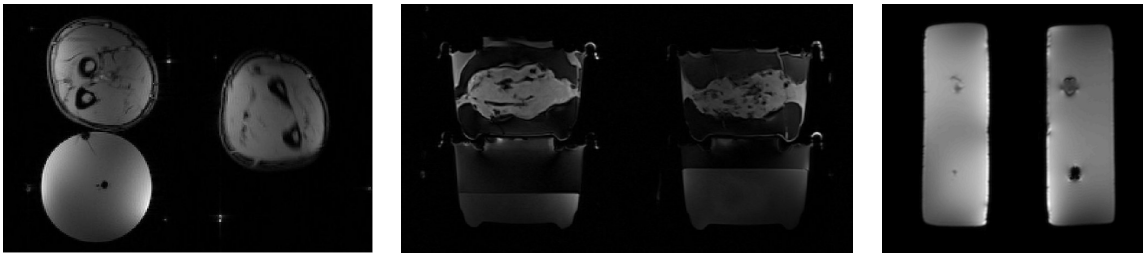

Figure 6.6: Example MR Imaging with GenIII platform. (left) Images of copper sulfate phantom and human forearms, showing the fiducial markers used for image co-registration. (center) A phantom composed of ground turkey, vegetable shortening (Crisco), and saline (phantom suggested by Dr. Sarah Englander, based on earlier work on breast tissue quantification[243]) atop a phantom of cooking oil and saline. (right) Joint Optical/MR phantoms composed of gelatin, Liposyn, and ink, with inclusions containing Gd chelate (MultiHance) and ICG.

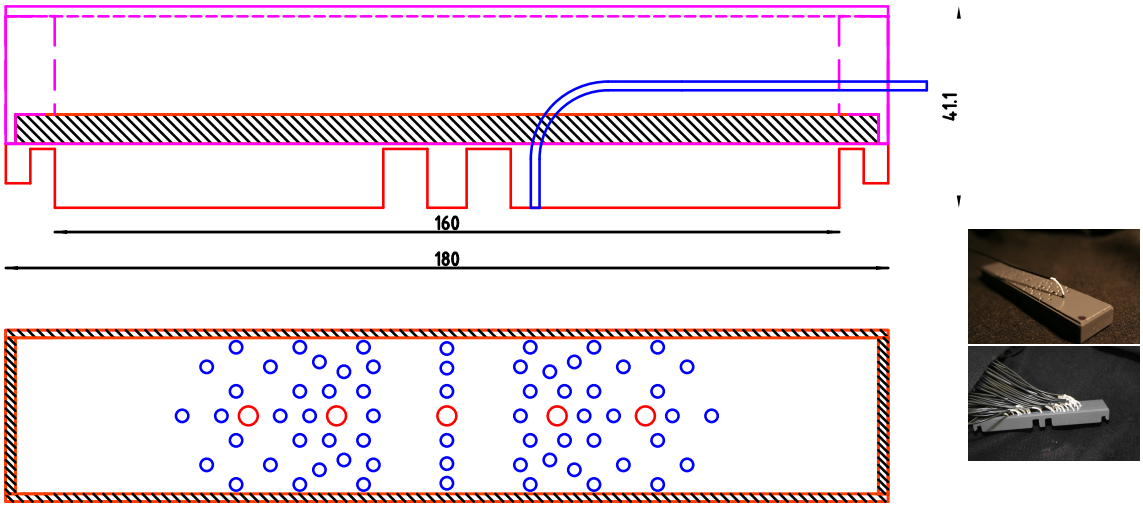

Figure 6.7: Example detector fiber module for the GenIII system. (left, top) Schematic of side view, showing (blue) optical fiber, mounting plate, and protective cover; bottom view, showing placement of 1 mm (CW) and 3 mm (TD) fiber optics. (left, bottom) Top view of detector module, showing the layout of fiber optics the larger, 3 mm, holes are for the TD detectors. The walls of the protective cover (magenta) are made of $1/16^{th}$ inch PVC; $1/4^{th}$ inch PVC is used for the end pieces. (right) Photos of fiber optic modules without protective back cover. The tissue face of this module is shown in Figure 6.9. Dimensions are in mm.

positions, a significant improvement over other reported systems (Table 3.2). Note, the current source module has additional fibers pre-positioned to be utilized for additional CW/TD sources (12) and single mode fibers for use as DCS detector fibers (12).

In addition to the changes in the fiber optical mounts, we attempted to utilize the information gathered over the course of our study to improve subject comfort during the exam: not only would this reduce the strain on our subjects, but comfortable subjects are less likely to move during the exam, improving our data quality. The most common complaint from our subjects was neck pain due to laying on the right or left side

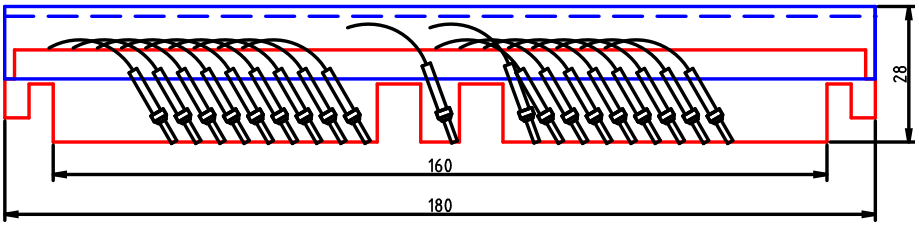

Figure 6.8: Example of GenIII source fiber module. Source fibers were inserted at 20 or 30 degree angles to reduce the bending radius of the fibers. The walls of the protective cover (blue) are made of $1/16^{th}$inch PVC; $1/4^{th}$inch PVC is used for the end pieces. The tissue face of this module is shown in Figure 6.9. Dimensions are in mm.

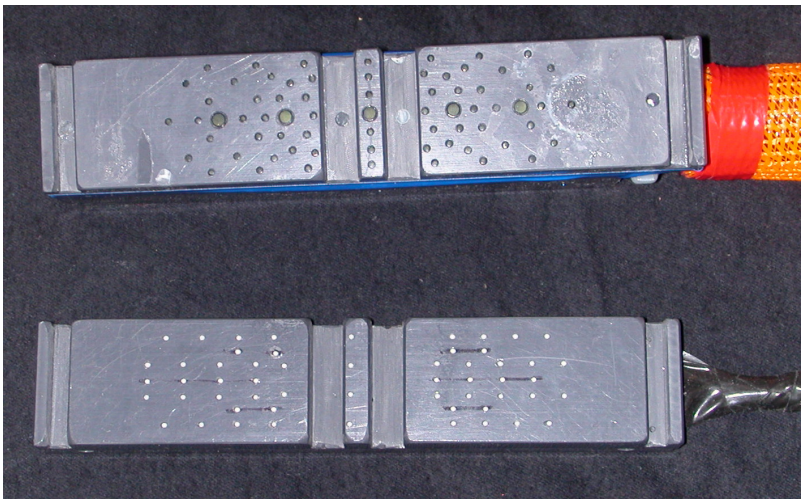

Figure 6.9: GenIII source and detector fiber modules, both 3.5x18 cm. The source plate includes thirty two CW/TD multi-mode source fibers and ten single mode DCS detector fibers; the detector plate holds fifty four 1 mm CW detector, ten 1 mm DCS source, and five 3 mm TD detector fiber bundles. Schematics of the detector and source modules are shown in Figure 6.7 and Figure 6.8.

of the head. We addressed this by installing a 'face-pillow' from a massage table in the GenIII platform. The second most common complaint focused on the portion of the subject's weight which rested on her sternum. We addressed this by supporting both the shoulders and the abdomen in the updated platform (see Figure 6.2 and Figure 6.5) and by widening the sternum support from 5 to 5.5 cm.

The GenII platform was constructed of white PVC plastic which permitted considerable light reflection/scattering. Unfortunately, most black plastics utilize carbon black as a pigment; when tested, they all proved to cause artifacts in MR images. Note, this effect is related to the quantity of plastic used and the few grams of black Delrin and PVC in our fiber coverings have little effect on the MR signal. We therefore chose to construct the GenIII system out of gray PVC as a compromise between MR compatibility and stray light reduction.

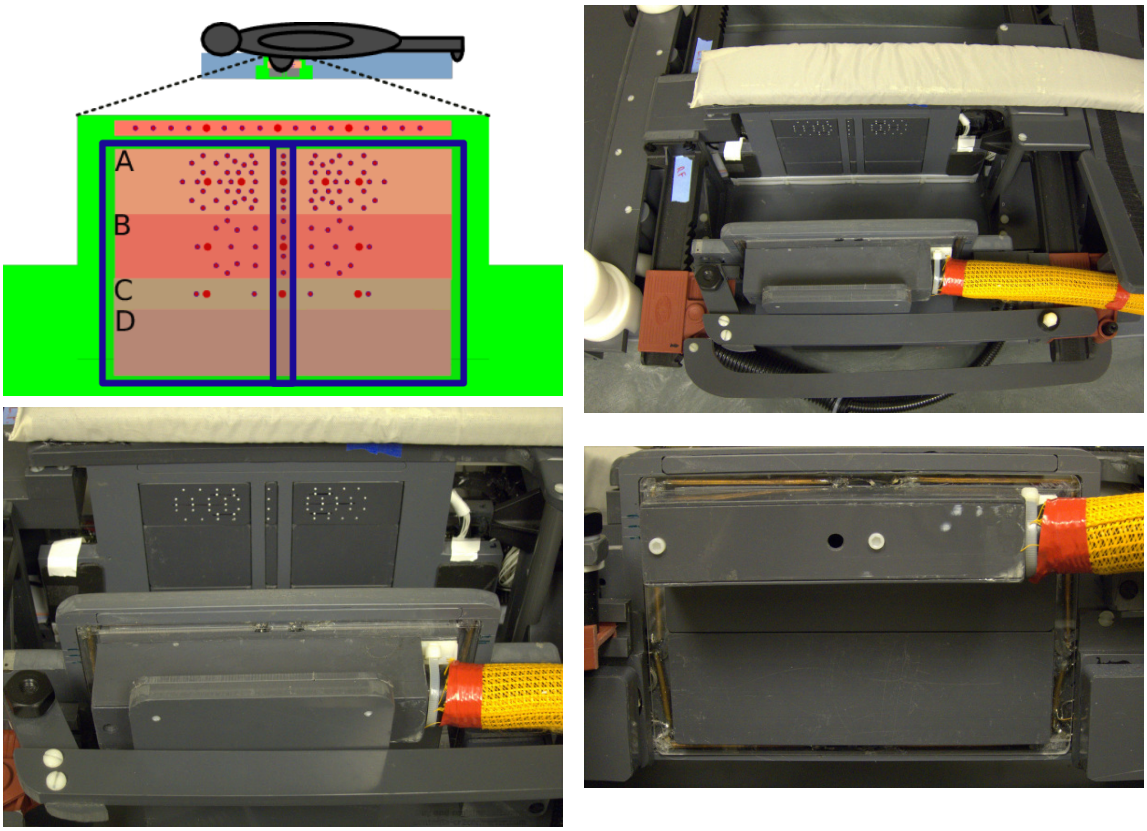

Figure 6.10: GenIII detector modules and compression plates. (left, top) a schematic of 5 detector modules (A, B, C, D, and a fixed module near the chest wall) mounted in the lateral compression plate. (right, top; bottom) Photos of a detector module (A in the left, top schematic) mounted in the imaging platform. This module is also shown in Figure 6.7 and 6.9. A source module is visible in the lower left and upper right images.

6.1.2 GenIII Opto-Electronics Design and Implementation

The GenIII TD opto-electronics are based on those of the GenIIm system; the critical changes are improved PMT cooling and the inclusion of shutters to protect the PMTs when fibers are not in direct tissue contact; David L. Minkoff and Han Y. Ban were instrumental in the construction of the PMT module and design of the shutter control system. Currently, we have both 830 and 838 nm lasers; we plan to replace the 830 nm with a 905 nm laser to improve quantification of lipid and water concentrations. The GenIII CW system is significantly different than the GenIIm CW components, using several additional wavelengths and significantly more spatial detector positions; these improvements are described below.

Figure 6.11 shows a schematic of the current GenIII opto-electronic system. As discussed above, a single pair of source and detector modules is currently undergoing testing; additional source and detector channels shown in Figure 6.12 will be added along with additional planned modules. Currently all CW detector

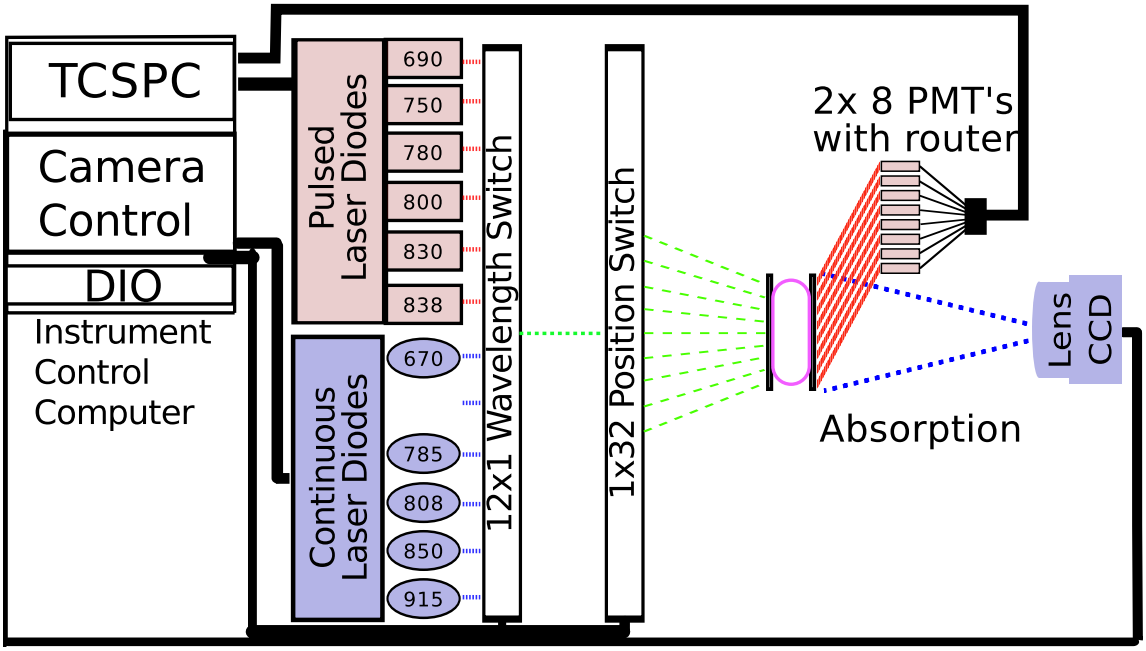

Figure 6.11: Schematic of GenIII current optical-MRI system. Six pulsed lasers and five steady-state lasers are multiplexed through a 12x1 wavelength and a 1x32 position switch and coupled through optical fibers to tissue. 54 CW detector fibers are lens-coupled to an Andor iKon-L CCD camera, permitting ~0.5s per source position and wavelength measurements of absorption. 5 TD detector fibers are coupled to photon counting PMTs and TCSPC electronics.

fibers are lens coupled to a single CCD (Andor, iKon-L; see Figure 6.13) for absorption measurements. Figure 6.12 also shows a fluorescence imaging system; as additional CW detector fibers become available, we will utilize a subset of the eventual 256 CW fibers for fluorescence imaging. The fluorescence CCD (Andor iXon-887 back illuminated) is currently integrated into the system, however, we have not yet begun collecting fluorescence data. Figure 6.14 shows the opto-electronic rack and components.

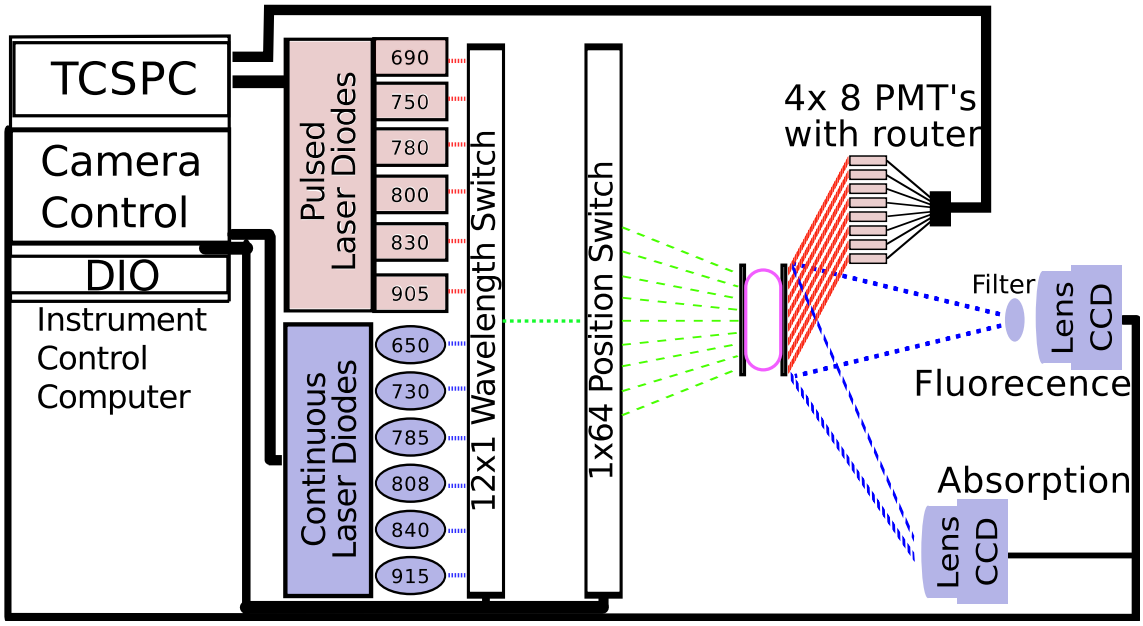

Figure 6.12: Schematic of GenIII complete optical-MRI system. Six pulsed lasers and six steady-state lasers are multiplexed through a 12x1 wavelength and a 1x64 position switch and coupled through optical fibers to tissue. 256 CW detector fibers are split between a pair of CCD cameras, permitting simultaneous measurement of both absorption and scattering. 32 TD detector fibers are coupled to photon counting PMTs and TCSPC electronics. GenIII has added CW $\lambda = 915$ nm and will add TD λ =$905nm$ to those available in the GenII system to permit stable measurement of H_2O and Lipid.

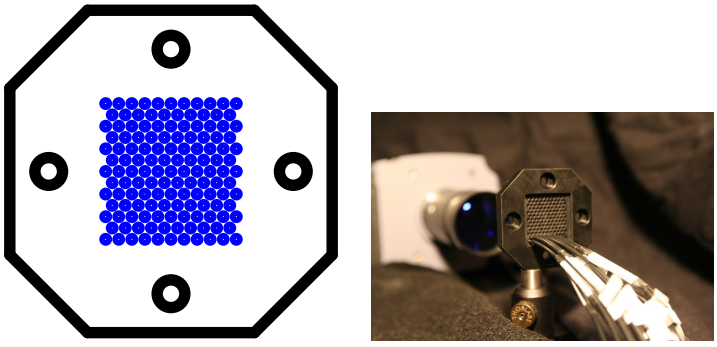

Figure 6.13: CW detector optics for GenIII system. (left) Diagram of CW Detection fiber bundle mount. (right) Fiber mount in use, coupling ~20 of 128 possible fibers to the CCD.

Figure 6.14: Photos of the mobile opto-electronics system for GenIII. Of special note are the CW CCD (Andor iKon, visible in upper left of right image), TD Laser Driver (Picoquant Sepia, second row in right image), Control Computer (containing the Becker and Hickl SPC-134 TCSPC cards), and shock-absorbing pneumatic wheels.

6.2 GenIII Results

6.2.1 Testing and Certification

After ∼30 minutes warm up, the CW laser intensity were stable to $< 1\%$; remaining power variations were normalized using the low power arm of a 97:3 splitter placed between the wavelength and position optical switch. The position switch exhibited similar stability. The time domain system requires ∼4 hrs. to stabilize, primarily due to jitter in the laser diode driver oscillator.

DOT image reconstruction requires both forward and inverse calculations (see Section 2.2.8). We used Finite Element Modeling (FEM) to compute the forward problem, with an optimized mesh created with TetGen (*http://tetgen.berlios.de/*). The inverse problem was solved using the Time-resolved Optical Absorption and Scattering Tomography (TOAST[85,86]) package made available by Arridge and collaborators at University College London. We chose to utilize Conjugate Gradient (CG) reconstruction as this permitted us to reconstruct more voxels (i.e. larger volumes or smaller voxels) at a lower computational cost. However, this technique is known to effectively provide a low pass spatial filter over heterogeneities (e.g., as in Corlu[244]) reducing the apparent contrast. Future work will include reconstruction with the more computationally intensive Levenberg-Marquardt (LM) method.

Simultaneous imaging with DOT and MRI also provides the opportunity to utilize the MR data in constraining the DOT reconstruction by setting spatial bounds on tissue types (e.g. so-called hard priors, as in Carpenter *et al.*[8]) or by incorporating MRI information into a reconstruction, but not assuming perfect alignment of contrasts across modalities (e.g. so-called soft priors, as in Intes *et al.*[188] and Guven *et al.*[235]).

The phantom data presented below was collected using a Siemens TIM Trio 3T clinical MR scanner and the joint optical/MR imaging platform, using clinical research imaging protocols. We constructed various phantoms from Liposyn, sodium chloride, various inks, ICG, gelatin, and water. Recipes are described in Appendix C.

We undertook a set of measurements with sealed liquid phantoms and a suspended balloon target. The background Liposyn and saline solution had optical properties of μ_a =0.04 cm^{-1} and μ_a =8 cm^{-1} at 800 nm. ICG was added to the target solution create a 4:1 optical contrast along with ∼0.5 mM MultiHance (clinical Gd-Chelate contrast agent) to create an MR contrast. A latex balloon (∼8 cc) was filled with the target solution and suspended partially in the optical field of view. Data was normalized to measurements performed on the phantom without the target balloon in place; optical reconstructions were performed using TOAST[85,86]. Figure 6.15 shows preliminary reconstructions from both modalities. Note that the optical reconstructions in Figure 6.15 do *not* utilize spatially dependent regularization as this has not yet been implemented in the current incarnation of TOAST.

We also produced a pair of semi-rigid gelatin phantoms, ∼16x16x6.3 cm, with μ_a =0.04 cm^{-1} and μ_a

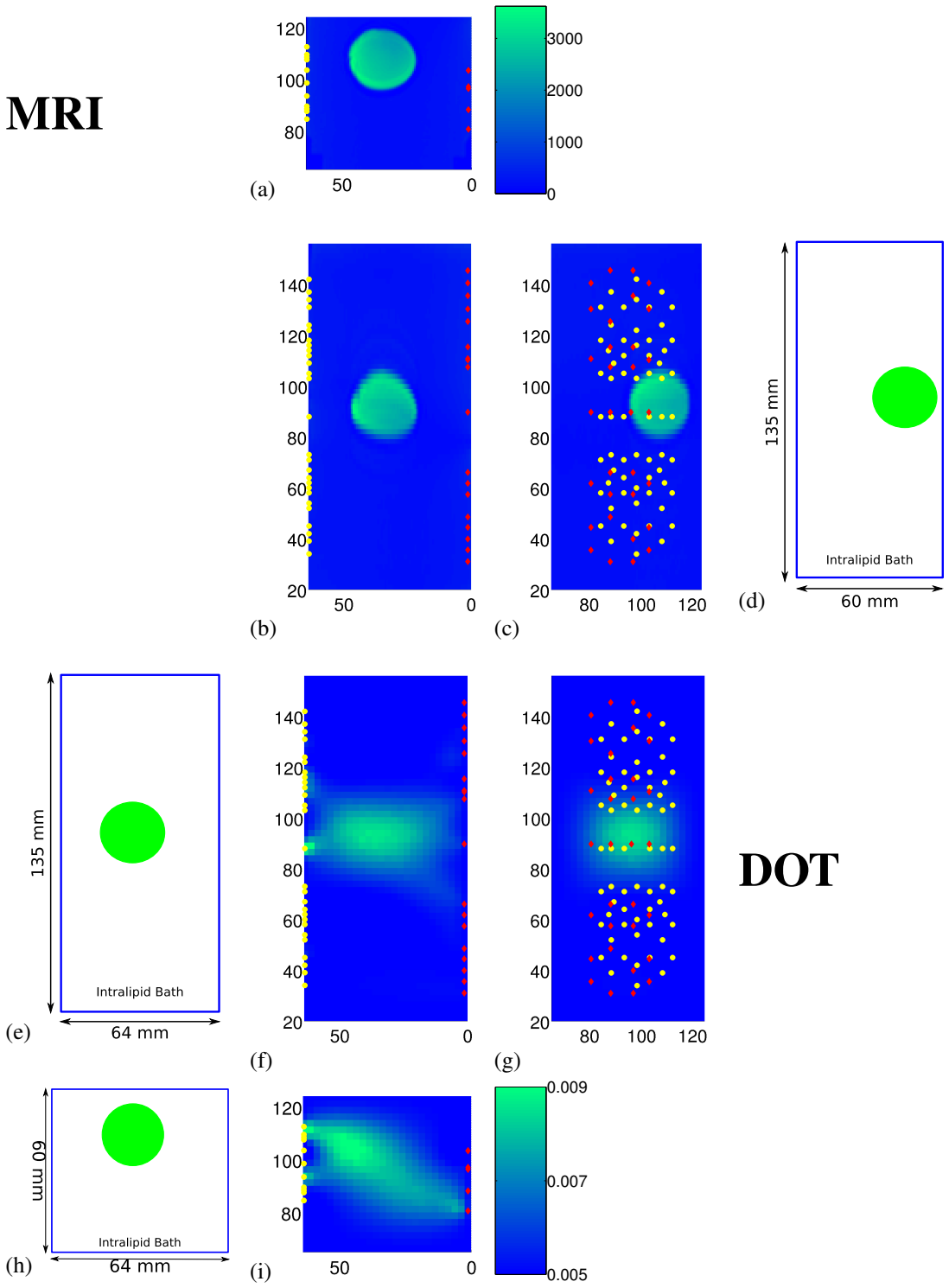

Figure 6.15: GenIII phantom imaging: Slices through the target center in a 3D reconstruction of a multi-modality phantom from MR (a,b,c) and DOT (f,g,i) imaging; (d,e,h) show schematics of the phantom geometry. Sources (red diamonds) and Detectors (yellow circles) are marked in all images. All dimensions are in mm. MRI is 3D T_1-weighted spoiled gradient echo imaging with fat saturation. (a,h,i) are axial, (b,e,f) are coronal, (c,d,g) are sagittal slices. See text for details.

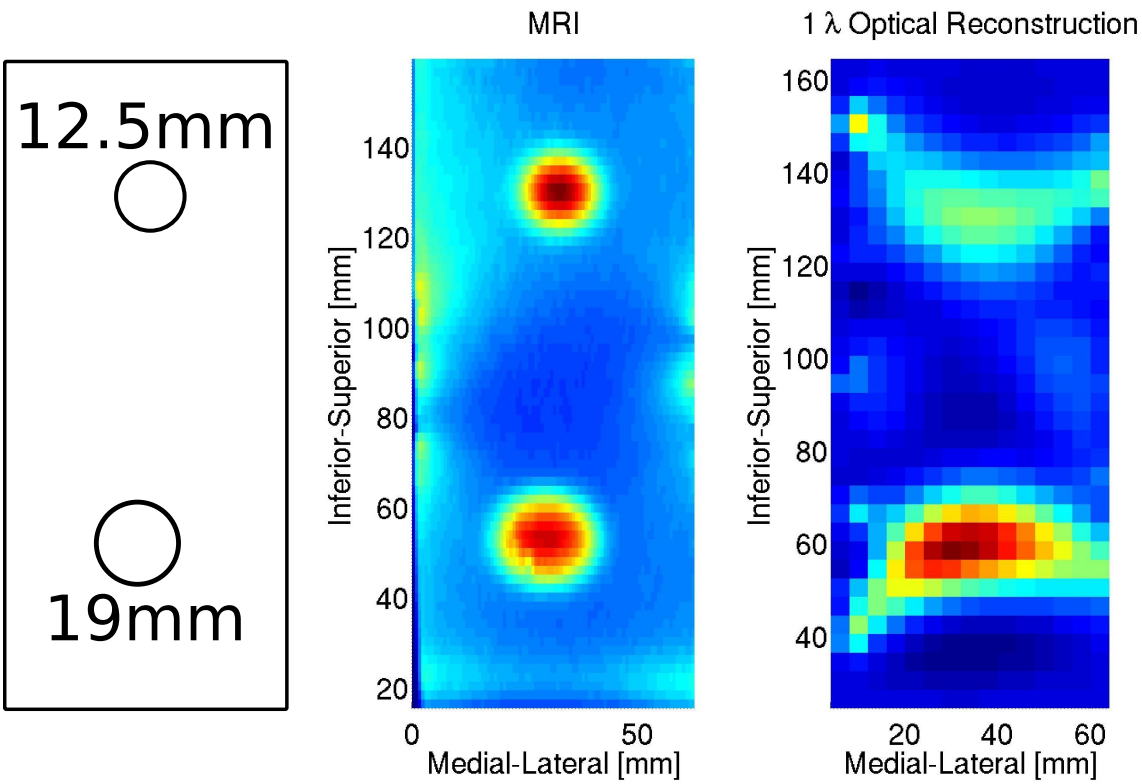

Figure 6.16: Example phantom reconstructions from the GenIII system. (left) Phantom Schematic. (center) 3D T_1-weighted spoiled gradient echo imaging with fat saturation; slice through a gelatin-saline phantom with Gd chelate (0.5 mM MultiHance) in targets. (right) Optical reconstruction using TOAST (see text). Optical contrast is 4:1; background does not contain any MultiHance MR contrast agent.

=8 cm^{-1}, at 800 nm. Cylindrical inclusions were cut in one of the phantoms and filled with a gelatin mixture similar to the background, to which ICG to create a 4:1 optical contrast and ∼0.5 mM MultiHance for MR contrast had been added. These phantoms were reconstructed utilizing spatially dependent regularization as described in Section 2.2.8. Gelatin phantoms are convenient for measurement in the MRI suite, but are vulnerable to air bubbles and are difficult to integrate into dynamic phantoms.

The results presented above demonstrate that the GenIII system can generate DOT images during simultaneous MR data acquisition. Reconstruction and data collection are not optimized however. Future data sets will have more optode positions, extending over a greater vertical distance (posterior-anterior, currently ∼4 cm), additional spectral data as more laser wavelengths are added, and improved data collection protocols. Future reconstructions well benefit from our expanding spatial regularization techniques, optimized reconstruction parameters, and improved data pre-processing.

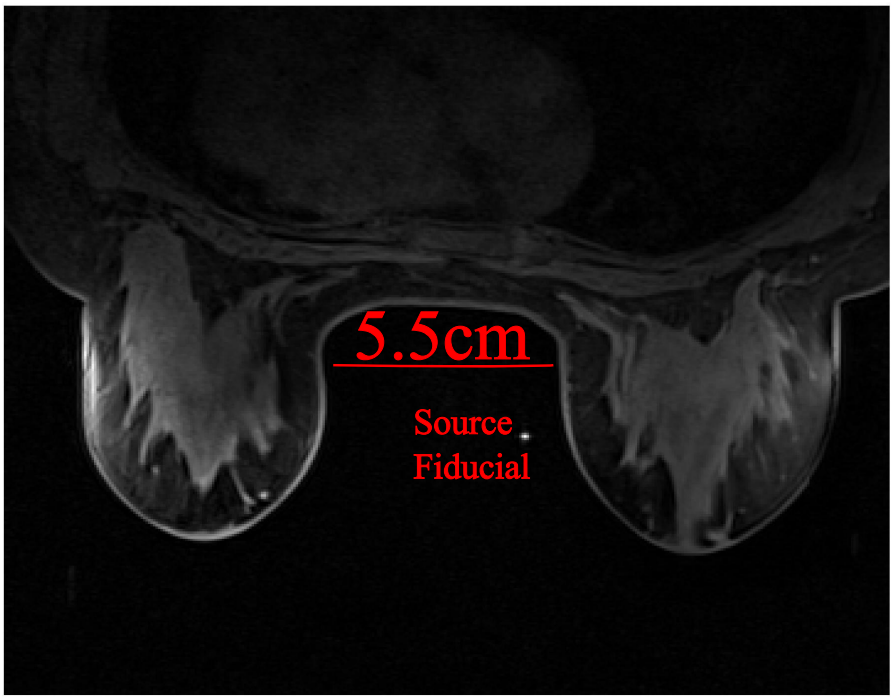

Figure 6.17: Initial human subject MR imaging with GenIII Opt/MR imaging platform. No optical data was collected during this MR certification test, but source and detector fiber modules were in place. Source modules are mounted in the medial 5 cm space; a fiducial marker on the source plate can be seen in this image. This bilateral MR scan is intended for Gd-Uptake imaging (3D T_1-weighted spoiled gradient echo imaging with fat saturation- fat produces less signal and is therefore darker).

6.2.2 Initial Human Subject Data

We are currently awaiting recruitment of our first human subject; research has been approved by the University of Pennsylvania Institutional Review Board under protocol 809792. MR only imaging from a healthy volunteer is shown in Figure 6.17. In addition to the phantom measurements discussed in Section 6.2.1, a single source-detector pair of the GenIII opto-electronic system has been utilized in the compression studies discussed in Section 8.4.

6.3 Future Work with the GenIII system

Microvascular blood flow can be measured using Diffuse Correlation Spectroscopy, as discussed in Section 3.1.1. During construction of the GenIII system, we provided for the opportunity to collect DCS data

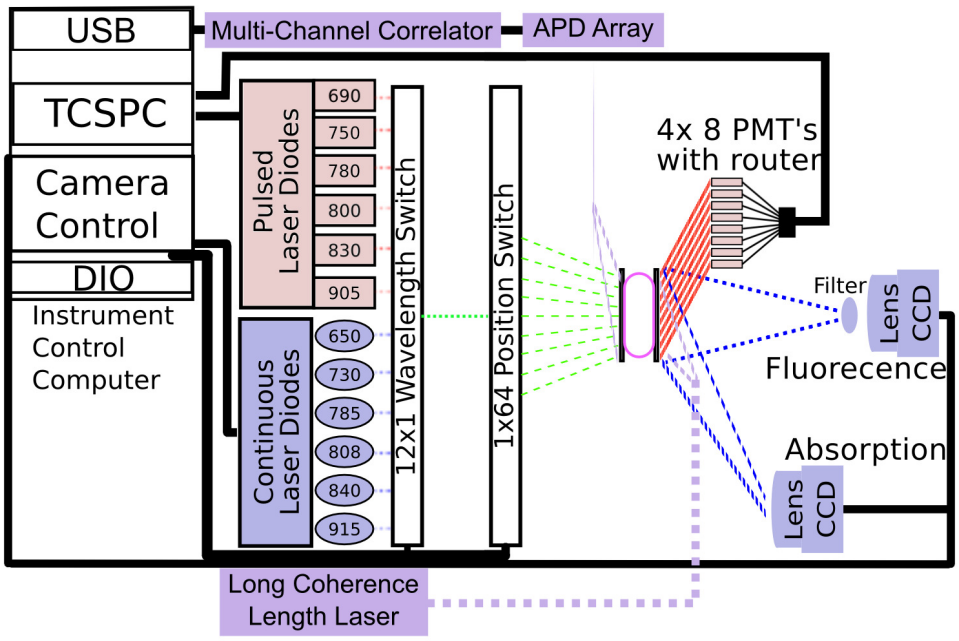

Figure 6.18: GenIII system with DCS upgrade. An additional long coherence length laser source (CrystaLaser) is coupled into the breast tissue; single mode fibers collect light from the opposite side. Due to the space constraints in the Optical/MR platform, the source and detector plates were switched for DCS compared to the DOT measurements as the single-mode DCS detector fibers are better able to fit into the medial plates than the ∼1 mm DCS source fibers. The APD array (Perkin-Elmer) and multi-channel correlator (*correlator.com*) have already been interfaced with existing instrumentation for the compression measurements described in Section 8.4.

simultaneously with MRI with up to 20 sources and 48 detectors when the complete set of optical modules has been constructed. This large data set, especially utilizing MR images for spatial constraint of reconstruction, is potentially a significant step towards Diffuse Correlation Tomography (DCT). Such optical reconstructions of tissue blood flow are of especial interest at University of Pennsylvania as our colleagues have previously shown the feasibility of measuring blood flow in breast tissue using ASL MRI[236] (Arterial Spin Labeling). The modular nature of the GenIII system permits potential adaptation to 7T MRI (available at Hospital of the University of Pennsylvania Center for Magnetic Resonance and Optical Imaging) where ASL MRI is expected to have higher SNR. A schematic of this system is shown in Figure 6.18.

The GenIII system will allow acquisition of significantly more DOT spatial data than previously reported systems. This additional information will allow comparison of independent DOT reconstruction to MRI and enhancement of DOT reconstruction using MRI spatial information. The first allows direct validation of DOT results with clinically established contrast-enhanced MRI; the second permits exploration of

improvements to sensitivity and specificity through combined data. We will explore both of these avenues. We have previously developed a computer aided detection algorithm for stand-alone DOT data, sequentially registered with MRI[245] (see Chapter 7). Simultaneous DOT and MRI allows advancement of this work by providing near perfect co-registration of modalities and by allowing use of both DOT and MRI data in the algorithm.

6.4 Hints and Pitfalls in Combining DOT and MRI

This section informally summarizes some of the challenges associated with building a diffuse optical imaging system to function in a 3 T MRI in the hopes of easing the paths of future researchers.

Materials Choice

The high magnetic fields in an MRI preclude the use of ferrous materials. During an MR imaging session, the magnetic field of the gradient coils oscillates at radio frequencies (e.g., hydrogen imaging is conducted at 63 MHz for 1.5 T and 127 MHz for 3 T magnets). The oscillating magnetic fields will induce currents in conducting materials placed in the magnet bore. These currents can quickly heat conducting materials to hazardous levels. Furthermore, conducting materials may form current-carrying loops with portions of a subject's body, potentially resulting in burns. In addition to these safety hazards, conducting materials locally perturb the magnetic field and therefore result in artifacts in the reconstructed images.

Materials one wouldn't normally consider conducting can still have sufficient conductivity to perturb the local magnetic field. For example, many black plastics use carbon black as a pigment. Our GenII combined imaging platform was made out of white plastic. In an attempt to reduce reflection of stray light, I originally intended to make the GenIII platform out of black plastic (e.g., black Delrin). However, after testing a wide variety of available plastics, I determined that the quantity of black plastic necessary to construct the platform in its entirety would cause significant MR image artifacts. These artifacts are local: I could have chosen to use black plastic to form those portions of the platform well away from the imaging volume, but did not follow this path. I chose to use gray PVC for the entirety of the platform, including the breast compression plates. PVC is somewhat troublesome to machine, but utilizes an organic dye and does not cause image artifacts.

I note that the MR signal from small amounts of black plastic can be quite useful- the $\sim$0.1 mm thick black Delrin cladding on my optical fibers makes them visible in MR images.

I utilized nylon screws to secure the sections of the platform. These screws are delicate- one can easily strip threads or remove the screw head using a hand-held screwdriver. They will also snap, especially if sheared. This property can provide a 'mechanical fuse' or known break-point for some portions of the

platform which might be subject to high stress. Snapped off nylon screws are generally quite easy to remove by tapping an appropriately sized straight screwdriver into the screw shaft.

Glues

Certain glues give a significant MR artifact in standard clinical imaging pulse sequences. Moreover, the signal from some of these glues changes significantly with time. I strongly suggest testing glues in your particular application prior to use.

Fiducial Markers

Co-registration of DOT and MR images is a critical component of simultaneous imaging. The transformation matrix between coordinate systems must be measured for each exam. I accomplished this task by rigidly fixing fiducial markers to the fiber optic mounting plates and locating these markers in MR images. Vitamin E pills are often used clinically, as they can easily be taped onto the surface of the breast. However, they tend to be large ($\sim$1x0.5 cm), which reduces the accuracy to which they can be located, and are not suitable for rigid mounting to an optical module. The GenII system utilized $\sim$2 mm NMR tubes, cut to $\sim$2 cm long and capped, full of coper sulfate solution. I later made plastic versions of these tubes to increase durability. Despite sealed caps, the water in the copper sulfate solution evaporated over the course of $\sim$6 months and needed to be replaced. The most useful commercial fiducials I have found is the multi-modality markers from ONC Solutions (Acton, MA), which are $\sim$1 mm in diameter and $\sim$1 cm long. These metal 'beads on a string' can easily be included in one's mechanical design.

Metal Chips

Small chips of metal can be transfered to your plastic components during machining. This is especially true if you use a set of files without first giving them a thorough cleaning. Small metal chips from the file can become embedded in the plastic and produce MR image artifacts. I suggest purchasing a new set of files and using them solely for plastics.

Fiber Optic Components

The source fibers are based around 10 m flat 48 strand optical cables (Molex Inc.). The proximal ends are broken out into 48 FC connectors and attach to an optical switch. The distal ends terminate in MPT male connectors. MPT female connectors then connect $\sim$1 m break out cables terminated with plastic and ceramic LC/PC connector ferrules (e.g., Figure 6.8), which are in turn embedded in the gray PVC fiber modules. The MPT connectors have small metal parts, but we were able to remove the largest spring without damaging the functionality and the remaining metallic components are both small and embedded

in larger objects. Additionally, these components are ∼40 cm from the imaging volume. Through testing, we determined that these small pieces of metal would not in practice cause either safety issues or artifacts in the MRI. The MPT connectors allow swift disconnection of source modules attached to the cumbersome 10 m fiber optic bundle connection with the opto-electronics. This ability to disconnect the source without removing the source modules from the optical platform greatly reduces the in-magnet setup/take-down time of the platform, as the source modules can be pre-positioned and left in place when the imaging platform is removed from the MR suite.

I chose to utilize standard fiber optic terminators for all of my source fibers, rather than custom ferrules (e.g., as used in the GenI and GenII systems). This choice allows considerably more flexibility in which venders undertake to supply these fibers.

The CW detector fibers are 1 mm diameter bundles, 12 m long, terminated on the proximal end with stainless steel tubing and on the distal end with a fixed 90 degree bend and a thin cladding of black Delrin. The TD detector fibers are 3 mm diameter bundles, otherwise identical to the CW fibers.

In both source and detector modules strain relief is critically important to reducing breakage at the distal fiber tips. I find self adhesive silicone tape (red and black examples of which are visible in Figure 6.9) to be quite helpful in protecting optical fibers under the transition between loose fibers and semi-rigid spiral wrap used to protect the length of the fiber optic bundles. These spiral wraps are in turn mechanically connected to the body of the fiber optic modules and therefore prevent mechanical stress from being transmitted to the fiber-module joint. At the proximal end, the spiral wrap around each fiber optic bundle is connected to the opto-electronics rack with an elastic cord.

Tools

Beryllium copper (BeCu, copper beryllium, beryllium bronze, or spring copper) tools allow you to safely adjust your imaging platform in the MR suite.

Certain brands/colors of permanent (‘magic’) markers can cause MR artifacts when used inside imaging field of view. I suggest testing prior to making marks on a finished part.

6.5 Conclusions

The current GenIII DOT system provides the largest spatial optical data set for simultaneous DOT and MRI. When the fiber optic module design is validated through human use and additional modules are constructed, it will provide as many source-detector pairs as a number of existing stand alone DOT systems. Six wavelength TD data will provide bulk optical properties; CW absorption data will permit reconstruction of endogenous chromophores. CW fluorescence data will permit imaging of both ICG and any additional

contrast agent which becomes available over the next several years. Simultaneous collection of Diffuse Correlation Spectroscopy data with MRI may permit development of clinically useful Diffuse Correlation Tomography protocols.

Chapter 7

Statistical Approaches for Automated Tumor Localization: Towards DOT Computer Aided Detection (CAD)

7.1 Introduction

In this chapter, I will describe my work searching for multi-parameter optically-derived signatures of breast cancer. I have developed techniques to calculate a probability of malignancy in each voxel (volume element) of a DOT image, as described in a recent publication[245] and several conference presentations[246–248]. Specifically, a logistic regression model employing tissue Hb_t, StO_2, and μ_s' is used to calculate a probability of malignancy in 3D reconstructions of breast tissue in subjects drawn from a clinical study by Choe *et al.*[31]. This chapter, besides introducing the new ideas, will focus on applications of the approach for computer-aided detection of malignancies in diffuse optical tomographic images.

7.1.1 Diffuse Optics and Automated Cancer Diagnosis

While current incarnations of multi-wavelength DOT provide three-dimensional (3D) images of several physiological parameters associated with cancer metabolism and growth, unambiguous 3D maps of healthy and malignant tissue are sometimes elusive. DOT images beg for interpretation of multi-parameter data at each spatial point. DOT images also sometimes exhibit significant inter- and intra-subject variation in the absolute and relative values of these parameters. Together, these factors limit DOT image analysis to skilled practitioners. In this chapter, we introduce a novel algorithm which makes possible automated identification

of malignant and healthy tissue; this approach is based on a statistical analysis of diffuse optical data from a population of known cancers.

The requirement for skilled readers is not unique to optics; most clinical imaging technologies have similar constraints and various techniques for automated breast cancer detection and diagnosis have been explored to ameliorate this situation. Computer Aided Detection (CAD) in X-Ray mammography screening, for example, relies upon high-spatial-resolution 2D intensity projections to automatically identify tumors in images based on structural features such as spiculation and micro-calcification[249–251].

The formalism presented herein for DOT-CAD employs multi-parameter, multi-voxel, multi-subject measurements to derive a simple function which transforms DOT images of tissue chromophores and scattering into a 'probability of malignancy' tomogram. Importantly, the formalism incorporates both intra-subject spatial heterogeneity and inter-subject distributions of physiological properties derived from a population of cancer-containing breasts (i.e., the 'training set'). We ultimately extract a weighted combination of physiological parameters from the training set to define a 'Malignancy Parameter' ($\mathcal{M}$), with the weighting factors optimized to separate training-set voxels of healthy tissue from those of cancerous tissue. We then examine the utility of $\mathcal{M}$, using 3D DOT images from additional subjects (i.e., the 'test set').

7.1.2 Limitations in Current Diffuse Optical Imaging Analysis

To better appreciate the potential value of DOT-CAD, consider the typical breast cancer analysis scheme currently employed in the field. First, the lesions in each subject are identified, then tissue is divided into 'healthy' and 'lesion' regions, and then average optical properties are computed for each region. Finally, these regionally averaged optical properties and differences thereof are assessed across the population. With this approach, the spatial information from DOT images is reduced to a few numbers, e.g., one for normal tissue and one for the lesion. Such an analysis ignores the spatial heterogeneity of cancers[252–254] and healthy tissues[116].

Grand averages of DOT data across multiple studies[1] suggest that malignant lesions can be differentiated from healthy tissue by Hb_t. In recent work[31] we performed such regional averaging from DOT images, and we demonstrated that benign and malignant lesions could be separated with a univariate analysis of the ratio of mean lesion to healthy tissue Hb_t, μ_s', and an empirically derived optical index combining Hb_t, μ_s', and StO_2. For example, this work found that the benign and malignant lesions had a statistically significant *different* ratio of Hb_t region means (e.g., $\frac{<Hb_t>_{Lesion}}{<Hb_t>_{Healthy}}$).

Volume element histograms of rHb_t ($rHb_t = \frac{Hb_t}{<Hb_t>_{Healthy}}$) contain more information than distribution means, of course. Histograms of Hb_t in two subjects are shown in Figure 7.1. Figure 7.1a shows an optimal subject wherein the lesion is clearly distinguishable from healthy tissue. Figure 7.1b shows a problematic subject; here variations in the healthy region (which include possible image reconstruction artifacts) extend

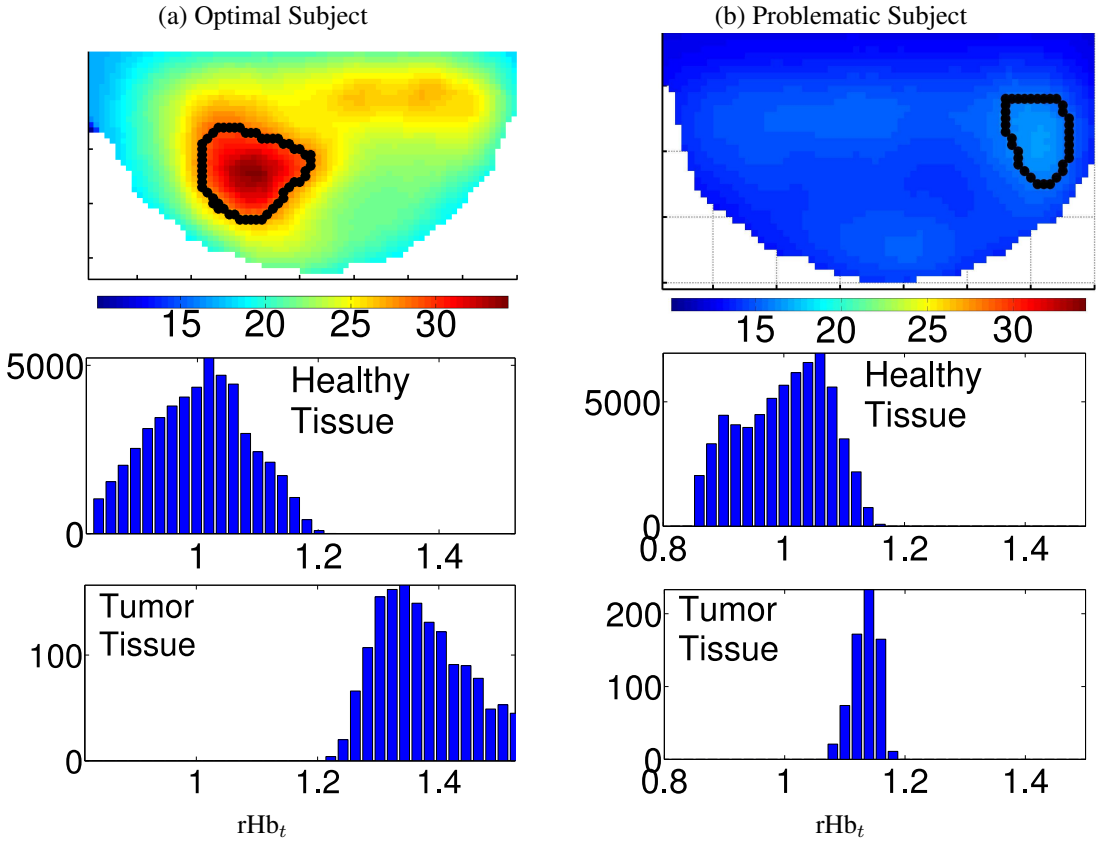

Figure 7.1: (Top row) Slices from 3D tomograms from subjects with breast cancer. Lesions are denoted by the thick black line. Histogram of rHb$_t$ for Healthy (Middle row) and Cancer (Bottom row) Voxels, segmented as shown in top row. Data are normalized as $rHb_t = \frac{Hb_t}{\langle Hb_t \rangle_H}$ for each subject. This is a typical normalization for DOT analysis, as used in our previous work[31]. The left column (a) shows a lesion clearly separated means and distinct distributions; the right column (b) shows a subject wherein the the healthy rHb$_t$ distribution overlays that of the cancer region. This normalization approach is standard in the 'typical' DOT analysis, and the example is taken from our previous work[31].

into the range of cancer tissue rHb$_t$. The first lesion (Figure 7.1a) can be readily identified with the simple normalization procedures described above and a cut-off of $rHb_t = 1.2$. The same procedure and cut-off for case two (Figure 7.1b), however, would miss the cancer completely; furthermore, adjustment of the cut-off to include the tumor causes incorrect assignment of some healthy regions. These observations suggest that a more sophisticated analysis using all available subject and spatial information is desirable. Additionally, simple thresholding in a single optical parameter ignores the potential utility of multi-parameter data and ignores possible spatially heterogeneous signatures of cancers and healthy tissues.

Thus far, a few groups have applied statistical analysis techniques to multi-parameter optical measurements, including applications to arthritic joints[255], high-risk[256] or high mammographic density[257,258] breast tissue, and to various 'endoscopic' measurements or excised tissues[259]. The data sets employed thus far,

however, have limited spatial information and orders of magnitude fewer measurements per subject than, for example, the breast tomograms utilized in the analysis to be presented herein. A few researchers have implemented automated image methods with DOT to identify lesions in a particular subject[260–262]. This per-subject analysis, however, neglects information about the common signatures of cancer across a population. Still other researchers (including our lab) have pursued hypothesis-driven multi-parameter optical metrics with DOS[74,164] and DOT[29,31]. Such metrics are dependent on underlying hypotheses, however, and are often empirically chosen combinations of equally weighted parameters. Chance *et al.*[75] have explored two-parameter signatures of breast cancer, graphically identifying malignant lesions, but the separation lines were manually selected for the specific data set (i.e., the test and training sets were identical).

Thus, previous studies fall into two groups. Some have considered spatial variation in cancers, but neglected common signatures across a population. Others have considered population signatures, but have used only regionally averaged measurements. Furthermore, few, if any, have applied statistical optimization techniques to multi-parameter optical signatures of cancer across a population. By contrast, the methods we introduce and demonstrate herein utilize data from many voxels in many subjects in order to statistically optimize a multi-parameter 'probability of malignancy'.

7.1.3 Existing Statistical Analysis of Breast Cancer DOS/DOT Data

As mentioned above in Section 3.1.1, clinical diffuse optical measurements frequently attempt to separate one group from another using endogenous contrasts or combinations thereof. In breast cancer studies, these groups are often malignant tumors from benign lesions or healthy tissue. Several groups have developed indices which combine two or more of the parameters measured through DOT/DOS to enhance the contrast between malignant lesions and normal tissue. Researchers at the University California at Irvine have developed and clinically tested a 'Tissue Optical Index' (TOI)[263] combining Hb_t, H_2O, StO_2, and lipid, and later modified to H_2O, lipid, and Hb[74]. Similarly, Choe *et al.*[31] have shown the ability to distinguish 10 benign from 41 malignant lesions (all biopsy-verified) using a CW/FD tomographic device and an 'Optical Index' (OI) combining relative values of Hb_t, StO_2, and μ_s' (for each parameter, the relative value, $rX = \frac{X}{<X>_{Healthy}}$). Choe found tumor-to-bulk contrast of $\sim$1.8 using this OI and the UCI group reported a tumor contrast of $\sim$3 using their TOI. (Note, both approaches consider equally weighted linear combinations of optical parameters or their inverses.)

Kukreti and colleagues[264] have developed 'double differential spectroscopy' in their search for the signatures of malignant tumors. This technique examines the difference between spectra measured on a lesion, spectra of healthy tissue measured on the same subject, and a linear combination of known chromophore spectra. The 'double differential spectra' output from their algorithm contains spectral features specific to

malignancy. Lilge's group[256–258] has developed 'Transillumination Breast Spectroscopy' (TIBS) in an attempt to determine the risk of future cancer development in women with high breast density. Both of these techniques rely upon spectroscopic data at many wavelengths and do not extract chromophore concentrations directly.

An empirical approach to separate lesion types that relies on plotting multi-dimensional data and then looking for clusters corresponding to lesion types was explored by Chance *et al.*[75], using manual segmentation in rHb_t and $rStO_2$. Automated cluster analysis schemes permit consideration of more dimensions and more complicated weighting schemes (e.g., work by Klose[255] on optical measurements of rheumatoid arthritis). Wang and colleagues[262] utilize a support vector machine analysis of the refractive index, μ_a, and μ_s' to identify and separate malignant from benign breast lesions, with a sensitivity of $\sim$82% and a specificity of $\sim$92%. Such techniques permit multi-dimensional weighting of parameters. Finally, Song, Pogue, and colleagues[260,261,265] have demonstrated some statistical image processing tools to determine the detectibility of a lesion in a tomographic reconstruction using contrast-to-noise considerations.

7.2 Methods

7.2.1 The Breast Cancer Data Sets

The hand-held techniques described in Section 2.3.2 do not use (or give) spatial information about the lesion, beyond the probe placement. As cancers are known to be heterogeneous[252,253] in gene expression and metabolism[254], this approach has obvious limitations. Furthermore, in our discussion of lesion mean optical properties, we have so far ignored how the lesion was localized and segmented from healthy tissue in the first place. Tomographic reconstructions for each of several chromophores in 3D present multi-parameter signatures of malignant lesions that are generally difficult to fully grasp. Additionally, DOT reconstructions sometimes have image artifacts, especially when only a single chromophore is visualized and/or when lesions are near instrument boundaries.

Our data set consists of 3D tomograms of total hemoglobin concentration (Hb_t), blood oxygen saturation (StO_2), and reduced scattering coefficient (μ_s') in 35 biopsy-confirmed cancer-bearing breasts. DOT images from these subjects were collected with a parallel plate optical imaging system described in previous work[31]. This present data sample is somewhat smaller than that reported by Choe *et al.*[31] (total: 51) as we excluded subjects with multiple (1) or benign (10) lesions. Additionally, a few subjects with very little healthy tissue or large reconstruction artifacts in the optical field of view were excluded from both test and training sets (5). Table 7.1 contains the demographics and clinical diagnosis of the population used in this analysis.

The cancers in this analysis had an average volume of 6.7 ± 5.2 cm^3, corresponding to 841 ± 656 image voxels. The average size of the entire breast was 374 ± 231 cm^3, corresponding to $4.7 \times 10^4 \pm 2.9 \times 10^4$

#	Diagnosis	Age [yrs]	BMI [kg/m^2]	Tumor Size [cm^3]
8	IDC	44±11	27±6.2	2.9±1.2
2	DCIS	60±4.9	29±6.6	0.7±0.28
2	ILC	62±3.5	22±2	1.4±0.35
22	IDC & DCIS	49±10	28±7	1.8±0.97
1	DCIS & LCIS	39±0	19±0	5±0
35	All	49±11	27±6.5	2.1±1.2

Table 7.1: Demographic breakdown of cancers in this study. IDC: Invasive Ductal Carcinoma; DCIS: Ductal Carcinoma *In Situ*; ILC: Invasive Lobular Carcinoma; LCIS: Lobular Carcinoma *In Situ*; BMI: Body Mass Index. Numeric data are given as mean ± standard deviation. 16 subjects were pre-menopausal and 19 were post-menopausal.

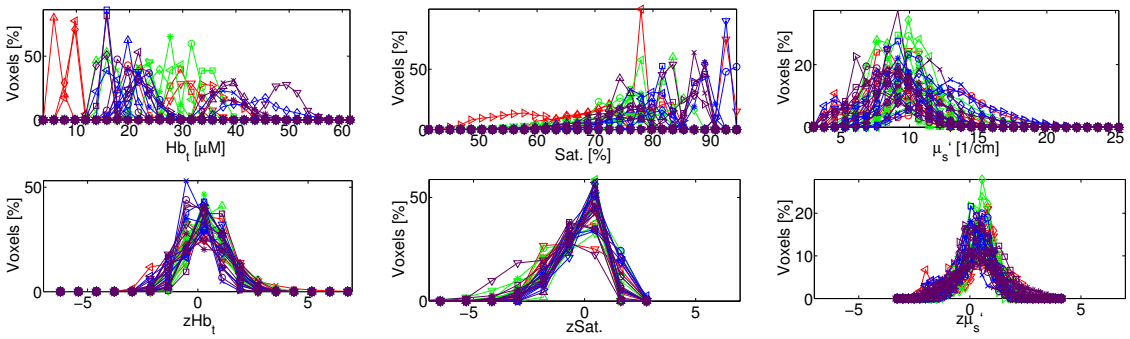

Figure 7.2: Intra-subject data normalization brings inter-subject data distributions close to a normal distribution. The top row shows, for the full population, absolute values of Hb_t, StO_2, and μ_s' [785 nm]; the bottom row shows the population distribution of Z-transformed variables after intra-subject normalization; see Eqn. 7.1 and note that each subject is normalized individually. Each trace represents the healthy region of one subject. For clarity of presentation, the vertical axis is normalized to the total number of voxels in each subject. Section 7.5 shows similar plots for Hb and HbO_2.

image voxels (mean ± standard deviation). Note, for each parameter, traditional regional averaging analysis of this data, as described above, reduces these $\sim 5 \times 10^4$ data points per subject to two numbers (cancer and healthy region averages). Figure 7.1 shows sample intra-subject spatial heterogeneity of these regions and Figure 7.2 plots the distribution of Hb_t, StO_2, and μ_s' [785nm] for the healthy regions of all subjects.

We demonstrate our new statistical analysis method with a leave-one-out cross-validation (e.g. as described by Hastie *et al.*[266]), in which 34 of our 35 subjects serve as the training set and the remaining subject provides the test data. Permuting these sets, such that each subject serves as the test set once, provides 35 training/test data combinations and enables an estimation of classification accuracy. Note, *Gold-Standard* segmentation of the DOT images into tumor and healthy regions is required for the training set and is required for the test set classification validation (i.e., to assess how well the classifier performed compared to the gold-standard).

Both training set normalization (described below) and testing of our method require 'gold standard'

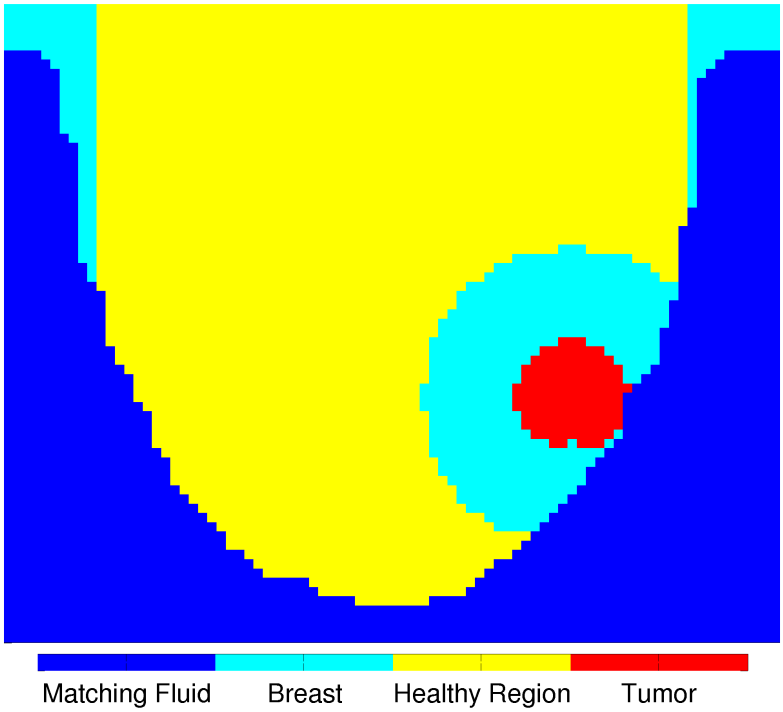

Figure 7.3: Example of masks applied to segment breast tissue for CAD; a slice through the center of the tumor is shown. The background matching fluid (blue) is first segmented from the remainder of the tissue and the chest wall removed from the data set (the chest wall is not shown in this figure). The remaining data is the breast tissue (cyan). This is further segmented into the tumor region (red). The healthy region (yellow) is defined as that breast tissue 2 cm away from the lateral sides of the image and from the tumor; voxels within 1 cm of the source and detector planes were also excluded.

spatial localization of the cancers; a full description of the procedure utilized to identify cancer regions is given by Choe *et al.*[31]. Briefly, a traditional clinical imaging method, typically MRI, was used to approximately locate each tumor. We then selected nearby regions of high optical contrast as the starting point for a region-growing algorithm to identify the spatial extent of the tumor. A 2 cm border region about the tumor (e.g. Figure 7.3) and voxels within 1 cm of the source and detector planes were excluded from the training data; the remainder of the breast is defined as healthy tissue. We exclude these boundary regions to reduce the effect of physiological changes near the tumor, errors in tumor positioning, and optode artifacts. In the training set, we assume perfect segmentation into malignant and healthy tissue. In the test set, gold standard segmentation is used only to determine the accuracy of our malignancy prediction.

7.2.2 Algorithm to Calculate Probability of Malignancy

The image analysis has two parts: first, we determine the 'probability of malignancy' function based on a population of known cancers. Then, we test the resulting function on another data set. We iterate this

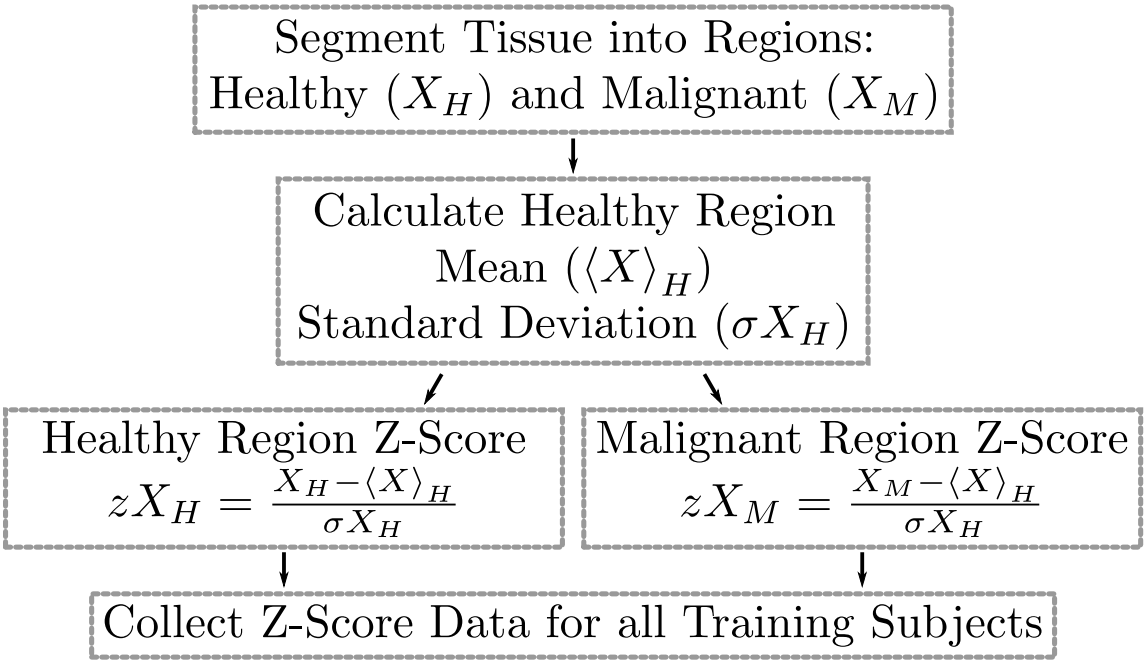

Figure 7.4: Flow chart of CAD data processing for a single training subject. Segmentation is based on clinical imaging (e.g. MRI). Note that data is normalized for each subject individually prior to combination across all members of the training set.

process, exchanging members of the training and test sets to improve the generalizability of our results.

We chose Hb_t, StO_2, and μ_s' as our fundamental physiological variables. We also tested the combination of Hb, HbO_2, and μ_s', but little difference was found (see Section 7.5).

7.2.2.1 Intra-Subject Normalization

The first step of this analysis is to normalize the tomographic data across the training sample, as distributions of optical properties vary significantly between subjects. A schematic of this process is shown in Figure 7.4; Figure 7.5 provides an overview of the normalization, analysis, and testing protocol.

We carry out this normalization procedure for each physiological parameter in both healthy and cancer tissue. To illustrate, we consider total hemoglobin concentration, Hb_t. Figure 7.2a shows reconstructed Hb_t for all healthy tissue voxels in all subjects. We see that the spread of Hb_t values is quite large, complicating use of such data across the sample. Therefore, for each subject, we compute $X = \ln[Hb_t]$, the healthy tissue mean $\langle X \rangle_H$, and the healthy tissue standard deviation σX_H. Note $\langle X \rangle_H$ and σX_H are calculated individually over the healthy regions in each subject, thereby capturing both inter- and intra-subject tissue heterogeneity. A similar set of data (i.e., $X = \ln[Hb_t]$) is obtained for malignant tissue in each subject in the training set. Together, these quantities permit calculation of the 'Z-Score' for each physiological variable

in each voxel of each subject, e.g.,

$$zHb_{t_d}^{(s,k)} = \frac{X_d^{(s,k)} - \langle X^s \rangle_H}{\sigma X_H^s} = \frac{\ln\left[Hb_{t_d}^{(s,k)}\right] - \langle \ln\left[Hb_t{}^s\right] \rangle_H}{\sigma\left[\ln\left[Hb_t{}^s\right]\right]_H}. \tag{7.1}$$

A schematic of this process for a single subject and optical property is shown in Figure 7.4. Here, the subscript index, $d = H, M$, specifies healthy (H) and malignant (M) regions; the superscript index, $s = 1$ to N_s, specifies a subject in the training set, and the superscript index, $k = 1$ to $N_v^{(s,d)}$, specifies a voxel within the healthy or malignant region in each subject. Note that the Z-Score for both the healthy and malignant regions depends on the mean and standard deviation of the corresponding tissue property in the healthy region of the same subject.

After the Z-Score procedure, the distributions of physiological parameters in each voxel across subjects in the sample are much more similar and well behaved. Figure 7.2b shows this for Hb_t in the healthy regions across 35 subjects. Note that this *intra*-subject normalization brings the *inter*-subject voxel chromophore distribution close to a zero-centered Gaussian distribution, permitting us to more sensibly combine data across multiple subjects.

A particularly attractive feature of this data normalization is the explicit inclusion in the normalized variable of the subject-dependent characteristic spatial fluctuations in each parameter via the distribution width (σX_H). Previous work in the field[31, 121, 125, 130, 163, 267–273] accounts for the wide variation in mean parameter values between subjects, but it ignores the differences in optical parameter distribution widths found in each subject's healthy tissue. With the normalization scheme described here, lesion contrast is scaled to the variation in healthy tissue. Similarly, we compute the Z-score for StO_2 and μ_s' (data shown in Figure 7.2).

For the remainder of this chapter, we will be computing and manipulating the *normalized* (i.e., Z-score) physiological variables: $zHb_{t_d}^{(s,k)}$, $zStO2_d^{(s,k)}$, and $z\mu_{sd}'^{(s,k)}$. Results using $zHb_d^{(s,k)}$, $zHbO2_d^{(s,k)}$, and $z\mu_{sd}'^{(s,k)}$, that have not been reported in the literature, are included in Section 7.5.

Since we use identical sized voxels for all subjects, we expect that each tissue type (H, M) in each subject to have a different number of voxels; i.e., $N_v^{(s,d)}$ is not constant. In order to avoid weighting the data unduly towards healthy or malignant tissue, we set $N_v^{(s,d)} = N_v = 40$. Therefore, the same number of voxels randomly selected from each region and each subject is used for the next level of our analysis. We chose $N_v = 40$ because the smallest tumors in our data set had $\sim$140 voxels and our analysis scheme depends on independent measurements from each voxel. With this choice for N_v, the median voxel separation in the 35 tumor regions was 1.2 cm. We therefore do not expect spatial correlations due to finite DOT resolution to strongly affect the results (i.e., by reducing the independence between voxels).

Drawing $N_v = 40$ voxels from the tumor and healthy regions in each of 35 subjects provides a set of 1,400 tumor and 1,400 healthy voxels defined by our gold-standard segmentation. We utilize this set

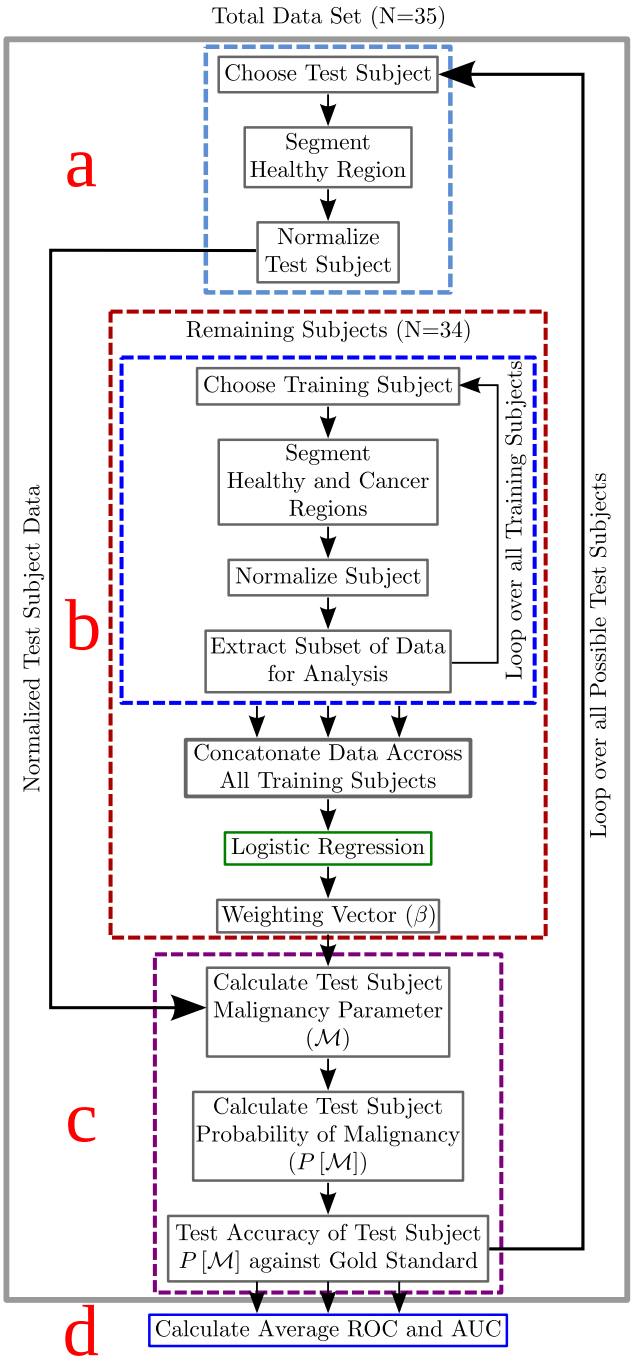

Figure 7.5: Flow chart of data analysis scheme. (a) A test subject is selected from the population and the data from this subject is normalized to an empirically chosen healthy tissue region (Section 7.2.3; i.e., the subject's Z-scores are determined). (b) Data from the remaining 34 subjects is individually normalized (Section 7.2.2.1) and a subset of the healthy and malignant region data is extracted. These data subsets are combined for all training subjects and logistic regression is used to identify the parameter weighting vector ($\boldsymbol{\beta}$) which best separates the two groups of voxels. (c) The probability of malignancy ($P[\boldsymbol{\mathcal{M}}]$) for the normalized test subject data is calculated using $\boldsymbol{\beta}$ from the training set. $P[\boldsymbol{\mathcal{M}}]$ is then tested against the clinical imaging based segmentation to calculate the classification rates (see Section 7.3). (d) The average classification rates are calculated for all test-training set combinations, using a leave-one-out protocol.

of voxels in our leave-one-out protocol, removing all voxels of the test subject from the total data set so that the remaining 1,360 voxels from each region serve as the training set for classification. The trained classification rule is then applied to the test set to predict malignancy. The entire procedure is then repeated for the other test subjects. Choosing an equal number of voxels from each region improves our estimate of the accuracy of our classification technique under the leave-one-out cross-validation protocol, which will be discussed in Section 7.3.

7.2.2.2 Training Set Analysis Procedure

The tomographic data of all subjects in the training set, i.e., data from all chromophores in N_v voxels of the healthy and malignant regions of each of N_s subjects, are combined into a single matrix. Using a logistic regression model with the known malignancy status of each voxel as the outcome and the normalized tomographic data (Z-parameters) as predictors, we fit a weight vector $\boldsymbol{\beta} = [\beta_{zHb_t}, \beta_{zStO_2}, \beta_{z\mu'_s}, \beta_0]$ and compute the vector $\boldsymbol{\mathcal{M}}_d^{(s,k)}$, whose elements define a malignancy parameter (a scalar) for each voxel in each region of each subject. For the logistic regression model, $\boldsymbol{\mathcal{M}}$ is the log odds of malignancy.

In forming $\boldsymbol{\mathcal{M}}_d^{(s,k)}$, we thus account for measurements taken across multiple subjects and measurements taken across multiple spatial locations in each subject. The right most column of 1's in the Z-matrix relates to β_0 and introduces an offset that could, in principle, include effects from additional parameters (e.g., variations in tissue fat content, age, etc.) not considered in the present analysis; see Pepe[274] and Breslow[275] for more details on this latter point.

$$\boldsymbol{\mathcal{M}}_d^{(s,k)} = \begin{bmatrix} \boldsymbol{\mathcal{M}}_H^{1,1} \\ \vdots \\ \boldsymbol{\mathcal{M}}_H^{1,N_v} \\ \vdots \\ \approx \\ \vdots \\ \boldsymbol{\mathcal{M}}_H^{N_s,1} \\ \vdots \\ \boldsymbol{\mathcal{M}}_H^{N_s,N_v} \\ \\ \boldsymbol{\mathcal{M}}_M^{1,1} \\ \vdots \\ \boldsymbol{\mathcal{M}}_M^{1,N_v} \\ \vdots \\ \approx \\ \vdots \\ \boldsymbol{\mathcal{M}}_M^{N_s,1} \\ \vdots \\ \boldsymbol{\mathcal{M}}_M^{N_s,N_v} \end{bmatrix} = \begin{bmatrix} zHb{t_H}^{1,1} & zStO{2_H}^{1,1} & z\mu'{}_{sH}^{1,1} & 1 \\ \vdots & \vdots & \vdots & \vdots \\ zHb{t_H}^{1,N_v} & zStO{2_H}^{1,N_v} & z\mu'{}_{sH}^{1,N_v} & 1 \\ \vdots & \vdots & \vdots & \vdots \\ \approx & \approx & \approx & \approx \\ \vdots & \vdots & \vdots & \vdots \\ zHb{t_H}^{N_s,1} & zStO{2_H}^{N_s,1} & z\mu'{}_{sH}^{N_s,1} & 1 \\ \vdots & \vdots & \vdots & \vdots \\ zHb{t_H}^{N_s,N_v} & zStO{2_H}^{N_s,N_v} & z\mu'{}_{sH}^{N_s,N_v} & 1 \\ \\ zHb{t_M}^{1,1} & zStO{2_M}^{1,1} & z\mu'{}_{sM}^{1,1} & 1 \\ \vdots & \vdots & \vdots & \vdots \\ zHb{t_M}^{1,N_v} & zStO{2_M}^{1,N_v} & z\mu'{}_{sM}^{1,N_v} & 1 \\ \vdots & \vdots & \vdots & \vdots \\ \approx & \approx & \approx & \approx \\ \vdots & \vdots & \vdots & \vdots \\ zHb{t_M}^{N_s,1} & zStO{2_M}^{N_s,1} & z\mu'{}_{sM}^{N_s,1} & 1 \\ \vdots & \vdots & \vdots & \vdots \\ zHb{t_M}^{N_s,N_v} & zStO{2_M}^{N_s,N_v} & z\mu'{}_{sM}^{N_s,N_v} & 1 \end{bmatrix} \begin{bmatrix} \beta_{zHb_t} \\ \beta_{zStO_2} \\ \beta_{z\mu'_s} \\ \beta_0 \end{bmatrix} \tag{7.2}$$

From $\boldsymbol{\mathcal{M}}$, we compute a probability of malignancy using the function:

$$P\left[\boldsymbol{\mathcal{M}}_d^{(s,k)}\right] = \frac{1}{1+e^{-\boldsymbol{\mathcal{M}}_d^{(s,k)}}}. \tag{7.3}$$

Our goal is to identify a weighting vector $\boldsymbol{\beta}$ which maximizes the difference in probability between voxels in healthy $\left(P\left[\boldsymbol{\mathcal{M}}_H^{(s,k)}\right]\right)$ and malignant $\left(P\left[\boldsymbol{\mathcal{M}}_M^{(s,k)}\right]\right)$ regions in our training set. In performing this logistic regression, we assume each element of $\boldsymbol{\mathcal{M}}$ is independent. $\boldsymbol{\beta}$ is optimized by minimizing the difference between $P[\boldsymbol{\mathcal{M}}]$ and the gold standard diagnosis, plotted against $\boldsymbol{\mathcal{M}}$; see McCullagh[276] for a more detailed description of logistic regression (optimization was performed with the `mnrfit` function from the Matlab©Statistics Toolbox). This approach results in a $\boldsymbol{\beta}$ such that $P\left[\boldsymbol{\mathcal{M}}_H^{(s,k)}\right] \simeq 0$ and $P\left[\boldsymbol{\mathcal{M}}_M^{(s,k)}\right] \simeq 1$. Optimized $\boldsymbol{\mathcal{M}}$ and $P[\boldsymbol{\mathcal{M}}]$ are shown in Figure 7.6 for typical training and test sets.

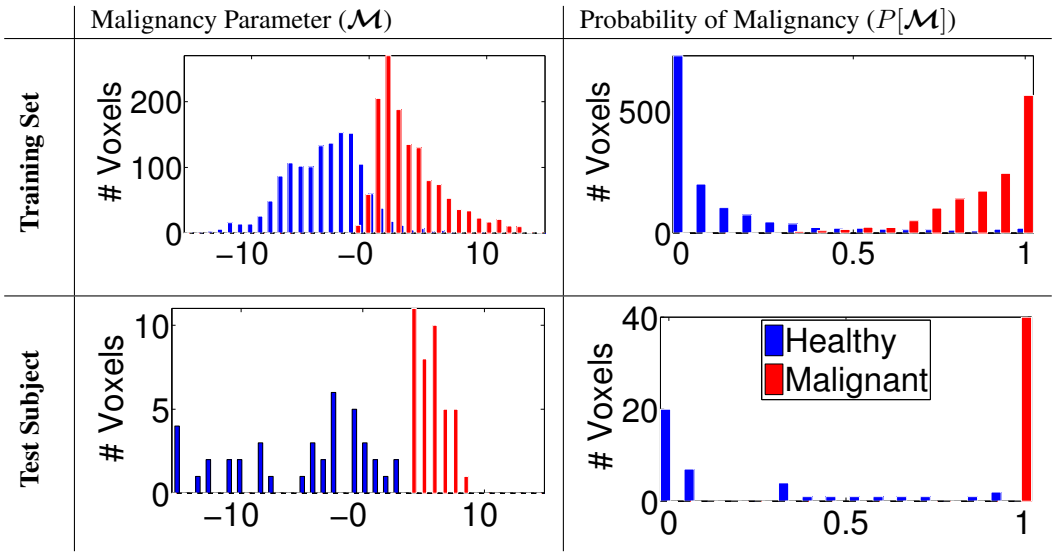

Figure 7.6: Example of training (34 subjects, top row) and test (1 subject, bottom row) set $\mathcal{M}$ and $P[\mathcal{M}]$. $N_v = 40$ voxels were randomly selected from each region in each subject, as described in Section 7.2.2.1 (i.e. 1360 voxels from each of the training healthy and tumor regions and 40 voxels from the healthy and tumor regions of the test subject). The malignant regions were defined based on clinical imaging and malignancy confirmed via biopsy. Left column: Malignancy Parameter ($\mathcal{M}$) for each subject (s), voxel in training set (k), and diagnosis $\mathcal{M}_d^{(s,k)}$. Right column: Optimized probability of malignancy $P[\mathcal{M}_d^{(s,k)}]$, as calculated on $\boldsymbol{\beta}$ derived from the training set. The test subject is also shown in Figure 7.1a; note the improved separation between the malignant and healthy regions.

7.2.3 Test Subject Normalization

The output from the logistic regression described in Section 7.2.2.2 is the parameter weighting vector, $\boldsymbol{\beta}$, which we then apply to data from an independent test subject (i.e., DOT data from the 'leftover' subject). Such an application derives a predicted 'probability of malignancy' for each voxel in the test subject.

Normalization of the test data set is slightly more complicated than that of the training data, as we must not assume knowledge of the cancer location in the test subject's breast. We therefore empirically define the healthy region as those voxels in which both Hb_t and μ_s' are less than the whole-breast mean plus 2 standard deviations. This particular choice of cutoff values was determined by the nature of the data distribution: both malignant regions and artifacts tended to skew towards larger values; Figure 7.7 and 7.8 show several examples where the upper values are greater than 3 standard deviations from the mean. Note the results turned out to be only mildly sensitive to the particular choice of 'healthy' criterion, as the cancers usually do not occupy a large fraction of the breast.

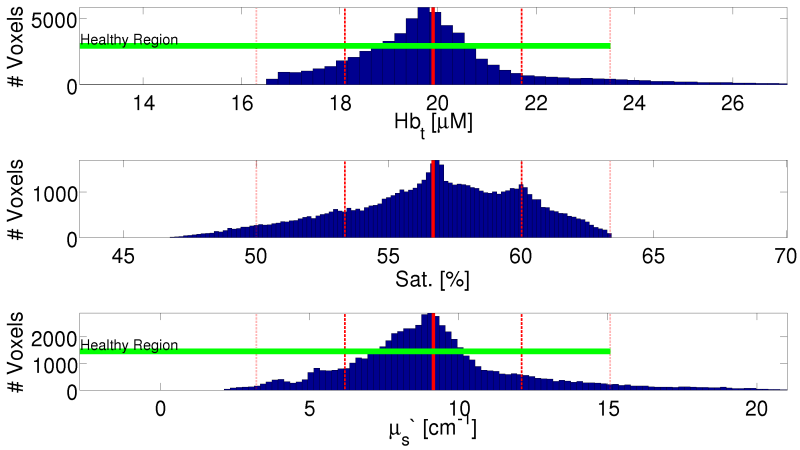

Figure 7.7: An example of distributions of tissue optical properties in a single subject. The horizontal green line designates the region designated as 'healthy' for test subject Z-score normalization. The solid red line designates the mean, the heavy dashed lines the first standard deviation from the mean, and the light dashed lines the second standard deviation from the mean.

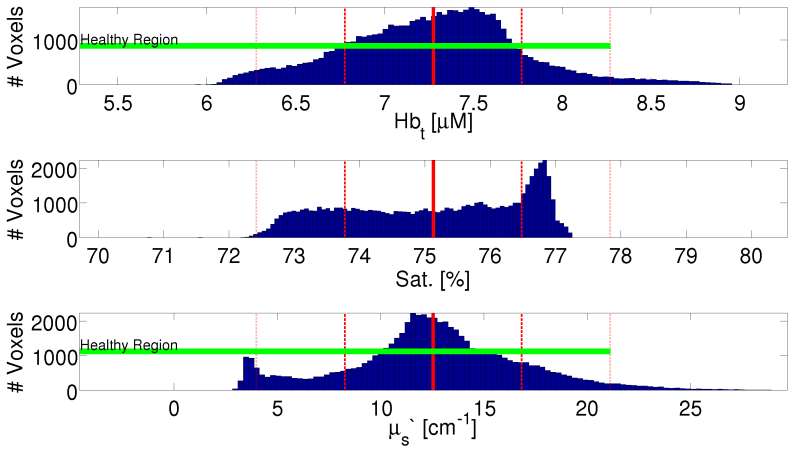

Figure 7.8: A second example of distributions of tissue optical properties in a single subject. The horizontal green line designates the region designated as 'healthy' for test subject Z-score normalization. The solid red line designates the mean, the heavy dashed lines the first standard deviation from the mean, and the light dashed lines the second standard deviation from the mean.

7.3 Identification of Malignant Regions in Diffuse Optical Tomograms

Figure 7.9 shows P vs. $\mathcal{M}$ for two subjects; example slices through the center of the cancers for the same subjects are shown for relative optical properties, $\mathcal{M}$, and $P[\mathcal{M}]$ in Figure 7.10. A probability cut-off is readily applied to the data (i.e. a horizontal line in Figure 7.9) in order to provide a concrete criterion to create spatial masks of regions that are highly suspicious for malignancy (Figure 7.10). One can then compare these masks to the gold standard malignant and healthy regions for each test subject.

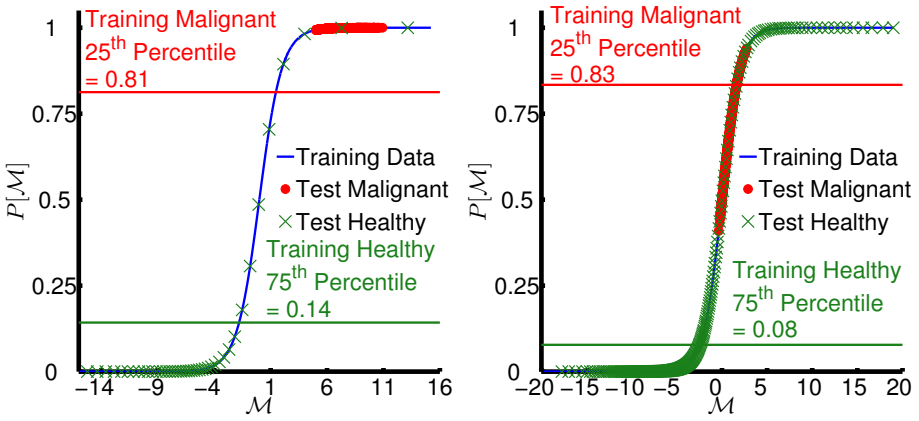

a) Invasive Carcinoma b) *In Situ* Carcinoma

Figure 7.9: Example Probability of Malignancy ($P[\mathcal{M}]$) calculated for two test subjects. The function $P[\mathcal{M}]$ (blue line) is derived from the training set, as described in Section 7.2.2.2. This function is then applied to the remaining test subject in each case; using the gold standard segmentation described in Section 7.2.1, voxels are labeled as healthy (green crosses) or malignant (red diamonds). Image slices from the same subjects are shown in Figure 7.10. For clarity, only every hundredth voxel is plotted. (a) Typical invasive cancer that shows very good separation between healthy and malignant regions. (b) Case Study: *In situ* lesion; this lesion is not as well separated from the background healthy tissue. $P[\mathcal{M}]$ for this *in situ* lesion is more heterogeneous, with a lower average than the invasive lesion and more overlap between malignant and healthy tissue.

To quantify the quality of spatial maps of $\mathcal{M}$, such as those shown in Figure 7.10, we examine the distributions of $\mathcal{M}$ and $P[\mathcal{M}]$ for $N_v = 40$ voxels in gold standard healthy and malignant regions across the entire set of test subjects; for this task we use the same randomly selected voxels as described in Section 7.2.2.1. Figure 7.11a shows a histogram of $\mathcal{M}$ drawn from test subject healthy and malignant regions in each iteration of the leave-one-out protocol; Figure 7.11b is a box plot of the $P[\mathcal{M}]$ distributions. Notice that the voxels from the tumor region are distributed narrowly about $P[\mathcal{M}] \sim 1$, but the distribution has a small tail of outliers. Similarly, the healthy region voxels are concentrated near $P[\mathcal{M}] \sim 0.1$, but the central quartiles of the distribution extend from ~0.01 to ~0.2 and the 4^{th} quartile extends to ~0.6, with outliers up

to $\sim$1. This wide distribution of values in the healthy region can also be seen in Figure 7.9; this distribution carries over into the probability of malignancy, as shown in Figure 7.12.

We next impose a probability of malignancy cut-off, P_{cut}: voxels with probability above P_{cut} are predicted to be malignant, those below P_{cut} are predicted to be healthy. Finally, we compare this prediction to the gold-standard diagnosis. For each value of P_{cut}, some test subject voxels are malignant and correctly predicted to be malignant (true positive, TP); some test subject voxels are malignant, but incorrectly predicted to be healthy (false negative, FN); some test subject voxels are healthy, but incorrectly predicted to be malignant (false positive, FP); and some test subject voxels are healthy and correctly predicted to be healthy (true negative, TN).

These quantities can be expressed as rates by dividing each of these classifications by the total number of voxels in the healthy or malignant regions. We can thus calculate true and false positive rates (True Positive Rate$= TP/(TP+FN)$, False Positive Rate$= FP/(TN+FP)$) and true and false negative rates (True Negative Rate$= TN/(TN+FP)$, True Positive Rate$= FN/(FN+TP)$) functions of P_{cut}. The Receiver Operator Characteristic (ROC) curve plots TPR against FPR; ROC curves are shown in Figure 7.13. Note, these quantities are often referred to as sensitivity (TPR) and specificity (1-FPR). Rates are averaged over 35 permutations of our training/test subjects. Average TPR, FPR, FNR, and TNR across all test subjects for several values of P_{cut} are tabulated in the insets of Figure 7.13.

For the purposes of cancer detection, FNR is critical, as this determines how many cancers are missed. With the sample used in this analysis, a probability cut-off of $P_{cut} = 0.95$ yields FNR of 11%. At the same cut off, 89% of the voxels predicted to be cancerous are correctly classified (TPR) and 6% of the voxels in the healthy region are incorrectly predicted to be cancerous (FPR) while the remaining 94% of the healthy region voxels are correctly labeled. The cut-offs can be tuned to suit particular clinical needs; see insets to Figure 7.13 for classification rates corresponding to other values of P_{cut}.

Since the Z-Score is in 'units' of standard deviation, we can directly compare the magnitudes of derived coefficients $\boldsymbol{\beta}$ to determine the relative importance of each parameter for identifying malignancy. Averaging over 35 combinations of 34 subjects in the training set gives (mean $\pm$ standard deviation), $\langle \beta_{zHb_t} \rangle = 0.83 \pm 0.06$, $\langle \beta_{zStO_2} \rangle = -0.19 \pm 0.04$, and $\langle \beta_{z\mu_s'} \rangle = 2.68 \pm 0.12$, suggesting that of the three optical parameters, difference in μ_s' offers the strongest evidence of malignancy. It should be noted that the weights are coefficients derived from a logistic regression model and can be interpreted precisely in terms of changes in the log odds of malignancy. For example, a one unit change in $z\mu_s'$ implies an estimated 2.7 fold increase in the log odds of malignancy for that voxel, or equivalently a 14.9 fold increase in the odds of malignancy. However, when $\boldsymbol{\beta}$ is calculated across all 35 subjects, we find the significance ('p-value') of each element in $\boldsymbol{\beta}$ to be < 0.005, suggesting that all three parameters should be retained in the model.

The analysis described above assumes that each 2x2x2 mm voxel in the 3D tomogram is independent of

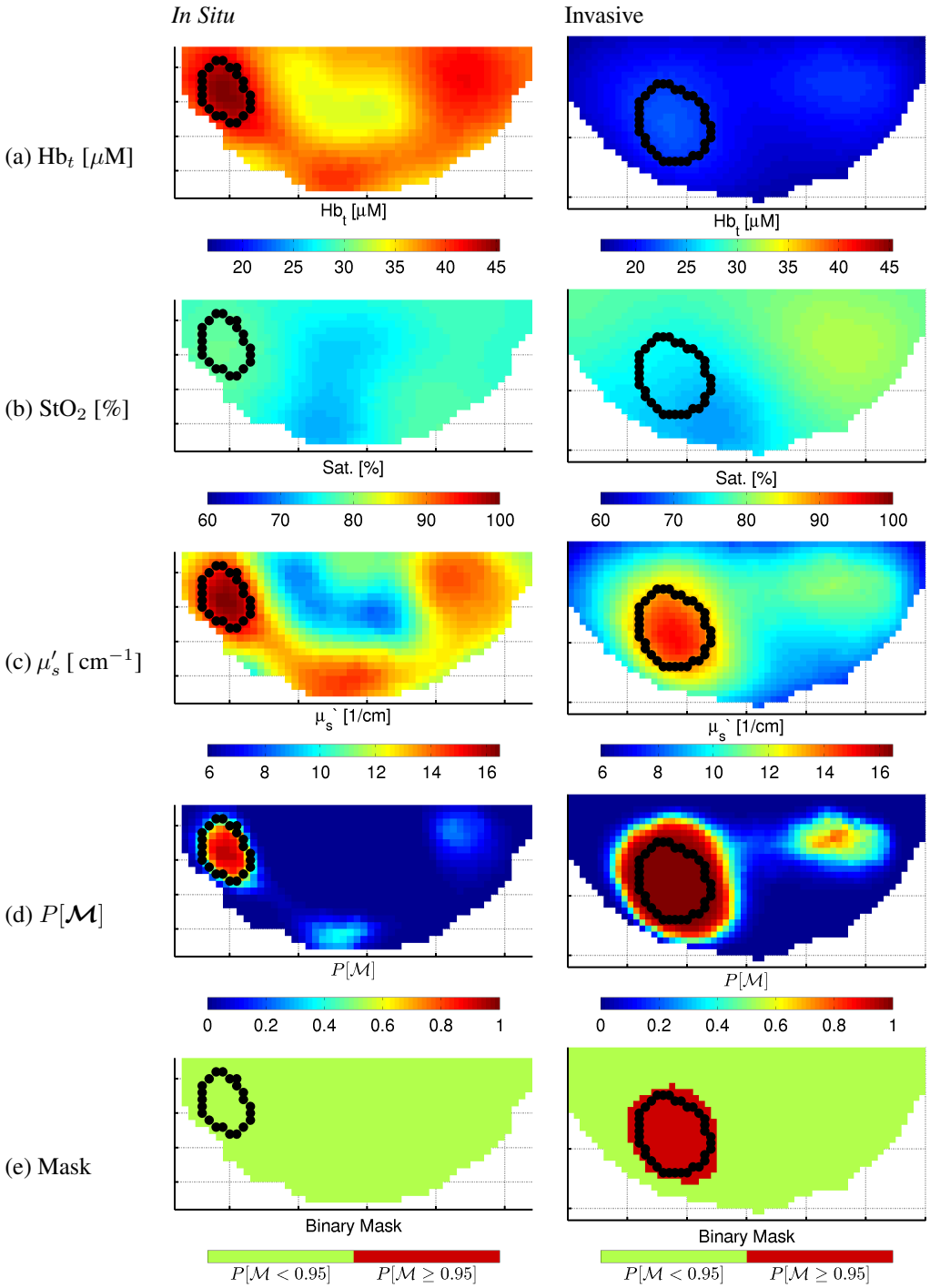

Figure 7.10: Slices from 3D images of subjects in Figure 7.9, showing total hemoglobin concentration (a, Hb$_t$), blood oxygen saturation (b, StO$_2$), reduced scattering coefficient (c, μ_s'), Probability of Malignancy (d, $P[\boldsymbol{\mathcal{M}}]$), and a binary cancer mask (e) using a cut-off of $P[\boldsymbol{\mathcal{M}}] = 0.95$. The *in situ* lesion in the left column provides an interesting case study, with the $P[\boldsymbol{\mathcal{M}}]$ falling between the malignant lesions and the healthy regions.

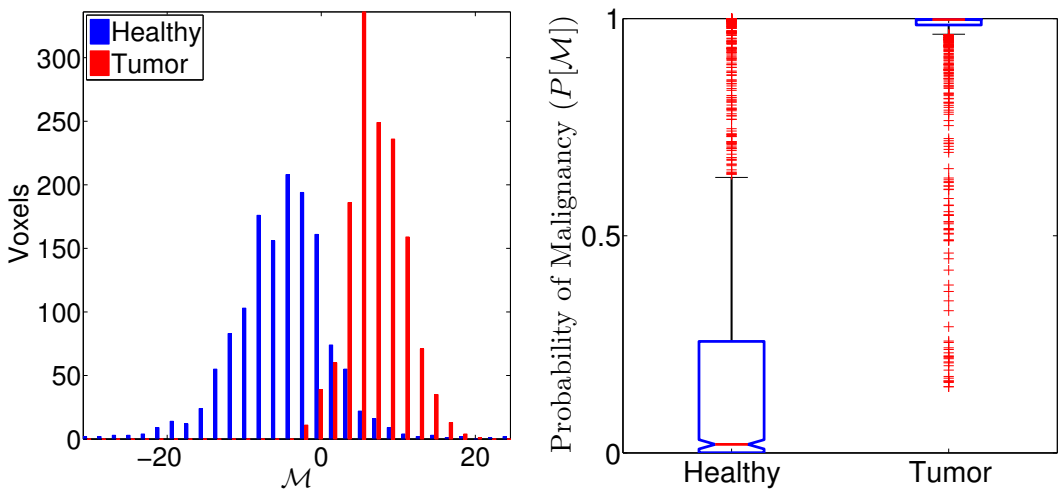

Figure 7.11: (a) Histogram of $\boldsymbol{\mathcal{M}}$ for the healthy and tumor regions of 35 test subjects, used to generate the box plot on the right. (b) Box plot of probability of malignancy ($P[\boldsymbol{\mathcal{M}}]$) of $N_v = 40$ voxels from all test subjects (red lines mark median values, 50^{th} percentile; boxes denote interquartile range, 25-75^{th} percentiles; and lines indicate outer 2 quartiles, $\sim 1^{st}$-99^{th} percentiles; and crosses mark outliers). See the insets to Figure 7.13 for a tabulation of mean classification rates at several values of P_{cut}. Median $P[\boldsymbol{\mathcal{M}}]$= 0.998 for tumor voxels and 0.019 for healthy voxels. Both of these plots show 1400 healthy and tumor voxels.

the others. However, it is known that the spatial point spread function of light transport in tissue limits DOT spatial resolution to $\sim$0.5-1 cm[90,277–279] in breast tissue at biological contrast levels. Furthermore, there are likely to be physiological correlations between different spatial locations in the breast (e.g. all voxels drawn from adipose tissue). To this end, we explored a simple model of correlated voxels, in which we identified 'clumps' of the same size as the tumor in each breast and then compared the average value of the probability of malignancy in these clumps to that of the tumors. Interestingly, we found the distribution of $P[\boldsymbol{\mathcal{M}}]$ to have fewer outliers than Figure 7.11 and values in the confusion matrix to be within $\sim\pm 5\%$ of the per-voxel values presented in the insets of Figure 7.13 at $P_{cut} = 0.95$.

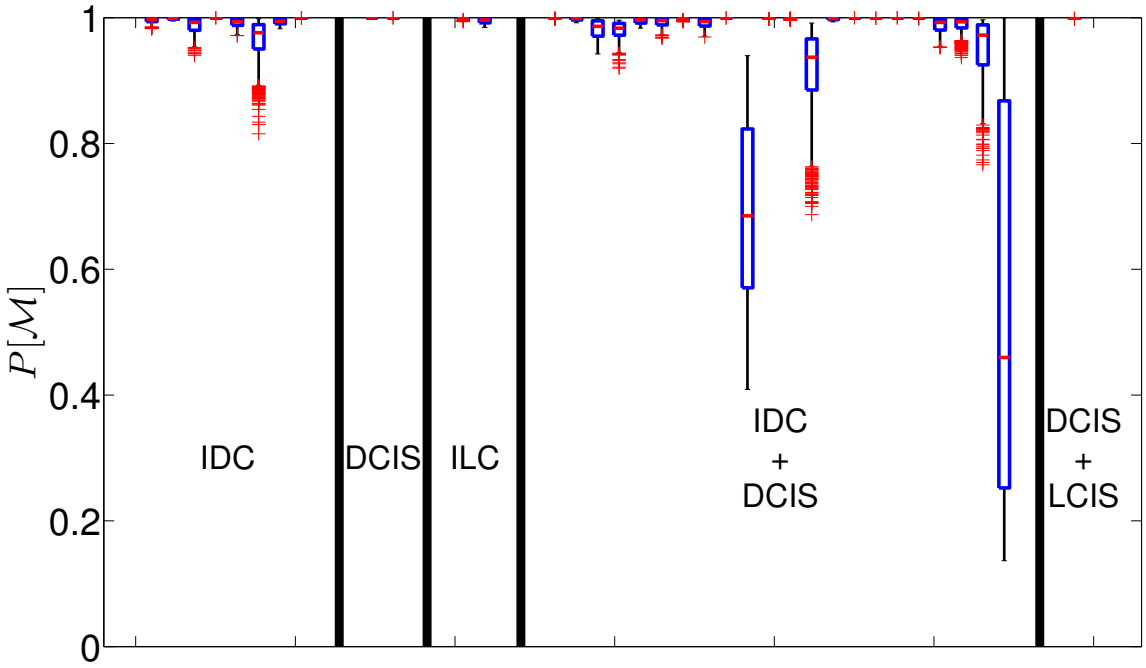

Figure 7.12: Box plot of calculated probability of malignancy for each tumor voxel in all 35 malignant cancers, separated by diagnosis. Note the significant intra- and inter- subject variation in the output probability. IDC: Invasive Ductal Carcinoma. DCIS: Ductal Carcinoma *In Situ*. ILC: Invasive Lobular Carcinoma. LCIS: Lobular Carcinoma *In Situ*.

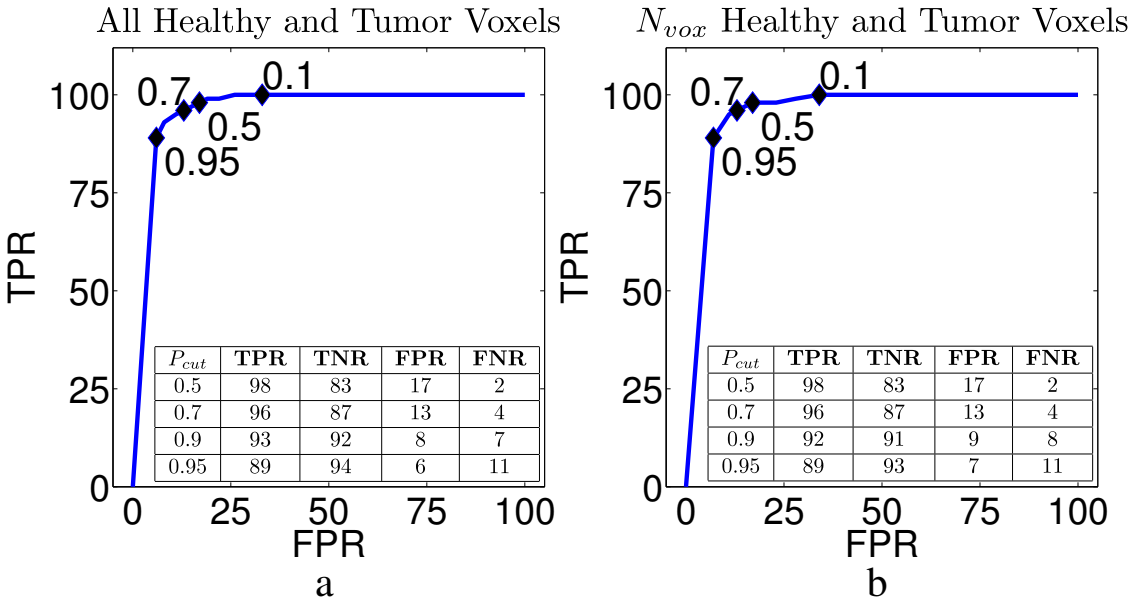

P_{cut}	TPR	TNR	FPR	FNR
0.5	98	83	17	2
0.7	96	87	13	4
0.9	93	92	8	7
0.95	89	94	6	11

P_{cut}	TPR	TNR	FPR	FNR
0.5	98	83	17	2
0.7	96	87	13	4
0.9	92	91	9	8
0.95	89	93	7	11

Figure 7.13: (a) Average ROC curve for all healthy and tumor voxels for each of 35 test subjects. (a, inset) Classification Rates calculated using all voxels from cancerous and healthy tissue, as defined by our gold standard. Black diamonds mark TPR$[P_{cut}]$ vs. FPR$[P_{cut}]$ values for P_{cut} given by the numeric labels. (b) Rates calculated only using the $N_v = 40$ training voxels from each region in each subject. (b, inset) Average Classification Rates calculated over N_v voxels. (insets) Mean True Positive Rates (TPR), False Positive Rates (FPR), False Negative Rates (FNR), and True Negative Rates (TNR) as a function of P_{cut}. Healthy voxels are defined as $P[\mathcal{M}] \leq P_{cut}$. Note, a low FNR is desirable for cancer diagnosis. Rates are averaged over all test subjects used in the leave-one-out protocol and given as percentages.

7.4 Application to Benign Lesions

As shown above, DOT-CAD can separate healthy from malignant tissue. In our limited data set, we lacked sufficient subjects to apply the analysis described above to benign lesions. However, we could examine the results when we applied the weighting vectors calculated from the 35 malignant subjects described above to 8 benign subjects in our data base. These subjects did *not* have a biopsy prior to the DOT exam. Demographics are broken down in Table 7.2; we note that with only 8 benign lesions and 4 different types of lesions, all conclusions will be tentative. However, we consider it promising that the calculated probability of malignancy for benign lesions is intermediate between malignant and healthy lesions (Figure 7.14). This trend becomes more obvious when we average the probability over the tumor and similarly sized healthy regions in each woman, as shown in Figure 7.15.

The range of voxel and regionally averaged probability of malignancy (Figure 7.16) inside individual and between types of benign lesions suggests that the binary (health/malignant) classifier used in this study is less than ideal.

The results shown in Figure 7.15 suggested we may be able to utilize the formalism developed above to produce maps of cancerous, suspicious, and healthy regions. An example of such a plot is shown in Figure 7.17, wherein we have preserved the definition of malignant tissue as those voxels with $P[\mathcal{M}] \geq 0.95$. 'Suspicious' tissue is defined as $0.5 \leq P[\mathcal{M}] < 0.95$ and healthy tissue as $P[\mathcal{M}] < 0.5$.

Note that the *in situ* lesion shown in Figure 7.17 is identified as suspicious and that a cutoff of $P[\mathcal{M}] \geq 0.5$ would identify all of the malignant lesions shown in Figure 7.15 as 'suspicious' or 'malignant' and the majority of benign lesions as 'suspicious'. The relatively simple binary (tumor/healthy) classification scheme used to generate the probability maps would identify all but one of the benign lesions shown in Figure 7.14 as 'suspicious'. We hope to improve this identification with improved classifiers in future work, in particular by implementing a trinary classification scheme (tumor/benign/healthy) on a larger data set.

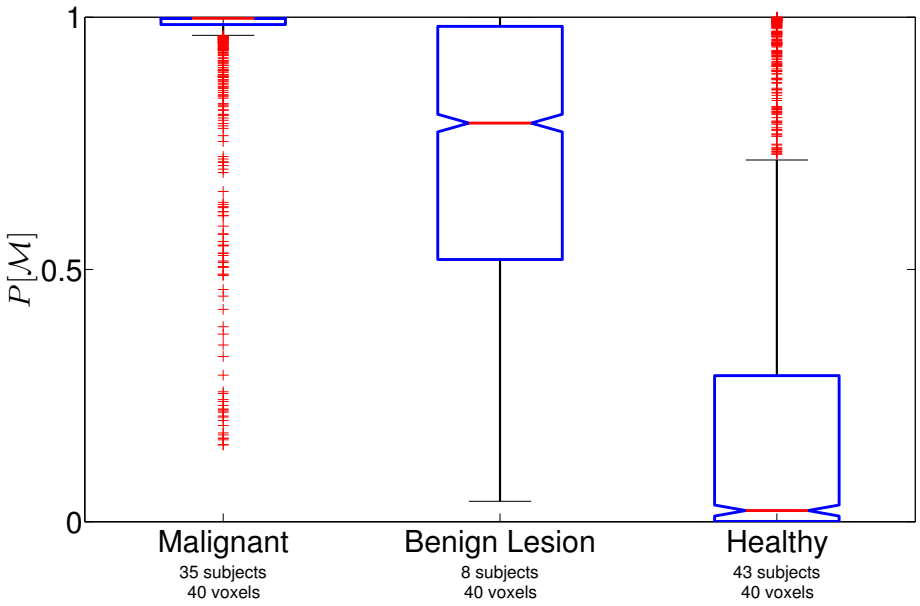

Figure 7.14: Comparison of voxel calculated probability of malignancy for cancerous, benign, and healthy regions, using weighting coefficients calculated for healthy/malignant voxels as described in the text. Note that the healthy and cancerous voxels from subjects with malignant lesions are the same as shown in Figure 7.11. Red lines mark median values, 50^{th} percentile; boxes denote interquartile range, 25-75^{th} percentiles; and lines indicate outer 2 quartiles, $\sim 1^{st}$-99^{th} percentiles; and crosses mark outliers.

#	Diagnosis	Age [yrs]	BMI [kg/m^2]	Tumor Size [cm^3]
1	LCIS	57	30.9	1.8
4	Fibroadenoma	34±12	23.8±3.7	1.7±1.2
1	Fibrocystic	47	36.7	NA
2	Cyst	43, 53	25, 21.6	0.4, 0.8
8	All	42±12.3	26.2±7.6	2.1±1.4

Table 7.2: Demographic breakdown of cancers in this study. LCIS: Lobular Carcinoma *In Situ*; BMI: Body Mass Index. Numeric data are given as mean ± standard deviation. 4 subjects were pre-menopausal and 4 were post-menopausal.

Example Regional Isosurfaces

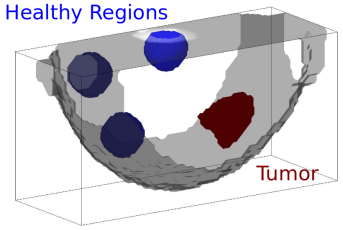

Box Plot of Regional $P[\mathcal{M}]$

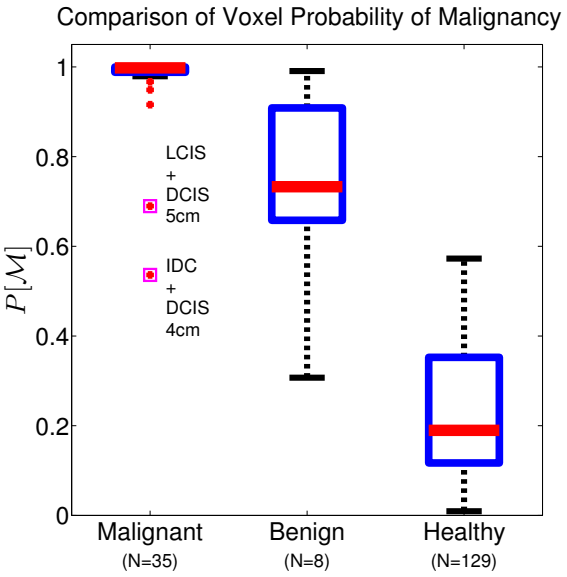

Figure 7.15: Regionally averaged comparison of probability of malignancy between cancerous, benign, and healthy regions. Weighting vectors were calculated for the malignant and healthy voxels only, using the leave-one-out protocol described above; benign lesions were weighted with the weighting vector calculated for all 35 malignant tumors. (left) Example segmentation of a malignant tumor (red), along with 3 non-overlapping regions of healthy tissue with equal volume (blue). Note, the healthy region volume is set to match the tumor volume for each subject individually. (right) Regionally averaged probability of malignancy ($P[\mathcal{M}]$) over malignant and benign lesions, compared to three healthy regions of the same volume in the healthy region of each subject's breast. Red lines mark median values, 50^{th} percentile; boxes denote interquartile range, 25-75^{th} percentiles; and lines indicate outer 2 quartiles, $\sim 1^{st}$-99^{th} percentiles; and crosses mark outliers.

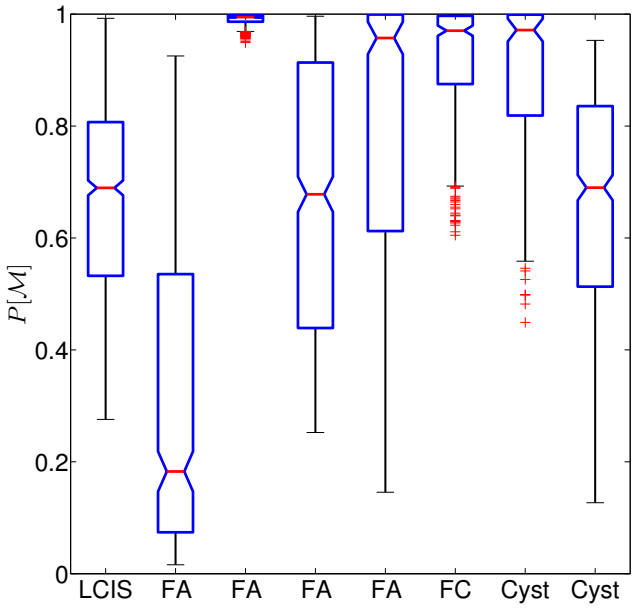

Figure 7.16: Distribution of probability of malignancy by type of benign lesion. LCIS: Lobular Carcinoma *In Situ*. FA: Fibroadenoma. FC: Fibrocystic disease. Red lines mark median values, 50^{th} percentile; boxes denote interquartile range, 25-75^{th} percentiles; and lines indicate outer 2 quartiles, $\sim 1^{st}$-99^{th} percentiles; and crosses mark outliers.

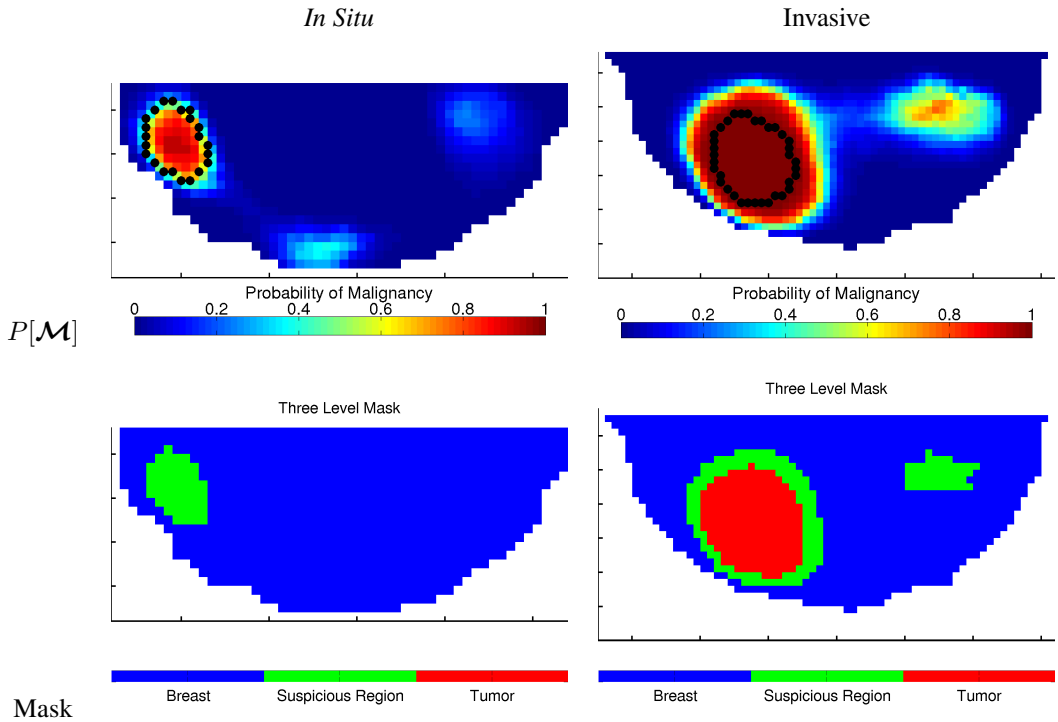

Figure 7.17: Examples of a three level mask of Probability of Malignancy segmenting healthy ($P[\mathcal{M}] < 0.5$), suspicious ($0.5 \leq P[\mathcal{M}] < 0.95$), and malignant ($0.95 \leq P[\mathcal{M}]$) regions. These are the same subjects as shown in Figure 7.10.

7.5 Statistical Analysis with Alternate Optical Data

This section includes results obtained by applying the analysis described in the preceding sections to HbO_2, Hb, and μ_s', instead of Hb_t, StO_2, and μ_s'. Each figure is referenced to the corresponding figure with its description in the analysis described above. This analysis produced overall similar results to that using Hb_t, StO_2, and μ_s', although the regionally averaged results shown in Figure 7.22 show more, but less extreme, outliers. Similarly, the voxel level analysis shown in Figure 7.19 has a slightly (0.012 vs. 0.019) lower value for $\mathcal{M}$ of healthy voxels, but more outliers than Figure 7.11.

Hb, HbO_2, and μ_s' data is shown in Figure 7.18, along with the corresponding Z-Score normalized parameters. As with the parameters shown in Figure 7.2, the intra-subject normalization decreases the inter-subject variability in parameter distributions.

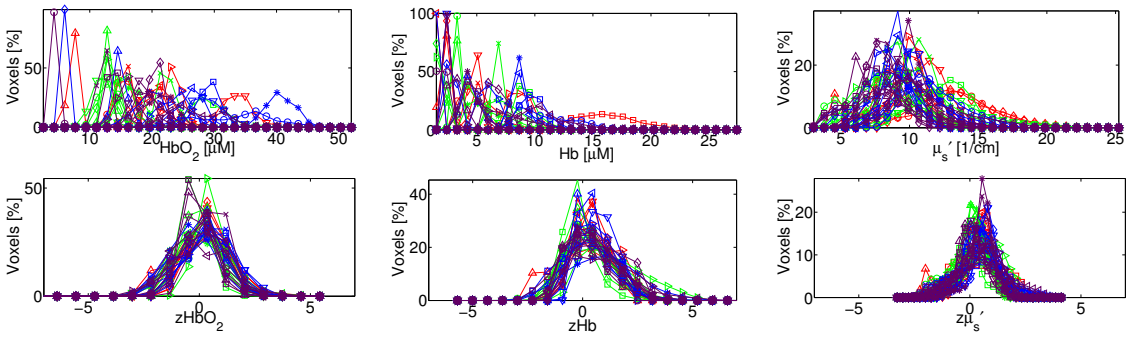

Figure 7.18: Intra-subject data normalization brings inter-subject data distributions close to a normal distribution. The top row shows, for the full population, absolute values of HbO_2, Hb, and μ_s' [785 nm]; the bottom row shows the population distribution of Z-transformed variables after intra-subject normalization; see Eqn. 7.1 and note that each subject is normalized individually. Each trace represents the healthy region of one subject. For clarity of presentation, the vertical axis is normalized to the total number of voxels in each subject.

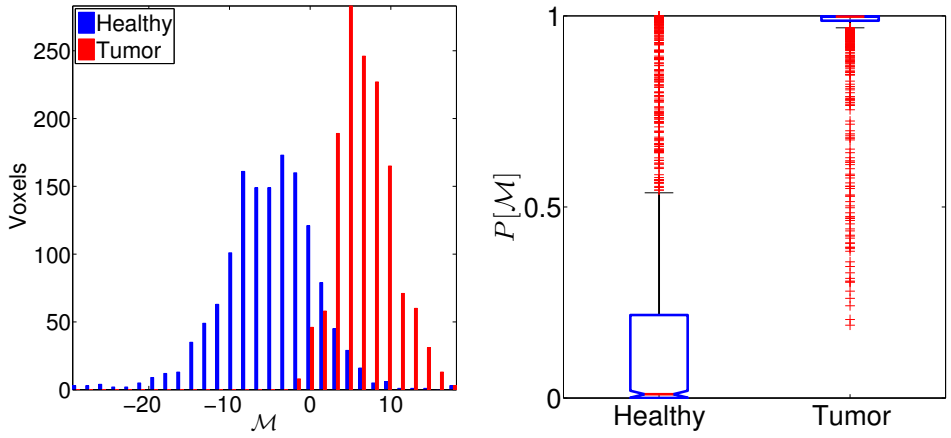

Figure 7.19: (left) Histogram of $\boldsymbol{\mathcal{M}}$ for the healthy and tumor regions of 35 test subjects, used to generate the box plot on the right. (right) Box plot of probability of malignancy ($P[\boldsymbol{\mathcal{M}}]$) of $N_v = 40$ voxels from all test subjects (bold lines mark median values, boxes denote interquartile range, dashed lines indicate outer 2 quartiles, and squares mark outliers). Median $P[\boldsymbol{\mathcal{M}}]$= 0.998 for tumor voxels and 0.012 for healthy voxels. Both of these plots show 1400 healthy and tumor voxels. Analysis using Hb_t, StO_2, and μ_s' is shown in Figure 7.11. Red lines mark median values, 50^{th} percentile; boxes denote interquartile range, 25-75^{th} percentiles; and lines indicate outer 2 quartiles, $\sim 1^{st}$-99^{th} percentiles; and crosses mark outliers.

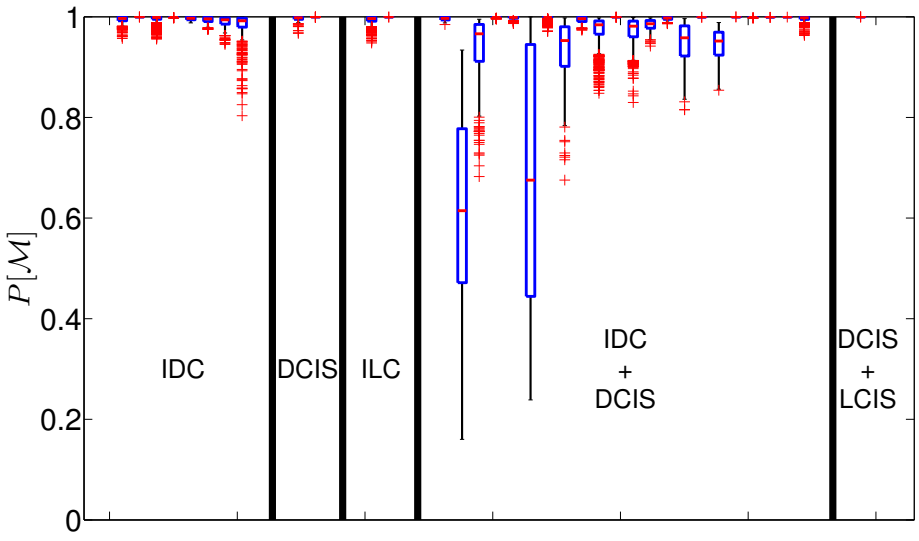

Figure 7.20: Box plot of calculated probability of malignancy for each tumor voxel in all 35 malignant cancers, separated by diagnosis. Note the significant intra- and inter- subject variation in the output probability. IDC: Invasive Ductal Carcinoma. DCIS: Ductal Carcinoma *in situ*. ILC: Invasive Lobular Carcinoma. Analysis using Hb_t, StO_2, and μ_s' is shown in Figure 7.12. Red lines mark median values, 50^{th} percentile; boxes denote interquartile range, 25-75^{th} percentiles; and lines indicate outer 2 quartiles, $\sim 1^{st}$-99^{th} percentiles; and crosses mark outliers.

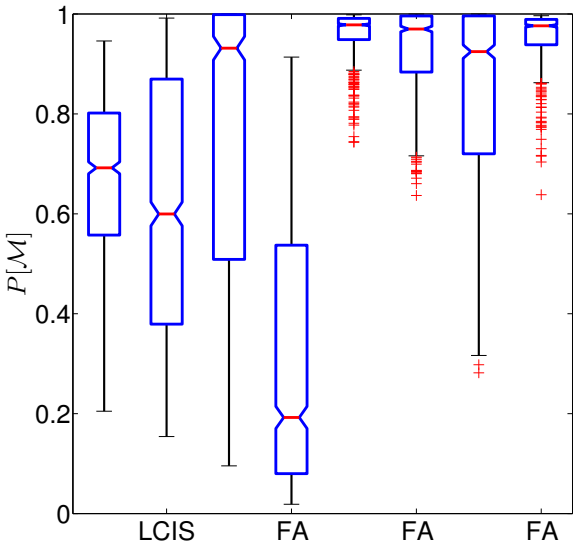

Figure 7.21: Distribution of probability of malignancy by type of benign lesion. LCIS: Lobular Carcinoma *In Situ*. FA: Fibroadenoma. FC: Fibrocystic disease. Analysis using Hb_t, StO_2, and μ_s' is shown in Figure 7.14. Red lines mark median values, 50^{th} percentile; boxes denote interquartile range, 25-75th percentiles; and lines indicate outer 2 quartiles, $\sim 1^{st}$-99^{th} percentiles; and crosses mark outliers.

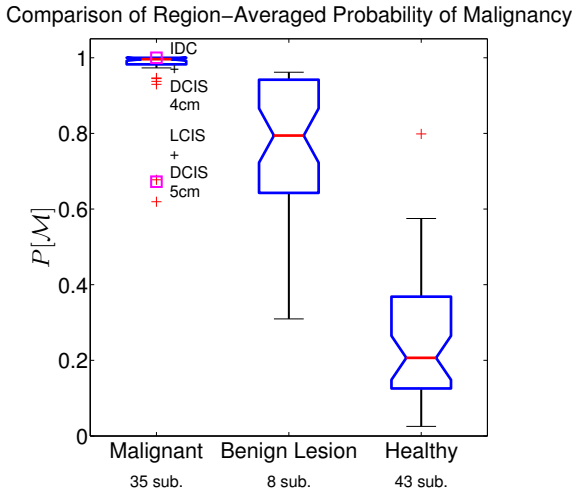

Figure 7.22: Regionally averaged comparison of probability of malignancy between cancerous, benign, and healthy regions. Weighting vectors were calculated for the malignant and healthy voxels only, using the leave-one-out protocol described above; benign lesions were weighted with the weighting vector calculated for all 35 malignant tumors. (left) Example segmentation of a malignant tumor, along with 3 non-overlapping regions of healthy tissue with equal volume. Note, the healthy region volume is set to match the tumor volume for each subject individually. (right) Regionally averaged probability of malignancy ($P[\boldsymbol{\mathcal{M}}]$) over malignant and benign lesions, compared to three healthy regions of the same volume in the healthy region of each subject's breast. Analysis using Hb_t, StO_2, and μ_s' is shown in Figure 7.22; the magenta boxes marked in this figure are the same as those in Figure 7.22. Red lines mark median values, 50^{th} percentile; boxes denote interquartile range, 25-75th percentiles; and lines indicate outer 2 quartiles, $\sim 1^{st}$-99^{th} percentiles; and crosses mark outliers.

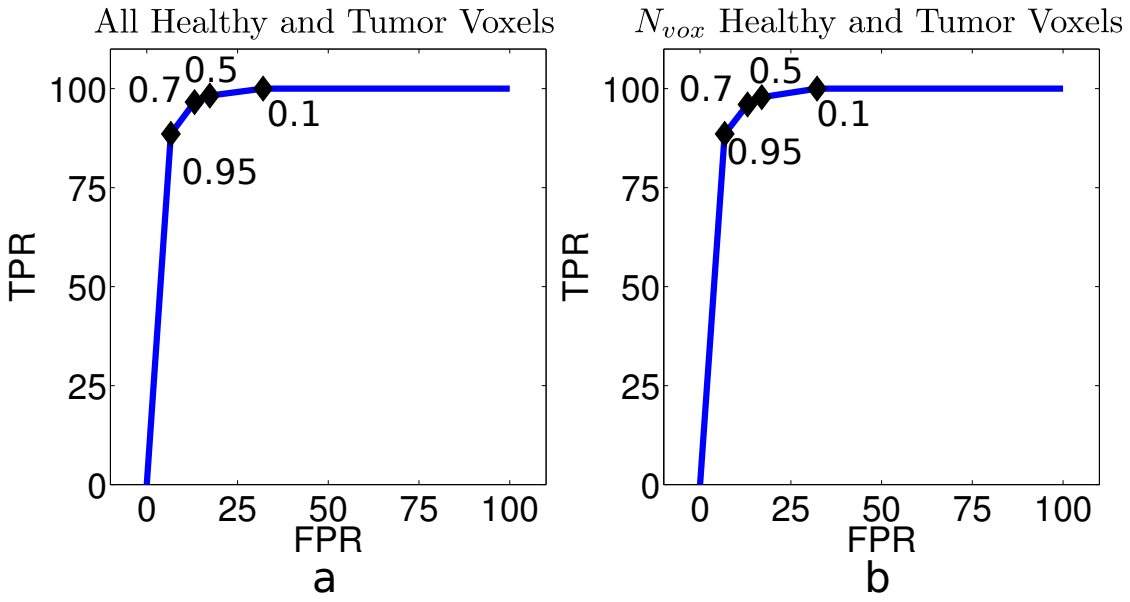

Figure 7.23: (a) Average ROC curve for all healthy and tumor voxels for each of 35 test subjects using Hb, HbO_2, and μ_s' as inputs to the classification algorithm. (a, inset) Classification Rates calculated using all voxels from cancerous and healthy tissue, as defined by our gold standard. Black diamonds mark TPR$[P_{cut}]$ vs. FPR$[P_{cut}]$ values for P_{cut} given by the numeric labels. (b) Rates calculated only using the $N_v = 40$ training voxels from each region in each subject. (b, inset) Average Classification Rates calculated over N_v voxels. Results using Hb_t, StO_2, and μ_s' are given in Figure 7.13.

7.6 Applications of Statistical Approach in Pilot Study of Chemotherapy Monitoring

Neoadjuvant chemotherapy is an important clinical technique to reduce tumor burden prior to excision for women with locally advanced breast cancer. An especially important aspect of neoadjuvant chemotherapy is the opportunity to image the primary tumor during therapy, using changes in the primary tumor as a proxy for effect on potential micro-metastases[280,281]. A critical question in any clinical therapy choice is how effective it is for a particular subject; initial results in small pilot studies[72,115,138] suggest diffuse optics may be a useful technique for early detection of therapeutic impacts on tissue metabolism, through hemodynamic contrasts.

The data presented here are a single subject pilot study, not a complete analysis of the effectiveness of DOT-CAD in chemotherapy treatment monitoring. The example subject shown here withdrew from our study after 2 DOT imaging sequences; furthermore, clinical imaging data was collected at different time points than DOT, and no MR imaging was performed. This subject 47 year old post-menopausal subject with a BMI of 22 began chemotherapy with a large mass (4x4x4.5 cm in heterogeneously dense tissue in mammograms; 3 cm in ultrasound), identified as invasive ductal carcinoma using core biopsy. DOT

imaging was performed prior to the first round of chemotherapy (9 days after core biopsy) (adriamycin doxorubicin and cytoxan cyclophosphamide; AC) and, again, after the third round. After the completion of chemotherapy, X-Ray and ultrasound imaging showed the primary tumor significantly smaller (Table 7.3) and the core biopsy diagnosis was confirmed by resection.

We utilized the same form of analysis described in Section 7.2, but replaced the population of subjects with cancer in the training set with the initial DOT image and all time points as the test set. As this calculation is performed on the same subject, we are interested primarily in changes, not the absolute value of the calculated probability of malignancy. The steps for this analysis are enumerated below.

1 Use clinical imaging to segment the pre-chemotherapy DOT images into healthy and cancerous regions for the training data.

2 Normalize the training data using the Z-score (Equation 7.1).

3 Extract a subset of the healthy and malignant data and perform logistic regression (Section 7.2.2), providing a weighting vector $\boldsymbol{\beta}$.

4 Normalize the post-chemotherapy DOT images (Section 7.2.3).

5 Apply $\boldsymbol{\beta}$ to the training and test data to produce a set of spatial probability of malignancy maps for each time point ($P[\boldsymbol{\mathcal{M}}, \boldsymbol{r}, t]$).

6 Apply a cutoff to each map to define a tumor volume, compare tumor volumes as a function of time.

Note that the pre-chemotherapy data set is used both as the training set and as the baseline for comparison of later time points. This is a point of concern, but the current analysis uses 40-100 data voxels from the entire 3D tomogram of the pre-chemotherapy time point (many thousands of voxels). These data will not be entirely independent measurements, but are certainly not identical. Similar concerns are discussed in Section 7.3.

As shown in Figure 7.25, the change in the 'high probability' (as calculated using logistic regression) volume is reduced during the course of chemotherapy, as is the tumor volume in the clinical imaging modalities (Table 7.3). Note that we do not expect direct correspondence between structural (e.g. X-Ray and Ultrasound) imaging and DOT, as DOT is much more sensitive to hemodynamic rather than structural information. However, we find these pilot results, of significant volume change in the DOT-CAD calculated tumor volume considerably in advance of the structural imaging modalities, to be indicative of the potential utility of the approach in cancer therapy.

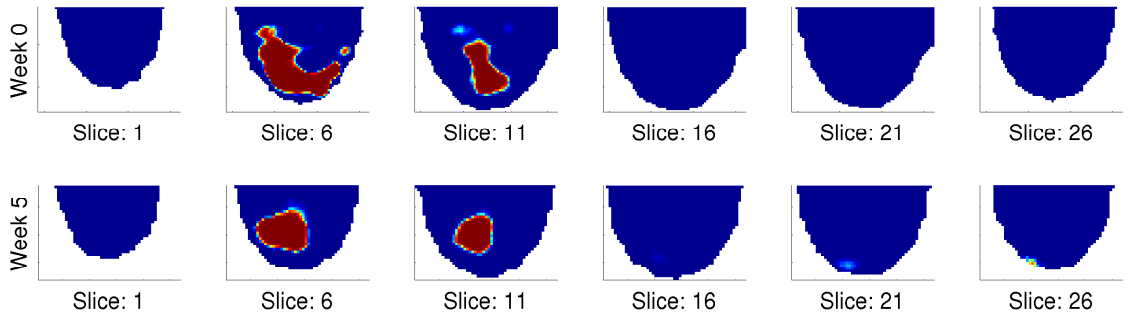

Figure 7.24: Slices of 3D probability of malignancy map, thresholded at $P[\mathcal{M}] > 0.85$ at pre- (top) and after 3 chemotherapy treatments (bottom) time points. Pre-chemotherapy measurement are used as a training set.

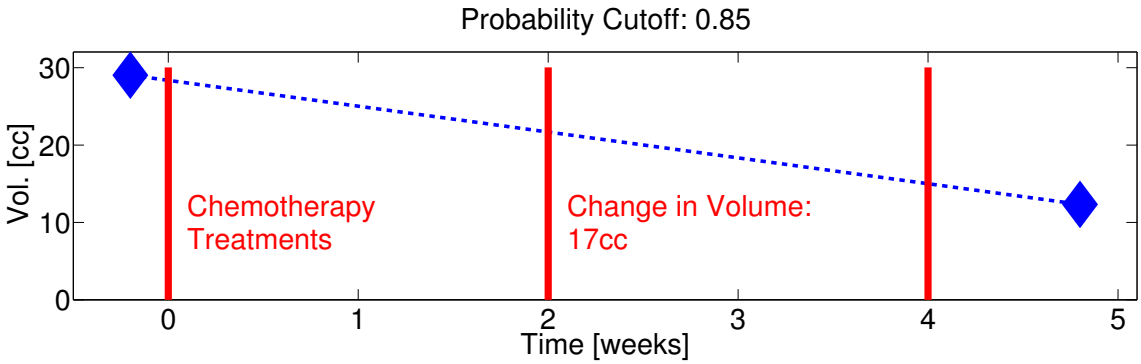

Figure 7.25: Change in volume of high Probability of Malignancy (>85%) calculated from DOT-CAD, using the pre-chemotherapy measurement as a training set, showing chemotherapy measurements. Red lines indicate chemotherapy treatments; blue diamonds indicate calculated 'high probability of malignancy' volume derived from DOT measurements described in the text.

Modality	Percentage Volume Change	Week
Ultrasound	-85%	15
X-Ray	-50%	15
DOT-CAD	-57%	5

Table 7.3: Comparison of change in tumor volume determined by DOT-CAD and clinical imaging modalities. DOT-CAD volume is calculated as those voxels with probability of malignancy ($> 85\%$), using the pre-chemotherapy measurement as a training set.

7.7 Discussion: Utility of CAD in DOT of Breast Cancer

The work described in this chapter demonstrates the potential for population-based statistical image processing of diffuse optical data. We have utilized logistic regression of three optically measured physiological parameters (Hb_t, StO_2, and μ_s') and a leave-one-out paradigm for 35 subjects to classify malignant/healthy tissue with an average true positive rate (TPR) of 89% and false positive rate (FPR) of 11%.

In Section 7.3, we noted $\left|\left\langle \beta_{z\mu_s'} \right\rangle\right| > |\langle \beta_{zHb_t} \rangle| > |\langle \beta_{zStO_2} \rangle|$, and therefore $z\mu_s'$ is the most important parameter for identification of malignancy, followed by zHb_t. The value of $\beta_{z\mu_s'}$ and β_{zHb_t} differed little between training sets. $\langle \beta_{zStO_2} \rangle$, on the other hand, was both smaller than the other coefficients and had a much larger variation between subjects ($\sim$20% vs. $\sim$5%). StO_2 is thus less important for differentiation of malignant regions in this data set, an observation consistent with our earlier results[31].

Interestingly, for the small number (3, see Table 7.1) of *in situ* cancers contained in our sample, we have noted a lower value of the malignancy parameter, $\mathcal{M}$, than for the more numerous invasive cancers (see Figure 7.9 for an example). Initial results also suggest that this type of data analysis may be useful for suppression of image artifacts, but we have not yet systematically studied the issue.

This preliminary study has several limitations and areas of potential concern, which are described and addressed in the remainder of this section.

The most significant limitation of this study is the small sample size. The small total number of subjects led us to select a 'leave-one-out' protocol to test the utility of the classification scheme. Future work with larger samples will use 'leave-Q-out', for $Q > 1$, a better approach to probing the generalizability of the method.

A more subtle issue that deserves further exploration was our assumption that each voxel used in the training is independent. As we discussed at the end of Section 7.3, we expect spatial correlations from both biological sources and reconstruction artifacts from DOT mammography. The logistic regression classification scheme assumes independent measurements; future work will utilize more sophisticated classifiers to take advantage of the biological correlation (e.g., between voxels from glandular tissue) and minimize the effects of correlation arising from DOT (e.g., resolution limits). Use of correlated measurements in the training set will result in underestimation of the variance in $\boldsymbol{\beta}$; however, our classifier does not use this variance: we only apply the point estimate of $\boldsymbol{\beta}$, which is unbiased even when the data are correlated, to the test set. Therefore, the classification rates remain valid, even through we did not explicitly take into account potential correlation between adjacent voxels. Roughly, correlation between our data points will narrow the distribution of values in $\boldsymbol{\beta}$, but will not effect $\langle \boldsymbol{\beta} \rangle$. However, this correlation in our data set is of concern for any future classifier we adopt, including those which utilize variation in $\boldsymbol{\beta}$ or similar metrics.

We also explored possible effects of DOT resolution on this analysis technique by eliminating the smallest tumors from our data set. The smallest tumor included in the sample has a total volume of 1.1 cm^3 (139 voxels). The median separation between the $N_v = 40$ randomly chosen voxels is 0.85 cm with an interquartile range (IQR) of 0.71 cm; this separation is within the expected ~0.5-1 cm resolution of the optical reconstruction technique. For comparison, in the same subject, the median separation in the $N_v = 40$ healthy tissue voxels was 4.5 cm and the IQR 3.5 cm. We then repeated the leave-one-out protocol described above on a sample of the 31 subjects with tumor volume greater than 2 cm^3 (250 voxels). We found the classification rates at $P_{cut} = 0.95$ changed very little (i.e. ~1%). Furthermore, $\boldsymbol{\beta}$ remained consistent, within our calculated error. We also tested the possibility of over-weighting small tumors through correlated measurements by extracting a fixed percentage (10%) of the total tumor voxels from each subject and using 10% of the total tumor voxels, up to a maximum of 40. These shifts in the training set selection changed the classification rates at $P_{cut} = 0.95$ by only ~2%. Alternately, we could select voxels from a sparse grid in the tissue regions to enforce a consistent or minimal voxel separation.

To test the effects of our random voxel selection, we repeated our analysis on the data sample five times, randomly selecting new training voxels with each iteration. The standard deviation of $\boldsymbol{\beta}$ extracted from the entire training set was $\sigma_{\beta_0} = 2\%$, $\sigma_{\beta_{z\mu_s'}} = 6\%$, $\sigma_{\beta_{zHb_t}} = 11\%$, and $\sigma_{\beta_{zStO_2}} = 29\%$. Recall, β_{zStO_2} had the smallest magnitude and most variation between different training sets (~20%).

Another potential source of error is the imperfect tissue segmentation we relied upon as the gold standard for assignment of each voxel as healthy or cancerous. This segmentation relies upon both non-concurrent clinical imaging (e.g. MRI) to locate the tumor and a region growing algorithm on each subject's optical tomogram to define the tumor boundaries, therefore potentially introducing discrepancies in the tissue segmentation. We excluded a 2 cm thick boundary region about each tumor from the corresponding healthy region to reduce effects of errors in spatial localization of the tumor boundary on the training healthy tissue data.

Although the analysis includes more spatial data than typically used, most of the data was still discarded, i.e. $N_v = 40 \ll 4.5 \times 10^4$ voxels drawn from the healthy region in each subject. We chose this limit for data selection in order to weight tumor and healthy regions equally and take only ~30% of voxels from the smallest tumors. This choice permits a more intuitive interpretation of $P[\boldsymbol{\mathcal{M}}]$ and improves quantification of classification accuracy. We are currently exploring other weighting schemes which permit use of all or most of the healthy tissue voxels, for example, by course graining the DOT healthy region to utilize larger voxels, thus averaging over small local variations. Additionally, no healthy subjects or benign lesions were included in the analysis presented in Section 7.3; inclusion would raise false positive rates, as the relative optical properties of some benign tumors overlapped those of cancers in our previous work[31] and the calculated probabilities of malignancy with this binary classifier for some of the benign data presented in Section 7.4

are similar to malignant lesions.

Logistic regression is a fairly simple binary classification scheme, which permits use of both continuous and classification variables. The analysis presented here did not include other classification variables (menopausal status, age, etc.), as our total sample is fairly small and classification based purely on optical data was sufficient to discriminate malignant from healthy tissue. For the same reason, we did not attempt to separate cancer types; we will apply such analysis to larger samples in future work. More sophisticated classification techniques, for example, could include more than two output categories (e.g. image artifact, malignant, benign, and healthy regions); again, sufficiently large data sets will permit us to differentiate between types of benign and malignant lesions.

7.8 Future Work: Expansions of Statistical Techniques to other Data sets and Applications

Arguably, the most interesting near-term project is to pursue the results of our chemotherapy tracking pilot study using the GenIII Optical/MR Imaging system described in Section 6. The first application of this work will be in conjunction with our collaborators' work on the ACRIN I-SPY 2 trial, measuring multiple time points on a single subject. This study will allow us to track the temporal evolution of our probability of malignancy metric during chemotherapy. Further, as we accumulate subjects in this chemotherapy tracking study, we will utilize the precisely co-registered concurrent DOT and MRI images of pre-chemotherapy time points to enhance and expand our statistical analysis data base. The precision co-registration of these data will improve our training set segmentation and therefore improve the quality of the classifier.

A second important arena for progress concerns potential of the method in the context of non-tomographic ('hand-held') data, such as that collected by Dr. Bruce Tromberg's group at University of California Irvine[74]. These studies are less demanding on subject compliance and thus frequently provide data sets with more subjects than tomographic studies, albeit with much less spatial information. Tromberg's group in particular utilizes a combination of optical properties (the Tissue Optical Index, TOI) to identify and track cancers. The method described in this chapter extracts a maximally effective malignancy index for a particular instrument/data set combination. We plan to test the generalizability of these indices across both instrumentation and different patient pools, with the goal of producing a general optical index of cancer.

Finally, future work will implement classification approaches such as support vector machines or neural networks that have demonstrated predictive capability in other applications, as in Klose[255].

7.9 Conclusion

This work introduced a new multi-subject, multi-voxel, multi-parameter statistical analysis of diffuse optical data and demonstrated its capability to identify and localize malignant tissue. This relatively simple statistical classification approach allows us to reproduce most of the results described by Choe *et al.*[31] *without* a lengthy analysis of each subject by a skilled researcher. This technique is therefore a significant step in the automated analysis of DOT images, producing an average true positive rate (TPR) of 89% and false positive rate (FPR) of 11%. Initial studies on a few benign lesions suggest the potential of increased specificity in DOT diagnosis. Intriguing results from pilot study on chemotherapy tracking has encouraged us to undertake further study and comparison with established modalities.

Together, these results are a starting point for development of diffuse optical tomography CAD algorithms. Such multi-parameter optical signatures of cancer may enhance the utility of an adjunct or standalone optical device in the clinical imaging environment.

Chapter 8

Blood Flow in Human Breast during Mammogram-like Compression

Tumor growth is often associated with angiogenesis, i.e., the formation of additional blood vessels in and near the tumor. Tumor blood vessels tend to be less well formed than those in healthy tissue, with leaky and chaotic networks[282] (see Figure 8.1). Thus, it is generally believed that blood vessels in tumors, and thus tumor blood flow, will respond differently to external perturbations than will healthy tissue. Furthermore, we expect these responses to change during the course of anti-angiogenic chemotherapy. The hemodynamics of breast tissue, therefore, potentially offer unique contrasts which have been the subject of many investigations[129,165–167,212,283]. The primary focus of the present chapter is to characterize blood flow responses of healthy breast tissue to compression. We use a mammogram-like compression, similar to that performed in clinical mammograms and current work on contrast-enhanced X-Ray tomosynthesis. The data presented here provide the first direct measurements of microvascular blood flow changes during compression, providing insight into healthy breast tissue response. Additionally, this data may provide guidance on contrast agent injection during X-Ray tomosynthesis.

X-Ray mammography is the standard of care for breast cancer screening in the United States[284] and around the world[285,286]. During this procedure, the breast is placed between two parallel plates and pressure applied. Typically, the breast is compressed to $\sim 5.5 \pm 1.5$ cm (e.g. Klein[287]). Radiographs are collected at several compression angles and these planar images are interpreted by a radiologist. Recent work in digital X-Ray Tomosynthesis (few-angle computed tomography), which often images the compressed breast before and after injection of a contrast agent[288,289], has brought forth yet another reason for understanding blood flow in breast tissue during compression. Depending on the scale of local changes in blood flow and volume, compression may significantly reduce cancer contrast; anecdotal reports suggest that increasing

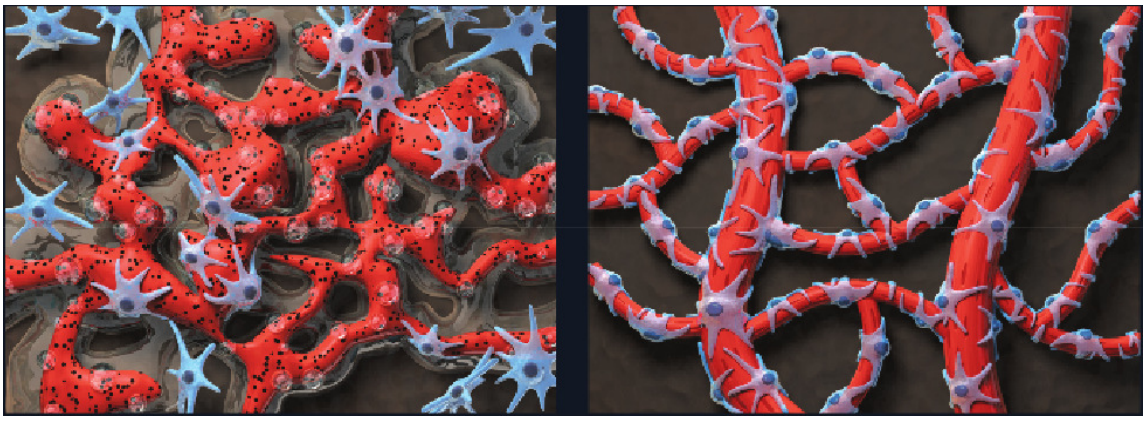

Cancerous Healthy

Figure 8.1: Cartoon of blood vessel growth (angiogenesis) in cancer compared with the normal hierarchical structure of blood vessels in healthy tissue. Note the blind ends and tortuous pathways in the cancerous tissue. From the Angiogenesis Foundation *www.angio.org/*.

breast compression prior to MR-guided biopsy can significantly reduce Gd-DTPA contrast compared to images of uncompressed tissue. As discussed in Section 2.2.7, Diffuse Correlation Spectroscopy (DCS) permits direct measurement of microvascular blood flow.

In DOT, several research groups utilize 'parallel-plate' breast imaging geometry in an axial[31,88,130,212,218], medio-lateral[5], or adjustable[96,97,132,220,290,291] orientation. In practice, this involves placing breast tissue under mild compression between two parallel plates; however, the effects of this compression are not generally considered in the analysis of the DOT results, despite various researchers' observations showing compression effects on the optical and physiological properties of breast tissue[129,165–167,212,218,283,292,293].

We have utilized our DCS instrumentation to measure blood flow in breast tissue under pressure perturbation. These measurements offer the first direct optical measurement of relative blood flow (rBF) under compression. In addition, we measured concentrations of HbO_2 and Hb by DOS. Our results show significant changes in Hb_t and rBF. In a pilot study of 15 healthy subjects, we observed average changes of 47% in Hb_t, 3% in StO_2, and 65% in rBF (Section 8.3.2) in response to a step increase in applied pressure to the breast.

We note also that these results[143–145,233] demonstrate the first *transmission* measurements of microvascular blood flow all the way through a human breast and therefore represent an important step towards Diffuse Correlation Breast *Tomography* (DCT). Volumetric imaging of microvascular blood flow with non-invasive, non-ionizing DCT is of potential interest to clinicians and researchers in diverse fields (e.g., neurology, cancer therapy response, and diabetes management). Clinical researchers at University of Pennsylvania are already applying regional measurements of rBF to brain hemodynamics and metabolism[294], stroke and brain injury monitoring [141,294–296], muscle function monitoring[70,142], cancer therapy[72], and breast tumor detection

and characterization[51].

8.1 Compression induced changes in blood flow, concentration, and saturation in the human breast

As discussed elsewhere in Section 3.2.1 the anatomical properties of the human breast (e.g. high fat and water, but low hemoglobin content and therefore low optical absorption in the NIR) permit relatively simple DOT or DOS measurements. Compression provides a perturbation to optical measurements of breast tissue, permitting differential analysis of metabolism (through StO_2) and study of vascular reactivity (through Hb_t and blood flow).

We measured these effects in a series of pilot studies, as described in Section 8.2, Section 8.3, and Section 8.4. Uniquely, our optical compression study utilized Diffuse Correlation Spectroscopy (DCS) to directly measure blood flow.

Blood flow variation under compression has not been well characterized in a healthy population: the work described below is a pilot study performing this characterization.[i]

As described in Section 3.1.1, Diffuse Correlation Spectroscopy (DCS) measures fluctuations in light intensity collected after transmission through turbid media. The blood flow indices extracted are dependent on the product of the number and speed of moving scattering bodies; a schematic is shown in Figure 2.13. Briefly, the larger the speed and number of moving scatterers, the faster the detected light field phase changes, and the more quickly the light field temporal autocorrelation function decays. DCS flow parameters are derived from the temporal decay rate of the diffuse light field/intensity autocorrelation function.

8.1.1 Optical Measurements of Breast Tissue Under Compression

Previous work on compression perturbation in the diffuse optics community[129,165–167,212,218,283,292,293] has focused mostly on absorption data (i.e. $\Delta\mu_a\ [\lambda\ ]$). These measurements directly measure ΔHb_t and ΔStO_2 due to compression, but they require modeling and physiological assumptions to extract blood flow[166,283,292]. Diffuse correlation spectroscopy[51,57,73] (DCS), on the other hand, permits *direct* measurement of blood flow.

External compression of the malleable breast can force out blood, reducing Hb_t, and even restrict blood flow into the breast; several groups[145,165–167] are currently working on optical measurements of externally applied compression. Additionally, both DOBI[ii] and ViOptix[167] are developing commercial devices using

[i] Human subject work described below was performed under University of Pennsylvania IRB protocols 803468, 700394, and 806403.

[ii] ComfortScan© *http://dobiglobal.com/dobisys1.html*, now available from *www.xinaomdt.com/en/*.

pressure modulation to affect diffuse optical signals.

Results from these studies are not entirely consistent (e.g., StO_2 were observed to vary with pressure and stay approximately consistent in studies at MGH[166] and Dartmouth[165], respectively). Discrepancies may be partially due to the test geometry (seated vs. prone), compression type (plate vs. ring), or simply the small population in each of the studies. Current diffuse optical compression studies are summarized in Table 8.1.1. The systems for measurement of the effects of breast compression presented herein are unique in combining transmission DCS with DOS and also for using an absolute TD-DOS measurement of baseline optical properties. Thus, accurate measurements of blood flow are combined with the more typically measured ΔHb_t and ΔStO_2.

	Institution	Subject Position	Data Type	Duration [s]	Peak Pressure or Load	Results
Hand-held	ViOptix[167]	Seated	CW	12	7.6 kPa	$\Delta \text{Hb}_t \sim$10-20% $\propto 1/P$
Ring	Dartmouth[165,293]	Prone	FD	$\sim$30	2 kPa	$\{\text{Hb}_t\} \propto 1/P$; small changes in scattering, StO_2, and H_2O; strong BMI effect
Parallel Plates	DOBI & Universite Paris Descartés	Standing	CW	60	0.67 and 1.3 kPa	Two-step serial compression. Dynamic model produced AUC=0.81[134].
	MGH[166,212,283]	Seated	FD	30	54 N	$\{\text{Hb}_t, \mu_s', \text{Sat}\} \propto 1/P$
	Penn Version 1	Seated	TD/DCS	$\sim$150	$\sim$1.3 kPa	See Section 8.2.
	Penn Version 2	Seated	TD/DCS/FD	$\sim$180	$<$100 N	See Section 8.3.
	Penn Version 3	Seated	TD/DCS	$\sim$60	$\sim$120 N $\sim$190 kPa	See Section 8.4.

Table 8.1: Existing work on pressure perturbation of optical signals in the breast using hand-held probes, pressure changes in the pleural cavity (Valsalva maneuver), a variable-diameter ring, and mammogram-like parallel compression plates. Optical Absorption Measurements: CW- Continuous Wave, FD- Frequency Domain, and TD- Time Domain. Optical blood flow measurements: DCS- Diffuse Correlation Spectroscopy. Note, MGH measured total load on the breast, not pressure at the skin and DOBI used a flexible membrane to support and apply pressure equally to the breast. See Table 8.2 for details on the Penn systems.

8.2 Version 1: Pilot Study of Transmission Diffuse Correlation Spectroscopy to Measure Blood Flow During Breast Compression

8.2.1 Concept of DCS-TRS Compression Measurements

Initial experiments with a 6 cm epoxy resin slab phantom (μ_a ~0.05 cm^{-1}, μ_s' ~10 cm^{-1} at 780 nm) and transmission measurements with hand-held fibers on a human volunteer, showed that the instrumentation had sufficient SNR for transmission DCS measurements in the human breast. This transmission DCS demonstration was an important finding that led us to the present work. Our design concept focused on permitting easy placement of the sensors and optodes directly against the skin in almost arbitrary positions using a mammograph-like compression scheme. During the course of our study, we developed three versions of the system. Features of these different versions are summarized in Table 8.2.

	Version 1 Pilot	Version 2 Preliminary	Version 3 Clinical
Sources	2	2	1
Wavelengths	6	6 TD, 3 FD	6 TD
Detectors	2	2	1*
Pressure Sensors	1	4	26
Total Force Gauge	No	No	Yes
Baseline $\mu_a^{(0)}$ and $\mu_s'^{(0)}$	Yes	Yes	Yes
Continuous $\Delta\mu_a$	No	Yes	Yes
Continuous Absolute μ_a and μ_s'	No	No	Yes
Number of Subjects	2	15	5
Section	8.2	8.3	8.4

Table 8.2: Comparison of systems developed for optical measurements under mammographic compression at the University of Pennsylvania. *Version 3 uses a bundle of 8 DCS detectors at each spatial positions, providing four times the signal to noise ratio; Version 3 allows for up to 2 sources and detectors, but initial data was taken with only one source and detector.

8.2.2 Version 1: TRS-DCS Combined Instrument

The DOS instrumentation for this study was the GenIIm TD system described in Section 4, with the 9 m x 5 mm detector fiber bundles replaced by 3 m x 3 mm bundles. Additionally, we utilized 2 channels in a modular eight channel DCS system developed in our lab and previously used for hand-held breast cancer studies[51,73]. This system consists of an eight channel, multi-τ correlator (correlator.com), eight photon-counting APD's (Perkin-Elmer), and a pair of long coherence length lasers (CrystaLaser); the modular system is shown in Figure 8.2.

The compression platform is based off a woodworking vise[iii]. The centers of the cast iron plates were

[iii] Pony 27090, Adjustable Clamp Company, Chicago, *http://www.adjustableclamp.com/*

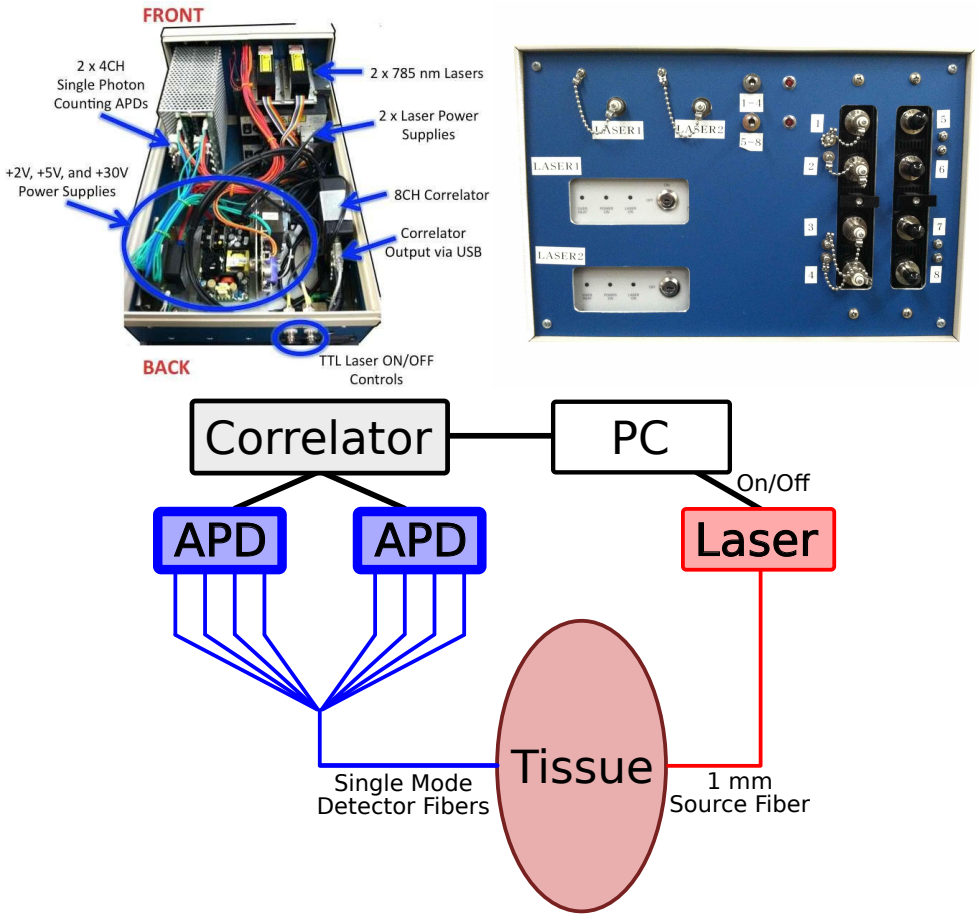

Figure 8.2: Modular DCS system: (top) photograph and (bottom) schematic, as described in the text. Photographs courtesy of Dr. Erin Buckley.

cut out and replaced with clear acrylic plates ∼0.70” thick. These acrylic plates were drilled and tapped for 9/16”-12 bolts, cut to ∼0.710”, in a quasi close packed pattern; a schematic is shown in Figure 8.3, along with a photograph of a balloon phantom in the device. (Phantoms for the compression study are described further in Appendix C.2.) Several bolts were in turn used to create fiber and pressure sensor holders; these bolt-adapters can be inserted into the grid, then optodes secured into the bolt-adapters using nylon set screws.

Subjects were seated on a rolling lab chair and secured to the lab bench with a seat-belt; pillows and other padding were placed such that the subject’s arms were fully supported.

The edges on the sides and toward the subject were cut into a radius and all holes counter-sunk to prevent scratching subjects. The platform was mounted on a laboratory bench such that the plates were horizontal with the fixed plate underneath. Sources and detectors were mounted in adapters inserted into the top and bottom plates, respectively. Additionally, a pressure sensor was placed in a similar adapter in the top plate. This sensor consisted of a ‘button load cell’ (Honeywell) held in a bolt-adapter (similar to the fiber optics)

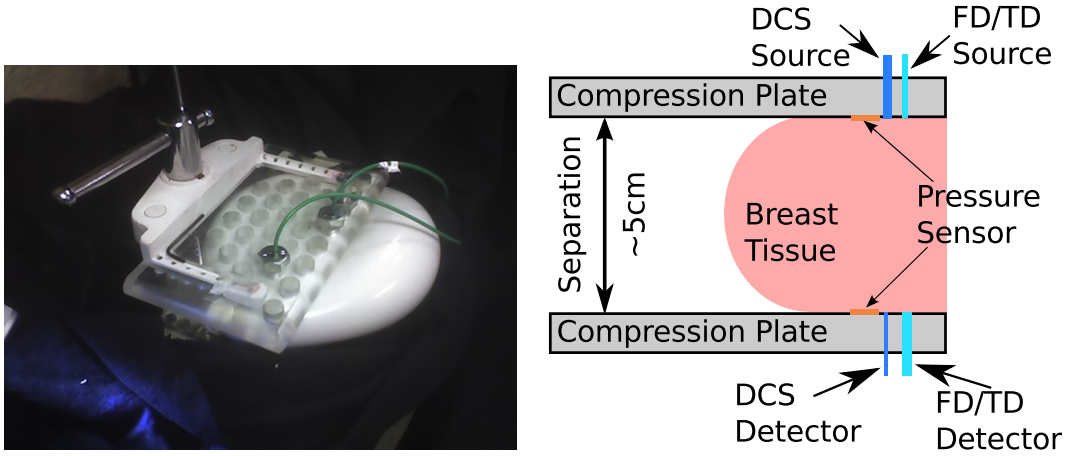

Figure 8.3: (Left) Compression plates Version 1, with balloon phantom and source fibers (green) mounted; detector fibers are hidden underneath the balloon phantom. (Right) Schematic of positioning a pair of optical fibers in compression plates for Version 1 and Version 2; as described in Section 8.5 below, Version 3 utilized a bundle of 8 DCS detector fibers and 26 pressure sensors. During all studies, the optodes were placed in the line of positions closest to the chest wall.

coupled to the tissue using an aluminum piston. Measurements of skin pressure proved problematic. Briefly, versions 1 and 2 of our compression system had significant issues with skin-sensor coupling and therefore sensor reliability. For example, as shown in Figure 8.9 for Subject 80228.1, the sensor did not record an increase in pressure during the second and third compression periods. Our phantom measurements suggest these difficulties may result from the piston becoming jammed in its track due to shear force. During data collection with version 2, we shifted to a significantly more reliable set of sensors (Tactilus® Free Form Sensors (Sensor Products Inc., Madison NJ). These flat resistive sensors enabled direct mounting on the compression plates and eliminated the coupling piston.

8.2.3 Version 1: Human Subjects Experimental Procedure

After explaining the procedure to the subject and obtaining informed consent, the subject was seated in a rolling chair and the height adjusted such that the inferior side of her breast was level with the top of the lower compression plate. The compression device was fully opened and the subject's breast placed upon the lower plate, centered on the optodes and pressure sensors. The upper compression plate was lowered until it was in light contact with the breast and all optodes were firmly in contact.

The experimental time-line for Version 1 of our compression system was dictated by our equipment limitations. The TD system used in this study lacked shutters in front of the PMTs, and therefore we were required to physically remove the TD detector fibers from their PMTs prior to collecting DCS data. Further, the DCS laser source was so much more powerful then the TD sources that even switching off the TD PMTs

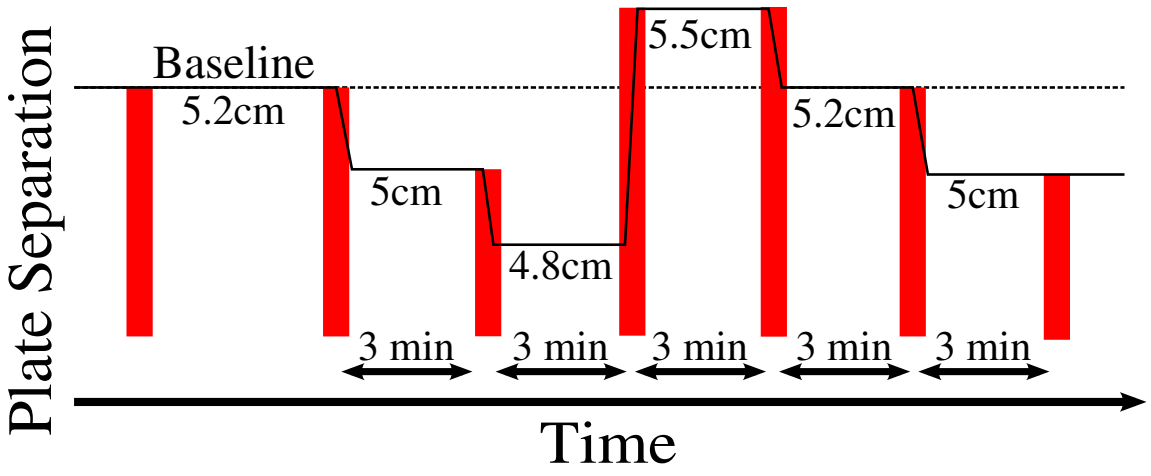

Figure 8.4: Time-line for compression study, Version 1. DCS measurements are collected continuously, *except* during TD-DOS data collection (red bars in schematic). DCS measurements are shown in Figure 8.6 and TD measurements in Figure 8.5.

during DCS measurements resulted in a significantly higher noise level in subsequent TD measurements. This restriction on rapid switching between TD-DOS and DCS measurements dictated our experimental protocol: long data collection intervals with each instrument and therefore, rather discontinuous data acquisition. We chose to alternate between TD and DCS measurements at each of several compression levels.

The long integration time ($\sim$10 s) required to obtain a reasonable SNR with the DCS system led us to restrict the DCS measurements to the static compression times in our protocol, while the TD system ($\sim$3 s integration) was used before, during, and after the periods in which we changed compression. This protocol is shown graphically in Figure 8.4; results for one subject are shown in Figure 8.5.

8.2.4 Version 1: Pilot Study Results

Our initial studies were performed on two healthy pre-menopausal female volunteers. Data from one of the volunteers was not useful: this subject had B-cup breasts and the compression instrument was unable to properly interface with her tissue. The second volunteer had D-cup breasts and fit into the compression instrument well; all results in this pilot study are from this 26 year old subject (BMI 21.5). Based on the results of our Version 1 pilot study, we biased our recruitment to women with C-cup or larger breasts in subsequent research. See Table 8.3 for a breakdown of demographics for subjects studied with Version 2 of the system.

TD measurements provided absolute values of μ_a and μ_s' for each compression step at 6 wavelengths (690, 750, 780, 808, 830, and 838 nm; see TD description in Section 4.3.2). Hb_t, StO_2, [Lipid], [H_2O], and μ_s' [λ] are computed from $\mu_a[\lambda]$; A and b are computed from $\mu_s'[\lambda]$ (see Section 3.1.1). Changes

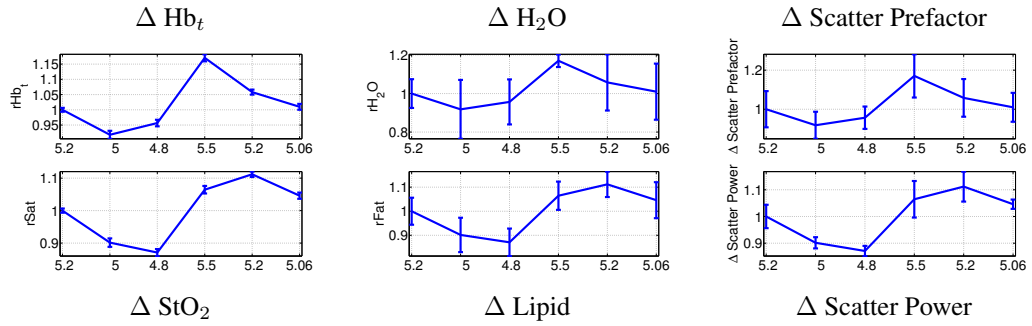

Figure 8.5: TD measurements of chromophore changes during compression of human breast tissue. Horizontal axis is the separation between compression plates in cm. See Figure 8.6 for the corresponding measurements of rBF. Data points correspond to red lines in Figure 8.6. The scatter power (b) and scatter prefactor (A) parameterize $\mu_s' = A\lambda^{-b}$ in the NIR range[140] (see Eqn. 3.5).

in these quantities from the baseline are given in Figure 8.5. Here, we observe ∼10% change in each parameter during 0.4 cm (7.5%) change in plate separation. Blood flow changed much more dramatically: Figure 8.6 shows a roughly 60% change in blood flow from baseline during the ∼10% change in plate separation. Additionally, we observe a ∼60% reactive hyperemia upon releasing the compression, consistent with published reports of DCS measurements of blood flow in human muscle[142].

In summary, this study demonstrated that we could obtain DCS signal in transmission through more than 5 cm of breast tissue. Furthermore, the results from this pilot study suggest that blood flow can change dramatically under mammogram-like compression.

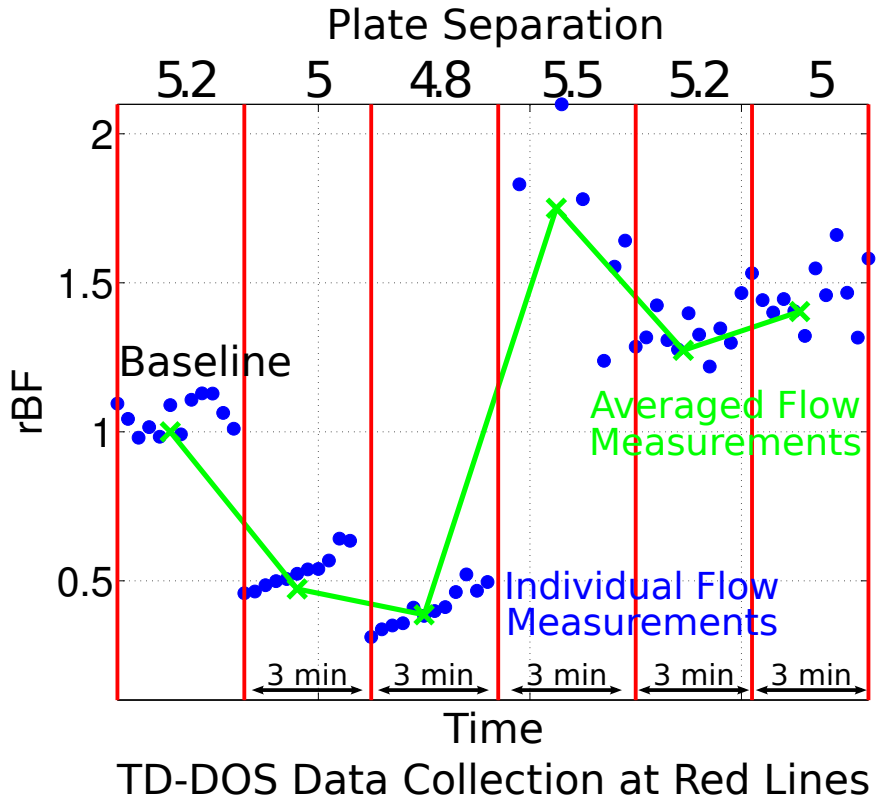

Figure 8.6: Relative Blood Flow (rBF) measurements in a 1 subject pilot study of transverse TD-DOS and DCS in the human breast. Blue dots are individual measurements; the average blood flow in each window is marked in green. Red lines indicated breaks where we paused DCS data collection and took TD-DOS data during the actual compression/release of the tissue. (Time line runs only during DCS measurements.) Black numbers above each window indicate the separation between compression plates. Note: a change in plate separation of 0.4 cm led to $\sim$60% ΔrBF.

8.3 Version 2: Continuous DOS and DCS Measurements of Serial Breast Compression

The results from the Version 1 instrument discussed in Section 8.2 encouraged us to continue our transmission blood flow measurements of breast tissue. Our pilot study, however, failed to tightly integrate the optical instrumentation for continuous measurements. As a result, the DCS measurements were almost continuous, but the TD-DOS measurements were collected in narrow time windows $\sim$3 minutes apart. We therefore chose to add an additional instrument for our follow up study. Instead of stopping DCS collection and manually shifting fibers to collect absorption and scattering (Hb_t, StO_2, Lipid, H_2O, and μ_s') data, as with the Version 1 system, the Version 2 system used the TD instrument to establish absolute measurements of baseline optical properties, but then monitored differential changes continuously with a FD-DOS/DCS instrument.

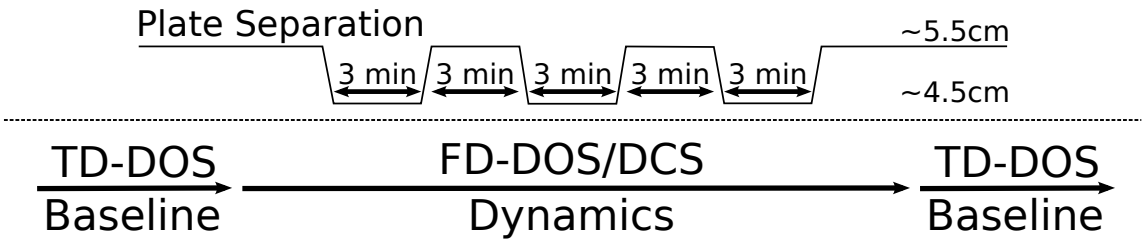

Figure 8.7: Time line for Version II instrumentation for continuous measurement of optical properties during mammographic compression. See Figure 8.8 for an example of Hb_t, StO_2, rBF, and pressure versus time.

8.3.1 Version 2: Experimental Protocol

During this study, we chose to utilize repeated compression-relaxation cycles (Figure 8.7) rather than a single compression. X-Ray mammograms are typically performed with several compressions, each in a different plane. Our study consisted of a TD-DOS baseline measurement, then dynamic FD-DOS/DCS measurements of three cycles of compression and relaxation (each lasting three minutes), and finally another static TD-DOS measurement. The baseline was taken at 'light compression', similar to that typically used in parallel plate DOT imaging. We note that these data were *not* collected from uncompressed breasts, but rather at a compression level where the breast tissue was in good contact with the optodes and a minimal acceptable SNR was obtained with DCS. (We attempted to address this potential confounding factor in our research in our Version 3 instrumentation; see Section 8.4.) Maximum compression levels were determined by subject comfort and compliance. Measurements of relaxed tissue were performed at the same plate separation as the baseline measurements.

8.3.2 Version 2: Results from Preliminary Study of 15 Subjects

The TD-DOS+FD-DOS/DCS instrument permits collection of both an absolute baseline and reasonably high temporal resolution (3-10s) data continuously during serial compression. Additionally, pressure sensors now permit monitoring of applied pressure at several points on the skin. We have determined that these pressure measurements were only useful for relative pressure monitoring, as calibration of the sensors used in Version 2 proved unstable; the Version 3 instrument replaced both the sensors and the read-in electronics to resolve this issue. Example data (pressure, Hb_t, StO_2, and rBF) collected with this instrument are shown in Figure 8.8 and Figure 8.9.

The values of Hb_t and StO_2 for the subject shown in Figure 8.8 return to baseline very quickly after each compression. Note the small change in StO_2 compared to Hb_t; this was a common observation across our population, although there was some scatter (see Figure 8.9 for individual time-traces and Figure 8.11 for population averaged results). Blood flow changed dramatically in this subject, to roughly 15% of baseline,

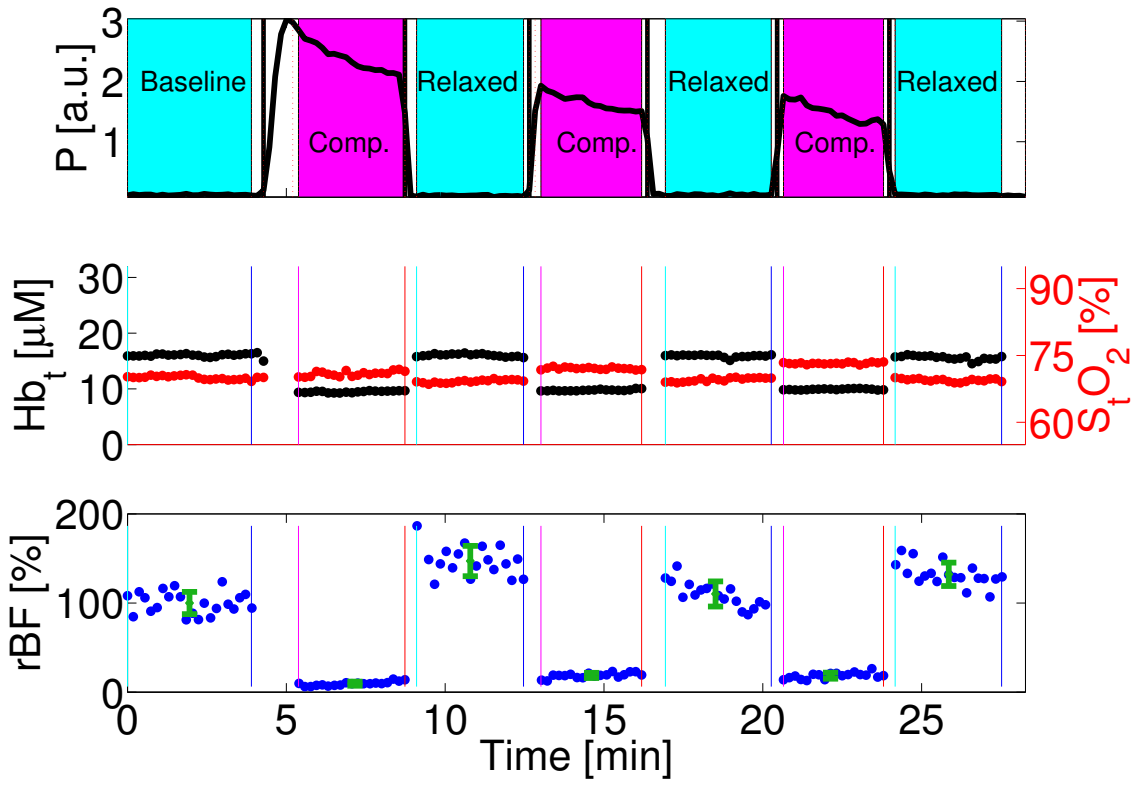

Figure 8.8: Example data from a single subject during breast compression. (Top) Pressure readout. Blue shading indicates a baseline or 'released' state; magenta indicates compression. (Center) Hb_t and StO_2. (Bottom) The green bars show mean±standard deviation of the blue dots in each time window. The first window (∼0-3 minutes) was used as a baseline. See text for details.

and it didn't recover significantly during the compression period. However, blood flow in some subjects did show significant recovery during the compression period (e.g. subject 80304.1 in Figure 8.9). DCS data was analyzed using $\mu_a^{(0)}$ and $\mu_s'^{(0)}$ (from TD-DOS) and $\Delta\mu_a[t]$ (from FD-DOS). However, we were not able to measure changes in scattering as a function of time. The increase in blood flow *following* the first compression is known as reactive hyperemia. Data from additional subjects are shown in Figure 8.9.

Our results demonstrated a hysteresis effect in the response of some subjects, indicating sequential compressions could not, in general, be combined. In other words, changes in Hb_t, flow, and surface pressure were inconsistent across repetitions. Figure 8.8 shows this inconsistent pressure response, but consistent Hb_t and rBF responses, to compression in a single subject. We observed a reduction in tissue surface pressure, both between compressions and during each compression period (e.g. Figures 8.8, 8.9, and 8.10) We suspect these changes are due to tissue remodeling in response to compression.

Although the pressure calibration in the Version 2 system was inconsistent, we could monitor relative pressure changes reasonably well. Recall that the Version 2 protocol calls for step compression: once the

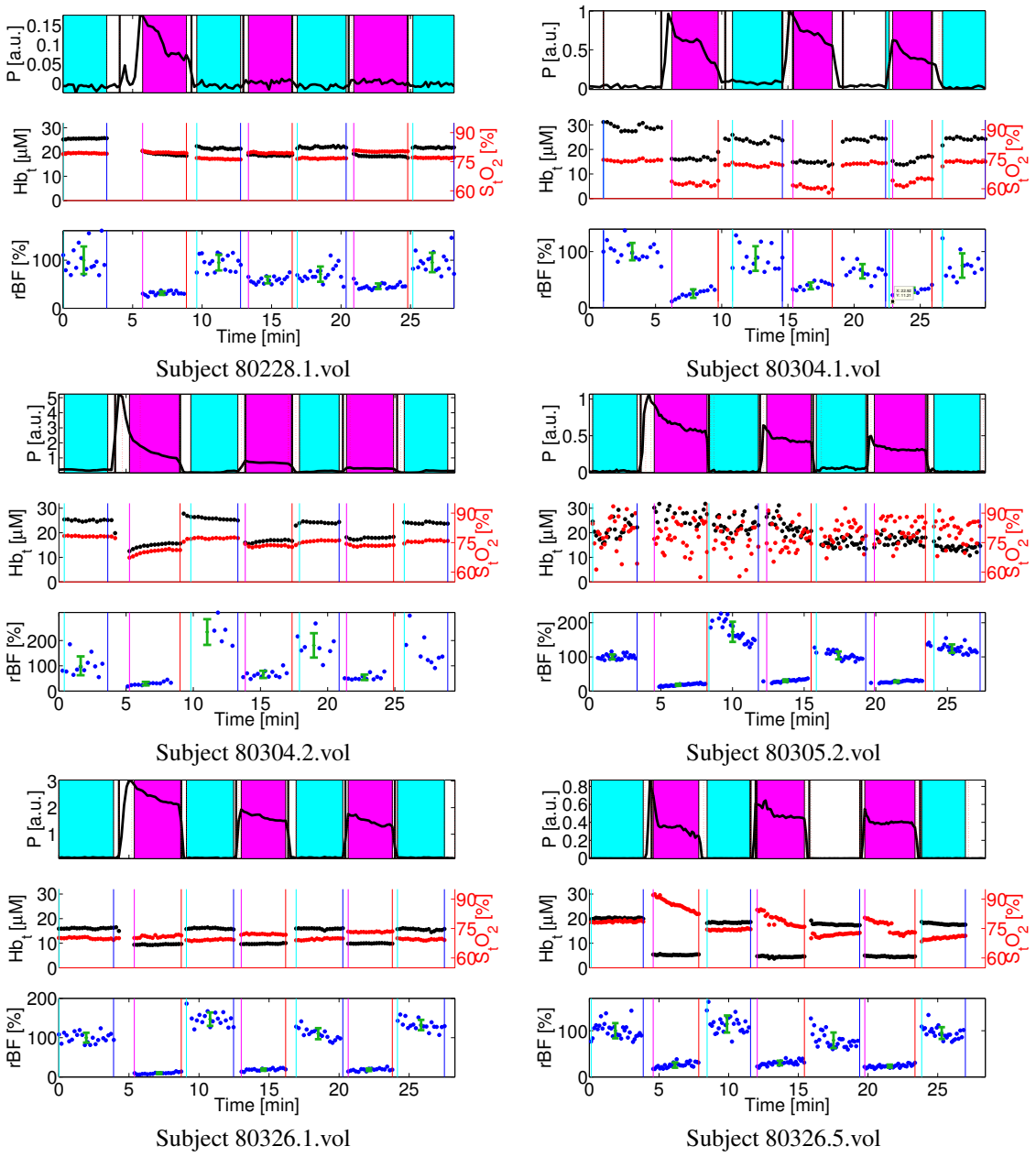

Figure 8.9: Example data from breast tissue in six subjects during mammogram-like compression. (Top) Pressure readout. Blue shading indicates a baseline or 'released' state; magenta indicates compression. (Center) Hb_t and StO_2. (Bottom) The green bars show mean$\pm$standard deviation of the blue dots in each time window. The first window ($\sim$0-3 minutes) was used as a baseline. The pressure readout for Subject 80228.1 displayed the lack of reliability for the 'piston ' pressure meter discussed in the text. Subject 80304.2 exhibited very noisy DOS data, but much higher SNR DCS data; this was possibly due to poor coupling between the DOS optodes and skin, as typically DOS SNR is much greater than DCS SNR.

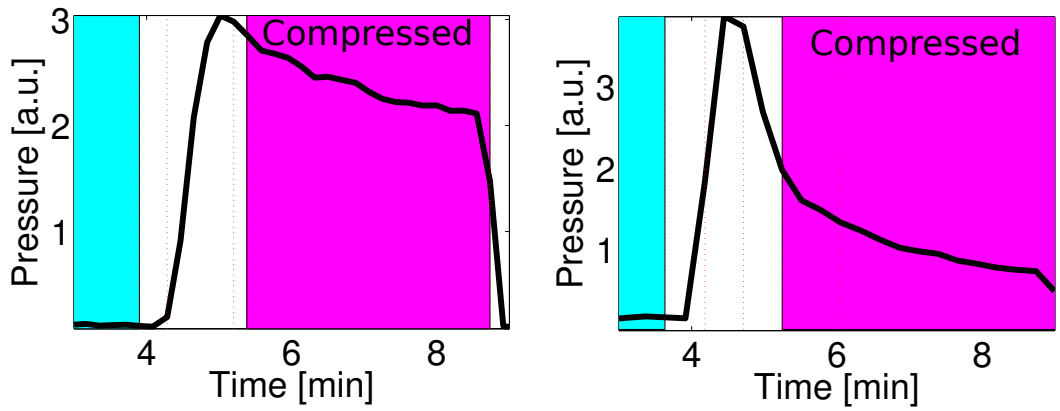

Figure 8.10: Pressure readings during the first of three 3 minute long compressions for subjects 80304.2 and 80326.1. Note the significant difference in the shape of the response. Blue shading indicates baseline period; magenta indicates compressed period. See more examples in Figure 8.9.

compressed period started, the plate separation is kept constant, but the load on the breast is permitted to vary. Figure 8.10 shows a comparison between a subject who maintained ∼60% skin pressure throughout the 3 minute compression period and a subject whose skin pressure fell off by ∼85%. This significant change in response to load may be due to tissue remodeling.

The results of our preliminary study of 15 subjects suggest relatively mild compression can induce significant changes in Hb_t (∼47%) and rBF (∼65%), but that StO_2 is minimally effected. Due to instrumentation limitations, μ_s' was only measured with the TD-DOS system before and after the series of compressions. Attempts to reduce the large degree of scatter observed in this data (∼30% in Hb_t and rBF) by separating our subject population into demographic groups (e.g pre- and post-menopausal) were not fruitful (data not shown), probably due to the small size of our population. The demographic breakdown of our study is given in Table 8.3.

Demographic Information		
$< Age >$	38±13	yrs
$< BMI >$	28.3±6.3	m/kg^2
Menopausal	Pre: 11	Post: 4

Bra Sizes	
<Chest Size>	36.1±4.4 in.
Cup	#
B	2
C	5
D	4
DD	3
DDD	1
Plate Separation	
$< d >$	5±1 cm

Table 8.3: Demographic data for 15 subjects in Version 2 compression study, as described in Section 8.3.2.(left) Average values across 15 subjects for preliminary study of compression effects on DOS and DCS data . Numeric values are given as mean ± standard deviation. (right) Breast sizes and compression plate separation. $< d >$ is the average starting plate separation.

Data taken from the change in optical properties between baseline and the first compression were found to be most reliable; this data is presented in Figure 8.11. In this analysis, we chose to use the fraction of change in plate separation as a proxy for load/pressure on the breast; this choice probably contributed to some of the scatter shown in Figure 8.11. Results from simultaneous measurement of the change in plate separation over the baseline plate separation ($\Delta d/d$), pressure, and load with our Version 3 compression system are discussed in Section 8.4.3.

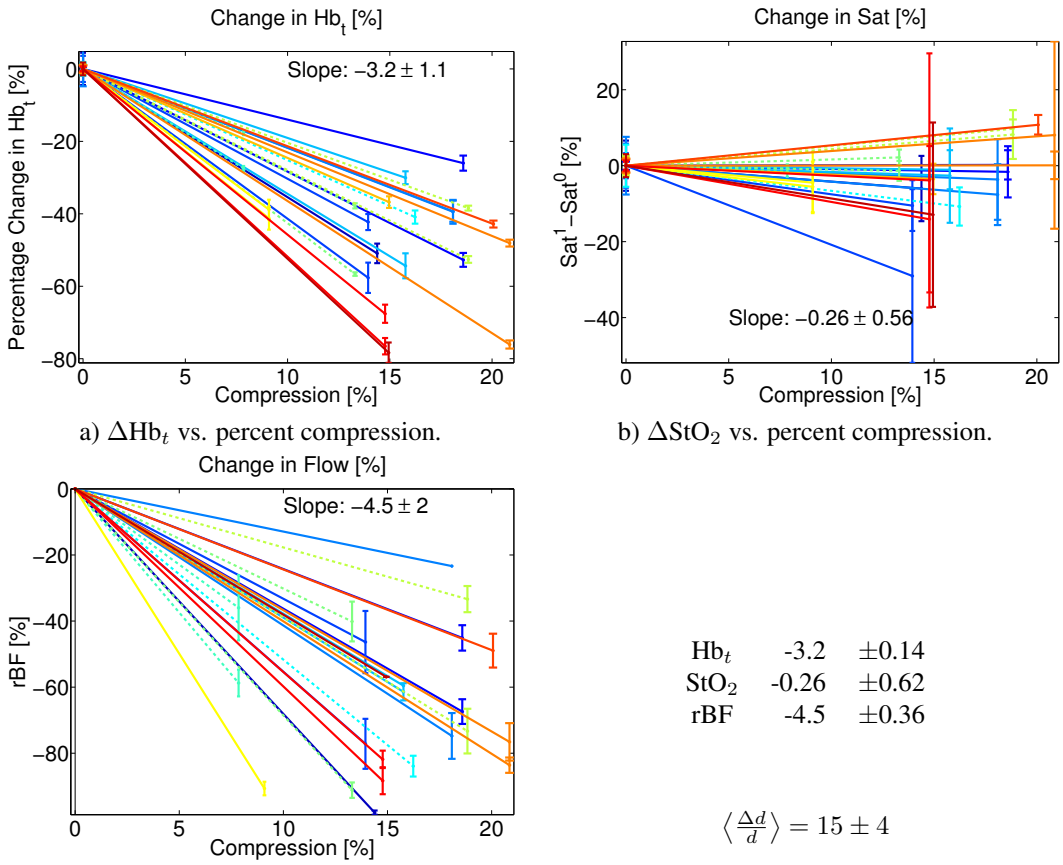

a) ΔHb_t vs. percent compression.

b) ΔStO_2 vs. percent compression.

c) ΔrBF vs. percent compression.

Hb_t	-3.2	$\pm$0.14
StO_2	-0.26	$\pm$0.62
rBF	-4.5	$\pm$0.36

$\left\langle \frac{\Delta d}{d} \right\rangle = 15 \pm 4$

d) Normalized fractional change

Figure 8.11: Scatter plot of changes in Hb_t, StO_2, and rBF in breast during compression from the Version 2 system. Compression measurements are expressed as percentage change in plate separation from the 'lightly compressed' baseline described in text and denoted by superscript 0 (X^0). Compression measurements are taken from the first of 3 compressions and designated by superscript 1 (X^1). Data from 15 subjects, with 2 measurements per subject are shown. (a) Percentage change in total hemoglobin concentration: $\Delta Hb_t = 1 - \frac{{Hb_t}^0 - {Hb_t}^1}{{Hb_t}^0}$. (b) Percentage change in blood oxygen saturation: $\Delta StO_2 = StO_2^0 - StO_2^1$. (c) Percentage change in relative blood flow: $\Delta rBF = 1 - \frac{rBF^1}{rBF^0}$. (d) Table summarizing results from Section 8.3.2; data is presented as mean $\pm$ standard deviation of the fractional change in each parameter divided by the fractional change in plate separation $\left(\left\langle \frac{\Delta X/X}{\Delta d/d} \right\rangle\right)$.

The observed reduction in compression-induced blood flow change may be important for future studies

of contrast agents injected under compression, as in X-ray tomosynthesis. For example, a protocol could include 3 'sham' compressions prior to the imaging and contrast agent injection compression. The distribution of blood flow responses to each compression is quite wide (Figure 8.11). This heterogeneity of response to compression suggests the potential use of the blood flow monitoring technique described above to optimize therapy or even contrast agent injection for individual subjects. However, we note that our study described above is limited to 15 subjects.

8.4 Version 3: Time Domain Diffuse Optical and Diffuse Correlation Spectroscopy of Stepped Breast Compression

In collaboration with our colleagues Dr. Andrew Maidment and Dr. Predrag Bakic[iv], we designed an improved study to more directly simulate hemodynamics during mammography. In particular, we shifted our compression metric from the fractional change in plate separation to total load applied, as in clinical systems. Additionally, we attempted to make a more accurate measurement of total hemodynamic change during mammographic compression by using a minimal level of compression for our baseline measurements. This reduction in baseline compression was possible due to the increased SNR in the Version 3 DCS. Our experimental timing was also shifted: instead of compressing one breast three times as in Section 8.3, we instead focused on bilateral compression at roughly one half and the full recommended load for mammography (60 and 120 N); the study protocol is described in Section 8.4.2.

8.4.1 Version 3: Instrumentation for TD-DCS Hemodynamic Measurements

Version 3 of the compression study took advantage of the inclusion of PMT shutters in the GenIII Opt/MRI system (Section 6.1.2) to integrate six wavelength TD-DOS measurements of absolute optical properties and DCS measurements[51,73] of microvascular blood flow at $\sim$5s temporal resolution. Additionally, we obtained a bundle of eight single mode optical fibers for our DCS measurements. Each fiber was connected to an individual APD and an independent autocorrelation function measured. Averaging across these fibers increased our SNR and permitted measurements at large plate separations.

A key limitation in the results presented so far in this chapter is our use of fractional change in plate separation $\left(\frac{\Delta d}{d}\right)$ as our measure of compression, i.e., as a surrogate for pressure inside the breast tissue. We do not expect the pressure on the surface of the breast to be consistent: 'external' geometry (e.g., the breast is wider nearer the chest wall), connective tissues (e.g., the rib cage is essentially rigid and attached to the breast), and 'internal' geometry (e.g. glandular verses adipose tissue, internal breast ligaments) all

[iv] Hospital of the University of Pennsylvania Department of Radiology, Physics Section

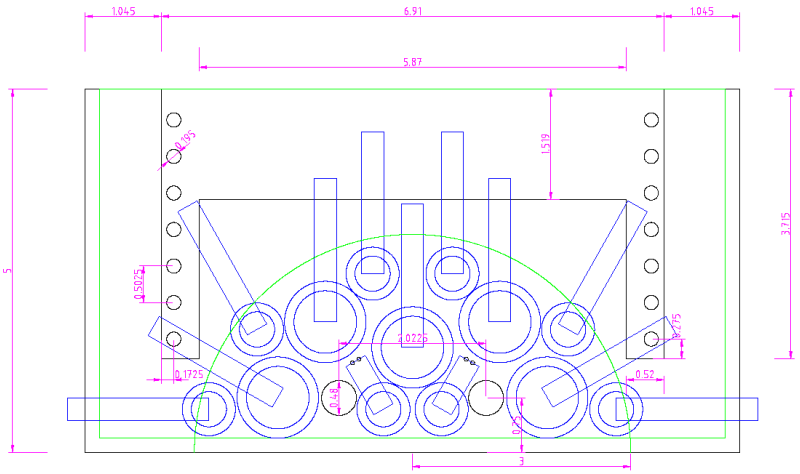

Figure 8.12: Design for multi-sensitivity, multi-position pressure mapping compression plate with 2 source and 2 detector positions. Pressure sensors are modular: we can choose to use up to 32 different sensors with arbitrary positioning. Both the plates are clear acrylic, permitting the operator to visually adjust the placement of the breast under the optical sensors. All dimensions are in inches. The sensitivity of the pressure sensors varies with area (Sensor Products Inc.).

suggest the presence of pressure inhomogeneity. Furthermore, the internal structure of the breast may lead to pressure differentials inside the breast volume. The latter is beyond our capacity to address non-invasively, but we seek to map the surface pressure distribution using a customized sensor array from Sensor Products Inc. (Madison, NJ); Figure 8.12 shows an example layout of the pressure sensors. In order to mount these additional sensors, we reduce the number of potential source/detector mounting positions, as shown in Figure 8.13.

8.4.2 Version 3: Experimental Prococol

Subjects were sequentially assigned to begin with the right or left breast. After the instrument was properly adjusted for the subject, we collected baseline measurements of load, pressure, TD-DOS, and DCS. Note, these DCS measurements had a relatively low SNR. The baseline plate separation was used for subsequent 'relaxed' measurements between compressions. We then applied a step compression to $\sim$60 N load (or maximum permitted by the subject), collected data for $\sim$45 s, and returned to the baseline plate separation. After $\sim$90 s, we applied a step compression of $\sim$120 N (or maximum permitted by the subject), collected data for $\sim$45 s, and returned to baseline plate separation. We then repositioned the subject's other breast in the instrument and repeated the above, except the objective load was 120 N during both repetitions. A time-line of this process is shown in Figure 8.14.

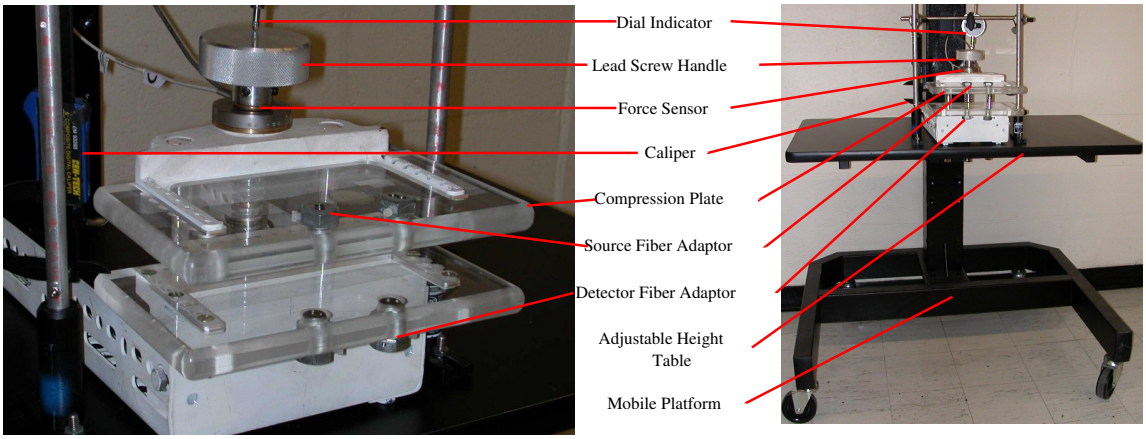

Figure 8.13: Updated compression plate system for optical measurements during mammographic compression. This design has been optimized to measure spatial variations in the surface pressure on the breast by eliminating all but 2 source and detector positions, thus permitting additional locations for pressure sensors. Pressure sensors are not shown in this image; a schematic can be found in Figure 8.12. Optical fiber adaptors are in position, but the fibers themselves have been removed for this photograph.

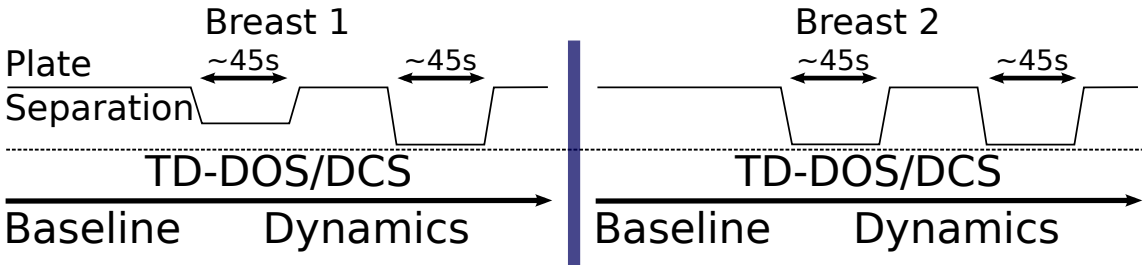

Figure 8.14: Schematic of the experimental time-line for the Version 3 mammographic compression study. The initial compression was to a nominal load of 60 N and the subsequent compressions were 120 N. Both of these loads were limited by subject compliance.

8.4.3 Version 3: Results from Combined TD-DCS Pilot Study

We conducted a pilot study with the Version 3 instrument; the healthy subjects presented here are described in Table 8.4. These initial data suggest that the fractional change in plate separation is not linearly related to either total load or peak skin pressure, especially at large compressions. Measured StO_2 changed little during compression, but Hb_t and rBF did change significantly. Example results from two subjects are shown in Section 8.4.3.1; the combined results across all subjects are shown in Section 8.4.3.2.

Demographic Information		
$< Age >$	35.2±13.9	yrs
$< BMI >$	29.8±9.1	m/kg^2
Menopausal Status	Pre: 5	Post: 0

Bra Sizes	
<Chest Size>	38±4.6 in.
Cup	#
C	4
D	1
Baseline Plate Separation	
$< d >$	6.1±0.5 cm

Table 8.4: Demographic data for 5 subjects in Version 3 compression study, as described in Section 8.4.3. (left) Average values across all subjects for preliminary study of compression effects on DOS and DCS data . Numeric values are given as mean ± standard deviation. (right) Breast sizes and compression plate separation. $< d >$ is the average starting plate separation.

8.4.3.1 Example Individual Results

Data from two healthy volunteers during the entire experimental sequence (Figure 8.14) are shown in Figures 8.15 and 8.16. These data are consistent with the results observed in the Version 2 system (e.g. Figure 8.9). However, unlike the Version 2 system, the Version 3 data provide calibrated pressure, total load, and absolute optical properties (Hb_t, StO_2, and μ_s') throughout the experimental protocol.

The Version 3 system has higher DCS SNR, enabling us to collect 'baseline' data at lower load levels to better approximate the completely uncompressed breast. Note that the average baseline plate separation Table 8.4 is 6.1±0.5 cm while the Version 2 data (Table 8.3) is 5±1 cm. However, the 'baseline' and 'relaxed' windows were both susceptible to motion artifacts, as the breast was not held firmly, and the optical signals had lower SNR than in the 'compressed' time windows. These factors led to the considerably wider observed distribution of calculated parameters in the 'baseline' and 'relaxed' periods relative to the 'compressed' windows.

Hb_t and StO_2 are calculated from six-wavelength TD-DOS data (opto-electronics from the GenIII system, Section 6.1); the absorption and scattering coefficients are then used in the analysis of the DCS data. Optical properties are not calculated during the transition periods as the exact plate separation is not known and the ambient light levels are significantly elevated. Clear reductions in Hb_t and rBF are observed in both of these subjects; changes in StO_2 data are less consistent.

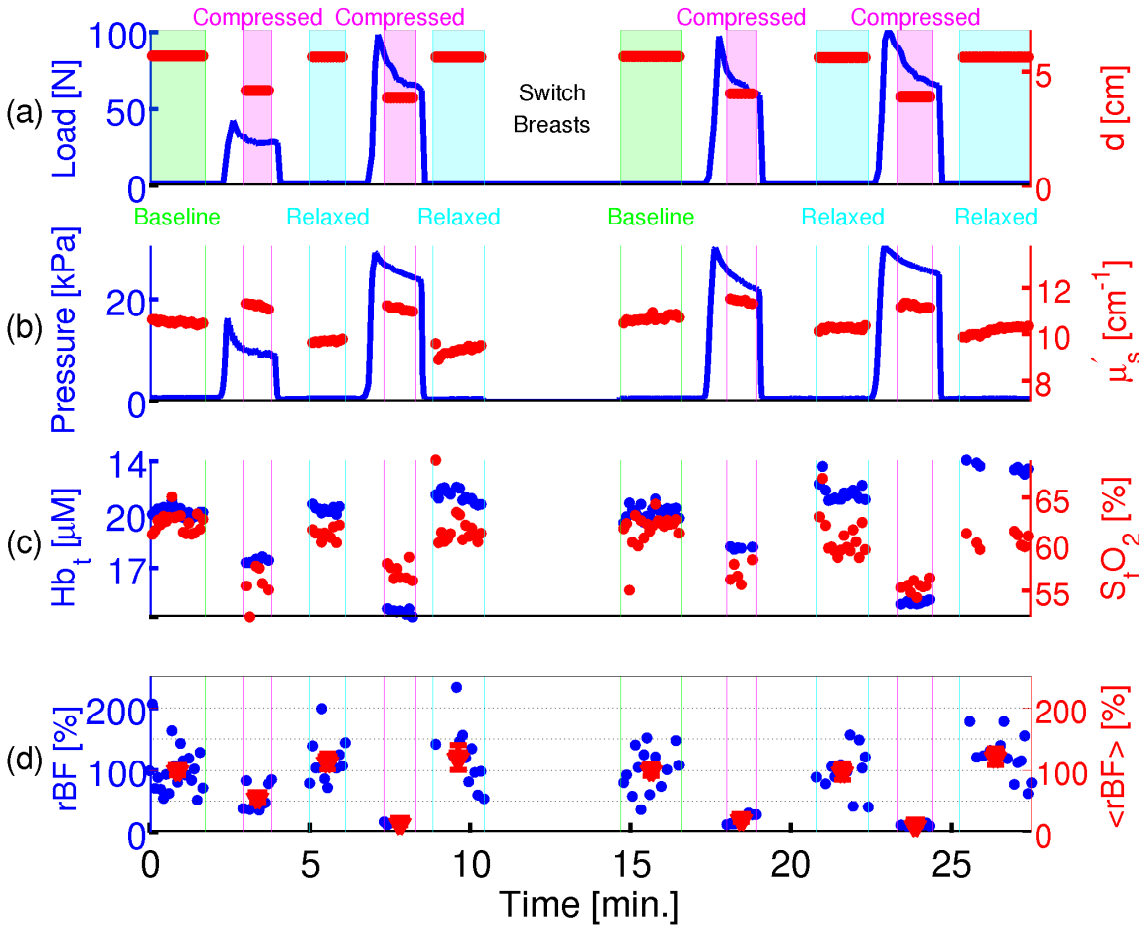

Figure 8.15: Time traces of (a) Load and Plate Separation (d), (b) Pressure and μ_s' [785nm], (c) Hb_t and StO_2, and (d) rBF for an example subject (28 years old, BMI= 19.6 kg m^{-2}) during sham mammographic compression. Left axes correspond to blue trace; right axes to red. Baseline time periods are marked with green in (a), relaxed periods with cyan, and compressed periods with magenta. Load and Pressure data are collected continuously; the remaining data types are not calculated during transition periods. Pressure data is the averaged across the five sensors with the highest readings during compression. Data are averaged over the time windows to produce the average results described in Section 8.4.3.2.

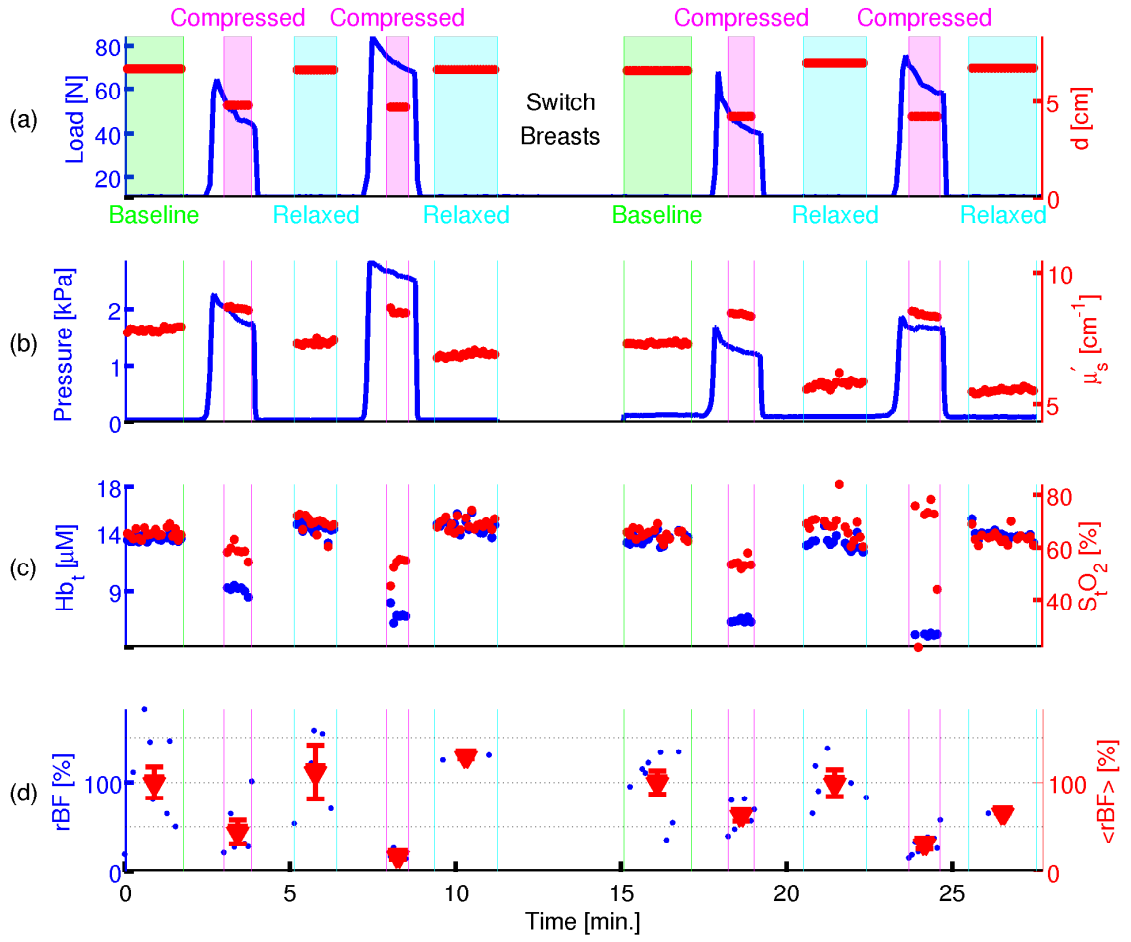

Figure 8.16: Time traces of (a) Load and Plate Separation (d), (b) Pressure and μ_s' [785nm], (c) Hb_t and StO_2, and (d) rBF for an example subject (54 years old, BMI= 37.3 kg m^{-2}) during sham mammographic compression. Left axes correspond to blue trace; right axes to red. Baseline time periods are marked with green in (a), relaxed periods with cyan, and compressed periods with magenta. Load and Pressure data are collected continuously; the remaining data types are not calculated during transition periods. Pressure data is the averaged across the five sensors with the highest readings during compression. Data are averaged over the time windows to produce the average results described in Section 8.4.3.2.

8.4.3.2 Population Averaged Results

We have so far collected data on five subjects with the Version 3 compression system; data from all subjects is included in the graphs below. We collected useful data sets from both breasts in only one of these five volunteers; we are currently improving our data collection protocol to increase volunteer compliance and data robustness. These data are preliminary; we are currently in the process of expanding the data set.

Changes in tissue physiological properties across the available subjects are shown in Figure 8.17, 8.18, and 8.19. We observed a small decrease in saturation during compression (Figure 8.17), but significantly greater changes were observed in both Hb_t (Figure 8.18) and rBF (Figure 8.19). The current ΔStO_2 and ΔHb_t data are shown with linear fits in Figure 8.17 and 8.18; this is function unphysical, as both quantities must approach -100% at sufficiently high external loads (i.e., total hemoglobin and blood oxygen saturation must be zero if all the blood is forced out of the breast). However, the data shown in Figure 8.18 and particularly Figure 8.17 is noisy. Furthermore, additional error is introduced as these data are averaged over time windows corresponding to significant changes in physiological properties (e.g., Figure 8.15 and 8.16). Our current data set contains only five volunteers; as our data set expands, we will segment the population by menopausal status, body mass index (Body Mass Index), and other factors. Additionally, we will group pre-menopausal women by the timing of the measurement in their menstrual cycle, as this may effect both mechanically[297] and optically[298] measured physiological properties.

The current rBF data suggests that a simple exponential function of load, fractional change in plate separation, or pressure may describe the reduction in blood flow. We note that applied average loads of roughly one half that used in X-Ray mammography (60 N) reduced blood flow by 90%. This reduction in flow would significantly hamper the delivery of a contrast agent administered during compression.

The lack of a clear functional form connecting Hb_t with load or pressure and a clear relationship between ΔHb_t and $\Delta d/d_0$ suggests the possibility of plate separation-dependent cross talk in the TD-DOS measurements. In measurements of a compressible homogeneous phantom (Section C.2), we identified a $\sim$5-10% change in absorption during $\sim$30% change in plate separation. This change is at lease partially due to boundary motion (i.e., the breast or phantom flattens out and the skin-air boundary changes position). We attempted to minimize the effect of this change in the boundary conditions by centering the optodes on the breast. However, as shown in Figure 6.17, glandular tissues are concentrated in the center of the breast and adipose on the periphery. External compression therefore may significantly change the fraction of glandular vs. adipose tissue probed optically, although we expect the transmission measurements described here to be less effected than remission measurements. Data from the Version 2 compression system (e.g. Section 8.3.2) is concentrated between $\Delta d/d_0 \approx 15 - 20\%$ and each subject was measured at a single compression. Both of these factors could potentially mask the phenomena observed in the Version 3 data and complicated direct comparisons between data sets.

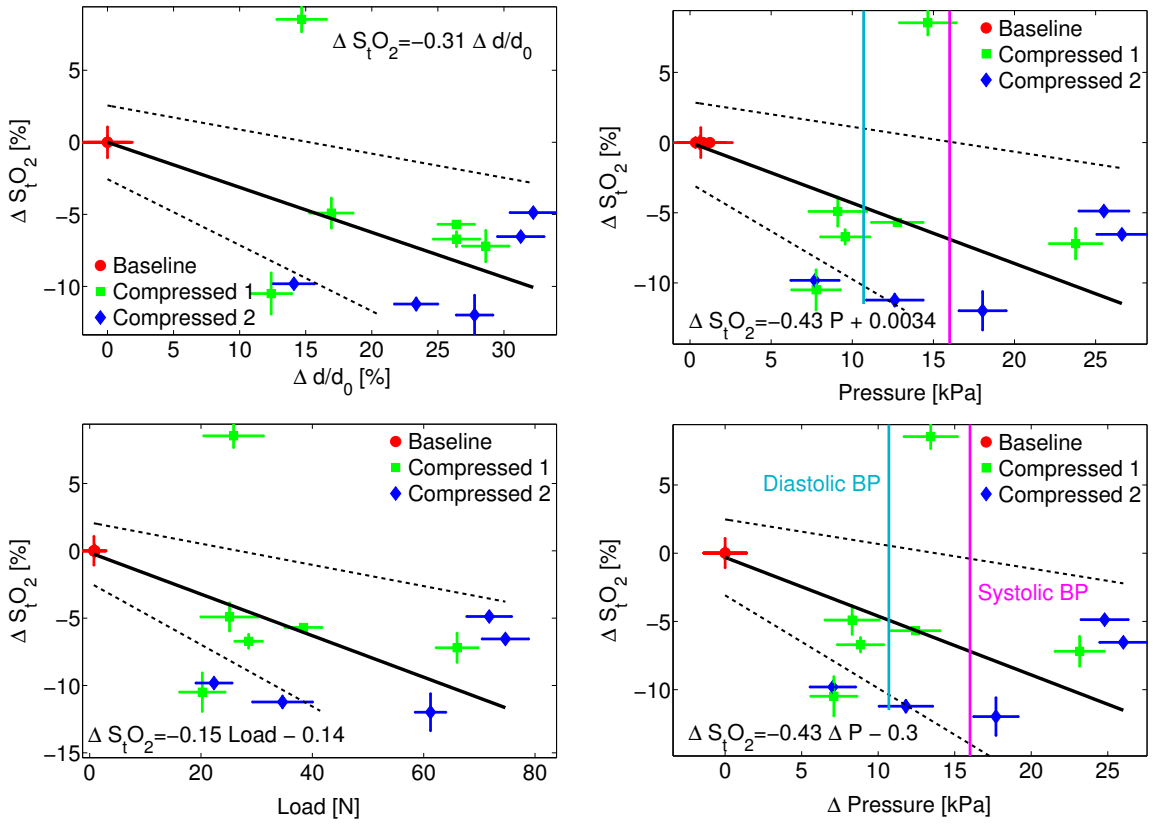

Figure 8.17: Observed changes in blood oxygenation (StO_2) versus Load, Pressure, and change in plate separation ($\Delta d/d_0$) in 6 measurement series (see Figure 8.14) on 5 subjects. Pressure reported is the average between the five sensors with highest pressure readings for a particular subject. Data from the first compression (green), second compression (blue), and baseline (red) periods are plotted separately, with corresponding individual and joint (black) fits. Normal systolic (magenta) and diastolic (cyan) blood pressures[66] are included for comparison. Dashed lines indicate 95% confidence intervals of the fit parameters.

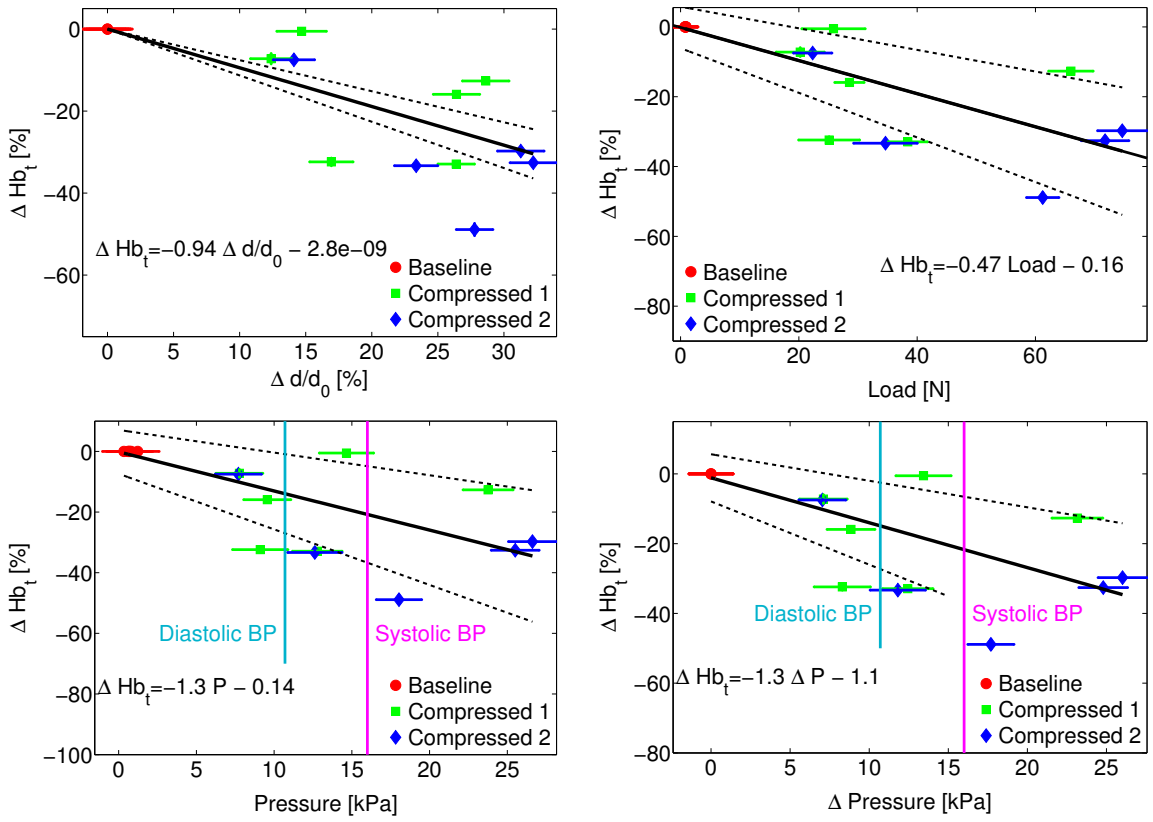

Figure 8.18: Observed changes in total hemoglobin concentration (Hb_t) versus Load, Pressure, and change in plate separation ($\Delta d/d_0$) in 6 measurement series (see Figure 8.14) on 5 subjects. Pressure reported is the average between the five sensors with highest pressure readings for a particular subject. Data from the first compression (green), second compression (blue), and baseline (red) periods are plotted separately, with corresponding individual and joint (black) fits. Normal systolic (magenta) and diastolic (cyan) blood pressures[66] are included for comparison. Dashed lines indicate 95% confidence intervals of the fit parameters.

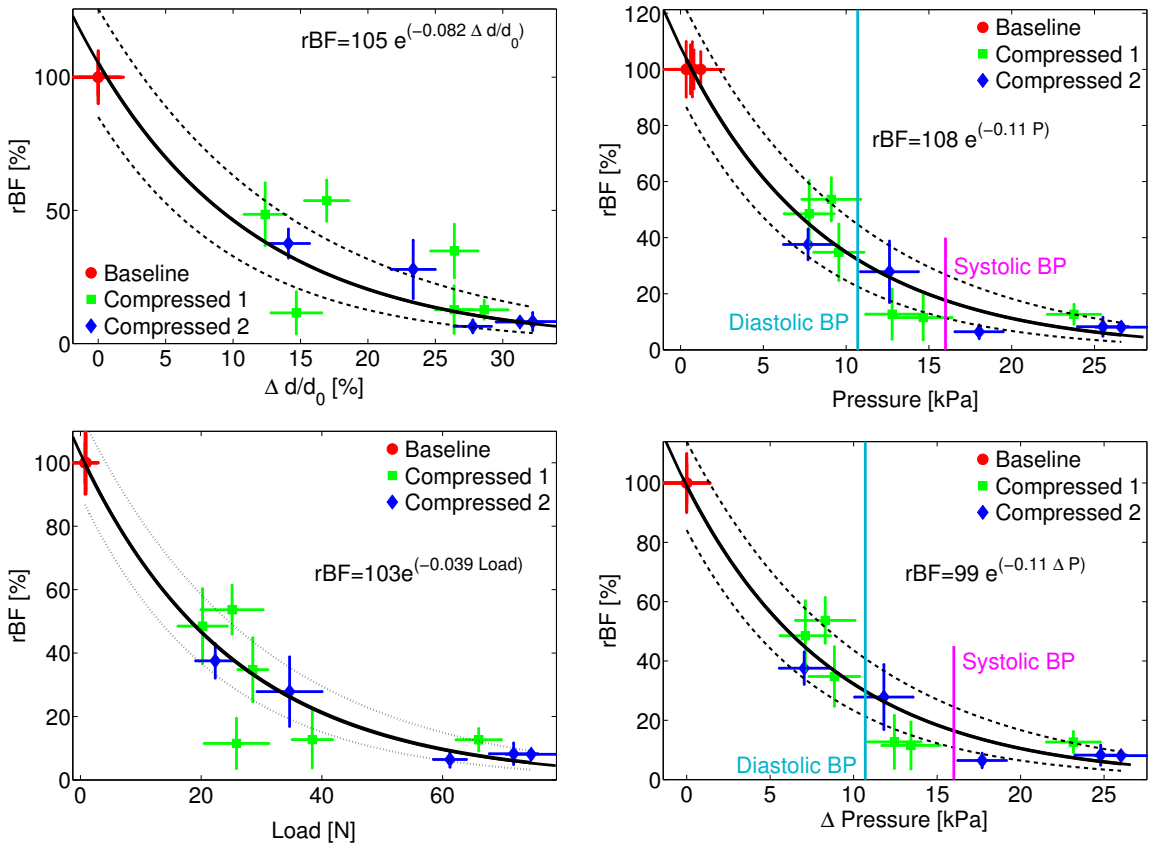

Figure 8.19: Observed changes in relative blood flow (rBF) versus Load, Pressure, and change in plate separation ($\Delta d/d_0$) in 6 measurement series (see Figure 8.14) on 5 subjects. Pressure reported is the average between the five sensors with highest pressure readings for a particular subject. Data from the first compression (green), second compression (blue), and baseline (red) periods are plotted separately, with corresponding individual and joint (black) fits. Normal systolic (magenta) and diastolic (cyan) blood pressures[66] are included for comparison. Dashed lines indicate 95% confidence intervals of the fit parameters.

The Version 1 and Version 2 compression systems utilized the fractional change in plate separation as a proxy for load and skin surface pressure. The preliminary results of the Version 3 system, shown in Figure 8.20, suggest that these experiments may have probed a regime ($\Delta d/d_0 < 20\%$) where $\Delta d/d_0$ was linearly related to total load/surface-pressure. However, more data is needed to fill in the $\Delta d/d_0 \sim 10\%$ portion of the curve in the Version 3 data. Load and surface pressure (averaged over five central detectors) appear to be linearly related over the range studied. Surface pressure was measured with discrete sensors of fixed area and should be less effected by geometrical factors (e.g., stretching skin and tendons away from the chest wall, increasing skin-plate contact area as the load increases). The linear relationship between surface pressure and load suggests that these geometrical factors do not dominate the load measurement. Note that the load and pressure signals vary (fall off quickly) during compression (Figures 8.15 and 8.16); averaging over this physiological change contributes to the calculated error. Additional plots showing fit results for the first and second compression data separately are included in Appendix B.

The various component tissue types in the breast have different strain responses to applied stress. In the linear regime, these quantities are expected to be related by the familiar Young's Modulus (Y):

$$Y = \frac{\sigma}{\epsilon} = \frac{F/A_0}{\epsilon} \tag{8.1}$$

where F is the applied force, A_0 is the initial cross-sectional area of the sample, σ is the stress, and ϵ is the strain. Several groups have measured the mechanical properties of excised breast tissue[299–302] and modeled the displacement of tumors during external conformation changes[303–305]. Elastography[306,307] creates 3D maps of tissue mechanical properties, exploiting these differences in mechanical properties between tissue types (e.g., cancers are stiffer than fat or fibroglandular tissue[299–301]). Note: data in Table 8.5 are taken at multiple non-zero 'pre-compression' strains and are thus properly refered to as the 'tangent' moduli, instead of Young's moduli. However, I will follow the literature in referring to these quantities as Young's moduli for the remainder of this section.

The data in Figure 8.21 emphasizes the similarity between these measurements and typical stress versus strain curves (i.e., applied force per area versus fractional change in sample length). We expect the pressure on the surface of the breast to be heterogeneous and for the area of contact between breast tissue and the compression plate to change during compression, but load and surface pressure may nonetheless provide a proxy for stress measurements and $\Delta d/d_0$ for strain. If we ignore complicating factors, the slope of a linear fit to the pressure versus $\Delta d/d_0$ data in Figure 8.21 can be thought of as an equivalent Young's modulus (Equation 8.1, $Y = 64$ kPa, 95% confidence interval, [46, 81] kPa). Note, for consistency with data presented in the proceeding sections, $\Delta d/d_0$ is reported as a percentage and the slope is therefore scaled by a factor of 100 to obtain Y. This falls within the wide-ranging values reported for normal breast tissue[299–301] (Table 8.5) at similar strains, despite the highly idealized analysis ignoring the internal breast structure.

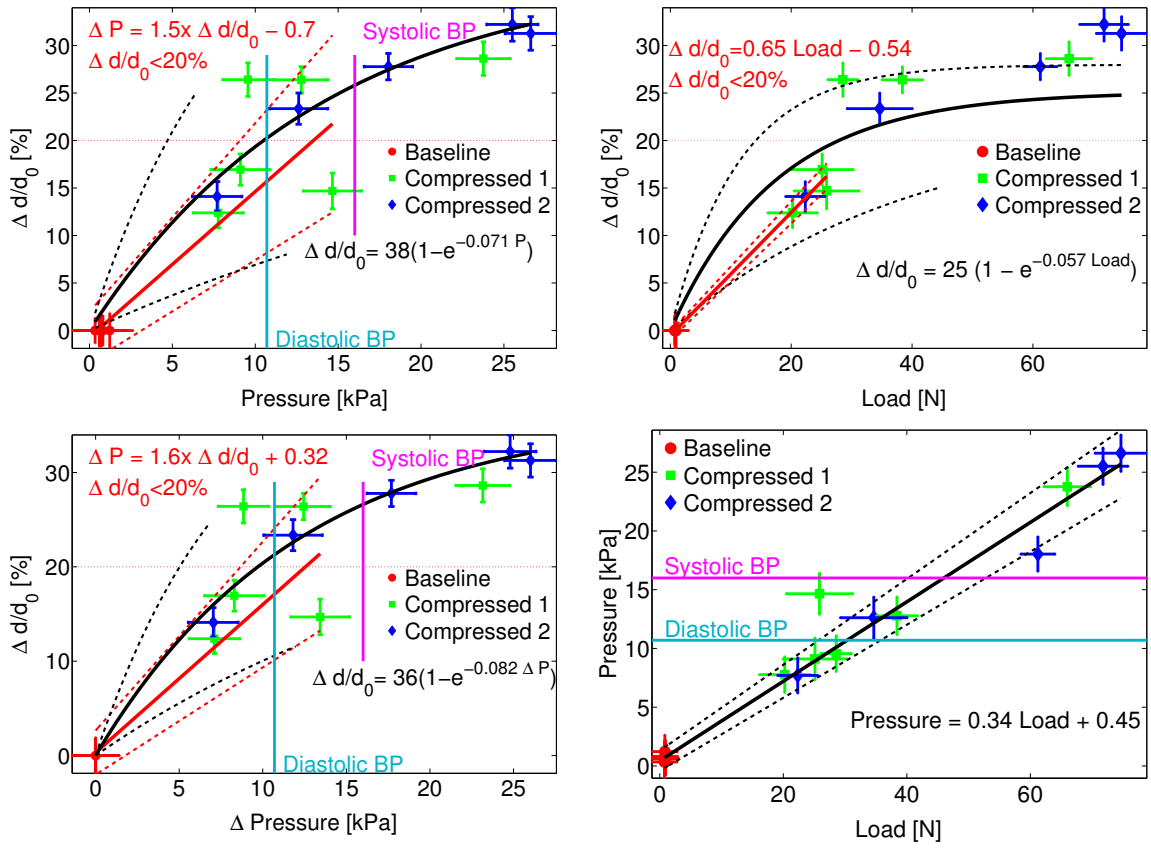

Figure 8.20: Comparison between Load, Pressure, and change in plate separation ($\Delta d/d_0$) in 6 measurement series (see Figure 8.14) on 5 subjects. Pressure reported is the average between the five sensors with highest pressure readings for a particular subject. Data from the first compression (green), second compression (blue), and baseline (red) periods are plotted separately, with corresponding individual and joint (black) fits, along with a linear fit to the low-compression region ($\Delta d/d_0 < 20\%$, red). Dashed lines indicate 95% confidence intervals of the fit parameters. Normal systolic (magenta) and diastolic (cyan) blood pressures[66] are included for comparison.

Table 8.5 shows the measured Young's moduli to increase with strain. We expect stretching of the skin and Cooper's ligaments (connecting skin to glandular tissue) provide most of the mechanical resistance to deformation. Fung[308,309] describes an exponential dependence of stress on strain in uniaxial extension of biomaterials:

$$Y = \frac{\partial \sigma}{\partial \epsilon} = \frac{\partial F/A_0}{\partial \Delta d/d_0} = be^{m\epsilon}, \tag{8.2}$$

which gives

$$\sigma = \frac{b}{m}(e^{m\epsilon} - 1) \tag{8.3}$$

for constants b and m. Others[301,303] have previously used this form of a strain-dependent Young's modulus (tangent modulus) in FEM modeling of breast tissue. Results of fitting Equation 8.2 to data from Krouskop and Wellman are in Table 8.6. The exponential increase in pressure and load due to increased $\Delta d/d_0$

(Figure 8.21) is in the range of the values for fatty and fibroglandular tissue reported in Table 8.6.

These data are preliminary and there are multiple possible refinements to our simplifying models. Of special concern to the assumption of homogeneity are the Cooper's ligaments connecting the skin to glandular tissues. Furthermore, Azar *et al.*[303] has suggested that fibroglandular and fatty tissues in the breast become compartmentalized and therefore differ in mechanical properties from isolated excised samples. Additionally, work by Lorenzen *et al.*[297] with MR elastography suggests large ($\sim\pm30\%$) changes in fibroglandular elasticity occur during the course of a woman's menstrual cycle. Despite these limitations, we are encouraged by the consistency of our initial data with published results.

The measured blood flow fell to less than 20% of baseline at an average load of ~40 N (Figure 8.19), significantly less than the load typically used for X-ray mammography, although measured surface pressures were well above normal systolic (16 kPa) and diastolic (10.7 kPa)[66] blood pressures. This large change in blood flow may have significant impact on the choice of protocols for contrast agent injection in compressed imaging.

	Strain	Tissue Type	Young's Modulus [kPa]
Samani *et al.*[299]	5%	Fat	3.25 ± 0.91
	5%	FG	3.24 ± 0.61
Wellman *et al.*[301]	5%	Fat	6.6 ± 7
	5%	FG	33 ± 12
	15%	Fat	174 ± 8.4
	15%	FG	271.8 ± 167.7
Krouskop *et al.*[300]	5%	Fat	18 ± 7
	5%	FG	28 ± 14
	20%	Fat	20 ± 8
	20%	FG	48 ± 15
Δ Pressure vs. $\Delta d/d_0$	$< 20\%$	Whole Breast	64

Table 8.5: Tabulation of Young's Moduli of Breast Tissue, from the literature. All of the literature data were collected by compressing excised samples; 'whole breast' fit is derived from data shown in Figure 8.20. Note, $\Delta d/d_0$ is expressed as a percentage in Figure 8.21 and the calculated slope is therefore multiplied by a factor of 100. FG: Fibroglandular.

		b/m	m
Krouskop *et al.*	Fat	18.50	0
Wellman *et al.*	Fat	4.46	7.4
Krouskop *et al.*	FG	27.5	3.64
Wellman *et al.*	FG	15.1	1.23
Δ Pressure vs. $\Delta d/d_0$	Whole Breast	4.5	5.8

Table 8.6: Non-linear stress-strain models of breast tissue. Data from Krouskop *et al.*[300] and Wellman *et al.*[301] fit to $Y = be^{m\epsilon}$ by Tanner *et al.*[305] and results from fits of data shown in Figure 8.21. Note, $\Delta d/d_0$ is expressed as a percentage in Figure 8.21 and the value calculated for m is therefore multiplied by a factor of 100. FG: Fibroglandular.

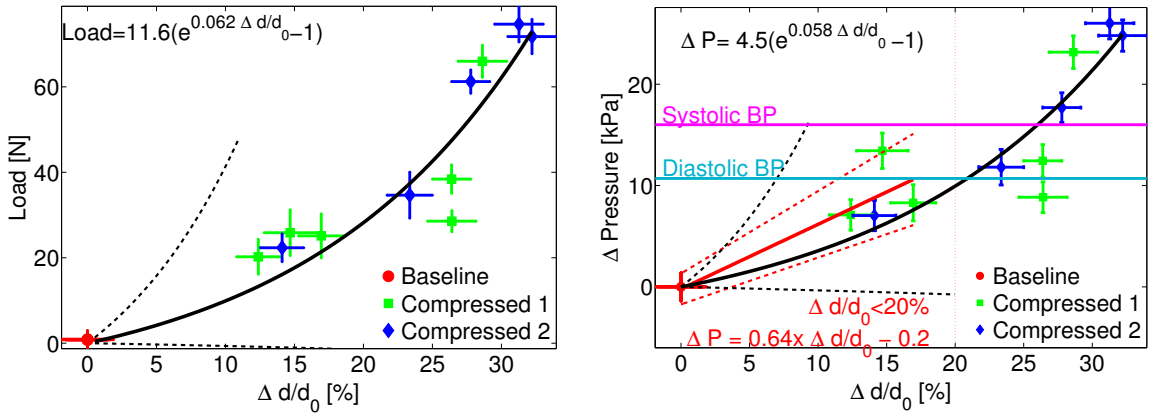

Figure 8.21: Comparison of applied Load and Pressure to fractional change in plate separation (strain) using the Version 3 compression system. ($\Delta d/d_0$) in 6 measurement series (see Figure 8.14) on 5 subjects. Pressure reported is the average between the five sensors with highest pressure readings for a particular subject. (top row) Data from the first compression (green), second compression (blue), and baseline (red) periods are plotted separately, with corresponding individual and joint fits. (bottom row) Combined data set with joint (black) fits, along with linear fits to the low-compression region ($\Delta d/d_0 < 20\%$, red). Data in these plots is also shown in Figure 8.20 with the abscissae and ordinates exchanged. Dashed lines indicate 95% confidence intervals of the fit parameters.

8.5 Ongoing Work

Future work on this project will be focused on additional healthy subject recruitment and translation into the clinical environment for measurement of cancer patients. We anticipate results from this work assisting clinicians in designing individualized treatment plans for patients.

8.5.1 Instrumentation Improvements

In conversation with our clinical collaborators, we determined that instruments needed for the oncology clinic should be small, quiet, unobtrusive, and convenient. As this study is intended to eventually measure hemodynamics in cancer patients, physician and patient acceptance will be critically important in determining subject recruitment. We therefore and built a combined TD-DOS and DCS system designed to function in this environment[310v]. A photo of this more clinician- and patient-friendly system is shown in Figure 8.22. In addition to the obvious reduction in size compared to the GenIII system (see Figure 6.14), this portable system has its own battery power supply, permitting ∼30 minutes of measurements untethered to a power source. This feature permits a system to be prepared in a back room, then wheeled out to whichever exam room is currently being used, and finally returned to storage.

This system is based around 2 TCSPC detector channels (SPC-130, with PMC-100 PMTs, Becker and Hickl) and 3 lasers at 650, 785, and 830 nm, pulsed at 50 MHz (BHLP-700, Becker and Hickl). These components achieve stability more quickly (∼15 min.) and are much smaller then our 6 wavelength system, described in Section 6.1. Furthermore, using independent TCSPC channels (i.e., no routers) enables higher photon counting rates and thus more rapid data collection. The data collection rate is not critical for the static TD measurements in the Opt/MRI GenIII DOT system (Section 6), but the rate is critical for the dynamic measurements in this breast compression study. Additionally, the PMC-100 PMTs can be switched on and off rapidly to prevent damage from the DCS laser, reducing the need for optical shutters.

8.5.2 Portable Compression Platform for Clinical Research

As a practical matter, measurements of cancer patients must take place in the hospital, preferably in the oncologist's office, not in a physics lab. We have therefore constructed a mobile compression system (Figure 8.13) which can be easily moved into clinical spaces for a series of measurements.

[v]David L. Minkoff performed most of the detailed mechanical design and construction necessary to miniaturize the opto-electronic enclosure.

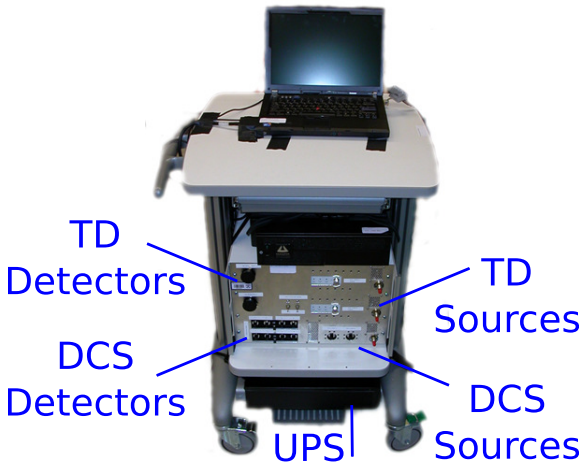

Figure 8.22: Portable TD and DCS system. DCS Sources: Crysta Laser (785 nm); DCS Detectors: Pacer SPCM-AQ4C APD; TD Source: Becker and Hickl BHLP-700 (685, 785, and 830 nm); TD Detector: Becker and Hickl PMC-100 with SPC-140 TCSPC card. UPS: Un-interruptible Power Supply

8.5.3 Future Research

The third version of our compression system will permit us to investigate scattering changes during compression and increase our data collection rate, through a higher SNR in our DCS system. We plan to continuously measure blood pressure during our studies. This will allow us to normalize our pressure measurements to each subject's current internal blood pressure and perhaps provide improved insight into individual hemodynamic responses. Furthermore, we are in discussions with colleagues in the Radiology Department on combining our compression system with their X-Ray Tomosynthesis device. Eventually, we will use the techniques and instrumentation developed here to advance our work on Diffuse Correlation Tomography (DCT), permitting us to make 3D differential images of blood flow in the breast using optical measurements.

8.6 Conclusion

Full volume-tomographic reconstructions of the breast require transmission measurements: the results of this study are the first transmission DCS measurements of the human breast. These data suggest that Diffuse Correlation Tomography (DCT) in the breast may be possible with current technologies. In Section 6.3, I described how the GenIII Opt/MRI system has been designed to permit DCS measurements and potentially permit DCT using spatial prior information from MRI. Such combined imaging also would permit us to compare blood flow measured by Arterial Spin Labeling[236] (ASL) and DCT in the breast.

Chapter 9

Conclusion

This thesis brings together three themes: the development and application of instrumentation for simultaneous DOT and MR Imaging (Chapter 4-6), introduction and application of a statistical analysis scheme for DOT images (Chapter 7), and reported instrumentation and the first results from transmission measurements of microvascular blood flow in the breast during mammographic compression (Chapter 8). The first theme has resulted in both co-registered contrast enhanced DOT-MR imaging and a flexible modular imaging platform to continue this work with 3 T MRI. The second theme provides proof of concept multi-parameter cancer detection and localization with DOT data; future work will bring the first and second themes together by including MR data in the statistical tools to identify and diagnose breast cancer. The third theme provides initial data for DCT in breast cancer; the GenIII Opt/MR imaging system will add optical flow measurements, allowing linkage of all three themes. The ultimate focus of this work is to extract maximally useful information for the identification, classification, and treatment of breast cancer.

Appendices

Appendix A

ICG Pharmacokinetics in Breast Cancer

As noted in Section 3.1.3, Indocyanine Green (ICG) is an FDA approved optical contrast agent which may have diagnostic utility through imaging of both uptake and washout kinetics. Cuccia[173] described a two-compartment model (schematic in Figure A.1) for ICG in tissue, under a set of simplifying assumptions.

Diffuse optical measurements sample many cubic centimeters of tissue, averaging over both microvasculature, extracellular space, and the various cells which make up a particular tissue. Therefore, the total concentration (C_T) of ICG derived from *in vivo* diffuse optical measurements is the volume weighted combination of the plasma (V_p,C_p) and extravascular, extracellular space (EES) (V_e,C_e) concentrations, assuming no ICG penetrates cell membranes.

$$C_T = V_p C_p + V_e C_e. \tag{A.1}$$

Note that we may constrain V_p with the measured total hemoglobin Hb_t concentration, provided we assume the distribution of red blood cells (RBC) throughout the plasma and the hemoglobin content of each RBC is consistent; see Eqn. A.5.

The change in concentration of ICG in the EES (the majority of volume probed optically) is

$$\dot{C}_e = k_{in} C_p - k_{out} C_e. \tag{A.2}$$

Bi-exponential elimination from the plasma by the liver is described as

$$C_p = A_1 e^{-\alpha_1 t} + A_2 e^{-\alpha_2 t} \tag{A.3}$$

where $\alpha_{1,2}$ are rate constants and $A_{1,2}$ are the amplitudes of the corresponding process.

Following Cuccia's solution for $C_T[t = 0]$, in the case where $\frac{1}{\alpha_{1,2}}$ and $\frac{1}{k_{in,out}}$ are much less then the

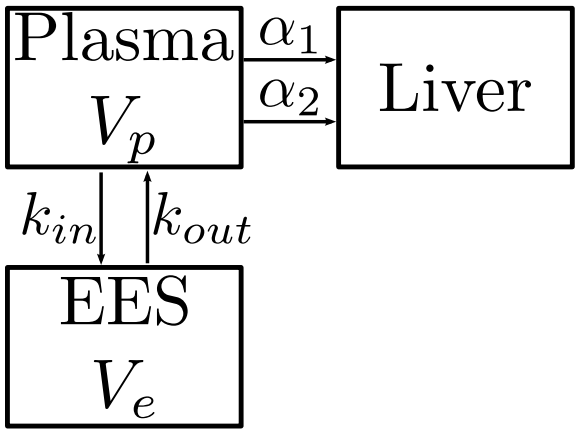

Figure A.1: Schematic of two-compartment model from Cuccia[173]. Compartments are blood plasma (volume, V_p) and extra-vascular, extracellular space (EES, volume, V_e). Cuccia assumes a bi-exponential (α_1 and α_2) elimination by the liver and exchange between the plasma and EES (k_{in}, plasma to EES and k_{out}, EES to plasma).

recirculation time (i.e. ignore the plasma distribution in the initial bolus) , we can derive:

$$\begin{aligned} C_T[t] =& A_1\left(V_p + \frac{V_e k_{in}}{k_{out}-\alpha_1}\right)e^{-\alpha_1 t} + A_2\left(V_p + \frac{V_e k_{in}}{k_{out}-\alpha_2}\right)e^{-\alpha_2 t} \\ &- \left[A_1\left(\frac{V_e k_{in}}{k_{out}-\alpha_1}\right) + A_2\left(\frac{V_e k_{in}}{k_{out}-\alpha_2}\right)\right]e^{-k_{out}t} \end{aligned} \tag{A.4}$$

This solution for $C_T[t]$ has eight parameters; we can improve the stability of the fit by reducing or constraining them. Note, V_e and k_{in} only appear as a product, permitting us to eliminate one variable by defining $\kappa = V_e k_{in}$. As noted above, V_p is proportional to measuredHb_t.

$$V_p = \frac{Hb_t}{Hb_B}\left(\frac{100 - Hct}{Hct}\right) = Hb_t\zeta \simeq 2.415 \times 10^{-4} \times Hb_t \tag{A.5}$$

where $Hb_B \simeq 5,421\mu M$ is the average concentration of hemoglobin in each blood cell (32-36 g/dL; ~27-33pg[66]) and Hct is the hematocrit; for convenience, these factors are lumped into ζ, a constant for any particular patient. In healthy adult females, the hematocrit is $\sim 36 - 45\%$[311]. (For other applications, note that male hematocrit is ~41-51%.) With these substitutions, Eqn. A.4 reduces to

$$\begin{aligned} C_T[t] =& A_1\left(Hb_t\zeta + \frac{\kappa}{k_{out}-\alpha_1}\right)e^{-\alpha_1 t} + A_2\left(Hb_t\zeta + \frac{\kappa}{k_{out}-\alpha_2}\right)e^{-\alpha_2 t} \\ &- \left[A_1\left(\frac{\kappa}{k_{out}-\alpha_1}\right) + A_2\left(\frac{\kappa}{k_{out}-\alpha_2}\right)\right]e^{-k_{out}t} \end{aligned} \tag{A.6}$$

We can further simplify this expression by noting that long term ICG elimination is on the order of hours, so $\alpha_1 \simeq 0$

$$\begin{aligned} C_T[t] =& A_1\left(Hb_t\zeta + \frac{\kappa}{k_{out}}\right) + A_2\left(Hb_t\zeta + \frac{\kappa}{k_{out}-\alpha_2}\right)e^{-\alpha_2 t} \\ &- \left[A_1\left(\frac{\kappa}{k_{out}}\right) + A_2\left(\frac{\kappa}{k_{out}-\alpha_2}\right)\right]e^{-k_{out}t} \end{aligned} \tag{A.7}$$

(Equation 5.1). ICG absorption data can then be fitted to this function. I thank Dr. Ulas Sunar for providing the original codes I used for this analysis. Note that Hagen[190] has recently reported fluorescence imaging of ICG in breast cancers up to 24 hours after a consistent (not bolus) infusion.

The two compartment fit described in Equation 5.1 above has six parameters after simplification. We also utilized a heuristic double exponential fit:

$$C[t] = A\left(-e^{-k_1(t-t_0)} + e^{-k_2(t-t_0)}\right) \tag{A.8}$$

(Equation 5.2). We found that the double exponential fit was more stable for low time resolution data, but it does not have the obvious physiological interpretation of Equation 5.1. Examples of data fit to both models is shown in Figure 5.4. Note that the double exponential model has difficulty fitting the lope of the curve; especially on peaked data such as shown here, the downslope tends to be over estimated.

Appendix B

Additional Plots for Compression Version 3 Results

This section expands on the data shown in Section 8.4.3 by showing separate fits (Figure B.1-B.4) to data from first and second breast compressions described in Section 8.4.2. We do not observe significantly different responses to sequential compression in the present data.

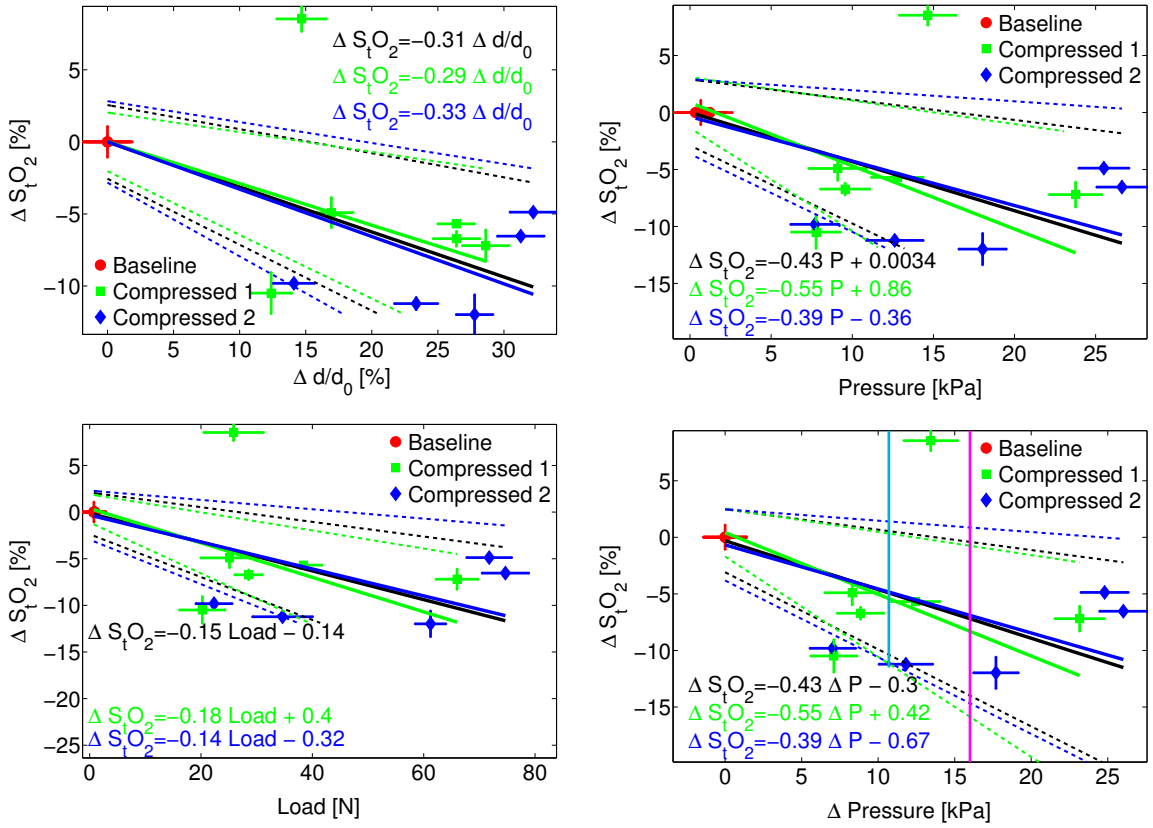

Figure B.1: Observed changes in blood oxygenation (StO_2) versus Load, Pressure, and change in plate separation ($\Delta d/d_0$) in 6 measurement series (see Figure 8.14) on 5 subjects. Pressure reported is the average between the five sensors with highest pressure readings for a particular subject. Data from the first compression (green), second compression (blue), and baseline (red) periods are plotted separately, with corresponding individual and joint (black) fits. Dashed lines indicate 95% confidence intervals. Note, the same data is shown in fig:compV3:res:deltaSat. Normal systolic (magenta) and diastolic (cyan) blood pressures[66] are included for comparison.

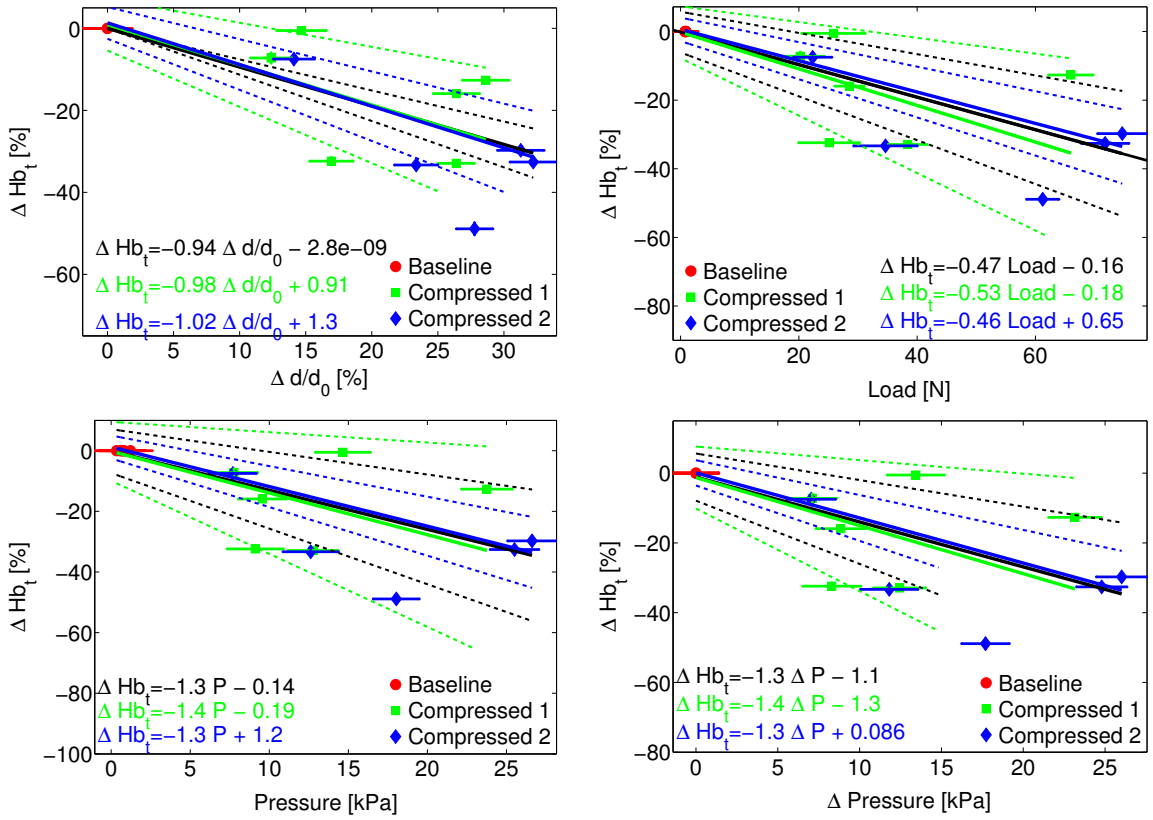

Figure B.2: Observed changes in total hemoglobin concentration (Hb_t) versus Load, Pressure, and change in plate separation ($\Delta d/d_0$) in 6 measurement series (see Figure 8.14) on 5 subjects. Pressure reported is the average between the five sensors with highest pressure readings for a particular subject. Data from the first compression (green), second compression (blue), and baseline (red) periods are plotted separately, with corresponding individual and joint (black) fits. Dashed lines indicate 95% confidence intervals. Note, the same data is shown in fig:compV3:res:deltaHb. Normal systolic (magenta) and diastolic (cyan) blood pressures[66] are included for comparison.

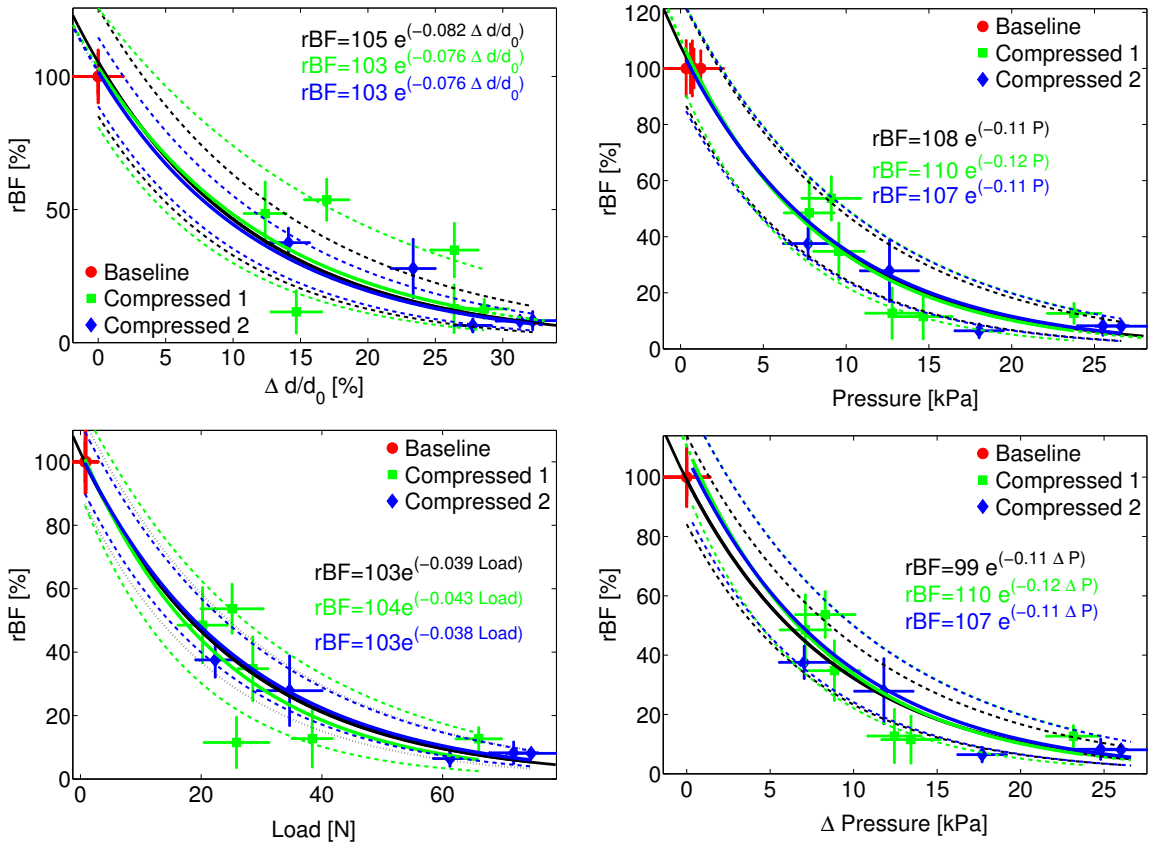

Figure B.3: Observed changes in relative blood flow (rBF) versus Load, Pressure, and change in plate separation ($\Delta d/d_0$) in 6 measurement series (see Figure 8.14) on 5 subjects. Pressure reported is the average between the five sensors with highest pressure readings for a particular subject. Data from the first compression (green), second compression (blue), and baseline (red) periods are plotted separately, with corresponding individual and joint (black) fits. Dashed lines indicate 95% confidence intervals. Note, the same data is shown in fig:compV3:res:deltaRBF. Normal systolic (magenta) and diastolic (cyan) blood pressures[66] are included for comparison.

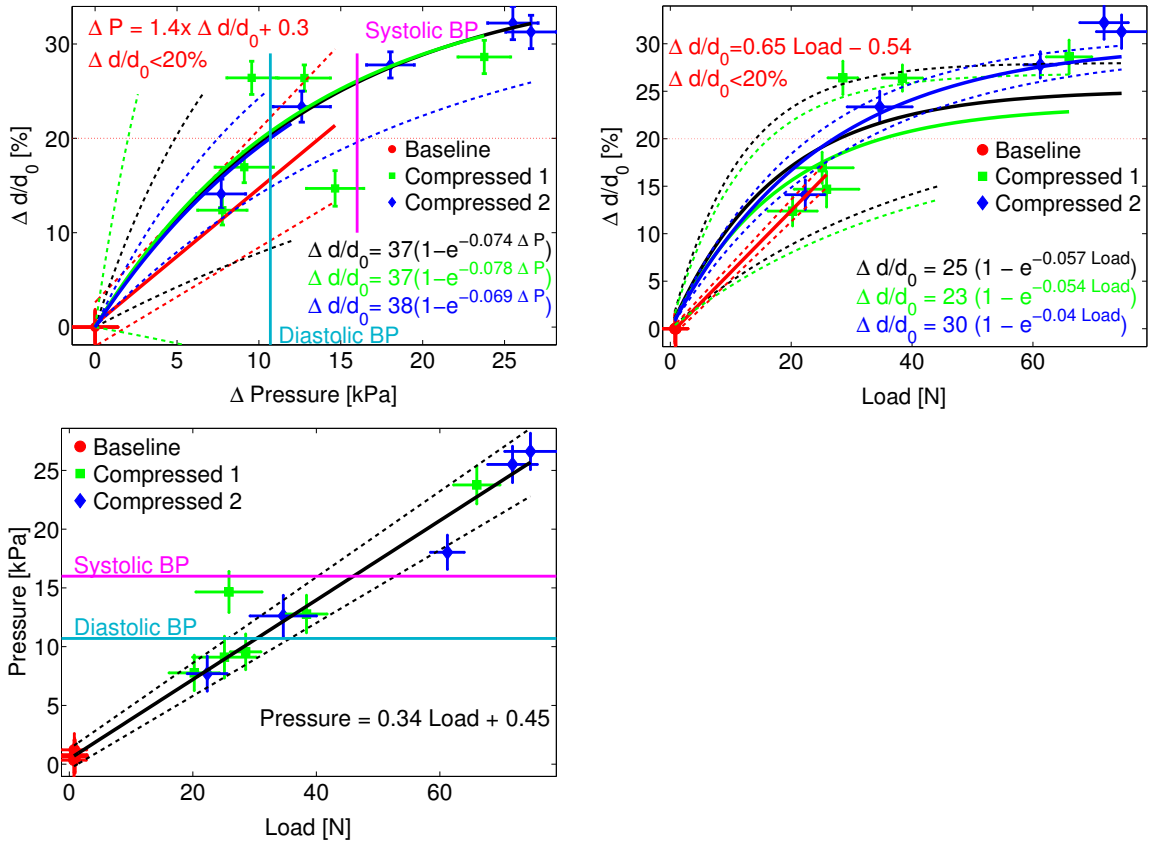

Figure B.4: Comparison between Load, Pressure, and change in plate separation ($\Delta d/d_0$) in 6 measurement series (see Figure 8.14) on 5 subjects. Pressure reported is the average between the five sensors with highest pressure readings for a particular subject. Data from the first compression (green), second compression (blue), and baseline (red) periods are plotted separately, with corresponding individual and joint (black) fits, along with a linear fit to the low-compression region ($\Delta d/d_0 < 20\%$, red). Dashed lines indicate 95% confidence intervals. Note, the same data is shown in fig:compV3:res:loadDistPres. Normal systolic (magenta) and diastolic (cyan) blood pressures[66] are included for comparison.

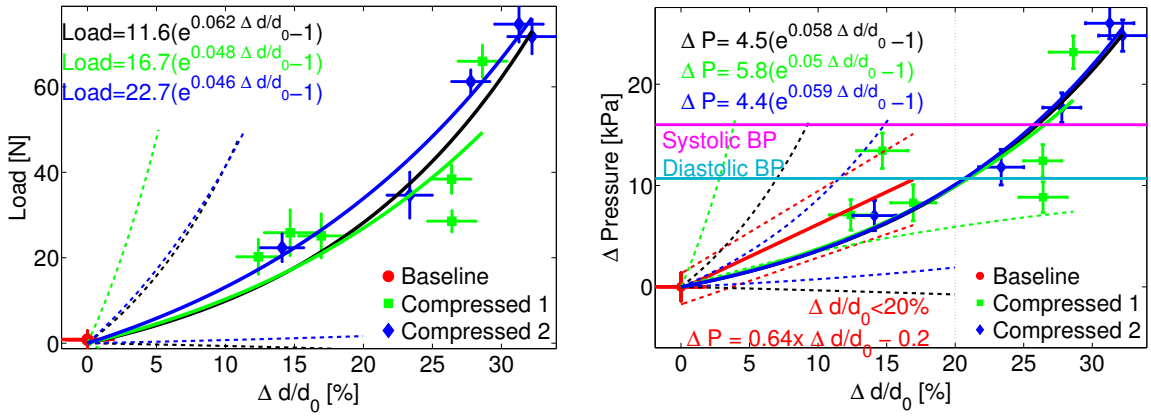

Figure B.5: Comparison of applied Load and Pressure to fractional change in plate separation (strain) using the Version 3 compression system. ($\Delta d/d_0$) in 6 measurement series (see Figure 8.14) on 5 subjects. Pressure reported is the average between the five sensors with highest pressure readings for a particular subject. (top row) Data from the first compression (green), second compression (blue), and baseline (red) periods are plotted separately, with corresponding individual and joint fits. (bottom row) Combined data set with joint (black) fits, along with linear fits to the low-compression region ($\Delta d/d_0 < 20\%$, red). Data in these plots is also shown in Figure 8.20 with the abscissae and ordinates exchanged. Dashed lines indicate 95% confidence intervals of the fit parameters.

Appendix C

Phantoms

C.1 Liquid and Gelatin Phantoms

This is a brief description of some of the phantoms I've used in my work with DOT/DOS. For a more complete explanation, I highly recommend Dr. Regine Choe's careful explanation of the recipes for various phantoms in her thesis[312]. This work has excellent step-by-step instructions for solid and liquid phantoms, including oxygenation phantoms using blood.

I have primarily utilized liquid phantoms in this work. This allowed me to adjust the absorption, scattering, and geometry to my experiment. Gelatin phantoms utilize the same ingredients as liquid phantoms, added to cooked gelatin during cooling. If one requires a phantom to function at only a single wavelength or one is not planning on using spectral priors in one's computations, a phantom with little or no wavelength dependence is both sufficient and simpler to construct. India ink provides an inexpensive and convenient choice of absorber, but tends to sediment out and the absorbence should be measured the day of the phantom construction. Absorption measured with a spectrophotometer at a specific wavelength allows calculation of the necessary concentration of ink in the final phantom volume. Note the difference in bases between typical spectrophotometer measurements (base 10) and μ_a (base e).

Given that much of the work in DOT and DOS focuses on measurement of blood concentration and oxygenation, it is natural to use for *in vitro* phantoms. One can control the oxygenation through the addition of yeast or carefully controlling the oxygen levels in the gas available for exchange with the phantom. However, blood phantoms are biohazards, cannot be used for more then a few hours, and, given variations in the blood supply, are somewhat difficult to reproduce accurately. Note that it is necessary to lyse red blood cells (as they are significant scatterers), remove the cell membranes, and measure the hemoglobin of each blood sample as the hematocrite can vary significantly between blood donors. As such, it is sometimes

convenient to use various colored inks to produce a more durable wavelength dependent phantom. Inks with features in the measured spectral window are useful for multi-spectral reconstructions or measurements.

Spectra of several useful inks are shown in Figure C.1 (Nigrosin[i], Higgins drawing inks[ii], ICG[iii], and Epolight 2717[iv]).

With the exception of the ink, the spectra for the chromophores mentioned above are available at the wonderfully helpful website of the Oregon Medical Laser Center[v]. Multi-dye phantoms (e.g. Nigrosin and Epolight 2717 in Figure C.1) allow independent titration and simulation of Hb and HbO_2 (e.g. Figure 3.3), permitting more convenient instrument testing than adjusting the saturation in blood phantoms.

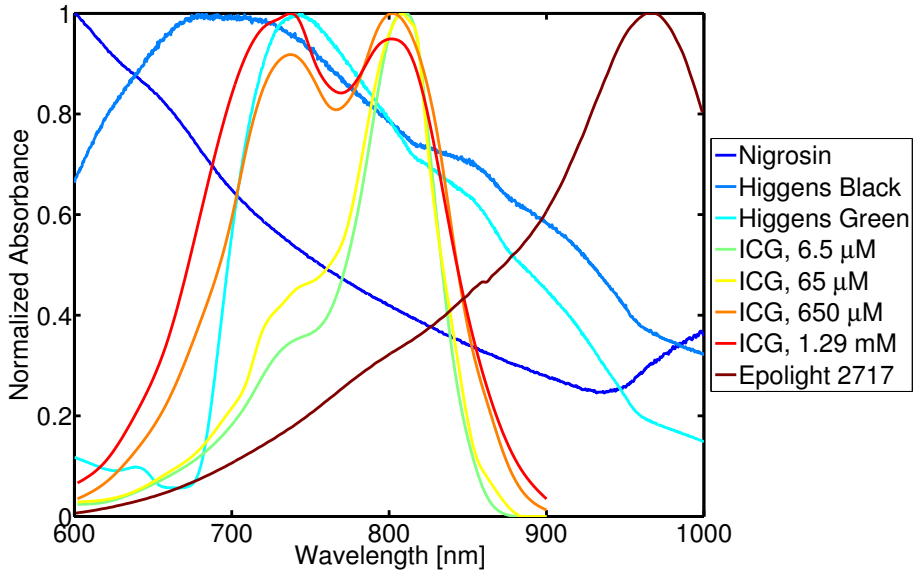

Figure C.1: Spectra of several inks used in DOS/DOT phantoms. Spectra are normalized for display purposes. Note that ICG spectra are concentration dependent. ICG spectra were obtained from *http://omlc.ogi.edu/spectra/*; the remaining spectra were measured in our lab.

Several different scattering agents are used in diffuse optics, including those listed in Table C.1. The soy emulsions are intended for therapeutic injection and are packaged in sterile vessels; this can be advantageous in phantoms or matching fluids which will come into contact with human subjects. Mono-dispersed microspheres allow calculation of scattering properties with Mie theory, but are generally too expensive for large volumes. The hollow latex spheres in Ropaque® Ultra E are much less expensive, but also much less well characterized. As much of the breast DOT work in our lab uses a scattering bath as a matching fluid, we made almost all of our liquid and gelatin phantoms with soy emulsions.

[i] Sigma-Aldrich, *www.sigmaaldrich.com*
[ii] Higgins *www.higginsinks.com/*
[iii] Akorn, *www.akorn.com*
[iv] Epolin, *www.epolin.com*
[v] *http://omlc.ogi.edu/spectra*, accessed June 2007.

Soy Emulsions	Intralipid	Pharmacia and Upjohn, Erlangen, Germany, invented by Wretlind[313]
	Liposyn II	Hospira Inc, Lake Forest IL.
Polymer Spheres	Ropaque® Ultra E	Rohm and Hass, Philadelphia PA
	Microspheres	Various suppliers
	Milk	Homogenized

Table C.1: Scattering agents used in DOS/DOT phantoms. Soy Emulsions were introduced into diffuse optics by Driver[314].

As my measurements included TRS data, I measured the absolute properties of each phantom at the time of use (with the exception of the high absorption of some targets produced by adding additional ink to the background fluid; these absorptions were calculated from spectroscopic measurements of serial dilutions of the ink added). However, I required a formula to calculate the approximate parameters of the phantom based on the ratio of ingredients so as to match the phantom to the particular task at hand. Determining the quantity of ink to add to the phantom simply requires a measurement with a spectrophotometer and then calculation of the dilution required to bring the phantom to the desired μ_a. I obtained a calibration curve to relate the quantity of 30% Liposyn III to the resulting scattering and found the relationship to be quite close to linear over the tested range of 5-15 cm^{-1} at 785 nm.

$$\mu_s' = 260x + 2.3 \tag{C.1}$$

where x is the fractional volume of Intralipid (i.e. for 60 ml in 2 L x=60/2000=0.03). The resulting values are in fairly close agreement with Choe[312] and van Staveren *et al.*[315].

We utilize gelatin phantoms for several studies where liquid phantoms are inconvenient. Our basic recipe, listed in Table C.2, is based of that from Soren D. Konecky and has contributions from Ellen Foster and Tiffany Alverna.

De-Gassed Water	4250 ml
Gelatin	300 g
NaCl	7.5 g
Sodium Azide	21 g
20% Intralipid	350 ml

Table C.2: Basic gelatin phantom recipe for phantoms totaling 4.25 L. Sodium Azide is a mitochondrial poison used to increase the phantom life and NaCl to make the phantom visible in MR images. Gelatin (from porcine skin, Sigma-Aldrich) is included at 70 g per liter.

We typically make gelatin phantoms with inclusions of contrasting absorption or scattering to serve as targets. These inclusions are best introduced to the gelatin phantom after the background has solidified overnight and just before the target solution solidifies.

The sequence of events for a typical phantom used with our imaging systems is as follows:

1 Mix 182 g gelatin to 2,600 ml *cold* stock solution.

2 Heat and stir solution (∼5 minutes in microwave) until gelatin is completely dissolved.

3 Pour solution into mold.

4 Add 1,200 ml (cold) stock solution.

5 Stir thoroughly.

6 Wait until solution reaches room temperature, *do not* allow to solidify.

7 Add 160 ml Intralipid and ink as appropriate for desired absorption.

8 Stir thoroughly.

9 Cover and place in refrigerator to solidify. If mold is sealed, rotating the mold during the solidification process improves homogeneity.

10 If inclusions are to be added, follow above procedure until target gelatin solution is almost solidified, cut an inclusion in background phantom, and add target solution.

We have noted that air bubble formation can be reduced by degassing any liquids used and by stirring the viscous gelatin solution slowly. We have found the optimal cooling technique to be placing the hot gelatin solution in a cold room on a stir plate with a large magnetic stir bar. This keeps the solution mixed until it solidifies.

C.2 Compression Phantoms

The compression systems required separate phantoms to test the optics and the load and pressure sensors. The optical phantoms were liquid-filled balloons, allowing adjustment of the plate separation. Production of liquid phantoms is described in Section C.1. Note: the use of large balloons (to minimize stretching), preferably one inside another, will reduce the rupture rate of this particular phantom.

The load sensor were calibrated using a digital scale and foam rubber to protect the pressure sensors. This calibration varied less than 5% over the course of a week.

Pressure sensors were calibrated using a rubber bladder and calibrated gas pressure gauge. We utilized a bladder from a thigh blood pressure cuff to apply equal pressure across the entire compression plate. We were somewhat concerned with the possibility of skin-sensor coupling, especially due to sheer forces. Differences between measurements with rubber bladders and volunteer's tissue was clearly observed for the 'piston' pressure sensor described in Section 8.2.2; we had much less difficulty using flat resistive sensors

described in the same section. We attempted to model the tissue-plate coupling during calibration by using $\sim$1.5 cm slices of meat and liver obtained from a local butcher. These phantoms displayed similar reductions in load after compression as tissue. At least part of this effect was due to the internal pressure forcing out remnant blood out of the meat and liver. Allowing for this falloff in pressure under compression, the resistive sensors showed little difference in results between plate to rubber bladder or plate to meat coupling.

Glossary

—— ——

λ Wavelength in nm.

μ_s' Reduced Scattering coefficient.

μ_a Absorption Coefficient.

ω Angular Frequency.

Ψ Photon Fluence Rate.

$\mathbf{z}_0$ $z_0 = {\mu_s'}^{-1}$. A diffuse optics source is often modeled as a point source displaced z_0 into the medum, instead of a source with a specified numerical aperature placed on the medium boundary.

—— A ——

ABI Advanced Breast Imaging Study, PI: Dr. Mitchell Schnall.

ACRIN American College of Radiology Imaging Network.

angiogenesis The development of new blood-vessels, often refering to vascular growth around a cancerous lesion.

ANSI American National Standards Institute.

APD Avalanche Photo Diode.

ASL Arterial Spin Labeling.

AUC Area Under the Receiver Operating Characteristic (ROC) Curve.

—— B ——

BH Becker and Hickl Gmbh.

Body Mass Index Body Mass Index, the ratio of a person's mass in kg to the square of his height in m.

BOLD Blood Oxygenation Level Dependent (fMRI signal).

—— C ——

c Speed of light in the relevant medium.

CCD Charge Coupled Device.

CE-MRI Contrast Enhanced Magnetic Resonance Imaging, typically with a gadolinium chelate such as Gd-DTPA.

CFD Constant Fraction Discriminator.

CMROI Center for Magnetic Resonance and Optical Imaging, an NIH-funded Research Resource at the University of Pennsylvania.

CAD Computer Aided Diagnosis; Use of computerized algorithms to assist in the identification of disease states.

CT X-Ray Computerized Tomography.

CW Continuous Wave (i.e. FD with ω =0).

—— D ——

D_0 Homogeneous Photon Diffusion Coefficient.

Da Dalton, a unit of mass equal to one twelfth of the rest mass of an unbound atom of carbon-12 in its nuclear and electronic ground state.

Dartmouth Dartmouth College.

DCS Diffuse Correlation Spectroscopy.

DCT Diffuse Correlation Tomography.

DOBI DOBI Medical International Inc, Mahwah, NJ. ComfortScan© *http://dobiglobal.com/dobisys1.html*, now available from *www.xinaomdt.com/en/*.

DOS Diffuse Optical Spectroscopy.

DOT Diffuse Optical Tomography.

DP Differential Path length (see DPF).

DPDW Diffuse Photon Density Wave.

DPF Differential Path length Factor.

DWS Diffusing Wave Spectroscopy.

—— E ——

EES Extravascular, Extracellular Space.

—— F ——

False Positive Rate Fraction of incorrectly classified 'positive' subjects in a binary classification test.

FD Frequency Domain.

FDA United States Food and Drug Administration.

FDG Fluoro-deoxyglucose, an F^{18} PET agent.

fDOS Functional DOS.

FDOT Fluorescent Diffuse Optical Tomography.

FEM Finite Element Method.

fiducial A fiducial marker allows registration of coordinate systems; here, the markers are rigidly fixed in the breast compression plates and are visible in the MR images.

fluence Flux of particles through a specified area.

fM Femto-Molar (10^{-12}).

fMRI Functional MRI.

fNIRS Functional NIRS.

FOV Field of View.

FWHM Full Width at Half Maximum value.

—— G ——

Gd Gadolinium, MRI contrast agent.

Gd-DTPA Gadolinium Diethylenetriamine Penta-acetic Acid; commonly used Gd chelate for MRI contrast.

Generation I, GenI First Generation University of Pennsylvania simultaneous time-resolved optical and magnetic resonance imaging system, built by V. Ntziachristos and X. Ma.

Generation II, GenII Second Generation University of Pennsylvania simultaneous time-resolved optical and magnetic resonance imaging system, built by X. Intes and J. Yu, used for clinical experiments by D. Busch and Z. Zhao.

Generation III, GenIII Third Generation University of Pennsylvania simultaneous time-resolved optical and magnetic resonance imaging system, built by D. Busch.

Gold-Standard A benchmark test, assumed to be perfectly accurate, to which other classification techniques are compared.

—— H ——

hematocrit Percentage of whole blood occupied by red blood cells.

Hb Hemoglobin.

HbO_2 Oxy-hemoglobin.

Hb_t Total hemoglobin concentration, Hb_t=Hb+HbO_2.

H_2O Water.

HUP Hospital of the University of Pennsylvania.

—— I ——

ICG Indocyanine Green.

IRB Institutional Safety Review Board.

IRF Instrument Response Function, in TD measurements, the convolution of the pulse width of the laser, the broadening introduced by the source and detector fibers, and the broadening introduced by the response time of the detector.

IV Intravenous, usually referring to a line for injection of drugs.

—— K ——

$\mathbf{k}_0$ Complex wavenumber of DPDW.

—— L ——

$\mathbf{l}_a$ Mean free path between absorption events.

LD Laser Diode.

$\mathbf{l}_s$ Mean free path between scattering events.

—— M ——

MFP Mean free path, the average distance traveled prior to a certain type of interaction, for example scattering.

MGH Massachusetts General Hospital.

MHz MegaHertz=10^6Hz.

MPE Maximum Permissible Exposure; regulatory limit on the optical power which may be applied to human tissue.

MR Magnetic Resonance.

MRI Magnetic Resonance Imaging.

—— N ——

NA Numerical Aperature; sine of the half acceptance angle to an optical system, multiplied by the index of rrefraction $NA = nSin[\theta]$.

NIR Near Infrared ($\sim$650-950nm).

NIRS Near Infrared Spectroscopy; synonym for DOS.

—— O ——

OI Optical Index. Composite parameter to increase breast cancer contrast developed at the University of Pennsylvania.

optodes Collectively, source and detector optical fibers, in analogy with 'electrodes'.

—— P ——

PD Photodiode.

PDT Photo-dynamic Therapy.

Penn Pennsylvania, University of.

PET Positron Emission Tomography.

—— D ——

D Photon Diffusion Coefficient, $D = \frac{v}{3\mu_s'}$ $[cm^2 s^{-1}]$.

—— P ——

PMT Photomultiplier tube.

ps Pico second, 10^-12s.

PTB Physikalisch-Technische Bundesanstalt, German national metrology institute.

—— R ——

RBC Red Blood Cell.

rBF Relative Blood Flow.

RF Radio Frequency.

ROC Receiver Operating Characteristic (ROC). Often, ROC curve; plot of the true positive vs. false positive rates of a particular test, e.g., of malignancy.

RTE Radiative Transport Equation.

—— S ——

saturation Blood Oxygen Saturation, StO_2 =HbO_2/Hb_t.

sensitivity Sensitivity of a test to a condition; the true positive rate.

SNL Sentinel Lymph Node.

SNR Signal to Noise Ratio.

specificity Specificity of a test; the true negative rate (1 minus the false positive rate).

SVD Singular Value Decomposition.

—— T ——

T_1 Population Decay Time, can be utilized to distinguish between fatty and glandular (more water bearing) tissue to provide information on tissue structure from MRI exams.

T_2 Phase Decay Time, from MRI.

TCSPC Time Correlated Single Photon Counting.

TD Time Domain.

TD-DOS Time Domain Diffuse Optical Spectroscopy.

TIBS Transit Time Spread.

TOAST Time-resolved Optical Absorption and Scattering Tomography software package, developed by Dr. Simon Arridge and Dr. Martin Schweiger at University College London[85,86].

TOI Tissue Optical Index. Composite parameter to increase breast cancer contrast developed at University of California at Irvine.

transillumination Transillumination: illuminating a quasi-slab shaped sample on one face and detecting the transmitted light on the other.

TRS Time Resolved Spectroscopy, often used as a synonym for TD-DOS.

True Negative Rate Fraction of correctly classified 'negative' subjects in a binary classification test.

True Positive Rate Fraction of correctly classified 'positive' subjects in a binary classification test.

True Positive Rate Fraction of correctly classified 'positive' subjects in a binary classification test.

tSVD Truncated Singular Value Decomposition, in which singular values less than some cutoff value are set to zero.

TTS Transit Time Spread.

—— U ——

UCI University of California, Irvine.

—— V ——

ViOptix Commercial optical instrument maker, constructed handheld breast compression device[167]; *www.vioptix.com*.

—— X ——

X-Ray Tomography CT reconstruction of tomographic images from a limited selection of angular projections.

—— Z ——

Z-Score A normalization procedure, in which a data vector is transformed by subtracting the mean and dividing the result by the standard deviation.

Bibliography

[1] D. R. Leff, O. J. Warren, L. C. Enfield, A. Gibson, T. Athanasiou, D. K. Patten, J. Hebden, G. Z. Yang, and A. Darzi. Diffuse optical imaging of the healthy and diseased breast: a systematic review. *Breast Cancer Research Treat* **108**(1), 9–22 Mar (2008).

[2] R. Boushel, H. Langberg, J. Olesen, J. Gonzales-Alonzo, J. Bulow, and M. Kjaer. Monitoring tissue oxygen availability with near infrared spectroscopy (NIRS) in health and disease. *Scandinavian Journal of Medicine & Science in Sports* **11**(4), 213 (2001).

[3] M. Wolf, M. Ferrari, and V. Quaresima. Progress of near-infrared spectroscopy and topography for brain and muscle clinical applications. *Journal of Biomedical Optics* **12**(6), 062104 (2007).

[4] G. Strangman, D. A. Boas, and J. P. Sutton. Non-invasive neuroimaging using near-infrared light. *Biolgical Psychiatry* **52**(7), 679–693 Oct (2002).

[5] V. Ntziachristos, A. G. Yodh, M. Schnall, and B. Chance. Concurrent MRI and diffuse optical tomography of breast after indocyanine green enhancement. *Proceedings of The National Academy of Sciences of the USA* **97**, 2767–2772 (2000).

[6] V. Ntziachristos, A. G. Yodh, M. D. Schnall, and B. Chance. MRI-guided diffuse optical spectroscopy of malignant and benign breast lesions. *Neoplasia* **4**, 347–354 (2002).

[7] B. Brooksby, S. Jiang, H. Dehghani, B. W. Pogue, K. D. Paulsen, J. Weaver, C. Kogel, and S. P. Poplack. Combining near-infrared tomography and magnetic resonance imaging to study in vivo breast tissue: implementation of a laplacian-type regularization to incorporate magnetic resonance structure. *Journal of Biomedical Optics* **10**(5), 051504 (2005).

[8] C. M. Carpenter, B. W. Pogue, S. Jiang, H. Dehghani, X. Wang, K. D. Paulsen, W. A. Wells, J. Forero, C. Kogel, J. B. Weaver, S. P. Poplack, and P. A. Kaufman. Image-guided optical spectroscopy provides molecular-specific information in vivo: MRI-guided spectroscopy of breast cancer hemoglobin, water, and scatterer size. *Optics Letters* **32**(8), 933–935 Apr (2007).

[9] Q. Zhu, T. Durduran, V. Ntziachristos, M. Holboke, and A. G. Yodh. Imager that combines near-infrared diffusive light and ultrasound. *Optics Letters* **24**, 1050–1052 (1999).

[10] A. Li, E. L. Miller, M. E. Kilmer, T. J. Brukilacchio, T. Chaves, J. Stott, Q. Zhang, T. Wu, M. Chorlton, R. H. Moore, D. B. Kopans, and D. A. Boas. Tomographic optical breast imaging guided by three-dimensional mammography. *Applied Optics* **42**(25), 5181–5190 Sep (2003).

[11] N. Shah, J. Gibbs, D. Wolverton, A. Cerussi, N. Hylton, and T. BJ. Combined diffuse optical spectroscopy and contrast-enhanced magnetic resonance imaging for monitoring breast cancer neoadjuvant chemotherapy: a case study. *Journal of Biomedical Optics* **10**(5), 051503 (2005).

[12] B. W. Pogue, S. P. Poplack, T. O. McBride, W. A. Wells, K. S. Osterman, U. L. Osterberg, and K. D. Paulsen. Quantitative hemoglobin tomography with diffuse near-infrared spectroscopy: pilot results in the breast. *Radiology* **218**(1), 261 (2001).

[13] S. Srinivasan, B. W. Pogue, B. Brooksby, S. Jiang, H. Dehghani, C. Kogel, W. A. Wells, S. P. Poplack, and K. D. Paulsen. Near-infrared characterization of breast tumors in vivo using spectrally-constrained reconstruction. *Technology in Cancer Researchearch and Treatment* **4**(5), 513–526 Oct (2005).

[14] C. Li, S. R. Grobmyer, N. Massol, X. Liang, Q. Zhang, L. Chen, L. L. Fajardo, and H. Jiang. Non-invasive in vivo tomographic optical imaging of cellular morphology in the breast: possible convergence of microscopic pathology and macroscopic radiology. *Medical Physics* **35**(6), 2493–2501 Jun (2008).

[15] Q. Zhu, S. H. Kurtzma, P. Hegde, S. Tannenbaum, M. Kane, M. Huang, N. G. Chen, B. Jagjivan, and K. Zarfos. Utilizing optical tomography with ultrasound localization to image heterogeneous hemoglobin distribution in large breast cancers. *Neoplasia* **7**(3), 263–270 Mar (2005).

[16] S. R. Arridge and M. Schweiger. Inverse methods for optical tomography. In *Information Processing in Medical Imaging (IPMI'93 Proceedings), Lecture Notes in Computer Science* volume 687 pages 259–277. Springer-Verlag (1993).

[17] S. R. Arridge and J. C. Hebden. Optical imaging in medicine: Ii. modelling and reconstruction. *Physics in Medicine and Biology* **42**(5), 841–853 May (1997).

[18] S. R. Arridge. Optical tomography in medical imaging. *Inverse Problems* **15**, R41–R93 (1999).

[19] D. A. Boas, T. Gaudette, G. Strangman, X. Cheng, J. J. Marota, and J. B. Mandeville. The accuracy of near infrared spectroscopy and imaging during focal changes in cerebral hemodynamics. *Neuroimage* **13**(1), 76–90 Jan (2001).

[20] A. G. Yodh and D. A. Boas. *Biomedical Photonics Handbook* chapter Functional Imaging with Diffusing Light, pages 21–1 – 21–45. CRC Press (2003).

[21] A. P. Gibson, J. C. Hebden, and S. R. Arridge. Recent advances in diffuse optical imaging. *Physics in Medicine and Biology* **50**, R1 (2005).

[22] S. L. Jacques and B. W. Pogue. Tutorial on diffuse light transport. *Journal of Biomedical Optics* **13**(4), 041302–1:19 (2008).

[23] A. Gibson and H. Dehghani. Diffuse optical imaging. *Philosophical Transactions of the Royal Society A: Mathematical, Physical and Engineering Sciences* **367**(1900), 3055 (2009).

[24] S. Arridge and J. Schotland. Optical tomography: forward and inverse problems. *Inverse Problems* **25**(12), 123010 (59pp) (2009).

[25] T. Durduran, R. Choe, W. B. Baker, and A. G. Yodh. Diffuse optics for tissue monitoring and tomography. *Reports on Progress in Physics* **73**(7), 076701 June (2010).

[26] S. H. Chung, A. E. Cerussi, C. Klifa, H. M. Baek, O. Birgul, G. Gulsen, S. I. Merritt, D. Hsiang, and B. J. Tromberg. In vivo water state measurements in breast cancer using broadband diffuse optical spectroscopy. *Physics in Medicine and Biology* **53**(23), 6713–6727 Dec (2008).

[27] P. Taroni, A. Pifferi, E. Salvagnini, L. Spinelli, A. Torricelli, and R. Cubeddu. Seven-wavelength time-resolved optical mammography extending beyond 1000 nm for breast collagen quantification. *Optics Express* **17**(18), 15932–15946 (2009).

[28] M. J. Holboke, B. J. Tromberg, X. Li, N. Shah, J. Fishkin, D. Kidney, J. Butler, B. Chance, and A. G. Yodh. Three-dimensional diffuse optical mammography with ultrasound localization in a human subject. *Journal of Biomedical Optics* **5**, 237–247 (2000).

[29] S. D. Konecky, R. Choe, A. Corlu, K. Lee, R. Wiener, S. M. Srinivas, J. R. Saffer, R. Freifelder, J. S. Karp, N. Hajjioui, F. Azar, and A. G. Yodh. Comparison of diffuse optical tomography of human breast with whole-body and breast-only positron emission tomography. *Medical Physics* **35**(2), 446–455 Feb (2008).

[30] F. S. Azar, K. Lee, A. Khamene, R. Choe, A. Corlu, S. D. Konecky, F. Sauer, and A. G. Yodh. Standardized platform for coregistration of nonconcurrent diffuse optical and magnetic resonance breast images obtained in different geometries. *Journal of Biomedical Optics* **12**(5), 051902 (2007).

[31] R. Choe, S. D. Konecky, A. Corlu, K. Lee, T. Durduran, D. R. Busch, B. J. Czerniecki, J. Tchou, D. L. Fraker, A. DeMichele, B. Chance, S. R. Arridge, M. Schweiger, J. P. Culver, M. D. Schnall,

M. E. Putt, M. A. Rosen, and A. G. Yodh. Differentiation of benign and malignant breast tuqmors by in-vivo three-dimensional parallel-plate diffuse optical tomography. *Journal of Biomedical Optics* **14**(2), 024020 (18pp) (2009).

[32] M. Cutler. Transillumination as an aid in the diagnosis of breast lesions. *Surgery Gynecology and Obstetetrics* **48**, 721–29 (1929).

[33] M. Cutler. Transillumination of the breast. *Annals of Surgery* **93**(1), 223–234 Jan (1931).

[34] F. F. Jobsis. Noninvasive, infrared monitoring of cerebral and myocardial oxygen sufficiency and circulatory parameters. *Science* **198**(4323), 1264–1267 (1977).

[35] K. M. Case and P. F. Zweifel. *Linear Transport Theory*. Addison-Wesley (1967). Lib. Congress 67-17256.

[36] A. G. Yodh and B. Chance. Spectroscopy and imaging with diffusing light. *Physics Today* , 34–40 March (1995).

[37] A. D. Klose and A. H. Hielscher. Optical tomography with the equation of radiative transfer. *International Journal of Numerical Methods for Heat and Fluid Flow* **18**(3/4), 443 (2008).

[38] V. G. Peters, D. R. Wyman, M. S. Patterson, and G. L. Frank. Optical properties of normal and diseased human breast tissues in the visible and near infrared. *Physics in Medicine and Biology* **35**(9), 1317 (1990).

[39] W. F. Cheong, S. A. Prahl, and A. J. Welch. A review of the optical properties of biological tissues. *Quantum Electronics, IEEE Journal of* **26**(12), 2166–2185 Dec (1990).

[40] R. C. Haskell, L. O. Svaasand, T. T. Tsay, T. C. Feng, M. S. McAdams, and B. J. Tromberg. Boundary-conditions for the diffusion equation in radiative-transfer. *Journal of the Optical Society of America* **11(10)**, 2727–2741 (1994).

[41] R. Aronson. Boundary conditions for diffusion of light. *Journal of Optical Society of America A* **12**(11), 2532–2539 Nov (1995).

[42] D. Contini, F. Martelli, and G. Zaccanti. Photon migration through a turbid slab described by a model based on diffusion approximation. i. theory. *Applied Optics* **36**(19), 4587–4599 Jul (1997).

[43] T. J. Farrell, M. S. Patterson, and B. Wilson. A diffusion theory model of spatially resolved, steady-state diffuse reflectance for the noninvasive determination of tissue optical properties in vivo. *Medical Physics* **19**(4), 879–888 (1992).

[44] M. S. Patterson, B. Chance, and B. C. Wilson. Time resolved reflectance and transmittance for the noninvasive measurement of tissue optical properties. *Applied Optics* **28**, 2331–2336 (1989).

[45] A. Liebert, H. Wabnitz, D. Grosenick, M. Mller, R. Macdonald, and H. Rinneberg. Evaluation of optical properties of highly scattering media by moments of distributions of times of flight of photons. *Applied Optics* **42**(28), 5785–5792 Oct (2003).

[46] S. R. Arridge, M. Cope, and D. T. Delpy. The theoretical basis for the determination of optical pathlengths in tissue: temporal and frequency analysis. *Physics in Medicine and Biology* **37**(7), 1531–1560 Jul (1992).

[47] S. R. Arridge, M. Hiraoka, and M. Schweiger. Statistical basis for the determination of optical pathlength in tissue. *Physics in Medicine and Biologyl* **40**(9), 1539–1558 Sep (1995).

[48] A. Sassaroli and S. Fantini. Comment on the modified beer-lambert law for scattering media. *Physics in Medicine and Biology* **49**(14), N255 (2004).

[49] A. Kienle and M. S. Patterson. Improved solutions of the steady-state and the time-resolved diffusion equations for reflectance from a semi-infinite turbid medium. *Journal of the Optical Society of America (A)* **14**(1), 246–254 (1997).

[50] B. W. Pogue and M. S. Patterson. Frequency-domain optical absorption spectroscopy of finite tissue volumes using diffusion theory. *Physics in Medicine and Biology* **39**, 1157–1180 (1994).

[51] T. Durduran, R. Choe, G. Q. Yu, C. Zhou, J. C. Tchou, B. J. Czerniecki, and A. G. Yodh. Diffuse optical measurement of blood flow in breast tumors. *Optics Letters* **30**, 2915–2917 (2005).

[52] B. J. Berne and R. Pecora. *Dynamic Light Scattering with Applications to Chemistry, Biology, and Physics*. Krieger Malabar, FL (1990).

[53] W. Brown. *Dynamic Light Scattering: The Method and Some Applications*. Clarendon New York (1993).

[54] B. Chu. *Laser Light Scattering, Basic Principles and Practice*. Academic New York (1991).

[55] P. A. Lemieux and D. J. Durian. Investigating non-gaussian scattering processes by using nth-order intensity correlation functions. *Journal of the Optical Society of America (A)* **16**(7), 1651–1664 (1999).

[56] D. A. Boas. *Diffuse Photon Probes of Structural and Dynamical Properties of Turbid Media: Theory and Biomedical Applications*. PhD thesis University of Pennsylvania Philadelphia, PA USA (1996).

[57] D. A. Boas, L. E. Campbell, and A. G. Yodh. Scattering and imaging with diffusing temporal field correlations. *Physical Review Letters* **75**(9), 1855–1858 (1995).

[58] M. J. Stephen. Temporal fluctuations in wave propagation in random media. *Physics Review B* **37**(1), 1–5 Jan (1988).

[59] F. C. MacKintosh and S. John. Diffusing-wave spectroscopy and multiple scattering of light in correlated random media. *Physics Review B.* **40**(4), 2383–2406 Aug (1989).

[60] C. Zhou. *In-Vivo Optical Imaging and Spectroscopy of Cerebral Hemodynamics*. PhD thesis University of Pennsylvania Philadelphia, PA USA (2007).

[61] C. Cheung, J. P. Culver, K. Takahashi, J. H. Greenberg, and A. G. Yodh. In vivo cerebrovascular measurement combining diffuse near-infrared absorption and correlation spectroscopies. *Physics In Medicine And Biology* **46**, 2053–2065 (2001).

[62] D. J. Pine, D. A. Weitz, P. M. Chaikin, and E. Herbolzheimer. Diffusing wave spectroscopy. *Physics Review Letters* **60**(12), 1134–1137 Mar (1988).

[63] D. A. Boas and A. G. Yodh. Spatially varying dynamical properties of turbid media probed with diffusing temporal light correlation. *Journal of the Optical Society of America (A)* **14**(1), 192–215 (1997).

[64] B. J. Ackerson, R. L. Dougherty, N. M. Reguigui, and U. Nobbman. Correlation transfer: Application of radiative transfer solution methods to photon correlation problems. *Journal Thermophysics and Heat Transport* **6**, 577–588 (1992).

[65] R. L. Dougherty, B. J. Ackerson, N. M. Reguigui, F. Dorri-Nowkoorani, and U. Nobbmann. Correlation transfer: Development and application. *Journal of Quantitative Spectroscopy and Radiative Transfer* **52**, 713–727 (1994).

[66] A. Despopoulos and S. Silbernagl. *Color Atlas of Physiology*. Theime 4 edition (1991).

[67] R. B. Buxton. *Introduction to functional magnetic resonance imaging: principles and techniques*. Cambridge Univ Pr (2002).

[68] E. R. Kandel, J. H. Schwartz, T. M. Jessell, S. Mack, and J. Dodd. *Principles of neural science* volume 3. Elsevier New York (1991).

[69] S. A. Carp, G. P. Dai, D. A. Boas, M. A. Franceschini, and Y. R. Kim. Validation of diffuse correlation spectroscopy measurements of rodent cerebral blood flow with simultaneous arterial spin

labeling MRI; towards MRI-optical continuous cerebral metabolic monitoring. *Biomed. Optics Express* **1**(2), 553–565 Sep (2010).

[70] G. Q. Yu, T. Durduran, G. Lech, C. Zhou, B. Chance, R. E. Mohler, and A. G. Yodh. Time-dependent blood flow and oxygenation in human skeletal muscles measured with noninvasive near-infrared diffuse optical spectroscopies. *Journal of Biomedical Optics* **10**, 024027–1–12 (2005).

[71] F. Jaillon, J. Li, G. Dietsche, T. Elbert, and T. Gisler. Activity of the human visual cortex measured non-invasively by diffusing-wave spectroscopy. *Optics Express* **15**(11), 6643–6650 (2007).

[72] U. Sunar, H. Quon, T. Durduran, J. Zhang, J. Du, C. Zhou, G. Yu, R. Choe, A. Kilger, R. Lustig, L. Loevner, S. Nioka, B. Chance, and A. G. Yodh. Noninvasive diffuse optical measurement of blood flow and blood oxygenation for monitoring radiation therapy in patients with head and neck tumors: a pilot study. *Journal of Biomedical Optics* **11**(6), 064021–064021 Nov-Dec (2006).

[73] C. Zhou, R. Choe, N. Shah, T. Durduran, G. Q. Yu, A. Durkin, A. Cerussi, D. Hsiang, R. Mehta, J. Butler, B. J. Tromberg, and A. G. Yodh. Diffuse optical monitoring of blood flow and oxygenation in human breast cancer during early stages of neoadjuvant chemotherapy. *Journal of Biomedical Optics* **12**, 051903 (2007).

[74] A. Cerussi, N. Shah, D. Hsiang, A. Durkin, J. Butler, and B. J. Tromberg. In vivo absorption, scattering, and physiologic properties of 58 malignant breast tumors determined by broadband diffuse optical spectroscopy. *Journal of Biomedical Optics* **11**, 044005 (16pp) (2006).

[75] B. Chance, S. Nioka, J. Zhang, E. F. Conant, E. Hwang, S. Briest, S. G. Orel, M. D. Schnall, and B. J. Czerniecki. Breast cancer detection based on incremental biochemical and physiological properties of breast cancers a six-year, two-site study. *Academic Radiology* **12**(8), 925–933 (2005).

[76] S. A. Walker, S. Fantini, and E. Gratton. Image reconstruction by backprojection from frequency-domain optical measurements in highly scattering media. *Applied Optics* **36**(1), 170–174 (1997).

[77] M. A. O'Leary, D. A. Boas, B. Chance, and A. G. Yodh. Experimental images of heterogeneous turbid media by frequency-domain diffusing-photon tomography. *Optics Letters* **20**, 426–428 (1995).

[78] A. C. Kak, M. Slaney, I. E. in Medicine, and B. Society. *Principles of Computerized Tomographic Imaging*. IEEE Press New York (1988).

[79] J. C. Schotland, J. C. Haselgrove, and J. S. Leigh. Photon hitting density. *Applied Optics* **32**(4), 448–453 (1993).

[80] R. Penrose. A generalized inverse for matrices. In *Proceedings of the Cambridge Philosphical Society* volume 51 pages 406–413 C655 (1955).

[81] Y. Chen. *Contrast Enhancement for diffuse optical spectroscopy and imaging: Phase cancellation and Targetted fluorescence in cancer detection*. PhD thesis University of Pennsylvania (2003).

[82] C. L. Lawson and R. J. Hanson. *Solving least squares problems*. Society for Industrial Mathematics (1995).

[83] P. C. Hansen. Analysis of discrete ill-posed problems by means of the l-curve. *SIAM review* **34**(4), 561–580 (1992).

[84] R. J. Gaudette, D. H. Brooks, C. A. DiMarzio, M. E. Kilmer, E. L. Miller, T. Gaudette, and D. A. Boas. A comparison study of linear reconstruction techniques for diffuse optical tomographic imaging of absorption coefficient. *Physics in Medicine and Biology* **45**(4), 1051–1070 Apr (2000).

[85] S. R. Arridge, M. Schweiger, M. Hiraoka, and D. T. Delpy. A finite element approach to modelling photon transport in tissue. *Medical Physics* **20**(2), 299–309 (1993).

[86] M. Schweiger, S. R. Arridge, and D. T. Delpy. Application of the finite element method for the forward and inverse problem in optical tomography. *Journal of Mathematical Imaging and Vision* **3**(3), 263–283 (1993).

[87] N. Deliolanis, T. Lasser, D. Hyde, A. Soubret, J. Ripoll, and V. Ntziachristos. Free-space fluorescence molecular tomography utilizing 360 geometry projections. *Optics Letters* **32**(4), 382–384 (2007).

[88] J. P. Culver, R. Choe, M. J. Holboke, L. Zubkov, T. Durduran, A. Slemp, V. Ntziachristos, B. Chance, and A. G. Yodh. Three-dimensional diffuse optical tomography in the parallel plane transmission geometry: Evaluation of a hybrid frequency domain/continuous wave clinical system for breast imaging. *Medical Physics* **30**, 235–247 (2003).

[89] A. Corlu, R. Choe, T. Durduran, M. A. Rosen, M. Schweiger, S. R. Arridge, and A. G. Yodh. Three-dimensional *in vivo* fluorescence diffuse optical tomography of breast cancer in humans. *Optics Express* **15**(11), 6696–6716 (2007).

[90] S. D. Konecky, G. Y. Panasyuk, K. Lee, V. A. Markel, A. G. Yodh, and J. C. Schotland. Imaging complex structures with diffuse light. *Optics Express* **16**(7), 5048–5060 (2008).

[91] V. A. Markel and J. C. Schotland. Inverse problem in optical diffusion tomography. i. fourier-laplace inversion formulas. *Journal of the Optical Society of America A* **18**(6), 1336–1347 (2001).

[92] V. A. Markel and J. C. Schotland. Inverse problem in optical diffusion tomography. ii. role of boundary conditions. *Journal of the Optical Society of America A* **19**(3), 558–566 Mar (2002).

[93] V. A. Markel, J. A. O'Sullivan, and J. C. Schotland. Inverse problem in optical diffusion tomography. iv. nonlinear inversion formulas. *Journal of the Optical Society of America A* **20**(5), 903–912 May (2003).

[94] B. Chance, J. S. Leigh, H. Miyake, D. S. Smith, S. Nioka, R. Greenfeld, M. Finander, K. Kaufmann, W. Levy, and M. Young. Comparison of time-resolved and -unresolved measurements of deoxyhemoglobin in brain. *Proceedings of the National Academy of Sciences of the USA* **85**(14), 4971–4975 Jul (1988).

[95] J. Selb, D. K. Joseph, and D. A. Boas. Time-gated optical system for depth-resolved functional brain imaging. *Journal of Biomedical Optics* **11**(4), 044008 (2006).

[96] X. Intes, S. Djeziri, Z. Ichalalene, N. Mincu, Y. Wang, P. St-Jean, F. Lesage, D. Hall, D. Boas, M. Polyzos, D. Fleiszer, and B. Mesurolle. Time-domain optical mammography softscan: initial results. *Academic Radiology* **12**(8), 934–947 Aug (2005).

[97] H. Rinneberg, D. Grosenick, K. T. Moesta, H. Wabnitz, J. Mucke, G. Wübbeler, R. Macdonald, and P. Schlag. Detection and characterization of breast tumours by time-domain scanning optical mammography. *Opto-Electronics Review* **16**(2), 147–162 (2008).

[98] A. Torricelli, A. Pifferi, L. Spinelli, R. Cubeddu, F. Martelli, S. D. Bianco, and G. Zaccanti. Time-resolved reflectance at null source-detector separation: improving contrast and resolution in diffuse optical imaging. *Physics Review Letters* **95**(7), 078101 Aug (2005).

[99] E. M. C. Hillman. *Experimental and theoretical investigations of near infrared tomographic imaging methods and clinical applications*. PhD thesis University College London (2002).

[100] E. Gratton, W. W. Mantulin, M. J. vandeVen, J. B. Fishkin, M. B. Maris, and B. Chance. The possibility of a near-infrared optical imaging system using frequency-domain methods. *Proceedings of the Third International Conference on Peace through Mind & Brain Science* , 183–189 (1990).

[101] A. Duncan, J. H. Meek, M. Clemence, C. E. Elwell, L. Tyszczuk, M. Cope, and D. T. Delpy. Optical pathlength measurements on adult head, calf and forearm and the head of the newborn infant using phase resolved optical spectroscopy. *Physics in Medicine and Biologyl* **40**(2), 295–304 Feb (1995).

[102] G. Alexandrakis, D. R. Busch, G. W. Faris, and M. S. Patterson. Determination of the optical properties of two-layer turbid media using a frequency domain hybrid monte carlo-diffusion model. *Applied Optics-OT* **40**(22), 3810–3821 (2000).

[103] T. O. McBride, B. W. Pogue, S. Jiang, U. L. Osterberg, K. D. Paulsen, P. McCullagh, and J. A. Nelder. A parallel-detection frequency-domain near-infrared tomography system for hemoglobin imaging of the breast *in vivo*. *Review of Scientific Instruments* , 1817–1824 (2001).

[104] G. Gulsen, B. Xiong, O. Birgul, and O. Nalcioglu. Design and implementation of a multifrequency near-infrared diffuse optical tomography system. *Journal of Biomedical Optics* **11**(1), 014020–1–9 January/Febuary (2006).

[105] M. A. Franceschini, K. T. Moesta, S. Fantini, G. Gaida, E. Gratton, H. Jess, W. W. Mantulin, M. Seeber, P. M. Schlag, and M. Kaschke. Frequency-domain techniques enhance optical mammography: initialclinical results. *Proceedings of the National Academy of Sciences of the USA* **94**(12), 6468–6473 Jun (1997).

[106] X. D. Li, T. Durduran, B. Chance, A. G. Yodh, and D. N. Pattanayak. Diffraction tomography for biochemical imaging with diffuse-photon density waves. *Optics Letters* **22**(8), 573–575 (1997).

[107] B. Pogue, M. Testorf, T. McBride, U. Osterberg, and K. Paulsen. Instrumentation and design of a frequency-domain diffuse optical tomography imager for breast cancer detection. *Optics Express* **1**(13), 391–403 (1997).

[108] S. J. Madsen, E. R. Anderson, R. C. Haskell, and B. J. Tromberg. Portable, high-bandwidth frequency-domain photon migration instrument for tissue spectroscopy. *Optics Letters* **19**(23), 1934–1936 (1994).

[109] F. Bevilacqua, A. J. Berger, A. E. Cerussi, D. Jakubowski, and B. J. Tromberg. Broadband absorption spectroscopy in turbid media by combined frequency-domain and steady-state methods. *Applied Optics* **39**(34), 6498–6507 (2000).

[110] E. M. Sevick-Muraca, G. Lopez, J. S. Reynolds, T. L. Troy, and C. L. Hutchinson. Fluorescence and absorption contrast mechanisms for biomedical optical imaging using frequency-domain techniques. *Photochemistry and Photobiology* **66**(1), 55–64 (1997).

[111] S. R. Arridge and W. R. Lionheart. Nonuniqueness in diffusion-based optical tomography. *Optics Letters* **23**(11), 882–884 Jun (1998).

[112] Y. Xu, X. Gu, T. Khan, and H. Jiang. Absorption and scattering images of heterogeneous scattering media can be simultaneously reconstructed by use of dc data. *Applied Optics* **41**(25), 5427–5437 Sep (2002).

[113] A. Corlu, T. Durduran, R. Choe, M. Schweiger, E. M. C. Hillman, S. R. Arridge, and A. G. Yodh. Uniqueness and wavelength optimization in continuous-wave multispectral diffuse optical tomography. *Optics Letters* **28**, 2339–2341 (2003).

[114] X. Intes and B. Chance. Multi-frequency diffuse optical tomography. *Journal of Modern Optics* **52**(15), 2139–2159 (2005).

[115] A. Cerussi, D. Hsiang, N. Shah, R. Mehta, A. Durkin, J. Butler, and B. J. Tromberg. Predicting response to breast cancer neoadjuvant chemotherapy using diffuse optical spectroscopy. *Proceedings of the National Academy of Science* **104**(10), 4014–4019 Mar (2007).

[116] N. Shah, A. E. Cerussi, D. Jakubowski, D. Hsiang, J. Butler, and B. J. Tromberg. Spatial variations in optical and physiological properties of healthy breast tissue. *Journal of Biomedical Optics* **9**(3), 534–540 (2004).

[117] A. Corlu, R. Choe, T. Durduran, K. Lee, M. Schweiger, E. M. C. Hillman, S. R. Arridge, and A. G. Yodh. Diffuse optical tomography with spectral constraints and wavelength optimization. *Applied Optics* **44**, 2082–2093 (2005).

[118] S. P. Gopinath, C. S. Robertson, R. G. Grossman, and B. Chance. Near-infrared spectroscopic localization of intracranial hematomas. *Journal of Neurosurgery* **79**(1), 43–47 Jul (1993).

[119] B. Chance, M. T. Dait, C. Zhang, T. Hamaoka, and F. Hagerman. Recovery from exercise-induced desaturation in the quadriceps muscles of elite competitive rowers. *American Journal of Physiology* **262**(3 Pt 1), C766–C775 Mar (1992).

[120] A. Li, R. Kwong, A. Cerussi, S. Merritt, C. Hayakawa, and B. Tromberg. Method for recovering quantitative broadband diffuse optical spectra from layered media. *Applied Optics* **46**(21), 4828–4833 Jul (2007).

[121] A. E. Cerussi, D. Jakubowski, N. Shah, F. Bevilacqua, R. Lanning, A. J. Berger, D. Hsiang, J. Butler, R. F. Holcombe, and B. J. Tromberg. Spectroscopy enhances the information content of optical mammography. *Journal of Biomedical Optics* **7**(1), 60–71 Jan (2002).

[122] D. S. Kepshire, S. C. Davis, H. Dehghani, K. D. Paulsen, and B. W. Pogue. Subsurface diffuse optical tomography can localize absorber and fluorescent objects but recovered image sensitivity is nonlinear with depth. *Applied Optics* **46**(10), 1669–1678 Apr (2007).

[123] J. Ge, B. Zhu, S. Regalado, and A. Godavarty. Three-dimensional fluorescence-enhanced optical tomography using a hand-held probe based imaging system. *Medical Physics* **35**(7), 3354–3363 (2008).

[124] L. C. Enfield, A. P. Gibson, N. L. Everdell, D. T. Delpy, M. Schweiger, S. R. Arridge, C. Richardson, M. Keshtgar, M. Douek, and J. C. Hebden. Three-dimensional time-resolved optical mammography of the uncompressed breast. *Applied Optics* **46**(17), 3628–3638 Jun (2007).

[125] S. P. Poplack, T. D. Tosteson, W. A. Wells, B. W. Pogue, P. M. Meaney, A. Hartov, C. A. Kogel, S. K. Soho, J. J. Gibson, and K. D. Paulsen. Electromagnetic breast imaging: results of a pilot study in women with abnormal mammograms. *Radiology* **243**(2), 350–359 May (2007).

[126] S. Nioka, Y. Yung, M. Shnall, S. Zhao, S. Orel, C. Xie, B. Chance, and L. Solin. Optical imaging of breast tumor by means of continuous waves. *Advances in Experimental Medicine and Biology* **411**, 227–232 (1997).

[127] J. H. Hoogenraad, M. B. van der Mark, S. B. Colak, G. W. Hooft, and E. S. van der Linden. First results from the philips optical mammoscope. *Photon Propagation in Tissues III* (1998).

[128] T. Nielsen, B. Brendel, R. Ziegler, M. van Beek, F. Uhlemann, C. Bontus, and T. Koehler. Linear image reconstruction for a diffuse optical mammography system in a noncompressed geometry using scattering fluid. *Applied Optics.* **48**(10), D1–D13 (2009).

[129] C. H. Schmitz, D. P. Klemer, R. Hardin, M. S. Katz, Y. Pei, H. L. Graber, M. B. Levin, R. D. Levina, N. A. Franco, W. B. Solomon, and R. L. Barbour. Design and implementation of dynamic near-infrared optical tomographic imaging instrumentation for simultaneous dual-breast measurements. *Applied Optics* **44**(11), 2140–2153 Apr (2005).

[130] T. Durduran, R. Choe, J. P. Culver, L. Zubkov, M. J. Holboke, J. Giammarco, B. Chance, and A. G. Yodh. Bulk optical properties of healthy female breast tissue. *Physics In Medicine And Biology* **47**, 2847–2861 (2002).

[131] D. Grosenick, H. Wabnitz, H. H. Rinneberg, K. T. Moesta, and P. M. Schlag. Development of a time-domain optical mammograph and first in vivo applications. *Applied Optics* **38**(13), 2927–2943 May (1999).

[132] L. Spinelli, A. Torricelli, A. Pifferi, P. Taroni, G. Danesini, and R. Cubeddu. Characterization of female breast lesions from multi-wavelength time-resolved optical mammography. *Physics in Medicine and Biologyl* **50**(11), 2489–2502 Jun (2005).

[133] A. Athanasiou, D. Vanel, L. Fournier, and C. Balleyguier. Optical mammography: a new technique for visualizing breast lesions in women presenting non palpable birads 4–5 imaging findings: preliminary results with radiologic–pathologic correlation. *Cancer Imaging* **7**(1), 34 (2007).

[134] L. S. Fournier, D. Vanel, A. Athanasiou, W. Gatzemeier, I. V. Masuykov, A. R. Padhani, C. Dromain, K. Galetti, R. Sigal, A. Costa, et al. Dynamic optical breast imaging: A novel technique to detect and characterize tumor vessels. *European Journal of Radiology* **69**(1), 43–49 (2009).

[135] S. Nioka and B. Chance. NIR spectroscopic detection of breast cancer. *Technology in Cancer Researchearch and Treatment* **4**(5), 497–512 Oct (2005).

[136] J. C. Hebden and D. T. Delpy. Diagnostic imaging with light. *British Journal of Radiology* **70 Spec No**, S206–S214 Nov (1997).

[137] V. Ntziachristos and B. Chance. Probing physiology and molecular function using optical imaging applications to breast cancer. *Breast Cancer Researchearch* **3**, 41–46 November (2001).

[138] R. Choe, A. Corlu, K. Lee, T. Durduran, S. D. Konecky, M. Grosicka-Koptyra, S. R. Arridge, B. J. Czerniecki, D. L. Fraker, A. DeMichele, B. Chance, M. A. Rosen, and A. G. Yodh. Diffuse optical tomography of breast cancer during neoadjuvant chemotherapy: A case study with comparison to MRI. *Medical Physics* **32**, 1128–1139 (2005).

[139] V. Ntziachristos and B. Chance. Accuracy limits in the determination of absolute optical properties using time-resolved NIR spectroscopy. *Medical Physics* **28**(6), 1115–1124 June (2001).

[140] J. R. Mourant, T. Fuselier, J. Boyer, T. M. Johnson, and I. Bigio. Predictions and measurements of scattering and absorption over broad wavelength ranges in tissue phantoms. *Applied Optics* **36**(4), 949–957 (1997).

[141] T. Durduran, C. Zhou, B. L. Edlow, G. Yu, R. Choe, M. N. Kim, B. L. Cucchiara, M. E. Putt, Q. Shah, S. E. Kasner, J. H. Greenberg, A. G. Yodh, and J. A. Detre. Transcranial optical monitoring of cerebrovascular hemodynamics in acute stroke patients. *Optics Express* **17**(5), 3884–3902 (2009).

[142] G. Yu, T. F. Floyd, T. Durduran, C. Zhou, J. Wang, J. A. Detre, and A. G. Yodh. Validation of diffuse correlation spectroscopy for muscle blood flow with concurrent arterial spin labeled perfusion MRI. *Optics Express* **15**, 1064–1075 (2007).

[143] D. R. Busch, C. Zhao, G. Yu, R. Choe, T. Durduran, M. Rosen, M. D. Schnall, and A. G. Yodh. Effects of compression on transillumination measurements of blood flow and chromophore concentrations in human breast tissue. In *OSA Biomedical Optics (BIOMED)*. OSA (2008).

[144] D. R. Busch, R. Choe, T. Durduran, S. M. D., M. A. Rosen, and A. G. Yodh. Change in microvascular blood flow and endogenous chromophores during mammographic-like compression of the human breast. In *European Conferences on Biomedical Optics* volume 19th page MO3 Munich, Germany (2009).

[145] D. R. Busch, R. Choe, T. Durduran, L. Chaby, M. A. Rosen, and A. G. Yodh. Measurement of microvascular blood flow in the human breast during compression with diffuse correlation spectroscopy. In *Photonics West BIOS* number 7174-75 in SPIE Proceedings. SPIE (2009).

[146] V. Ntziachristos, B. Chance, and A. G. Yodh. Differential diffuse optical tomography. *Optics Express* **5**, 230–242 (1999).

[147] S. R. Arridge and M. Schweiger. A gradient-based optimisation scheme for optical tomography. *Optics Express* **2**, 213 (1998).

[148] A. Liebert, H. Wabnitz, J. Steinbrink, M. Mller, R. Macdonald, H. Rinneberg, A. Villringer, and H. Obrig. Bed-side assessment of cerebral perfusion in stroke patients based on optical monitoring of a dye bolus by time-resolved diffuse reflectance. *Neuroimage* **24**(2), 426–435 Jan (2005).

[149] Laser Institute of America. American national standard for the safe use of lasers: Ansi z136.1-2000. Laser Institute of America, Suite 128, 13501 Ingenuity Drive, Orlando FL 32826 (2000).

[150] Food and Drug Administration. Code of federal regulations, title 21, volume 8. U. S. Government Printing Office via GPO Access April (2003). 21CFR1040.10.

[151] P. Bouguer. Essai d'optique sur la gradation de la lumiere. *Paris: C. Jombert; 164 p.: tavv. ft; in 12.; VII. 2.2. a* (1729).

[152] A. Beer. *Einleitung in die Elektrostatik, die Lehre vom Magnetismus und die Elektrodynamik*. (1854).

[153] M. Born and E. Wolf. *Principles of optics*. Pergamon Press New York 7th (expanded) edition (1999).

[154] D. T. Delpy, M. Cope, P. van der Zee, S. Arridge, S. Wray, and J. Wyatt. Estimation of optical pathlength through tissue from direct time of flight measurement. *Physics in Medicine and Biology* **33**(12), 1433–1442 (1988).

[155] M. Cope and D. T. Delpy. System for long-term measurement of cerebral blood and tissue oxygenation on newborn infants by near infra-red transillumination. *Medical and Biological Engineering and Computing* **26**(3), 289–294 (1988).

[156] H. Q. Woodard and D. R. White. The composition of body tissues. *British Journal of Radiology* **59**, 1209–19 (1986). Paper copy; from TD.

[157] M. K. Moaveni. *Multiple Scattering Field Theory Applied to Whole Blood*. University of Washington. (1970).

[158] J. M. Schmitt. *Optical measurement of blood oxygen by implantable telemetry*. Stanford University (1986).

[159] S. Takatani and M. D. Graham. Theoretical analysis of diffuse reflectance from a two-layer tissue model. *Biomedical Engineering, IEEE Transactions on* **BME-26**(12), 656–664 (2007).

[160] D. J. Segelstein. The complex refractive index of water. Master's thesis University of Missouri-Kansas City (1981).

[161] R. L. P. van Veen, H. Sterenborg, A. Pifferi, A. Torricelli, and R. Cubeddu. Determination of vis-nir absorption coefficients of mammalian fat, with time-and spatially resolved diffuse reflectance and transmission spectroscopy. In *Proceedings of OSA Biomedical Topical Meeting,CD-ROM, Paper SF5* volume SF5 Washington DC (2004). Optical Society of America.

[162] A. M. K. Nilsson, C. Sturesson, D. L. Liu, and S. Andersson-Engels. Changes in spectral shape of tissue optical properties in conjunction with laser-induced thermotherapy. *Applied Optics* **37**(7), 1256–1267 (1998).

[163] S. P. Poplack, K. D. Paulsen, A. Hartov, P. M. Meaney, B. W. Pogue, T. D. Tosteson, M. R. Grove, S. K. Soho, and W. A. Wells. Electromagnetic breast imaging: average tissue property values in women with negative clinical findings. *Radiology* **231**(2), 571–580 May (2004).

[164] B. J. Tromberg, A. Cerussi, N. Shah, M. Compton, A. Durkin, D. Hsiang, J. Butler, and R. Mehta. Imaging in breast cancer: diffuse optics in breast cancer: detecting tumors in pre-menopausal women and monitoring neoadjuvant chemotherapy. *Breast Cancer Research* **7**(6), 279–285 (2005).

[165] S. Jiang, B. W. Pogue, K. D. Paulsen, C. Kogel, and S. P. Poplack. In vivo near-infrared spectral detection of pressure-induced changes in breast tissue. *Optics Letters* **28**(14), 1212–1214 (2003).

[166] S. A. Carp, T. Kauffman, Q. Fang, E. Rafferty, R. Moore, D. Kopans, and D. Boas. Compression-induced changes in the physiological state of the breast as observed through frequency domain photon migration measurements. *Journal of Biomedical Optics* **11**(6), 064016 (2006).

[167] R. X. Xu, B. Qiang, J. J. Mao, and S. P. Povoski. Development of a handheld near-infrared imager for dynamic characterization of in vivo biological tissue systems. *Applied Optics* **46**(30), 7442–7451 (2007).

[168] K. T. Kotz, S. S. Dixit, A. D. Gibbs, J. M. Orduna, Z. Haroon, K. Amin, and G. W. Faris. Inspiratory contrast for in vivo optical imaging. *Optics Express* **16**(1), 19–31 Jan (2008).

[169] S. S. Dixit, H. Kim, C. Comstock, and G. W. Faris. Near infrared transillumination imaging of breast cancer with vasoactive inhalation contrast. *Biomedical Optics Express* **1**(1), 295–309 Aug (2010).

[170] E. M. Sevick-Muraca, J. P. Houston, and M. Gurfinkel. Fluorescence-enhanced, near infrared diagnostic imaging with contrast agents. *Current Opinion in Chemical Biology* **6**(5), 642–650 (2002).

[171] X. D. Li, B. Chance, and A. G. Yodh. Fluorescent heterogeneities in turbid media: limits for detection, characterization, and comparison with absorption. *Applied Optics* **37**, 6833–6844 (1998).

[172] S. Nioka, S. B. Colak, X. Li, Y. Yang, and B. Chance. Breast tumor images of hemodynamic information using a contrast agent with backprojection and fft enhancement. In *Advances in Optical Imaging and Photon Migration (AOIPM)* pages 266–270. Optical Society of America (1998).

[173] D. J. Cuccia, F. Bevilacqua, A. J. Durkin, S. Merritt, B. J. Tromberg, G. Gulsen, H. Yu, J. Wang, and O. Nalcioglu. *In vivo* quantification of optical contrast agent dynamics in rat tumors by use of diffuse optical spectroscopy with magnetic resonance imaging coregistration. *Applied Optics* **42**(16), 2940–2950 June (2003).

[174] K. R. Bhushan, E. Tanaka, and J. V. Frangioni. Synthesis of conjugatable bisphosphonates for molecular imaging of large animals. *Angew Chem Int Ed Engl* **46**(42), 7969–7971 (2007).

[175] X. D. Li, M. A. O'Leary, D. A. Boas, B. Chance, and A. G. Yodh. Fluorescent diffuse photon density waves in homogenous and heterogeneous turbid media: analytic solutions and applications. *Applied Optics* **35**, 3746–3758 (1996).

[176] M. A. OLeary, D. A. Boas, X. D. Li, B. Chance, and A. G. Yodh. Fluorescence lifetime imaging in turbid media. *Optics Letters* **21**, 158–160 (1996).

[177] M. A. Oleary, D. A. Boas, B. Chance, and A. G. Yodh. Reradiation and imaging of diffuse photon density waves using fluorescent inhomogeneities. *Journal Of Luminescence* **60-61**, 281–286 (1994).

[178] J. V. Frangioni. In vivo near-infrared fluorescence imaging. *Current Opinion in Chemical Biology* **7**(5), 626–634 (2003).

[179] E. M. Sevick-Muraca and J. C. Rasmussen. Molecular imaging with optics: primer and case for near-infrared fluorescence techniques in personalized medicine. *Journal of Biomedical Optics* **13**(4), 041303 (2008).

[180] J. S. Reynolds, T. L. Troy, R. H. Mayer, A. B. Thompson, D. J. Waters, K. K. Cornell, P. W. Snyder, and E. M. Sevick-Muraca. Imaging of spontaneous canine mammary tumors using fluorescent contrast agents. *Photochemistry and Photobiology* **70**(1), 87–94 (1999).

[181] S. Ke, X. Wen, M. Gurfinkel, C. Charnsangavej, S. Wallace, E. M. Sevick-Muraca, and C. Li. Near-infrared optical imaging of epidermal growth factor receptor in breast cancer xenografts. *Cancer Researchearch* **63**(22), 7870–7875 (2003).

[182] G. Soubrane, D. Kuhn, H. Oubraham, M. Quaranta, and G. Coscas. [new therapies for the treatment of age-related macular degeneration]. *Journal de la Société de biologie* **195**(2), 115–118 (2001).

[183] J. Klohs, A. Wunder, and K. Licha. Near-infrared fluorescent probes for imaging vascular pathophysiology. *Basic Research in Cardiology* **103**(2), 144–151 Mar (2008).

[184] V. Ntziachristos, J. P. Culver, and B. W. Rice. Small-animal optical imaging. *Journal of Biomedical Optics* **13**(1), 011001 (2008).

[185] C.-H. Tung. Fluorescent peptide probes for in vivo diagnostic imaging. *Biopolymers* **76**(5), 391–403 (2004).

[186] K. Licha, M. Schirner, and G. Henry. Optical agents. *Handbook of Experimental Pharmacology* **185**(1), 203–222 (2008).

[187] M. Hope-Ross, L. A. Yannuzzi, E. S. Gragoudas, D. R. Guyer, J. S. Slakter, J. A. Sorenson, S. Krupsky, D. A. Orlock, and C. A. Puliafito. Adverse reactions due to indocyanine green. *Opthamology* **101**(3), 529–533 March (1994).

[188] X. Intes, C. Maloux, M. Guven, B. Yazici, and B. Chance. Diffuse optical tomography with physiological and spatial a priori constraints. *Physics in Medicine and Biology* **49**(12), N155 (2004).

[189] A. Hagen, O. Steinkellner, D. Grosenick, M. Moller, R. Ziegler, T. Nielsen, K. Lauritsen, R. Macdonald, and H. Rinneberg. Development of a multi-channel time-domain fluorescence mammograph. *Proceedings of SPIE* **6434**, 64340Z (2007).

[190] A. Hagen, D. Grosenick, R. Macdonald, H. Rinneberg, S. Burock, P. Warnick, A. Poellinger, and P. M. Schlag. Late-fluorescence mammography assesses tumor capillary permeability and differentiates malignant from benign lesions. *Optics Express* **17**(19), 17016–17033 Sep (2009).

[191] D. Grosenick, A. Hagen, R. Macdonald, H. Rinneberg, A. Pllinger, S. Burock, and P. M. Schlag. Time-domain fluorescence imaging of breast cancer. In *European Conferences on Biomedical Optics* (2009).

[192] A. Poellinger, S. Burock, D. Grosenick, A. Hagen, L. Ludemann, F. Diekmann, F. Engelken, R. Macdonald, H. Rinneberg, and P. M. Schlag. Breast Cancer: Early-and Late-Fluorescence Near-Infrared Imaging with Indocyanine Green- Preliminary Study. *Radiology* **258**(2), 409 (2011).

[193] J. Patel, K. Marks, I. Roberts, D. Azzopardi, and A. D. Edwards. Measurement of cerebral blood flow in newborn infants using nearinfrared spectroscopy with indocyanine green. *Pediatric Research* **43**(1), 34–39 Jan (1998).

[194] E. Keller, A. Nadler, H. Imhof, P. Niederer, P. Roth, and Y. Yonekawa. New methods for monitoring cerebral oxygenation and hemodynamics in patients with subarachnoid hemorrhage. *Acta Neurochirurgica Supplement* **82**, 87–92 (2002).

[195] A. Liebert, H. Wabnitz, H. Obrig, R. Erdmann, M. Mller, R. Macdonald, H. Rinneberg, A. Villringer, and J. Steinbrink. Non-invasive detection of fluorescence from exogenous chromophores in the adult human brain. *Neuroimage* **31**(2), 600–608 Jun (2006).

[196] M. A. O'Leary, D. A. Boas, B. Chance, and A. G. Yodh. Reradiation and imaging of diffuse photon density waves using fluorescent inhomogeneities. *Journal of Luminescence* **60-61**, 281–286 (1994).

[197] X. Intes, J. Ripoll, Y. Chen, S. Nioka, A. G. Yodh, and B. Chance. *In vivo* continuous-wave optical breast imaging enhanced with indocyanine green. *Medical Physics* **30**(6), 1039–1047 (2003).

[198] V. Ntziachristos, X. H. Ma, and B. Chance. Time-correlated single photon counting imager for simultaneous magnetic resonance and near-infrared mammography. *Review of Scientific Instruments* **69**(12), 4221–4233 December (1998).

[199] Akorn Inc. IC-Green^{TM} Sterile Indocyanine Green. Drug Packaging Insert Version: 6-DCGN-01 (2006).

[200] E. M. Sevick-Muraca, R. Sharma, J. C. Rasmussen, M. V. Marshall, J. A. Wendt, H. Q. Pham, E. Bonefas, J. P. Houston, L. Sampath, K. E. Adams, D. K. Blanchard, R. E. Fisher, S. B. Chiang, R. Elledge, and M. E. Mawad. Imaging of lymph flow in breast cancer patients after microdose administration of a near-infrared fluorophore: feasibility study. *Radiology* **246**(3), 734–741 Mar (2008).

[201] E. M. Jung, L. Prantl, A. G. Schreyer, C. I. Schreyer, J. Rennert, M. Walter, W. Jung, P. Hoffstetter, T. Herold, N. Zorger, et al. New perfusion imaging of tissue transplants with Contrast Harmonic Ultrasound Imaging (CHI) and Magnetic Resonance Imaging (MRI) in comparison with laser-induced Indocyanine Green (ICG) fluorescence angiography. *Clinical hemorheology and microcirculation* **43**(1), 19–33 (2009).

[202] M. Bollow, M. Taupitz, B. Hamm, T. Staks, K. Wolf, and H. Weinmann. Gadolinium-ethoxybenzyl-DTPA as a hepatobiliary contrast agent for use in MR cholangiography: results of an in vivo phase-I clinical evaluation. *European Radiology* **7**(1), 126–132 (1997).

[203] N. Unno, M. Suzuki, N. Yamamoto, K. Inuzuka, D. Sagara, M. Nishiyama, H. Tanaka, and H. Konno. Indocyanine green fluorescence angiography for intraoperative assessment of blood flow: a feasibility study. *European journal of vascular and endovascular surgery* **35**(2), 205–207 (2008).

[204] H. Takao, H. Akai, T. Tajima, S. Kiryu, Y. Watanabe, H. Imamura, M. Akahane, N. Yoshioka, N. Kokudo, and K. Ohtomo. MR imaging of the biliary tract with Gd-EOB-DTPA: Effect of liver function on signal intensity. *European Journal of Radiology* (2009).

[205] M. R. Germans, P. C. de Witt Hamer, L. J. van Boven, K. A. H. Zwinderman, and G. J. Bouma. Blood volume measurement with indocyanine green pulse spectrophotometry: dose and site of dye administration. *Acta Neurochirurgica* **152**(2), 251–255 (2010).

[206] A. Jemal, R. Siegel, J. Xu, and E. Ward. Cancer statistics, 2010. *CA: A Cancer Journal for Clinicians* **60**(5), 277 (2010).

[207] E. D. Pisano, C. Gatsonis, E. Hendrick, M. Yaffe, J. K. Baum, S. Acharyya, E. F. Conant, L. L. Fajardo, L. Bassett, C. D'Orsi, R. Jong, M. Rebner, and D. M. I. S. T. D. I. Group. Diagnostic performance of digital versus film mammography for breast-cancer screening. *New England Journal of Medicine* **353**(17), 1773–1783 Oct (2005).

[208] M. Kriege, C. T. M. Brekelmans, C. Boetes, P. E. Besnard, H. M. Zonderland, I. M. Obdeijn, R. A. Manoliu, T. Kok, H. Peterse, M. M. A. Tilanus-Linthorst, S. H. Muller, S. Meijer, J. C. Oosterwijk, L. V. A. M. Beex, R. A. E. M. Tollenaar, H. J. de Koning, E. J. T. Rutgers, J. G. M. Klijn, and M. R. I. S. S. Group. Efficacy of MRI and mammography for breast-cancer screening in women with a familial or genetic predisposition. *New England Journal of Medicine* **351**(5), 427–437 Jul (2004).

[209] M. H. Gail, L. A. Brinton, D. P. Byar, D. K. Corle, S. B. Green, C. Schairer, and J. J. Mulvihill. Projecting individualized probabilities of developing breast cancer for white females who are being examined annually. *Journal of the National Cancer Institute* **81**(24), 1879 (1989).

[210] J. Chen, D. Pee, R. Ayyagari, B. Graubard, C. Schairer, C. Byrne, J. Benichou, and M. H. Gail. Projecting absolute invasive breast cancer risk in white women with a model that includes mammographic density. *Journal of the National Cancer Institute* **98**(17), 1215 (2006).

[211] T. J. Huppert, R. Hoge, S. Diamond, M. Franceschini, and D. Boas. A temporal comparison of bold, asl, and NIRS hemodynamic responses to motor stimuli in adult humans. *Neuroimage* **29**(2), 368–382 (2006).

[212] Q. Fang, S. A. Carp, J. Selb, G. Boverman, Q. Zhang, D. B. Kopans, R. H. Moore, E. L. Miller, D. H. Brooks, and D. A. Boas. Combined optical imaging and mammography of the healthy breast: optical

contrast derived from breast structure and compression. *IEEE Trans Med Imaging* **28**(1), 30–42 Jan (2009).

[213] M. Ohnishi, S. Masaki, K. Honda, N. Kusakawa, N. Hayashi, and K. Hirao. Evoked hemodynamic response of the auditory cortex measured by magnetoencephalography and near-infrared spectroscopy. *The Journal of the Acoustical Society of America* **100**, 2630 (1996).

[214] T. H. Sander, A. Liebert, B. M. Mackert, H. Wabnitz, S. Leistner, G. Curio, M. Burghoff, R. Macdonald, and L. Trahms. Dc-magnetoencephalography and time-resolved near-infrared spectroscopy combined to study neuronal and vascular brain responses. *Physiological Measurements* **28**(6), 651–664 Jun (2007).

[215] Q. Zhang, T. J. Brukilacchio, A. Li, J. J. Stott, T. Chaves, E. Hillman, T. Wu, M. Chorlton, E. Rafferty, R. H. Moore, D. B. Kopans, and D. A. Boas. Coregistered tomographic x-ray and optical breast imaging: initial results. *Journal of Biomedical Optics* **10**(2), 024033 (2005).

[216] Q. Zhu, E. B. Cronin, A. A. Currier, H. S. Vine, M. Huang, N. Chen, and C. Xu. Benign versus malignant breast masses: optical differentiation with us-guided optical imaging reconstruction. *Radiology* **237**(1), 57–66 Oct (2005).

[217] H. Jiang, C. Li, D. Pearlstone, and L. L. Fajardo. Ultrasound-guided microwave imaging of breast cancer: tissue phantom and pilot clinical experiments. *Medical Physics* **32**(8), 2528–2535 Aug (2005).

[218] G. Boverman, Q. Fang, S. A. Carp, E. L. Miller, D. H. Brooks, J. Selb, R. H. Moore, D. B. Kopans, and D. A. Boas. Spatio-temporal imaging of the hemoglobin in the compressed breast with diffuse optical tomography. *Physics in Medicine and Biology* **52**(12), 3619–3641 (2007).

[219] B. Brooksby, B. W. Pogue, S. Jiang, H. Dehghani, S. Srinivasan, C. Kogel, T. D. Tosteson, J. Weaver, S. P. Poplack, and K. D. Paulsen. Imaging breast adipose and fibroglandular tissue molecular signatures by using hybrid MRI-guided near-infrared spectral tomography. *Proceedings of the National Academy of Sciences of the USA* **103**(23), 8828–8833 Jun (2006).

[220] A. Kummrow, B. Ittermann, M. Moller, F. Seifert, F. Wojcik, W. Hoffmann, and H. Rinneberg. Concurrent multiple-projection optical and mr mammography. *Proceedings of SPIE* **5693**, 137 (2005).

[221] B. A. Brooksby, H. Dehghani, B. W. Pogue, and K. D. Paulsen. Near-infrared (nir) tomography breast image reconstruction with a priori structural information from MRI: Algorithm development for reconstructing heterogeneities. *IEEE JOURNAL OF SELECTED TOPICS IN QUANTUM ELECTRONICS* **9**(2), 199 (2003).

[222] M. A. Mastanduno, C. M. Carpenter, S. Srinivasan, S. Jiang, B. W. Pogue, and K. D. Paulsen. Three-Dimensional MR-Guided Optical Spectroscopy of the Breast: Optimizing Probe Placement for Improved Image Quality. *Digital Holography and Three-Dimensional Imaging* (2010).

[223] D. Thayer, N. Liu, B. Unlu, J.-H. Chen, M.-Y. Su, O. Nalcioglu, and G. Gulsen. Development of a combined multifrequency MRI-dot system for human breast imaging using a priori information. In F. S. Azar and X. Intes, editors, *Proceedings of SPIE* volume 7557 page 755711. SPIE (2010).

[224] B. Chance, Q. Luo, S. Nioka, D. C. Alsop, and J. A. Detre. Optical investigations of physiology. a study of intrinsic and extrinsic biomedical contrast. *Philosophical Transactions of the Royal Society B: Biological Sciences* **352**(1354), 707–716 (1997).

[225] A. Bassi, L. Spinelli, C. D'Andrea, A. Giusto, J. Swartling, A. Pifferi, A. Torricelli, and R. Cubeddu. Feasibility of white-light time-resolved optical mammography. *Journal of Biomedical Optics* **11**(5), 054035 (2006).

[226] D. Comelli, A. Bassi, A. Pifferi, P. Taroni, A. Torricelli, R. Cubeddu, F. Martelli, and G. Zaccanti. In vivo time-resolved reflectance spectroscopy of the human forehead. *Applied Optics* **46**(10), 1717–1725 Apr (2007).

[227] V. Ntziachristos. *Concurrent Diffuse Optical Tomography, Spectorscopy, and Magnetic Resonance Imaging of Breast Cancer*. PhD thesis University of Pennsylvania Philadelphia, PA USA (2000).

[228] V. Ntziachristos, X. H. Ma, A. G. Yodh, and B. Chance. Multichannel photon counting instrument for spatially resolved near infrared spectroscopy. *Review of Scientific Instruments* **70**, 193–201 (1999).

[229] X. Intes, J. Yu, A. G. Yodh, and B. Chance. Development and evaluation of a multi-wavelength multi-channel timeresolved optical instrument for nir/MRI mammography co-registration. *Bioengineering Conference, 2002. Proceedings of the IEEE 28th Annual Northeast* , 91–92 (2002).

[230] D. R. Busch, Z. Zhao, S. Nioka, A. G. Yodh, M. Schnall, B. Chance, and X. Intes. Fast CW imager for ICG and gd kinetics. In F. S. Azar and D. N. Metaxas, editors, *Proc. SPIE Vol. 6081, 60810R (Feb. 13, 2006)* number 60810R in Proceedings of the SPIE. SPIE Febuary (2006). Photonics West 2006.

[231] D. R. Busch, A. G. Yodh, Z. Zhao, X. Intes, B. Chance, and S. Nioka. Contrast agent pharmacokinetics in breast cancer: ICG and gd-dtpa. In *Fifth Inter-Institute Workshop on Optical Diagnostic Imaging from Bench to Bedside at the National Institutes of Health*. SPIE (2006). Poster.

[232] D. R. Busch, X. Intes, S. Nioka, and B. Chance. Comparison of imaged ICG and Gd kinetics with a DOT-MRI instrument. In *Biomedical Optics 2006 Technical Digest* number ME11 in Proceedings of the OSA. Optical Society of America, Washington, DC (2006).

[233] D. R. Busch, Z. Zhao, X. Intes, S. Nioka, M. A. Rosen, M. D. Schnall, B. Chance, and A. G. U. o. P. Yodh. Comparison of bulk optical and mr parameters in breast tissue. In *SPIE Optics East 6771 – Advanced Photon Counting Techniques II* number 6771-19 in Proceedings of the SPIE (2007).

[234] D. R. Busch, A. S. Rajput, T. Durduran, R. Choe, Z. Zhao, X. Intes, S. Nioka, B. Chance, M. A. Rosen, M. D. Schnall, and A. G. Yodh. A hybrid dynamical diffuse optical tomography & MRI mammography instrument. In *Photonics West BIOS* number 7171-21 in SPIE Proceedings. SPIE (2009).

[235] M. Guven, B. Yazici, X. Intes, and B. Chance. Diffuse optical tomography with a priori anatomical information. *Physics in Medicine and Biology* **50**(12), 2837 (2005).

[236] W. C. Wu, S. Englander, S. M. D., and D. J. Wang. Feasibility of arterial spin labeling in the measurement of breast perfusion. In *Proceedings of the International Society for Magnetic Resonance in Medicine* volume 13 page 2801. Proceedings of the International Society of Magnetic Resonance in Medicine (2007).

[237] E. M. Sevick-Muraca, J. P. Houston, and M. Gurfinkel. Fluorescence-enhanced, near infrared diagnostic imaging with contrast agents. *Current Opinion in Chemical Biology* **6**, 642–650 (2002).

[238] E. K. Insko, T. J. Connick, M. D. Schnall, and S. G. Orel. Multicoil array for high resolution imaging of the breast. *Magnetic Resonance in Medicine* **37**(5), 778–784 (1997).

[239] R. M. Mann, C. K. Kuhl, K. Kinkel, and C. Boetes. Breast MRI: guidelines from the European Society of Breast Imaging. *European Radiology* **18**(7), 1307–1318 Jul (2008).

[240] D. Saslow, C. Boetes, W. Burke, S. Harms, M. O. Leach, C. D. Lehman, E. Morris, E. Pisano, M. Schnall, S. Sener, R. A. Smith, E. Warner, M. Yaffe, K. S. Andrews, C. A. Russell, and A. C. S. B. C. A. Group. American cancer society guidelines for breast screening with MRI as an adjunct to mammography. *CA: A Cancer Journal for Clinicians* **57**(2), 75–89 (2007).

[241] S. P. Weinstein, A. R. Localio, E. F. Conant, M. Rosen, K. M. Thomas, and M. D. Schnall. Multimodality screening of high-risk women: a prospective cohort study. *Journal of Clinical Oncology* **27**(36), 6124 (2009).

[242] L. Dougherty, G. Isaac, M. A. Rosen, L. W. Nunes, P. J. Moate, R. C. Boston, M. D. Schnall, and H. K. Song. High frame-rate simultaneous bilateral breast dce-MRI. *Magnetic Resonance in Medicine* **57**(1), 220–225 Jan (2007).

[243] R. C. Boston, M. D. Schnall, S. A. Englander, J. R. Landis, and P. J. Moate. Estimation of the content of fat and parenchyma in breast tissue using MRI t_1 histograms and phantoms. *Magnetic Resonance Imaging* (2005).

[244] A. Corlu. *Multi-Spectral and Fluorescence Diffuse Optical Tomography of Breast Cancer*. PhD thesis University of Pennsylvania (2007).

[245] D. R. Busch, W. Guo, R. Choe, T. Durduran, M. D. Feldman, C. Mies, M. A. Rosen, M. D. Schnall, B. J. Czerniecki, J. Tchou, A. DeMichele, M. E. Putt, and A. G. Yodh. Computer aided automatic detection of malignant lesions in diffuse optical mammography. *Medical Physics* **37**(4) April (2010).

[246] D. R. Busch, R. Choe, T. Durduran, K. Lee, H. Y. Ban, M. E. Putt, W. Guo, M. A. Rosen, M. D. Schnall, and A. G. Yodh. Tissue-type image segmentation in optical mammography with population-derived probability functions: a step towards optical computer aided diagnosis. In *Photonics West BIOS* number 7174-30 in SPIE Proceedings. SPIE (2009).

[247] D. R. Busch, W. Guo, R. Choe, T. Durduran, S. Pathak, M. E. Putt, M. D. Schnall, M. A. Rosen, and A. G. Yodh. Computer aided detection for diffuse optical mammography. *Medical Physics, AAPM* **37**, 3405 (2010).

[248] D. R. Busch, W. Guo, R. Choe, T. Durduran, S. Pathak, M. E. Putt, M. D. Schnall, M. A. Rosen, and A. G. Yodh. Automatic tumor localization and characterization in diffuse optical tomography. In *Gordon Research Conferences* volume Lasers in Medicine and Biology Holderness, NH (2010).

[249] F. Winsberg, M. Elkin, J. Macy, V. Bordaz, and W. Weymouth. Detection of radiographic abnormalities in mammograms by means of optical scanning and computer analysis. *Radiology* **89**, 211–215 (1967).

[250] C. J. Vyborny, M. L. Giger, and R. M. Nishikawa. Computer-aided detection and diagnosis of breast cancer. *Radiol Clin North Am* **38**(4), 725–740 Jul (2000).

[251] S. J. Kim, W. K. Moon, N. Cho, J. H. Cha, S. M. Kim, and J.-G. Im. Computer-aided detection in full-field digital mammography: sensitivity and reproducibility in serial examinations. *Radiology* **246**(1), 71–80 Jan (2008).

[252] I. J. Fidler. Tumor heterogeneity and the biology of cancer invasion and metastasis. *Cancer Research* **38**(9), 2651–2660 Sep (1978).

[253] T. Reya, S. J. Morrison, M. F. Clarke, and I. L. Weissman. Stem cells, cancer, and cancer stem cells. *Nature* **414**(6859), 105–111 Nov (2001).

[254] Y. Chen, G. Zheng, Z. H. Zhang, D. Blessington, M. Zhang, H. Li, Q. Liu, L. Zhou, X. Intes, S. Achilefu, and B. Chance. Metabolism-enhanced tumor localization by fluorescence imaging: in vivo animal studies. *Optics Letters* **28**(21), 2070–2072 Nov (2003).

[255] C. D. Klose, A. D. Klose, U. Netz, J. Beuthan, and A. H. Hielscher. Multiparameter classifications of optical tomographic images. *Journal of Biomedical Optics* **13**(5), 050503 (3pp) (2008).

[256] M. K. Simick, R. Jong, B. Wilson, and L. Lilge. Non-ionizing near-infrared radiation transillumination spectroscopy for breast tissue density and assessment of breast cancer risk. *Journal of Biomedical Optics* **9**(4), 794–803 (2004).

[257] K. Blyschak, M. Simick, R. Jong, and L. Lilge. Classification of breast tissue density by optical transillumination spectroscopy: optical and physiological effects governing predictive value. *Medical Physics* **31**(6), 1398–1414 Jun (2004).

[258] K. M. Blackmore, J. A. Knight, R. Jong, and L. Lilge. Assessing breast tissue density by transillumination breast spectroscopy (tibs): an intermediate indicator of cancer risk. *British Journal of Radiology* **80**(955), 545–556 Jul (2007).

[259] C. Zhu, T. M. Breslin, J. Harter, and N. Ramanujam. Model based and empirical spectral analysis for the diagnosis of breast cancer. *Optics Express* **16**(19), 14961–14978 Sep (2008).

[260] X. Song, B. W. Pogue, S. Jiang, M. M. Doyley, H. Dehghani, T. D. Tosteson, and K. D. Paulsen. Automated region detection based on the contrast-to-noise ratio in near-infrared tomography. *Applied Optics* **43**(5), 1053–1062 (2004).

[261] B. W. Pogue, S. C. Davis, X. Song, B. A. Brooksby, H. Dehghani, and K. D. Paulsen. Image analysis methods for diffuse optical tomography. *Journal of Biomedical Optics* **11**(3), 033001 (16pp) (2006).

[262] J. Z. Wang, X. Liang, Q. Zhang, L. L. Fajardo, and H. Jiang. Automated breast cancer classification using near-infrared optical tomographic images. *Journal of Biomedical Optics* **13**, 044001 (10pp) (2008).

[263] N. Shah, A. E. Cerussi, D. Jakubowski, D. Hsiang, J. Butler, and B. J. Tromberg. The role of diffuse optical spectroscopy in the clinical management of breast cancer. *Disease Markers* **19**(2), 95–105 (2004).

[264] S. Kukreti, A. Cerussi, B. Tromberg, and E. Gratton. Intrinsic tumor biomarkers revealed by novel double-differential spectroscopic analysis of near-infrared spectra. *Journal of Biomedical Optics* **12**(2), 020509 (2007).

[265] X. Song, B. W. Pogue, T. D. Tosteson, T. O. McBride, S. Jiang, and K. D. Paulsen. Statistical analysis of nonlinearly reconstructed near-infrared tomographic images. ii. experimental interpretation. *IEEE Transactions on Medical Imaging* **21**(7), 764–772 (2002).

[266] T. Hastie, R. Tibshirani, and J. Friedman. *The Elements of Statistical Learning: Data Mining, Inference, and Prediction.* Springer Science+Business Media, LLC, New York, USA second (corrected 3rd printing) edition (2009).

[267] P. Taroni, G. Danesini, A. Torricelli, A. Pifferi, L. Spinelli, and R. Cubeddu. Clinical trial of time-resolved scanning optical mammography at 4 wavelengths between 683 and 975 nm. *Journal of Biomedical Optics* **9**(3), 464–473 (2004).

[268] P. Taroni, A. Torricelli, L. Spinelli, A. Pifferi, F. Arpaia, G. Danesini, and R. Cubeddu. Time-resolved optical mammography between 637 and 985 nm: clinical study on the detection and identification of breast lesions. *Physics in Medicine and Biologyl* **50**(11), 2469–2488 Jun (2005).

[269] D. Grosenick, H. Wabnitz, K. T. Moesta, J. Mucke, P. M. Schlag, and H. Rinneberg. Time-domain scanning optical mammography: Ii. optical properties and tissue parameters of 87 carcinomas. *Physics in Medicine and Biology* **50**(11), 2451–2468 Jun (2005).

[270] D. Grosenick, K. T. Moesta, M. Mller, J. Mucke, H. Wabnitz, B. Gebauer, C. Stroszczynski, B. Wassermann, P. M. Schlag, and H. Rinneberg. Time-domain scanning optical mammography: I. recording and assessment of mammograms of 154 patients. *Physics in Medicine and Biology* **50**(11), 2429–2449 Jun (2005).

[271] D. Grosenick, K. T. Moesta, H. Wabnitz, J. Mucke, C. Stroszczynski, R. Macdonald, P. M. Schlag, and H. Rinneberg. Time-domain optical mammography: initial clinical results on detection and characterization of breast tumors. *Applied Optics* **42**(16), 3170–3186 Jun (2003).

[272] B. W. Pogue, S. Jiang, H. Dehghani, C. Kogel, S. Soho, S. Srinivasan, X. Song, T. D. Tosteson, S. P. Poplack, and K. D. Paulsen. Characterization of hemoglobin, water, and NIR scattering in breast tissue: analysis of intersubject variability and menstrual cycle changes. *Journal of Biomedical Optics* **9**, 541 (2004).

[273] A. E. Cerussi, A. J. Berger, F. Bevilacqua, N. Shah, D. Jakubowski, J. Butler, R. F. Holcombe, and B. J. Tromberg. Sources of absorption and scattering contrast for near-infrared optical mammography. *Academic Radiology* **8**(3), 211–218 (2001).

[274] M. S. Pepe. *The Statistical Evaluation of Medical Tests for Classification and Prediction*. Oxford University Press, New York USA (2003).

[275] N. E. Breslow, N. E. Day, and W. Davis. *Statistical methods in cancer research (Vol. 1)?The Analysis of Casecontrol Studies. Number 32 in IARC Scientific Publications*. International Agency for Research on Cancer (1980).

[276] P. McCullagh and J. A. Nelder. *Generalized Linear Models*. Chapman & Hall/CRC (1989).

[277] J. Hebden, S. Arridge, and D. Delpy. Optical imaging in medicine: I. experimental techniques. *Physics in Medicine and Biology* **42**, 825–840 (1997).

[278] J. P. Culver, V. Ntziachristos, M. J. Holboke, and A. G. Yodh. Optimization of optode arrangements for diffuse optical tomography: A singular-value analysis. *Optics Letters* **26**, 701–703 (2001).

[279] V. A. Markel and J. C. Schotland. Scanning paraxial optical tomography. *Optics Letters* **27**(13), 1123–1125 Jul (2002).

[280] R. W. Carlson and A. M. Favret. Multidisciplinary management of locally advanced breast cancer. *Breast Journal* **5**(5), 303–307 (1999).

[281] B. Fisher, J. Bryant, N. Wolmark, E. Mamounas, A. Brown, E. R. Fisher, D. L. Wickerham, M. Begovic, A. DeCillis, A. Robidoux, et al. Effect of preoperative chemotherapy on the outcome of women with operable breast cancer. *Journal of Clinical Oncology* **16**(8), 2672 (1998).

[282] R. K. Jain. Molecular regulation of vessel maturation. *Nature medicine* **9**(6), 685–693 (2003).

[283] S. A. Carp, J. Selb, Q. Fang, R. Moore, D. B. Kopans, E. Rafferty, and D. A. Boas. Dynamic functional and mechanical response of breast tissue to compression. *Optics Express* **16**(20), 16064–16078 Sep (2008).

[284] U. S. Preventive Services Task Force. Screening for Breast Cancer: Recommendation statement. AHRQ Publication No. 10-05142-EF-2 November (2009).

[285] B. O. Anderson, C.-H. Yip, R. A. Smith, R. Shyyan, S. F. Sener, A. Eniu, R. W. Carlson, E. Azavedo, and J. Harford. Guideline implementation for breast healthcare in low-income and middle-income countries: overview of the breast health global initiative global summit 2007. *Cancer* **113**(8 Suppl), 2221–2243 Oct (2008).

[286] M. P. Coleman, M. Quaresma, F. Berrino, J.-M. Lutz, R. D. Angelis, R. Capocaccia, P. Baili, B. Rachet, G. Gatta, T. Hakulinen, A. Micheli, M. Sant, H. K. Weir, J. M. Elwood, H. Tsukuma, S. Koifman, G. A. E. Silva, S. Francisci, M. Santaquilani, A. Verdecchia, H. H. Storm, J. L. Young, and C. O. N. C. O. R. D. W. Group. Cancer survival in five continents: a worldwide population-based study (concord). *Lancet Oncology* **9**(8), 730–756 Aug (2008).

[287] R. Klein, H. Aichinger, J. Dierker, J. T. M. Jansen, S. Joite-Barfuss, M. Sabel, R. Schulz-Wendtland, and J. Zoetelief. Determination of average glandular dose with modern mammography units for two large groups of patients. *Physics in Medicine and Biology* **42**(4), 651–671 (1997).

[288] L. T. Niklason, B. T. Christian, L. E. Niklason, D. B. Kopans, D. E. Castleberry, B. H. Opsahl-Ong, C. E. Landberg, P. J. Slanetz, A. A. Giardino, R. Moore, et al. Digital tomosynthesis in breast imaging. *Radiology* **205**(2), 399–406 (1997).

[289] S. C. Chen, A.-K. Carton, M. Albert, E. F. Conant, M. D. Schnall, and A. D. A. Maidment. Initial clinical experience with contrast-enhanced digital breast tomosynthesis. *Academic Radiology* **14**(2), 229–238 Feb (2007).

[290] L. Spinelli, A. Torricelli, A. Pifferi, P. Taroni, G. M. Danesini, and R. Cubeddu. Bulk optical properties and tissue components in the female breast from multiwavelength time-resolved optical mammography. *Journal of Biomedical Optics* **9**(6), 1137–1142 (2004).

[291] H. Rinneberg, D. Grosenick, K. T. Moesta, J. Mucke, B. Gebauer, C. Stroszczynski, H. Wabnitz, M. Moeller, B. Wassermann, and P. M. Schlag. Scanning time-domain optical mammography: detection and characterization of breast tumors in vivo. *Technology Cancer Researchearch and Treatment* **4**(5), 483–496 Oct (2005).

[292] S. Nioka, S. Wen, J. Zhang, J. Du, X. Intes, Z. Zhao, and B. Chance. Simulation study of breast tissue hemodynamics during pressure perturbation. *Advances in Experimental Medicine and Biology* **566**, 17–22 (2005).

[293] S. D. Jiang, B. W. Pogue, and A. M. Laughney. Measurement of pressure-displacement kinetics of hemoglobin in normal breast tissue with near-infrared spectral imaging. *Applied Optics* **48**(10) (2009).

[294] T. Durduran. *Noninvasive measurements of tissue hemodynamics with hybrid diffuse optical methods*. PhD thesis University of Pennsylvania Philadelphia, PA USA (2004).

[295] T. Durduran, C. Zhou, B. L. Edlow, G. Yu, R. Choe, M. N. Kim, B. L. Cucchiara, M. E. Putt, Q. Shah, S. E. Kasner, J. H. Greenberg, A. G. Yodh, and J. A. Detre. Transcranial optical monitoring of cerebrovascular hemodynamics in acute stroke patients. *Optics Express* **17**(5), 3884–3902 (2009).

[296] M. Kim, T. Durduran, S. Frangos, B. Edlow, E. Buckley, H. Moss, C. Zhou, G. Yu, R. Choe, E. Maloney-Wilensky, R. Wolf, M. Grady, J. Greenberg, J. Levine, A. Yodh, J. Detre, and W. Kofke. Noninvasive measurement of cerebral blood flow and blood oxygenation using near-infrared and diffuse correlation spectroscopies in critically brain-injured adults. *Neurocritical Care* **12**(2), 173–180 April (2010).

[297] J. Lorenzen, R. Sinkus, M. Biesterfeldt, and G. Adam. Menstrual-cycle dependence of breast parenchyma elasticity: estimation with magnetic resonance elastography of breast tissue during the menstrual cycle. *Investigative radiology* **38**(4), 236 (2003).

[298] R. Cubeddu, C. D'Andrea, A. Pifferi, P. Taroni, A. Torricelli, and G. Valentini. Effects of the menstrual cycle on the red and near-infrared optical properties of the human breast. *Photochemistry and Photobiology* **72**(3), 383–391 (2000).

[299] A. Samani, J. Zubovits, and D. Plewes. Elastic moduli of normal and pathological human breast tissues: an inversion-technique-based investigation of 169 samples. *Physics in Medicine and Biology* **52**(6), 1565 (2007).

[300] T. A. Krouskop, T. M. Wheeler, F. Kallel, B. S. Garra, and T. Hall. Elastic moduli of breast and prostate tissues under compression. *Ultrasonic imaging* **20**(4), 260 (1998).

[301] P. Wellman, R. D. Howe, E. Dalton, and K. A. Kern. Breast tissue stiffness in compression is correlated to histological diagnosis. *Harvard BioRobotics Laboratory Technical Report* (1999).

[302] J. J. O'Hagan and A. Samani. Measurement of the hyperelastic properties of 44 pathological ex vivo breast tissue samples. *Physics in Medicine and Biology* **54**(8), 2557 (2009).

[303] F. S. Azar, D. N. Metaxas, and M. D. Schnall. Methods for modeling and predicting mechanical deformations of the breast under external perturbations. *Medical Image Analysis* **6**(1), 1 – 27 (2002).

[304] T. Carter, C. Tanner, N. Beechey-Newman, D. Barratt, and D. Hawkes. Mr navigated breast surgery: method and initial clinical experience. *Medical Image Computing and Computer-Assisted Intervention–MICCAI 2008* , 356–363 (2008). 3D MRI- prone during MRI, but supine during surgery. Deformation to account for; 5mm accuracy, quasi static. Waiting to get a copy of the book.

[305] C. Tanner, M. White, S. Guarino, M. A. Hall-Craggs, M. Douek, and D. J. Hawkes. Large breast compressions: Observations and evaluation of simulations. *Medical Physics* **38**(2), 682–690 (2011).

[306] J. Ophir, I. Cespedes, H. Ponnekanti, Y. Yazdi, and X. Li. Elastography: a quantitative method for imaging the elasticity of biological tissues. *Ultrasonic imaging* **13**(2), 111–134 (1991).

[307] A. L. McKnight, J. L. Kugel, P. J. Rossman, A. Manduca, L. C. Hartmann, and R. L. Ehman. Mr elastography of breast cancer: preliminary results. *American Journal of Roentgenology* **178**(6), 1411 (2002).

[308] Y. C. Fung. *Biomechanics: Mechanical Properties of Living Tissue*. Springer-Verlag (1981).

[309] J. Humphrey. Review paper: Continuum biomechanics of soft biological tissues. *Proceedings of the Royal Society of London. Series A: Mathematical, Physical and Engineering Sciences* **459**(2029), 3 (2003).

[310] D. L. Minkoff, D. R. Busch, E. M. Buckley, T. Durduran, D. J. Licht, and A. G. Yodh. SU-GG-I-171: Diffuse optical measurements of blood oxygenation and flow for monitoring CMRO_2 in neonates with congenital heart defects. *Medical Physics* **37**(6), 3141–3141 (2010).

[311] R. A. McPherson and M. R. Pincus. *Henry's clinical diagnosis and management by laboratory methods*. Saunders Elsevier Philadelphia 21st edition (2007).

[312] R. Choe. *Diffuse Optical Tomography and Spectroscopy of Breast Cancer and Fetal Brain*. Phd University of Pennsylvania Dept. Physics, UPenn, 209 S. 33rd St. Philadelphia PA 19104 (2005).

[313] A. Wretlind. Development of fat emulsions. *Journal of Parenteral and Enteral Nutrition* **5**(3), 230 (1981).

[314] I. Driver, J. W. Feather, P. R. King, and J. B. Dawson. The optical properties of aqueous suspensions of intralipid, a fat emulsion. *Physics in Medicine and Biology* **34**, 1927–1930 (1989).

[315] H. J. van Staveren, C. J. M. Moes, J. van Marie, S. A. Prahl, and M. J. C. van Gemert. Light scattering in intralipid-10% in the wavelength range of 400–1100 nm. *Applied Optics* **30**(31), 4507–4514 Nov (1991).

Index